



ScuDo

Scuola di Dottorato ~ Doctoral School
WHAT YOU ARE, TAKES YOU FAR



Doctoral Dissertation
Doctoral Program in Materials Science and Technology (31st Cycle)

Inconel 718 superalloy produced through Selective Laser Melting for harsh environment applications

Michele Calandri

* * * * *

Supervisor

Prof. D. Ugues

Doctoral Examination Committee:

Prof. S. Biamino, Politecnico di Torino,

Dipartimento Scienza Applicata e Tecnologia

Prof. Z. Brytan, Referee, Silesian University of Technology,

Institute of Engineering Materials and Biomaterials

Prof. M. Cabrini, Referee, Università degli Studi di Bergamo,

Dipartimento di Ingegneria e Scienze Applicate

Prof. M. Lombardi, Politecnico di Torino,

Dipartimento Scienza Applicata e Tecnologia

Prof. A. Miren, CEIT Centro de Estudios e Investigaciones Técnicas de Gipuzkoa,

Division of Materials & Manufacturing

Politecnico di Torino

2019

This thesis is licensed under a Creative Commons License, Attribution - Noncommercial - NoDerivative Works 4.0 International: see www.creativecommons.org. The text may be reproduced for non-commercial purposes, provided that credit is given to the original author.

I hereby declare that, the contents and organisation of this dissertation constitute my own original work and does not compromise in any way the rights of third parties, including those relating to the security of personal data.

Calandri Michele
Turin, June 6, 2019

Summary

The Additive Manufacturing (AM) is an innovative concept for the semi-automated production of components of very complex shape. The growing interest in this technology is justified by the unique possibility to produce parts which are difficult or even impossible to obtain with the conventional production techniques and with an important saving on the material and the costs of molds, dies and tools.

The additive production of nickel-based super-alloys from pre-alloyed powders is particularly interesting in the aerospace field and for applications in the chemical and energy production plants. However, the nickel-based superalloys are not all equally suitable for this application and whenever a new alloy is used in an additive technique, a preliminary study is required in order to find out the process parameters that allow to obtain a dense and defect-free product. Furthermore, the post processing heat treatment has to be optimized to account for the specific features of as built microstructure. The combination of processing parameters and post heat treatment condition highly affects the ultimate performance of the AM alloys, which in some cases may be even higher than those of traditional materials.

This thesis focuses on the processability, post-heat treatment and oxidation resistance of Inconel 718 alloy produced through Selective Laser Melting (SLM). The major target is to demonstrate the feasibility of using such alloy for the AM fabrication of complex components especially dedicated to high temperature service and harsh condition. The final type of components we have in mind is a high temperature heat exchanger, where the possibility to achieve safe and complex hollow structures is highly appealing.

After a preliminary study on the effect of the main process parameters on the residual porosity and the Brinell hardness, the microstructure of the as built SLM Inconel 718 was investigated. The collected observations are reported in chapter 3. A very heterogeneous microstructure and a strong [001] crystallographic texturing

was observed during this study. Other important features observed in the as built state are: the extremely fine dendritic sub-granular structure (the mean interdendritic distance is about 1 μm), the strong microsegregation with consequent non-equilibrium eutectic products formation and the high dislocations density at dendrites boundaries.

Starting from such highly heterogeneous structure, a post-heat treatment is normally required to optimize the final microstructure and remove the unwanted features. The study on the post heat treatment effects is reported at chapter 4. The response of the as built material to a thermal exposure was preliminary investigated by Differential Scanning Calorimetry (DSC) and Thermomechanical Analysis (TMA) in order to establish the solutioning range and the characteristic temperatures at which the precipitation of second phases occurs. Then, the optimization of the solution step was performed to obtain the maximum degree of dissolution of the eutectic phases present in the as-built state and to avoid the precipitation of new second unwanted phases and the occurrence of grain coarsening. At last, each step of the complete heat treatment cycle, i.e. solution annealing, first aging and second aging, has been optimized through the measurement of the hardness and the investigation of the as-treated microstructure.

The outcome of the thesis was the definition of the optimal heat treatment to maximize the oxidation resistance of the SLM Inconel 718. Few information is currently available in the scientific literature concerning the hot oxidation resistance of Inconel 718 produced through SLM. Therefore, short, medium and long-term oxidation tests have been performed and the results are reported in chapter 5. The structure and morphology of the oxide scale that forms after prolonged thermal exposure has also been investigated in detail. The oxidation resistance was assessed with oxidation runs up to 900 h at 850°C.

Finally, chapter 6 reports a study on the pack aluminization technique applied to SLM Inconel 718 for applications requiring additional surface protection. Such coating formation was studied to further improve the corrosion resistance of this alloy, trying to allow the possibility to work at even higher operating temperature.

The microstructures of the aluminized coatings resulting from different combinations of powder pack compositions and treatment temperatures have been investigated. Furthermore, the proposed mechanisms of coating formation and degradation are described. The coating oxidation and degradation occur both during the deposition process itself and during the subsequent thermal exposure. Despite of the work done, this technique especially on cavities and rough surfaces has to be highly improved, since it is very hard to obtain a defect-free and stable coating.

Acknowledgment

Part of the work reported in this thesis was supported by the European Space Agency (ESA Frame Contract number 4000112844/14/NL/FE) and was enabled by the CRANN Advanced Microscopy Laboratory (AML) at Dublin.

Furthermore, part of the work was funded by the European Union's Seventh Framework Programme for the Fuel Cells and Hydrogen Joint Technology Initiative under grant agreement n° 621210 for the HELMETH project (Integrated High-Temperature Electrolysis and Methanation for Effective Power to Gas Conversion).

I hereby would like to acknowledge Dr. Manfredi Diego and Lorusso Massimo of the Center for Sustainable Futures Technologies - CSFT@POLITO, Istituto Italiano di Tecnologia (IIT), Dr. Ambrosio Elisa Paola of the Research Support Department, Politecnico di Torino, and Dr. Calignano Flaviana of the Department of Management and Production Engineering (DIGEP), Politecnico di Torino, for their contribution regarding the production of all the analysed samples and for their precious help and advises during all the stages of the follow characterization.

I also would like to thank all people I am glad to have met during my period abroad at the Trinity College of Dublin for their friendship and willingness, especially Prof. Lupoi Rocco, Prof. Yin Shuo and Dr. Aldwell Barry for their fundamental collaboration.

Special thanks are due to my tutor Prof. Ugues Daniele and to Prof. Biamino Sara, Prof. Lombardi Mariangela, Prof. Pavese Matteo and all people of the Department of Applied Science and Technology (DISAT) staff I have had the pleasure to work with.

Finally, I would like to express my gratitude to my girlfriend Federica and to my parents Piero and Gabriella for their constant support even during the hardest periods of my Ph.D experience and for the love I receive by them every day.

*I would like to dedicate
this thesis to all people
that made it possible
with their technical,
economic or moral
support.*

Contents

1 Literature review	1
1.1 The superalloys	1
1.1.1 Production techniques	1
1.1.1.1 Casting.....	2
1.1.1.2 Wrought.....	2
1.1.1.3 Powder metallurgy and HIP	3
1.1.2 Superalloys categories.....	4
1.1.2.1 Iron-based superalloys.....	4
1.1.2.2 Nickel-based superalloys	5
1.1.2.3 Cobalt-based superalloys	6
1.2 Categories and features of nickel-based superalloys.....	6
1.2.1 Solid solution strengthened alloys.....	8
1.2.2 Precipitation hardening alloys	9
1.2.3 Weldability	9
1.3 Inconel 718 alloy	11
1.3.1 Microstructure and phases.....	11
1.3.1.1 Carbides.....	12
1.3.1.2 Topologically Close Packed (TCP) phases	13
1.3.1.3 Delta phase	14
1.3.1.4 Gamma double prime phase.....	16
1.3.1.5 Gamma prime phase.....	17
1.3.2 Solidification	19
1.3.2.1 Microsegregation: partition coefficient and Scheil's model ...	19
1.3.2.2 Morphology of the solidification front.....	23
1.3.2.3 The fast solidification path.....	25
1.3.3 The standard heat treatments.....	27
1.3.4 Physical and mechanical properties	29
1.3.5 Creep and high temperature fatigue resistance	33

1.3.6 Hot oxidation resistance	36
1.3.7 Pack aluminization	41
1.4 Additive manufacturing.....	47
1.4.1 SLM: general process features and most common defects	48
1.4.2 SLM applied to Inconel 718 alloy.....	53
1.4.2.1 Porosity and microstructure of SLM Inconel 718.....	54
1.4.2.2 Post process: heat treatments and HIP.....	59
2 Materials and characterization methods.....	65
2.1 Starting powders.....	65
2.2 SLM equipment and procedure	67
2.3 Preliminary study on the effects of the SLM process parameters.....	68
2.4 Heat treatment study.....	71
2.4.1 Solutioning	71
2.4.2 Study of the aging response	72
2.4.3 Optimization of the aging cycle	73
2.5 Oxidation tests.....	75
2.6 Pack aluminization tests	78
2.7 Microscopy.....	83
2.7.1 Metallographic preparation	83
2.7.2 Optical microscopy	83
2.7.3 SEM - scanning electron microscope.....	84
2.7.4 EBSD analysis.....	87
2.7.5 TEM microscopy and SAED analysis.....	91
2.8 Thermal analysis	95
2.8.1 DSC	95
2.8.2 TMA.....	96
2.9 XRD analysis.....	97
2.10 Durometers	98
2.10.1 Brinell tester	98
2.10.2 Vickers microhardness tester	98
3 Features and microstructure of SLM Inconel 718 alloy.....	101
3.1 Study on the SLM parameters process.....	101
3.2 As built microstructure features	107
3.2.1 Grains and laser related boundaries	107
3.2.2 Grain morphology and crystallographic texture	110

3.2.3 Sub-granular structure	115
3.2.4 Sub-dendrite structure	120
3.2.5 Origin of the as built microstructural features	127
3.3 Conclusion.....	132
4 Study on the effect of the post heat treatment	135
4.1 Microstructural response to thermal exposure	136
4.2 Response to the solution annealing	143
4.2.1 Solution annealing at 980°C.....	143
4.2.2 Solution annealing at 1065°C.....	147
4.2.3 Solution annealing at 1200°C.....	150
4.3 Optimization study of the complete heat treatment cycle	154
4.3.1 Solution annealing step	155
4.3.2 Aging response	157
4.3.3 Aged microstructure	159
4.3.4 First aging step	166
4.3.5 Second aging	171
4.4 Conclusion.....	173
5 Hot oxidation behavior.....	175
5.1 Short term oxidation tests.....	176
5.2 Middle term oxidation test	181
5.3 Long term oxidation test	184
5.4 Morphological and microstructural features of the oxide scale	187
5.5 Conclusion.....	193
6 Study on the pack aluminization process on SLM Inconel 718 alloy.....	195
6.1 Intermediate temperature aluminizing trials	196
6.1.1 The coating structure	196
6.1.2 Aluminate coating formation mechanism	201
6.1.3 Aluminate coating degradation mechanism	202
6.1.4 The over pack mode	207
6.1.5 Effect of the Al and activator contents in the pack	209
6.2 High temperature aluminizing test	210
6.3 Low temperature aluminizing test.....	212
6.4 Pack aluminization on hard-accessible internal surface.....	214

6.4.1 Aluminizing tests on modules	214
6.4.2 Cyclic oxidation test on aluminized modules	216
6.5 Conclusion.....	218
Overall conclusions	221
References	227
List of symbols and acronyms.....	247

List of Tables

Table 1.1. Nominal compositions of some Fe-based superalloys. Data from: [2].	.4
Table 1.2. Nominal compositions of some Ni-based superalloys.....	5
Table 1.3. Nominal compositions of some Co-based superalloys.....	6
Table 1.4. Tensile properties of some solid solution strengthening superalloys.	7
Table 1.5. Tensile properties of some precipitation hardening superalloys.	8
Table 1.6. Partition coefficients k of the alloying elements of Inconel 718 alloy. From: [56].	22
Table 1.7. Physical properties of Inconel 718 alloy. Data from: [66].	29
Table 1.8. Tensile properties of Inconel 718 alloy. Data from: [66].	30
Table 1.9. Hardness, porosity and tensile properties of heat treated (as-HT) and heat treated and HIPed (HIP) cast Inconel 718 alloy. Heat treatment: solution annealing at 980°C for 1 hour, nitrogen quench, double aging at 720°C for 8 hours and 620°C for 8 hours: HIP treatment at 1180°C and 175 MPa for 4 hours. Data from: [9].	32
Table 1.10. Creep data reported by Kuo et al. on Inconel 718 alloy after different heat treatment cycles (see text for the heat treatment recipes). Data from: [33].	34
Table 1.11. Values of the parabolic constant k_p reported after oxidation tests at different temperature and exposure time.	41
Table 1.12. Mechanical properties of SLM Inconel 718 varying the process parameters, the specimen orientation and the test temperature. The specimen orientation is given as the angle between the building direction of the tensile specimen and the load axis. The sets of SLM parameters are listed in the table	

below. RT: Room Temperature; P: laser power (W), v: scan speed (mm/s), hd: hatching distance (mm), PLT: Powder layer thickness (μm), OR: overlap ratio (%).	58
Table 1.13. Porosity of SLM Inconel 718 alloy at the as built state and after different post treatments. HT: solution annealed at 850°C for 2 hours; HIP: HIPed at 1180°C for 3 hours at 150 MPa; HIP + HT: HIPed + solution annealed at 1065°C for 1h + aged at 760°C for 10 hours + aged at 650°C for 8 hours. Source: ref. [179].	60
Table 1.14. Mechanical properties of SLM Inconel 718 in different post processing condition (heat treatment and eventual HIP) in comparison with the conventional wrought and cast alloy. The specimen orientation is given as the angle between the building direction of the tensile specimen and the load axis. T: testing temperature; HIP: Hot Isostatic Pressing; sol.: solution annealing; ag.: double aging.	62
Table 2.1. Nominal composition (%) of the Inconel 718 powders used in this study. Provided by EOS: [185].	65
Table 2.2. Factors and respective levels of the 3 ³ factorial plane on the study of the SLM process parameters and set of all the performed combinations of them.	69
Table 2.3. Set of all the recipes used for the investigation of the effect of the solution treatment on the microstructure of the SLM produced Inconel 718 alloy.	71
Table 2.4. Set of all the recipes used for the investigation of the effect of the solution treatment on the Brinell hardness of SLM Inconel 178 alloy.	72
Table 2.5. Set of all the heat treatments performed for the investigation of the aging response of SLM Inconel 718 alloy previously solution annealed at 1065°C for 2 hours.	73
Table 2.6. Set of all the heat treatments performed for the optimization study until the first aging step.	74
Table 2.7. Additional heat treatments performed to evaluate the effect of prolonging the solution annealing step or increasing the aging temperature.	74
Table 2.8. Set of the second aging recipes performed on samples previously submitted to solution annealing at 1065°C for 2 hours and first aging at 720°C for 8 hours. t_{tot} indicate the total duration of the aging step (including the cooling time).	75
Table 2.9. Durations (t_{cycle}) of the cycles performed during the short term oxidation tests and total oxidation time (t_{ox}) after each thermal cycle.	76

Table 2.10. Set of the samples used during the middle term oxidation test with the atmosphere of the preliminary solution annealing at 1065°C for 2 hours (air or vacuum) and the oxidation mode (isothermal or cycled oxidation).	77
Table 2.11. Nominal composition (%) of the aluminum powder used in this study. Provided by Alfa Aesar: [192].	78
Table 2.12. Set of the pack compositions used for the aluminizing test performed at 900 °C for 5 hours.	79
Table 2.13. Set of the pack compositions used for the aluminization of the bars half embedded in the powder mixture.	79
Table 2.14. Set of the pack compositions used for the aluminizing test performed at 1065 °C for 2 hours.	80
Table 2.15. Set of the pack compositions used for the aluminizing test performed at 800 °C for 5 hours.	80
Table 3.1. Analysis of Variance (ANOVA) on the dataset made by 5 Brinell hardness measurements for each sample of the 3 ³ factorial plane with the main effects of P, v and hd and their interactions until the second order. DOF: degrees of freedom; SS: sum of squares; MS: mean squares; F: F-ratio.	105
Table 4.1. Analysis of Variance (ANOVA) on the dataset made by 4 Brinell hardness measurements for each sample of the 2 ⁴ factorial plane with the main effects of the heat treatment factors, T _{sol} , t _{sol} , T _{ag1} , t _{ag1} , and their interactions until the second order. DOF: degrees of freedom; SS: sum of squares; MS: mean squares; F: F-ratio.	167
Table 4.2. Brinell hardness values evaluated with the linear regression model of equation 4.1 for each combination of T _{sol} , t _{sol} , T _{ag1} , t _{ag1}	169
Table 5.1. Estimated k _p values of the initial and stationary oxidation regimes at the oxidation temperature 850°C and estimated k _p values at the oxidation temperature 900°C.	181
Table 5.2. Analysis of Variance (ANOVA) for the main effects of the solubilization atmosphere (air or vacuum) and the oxidation modality (isothermal or cycled oxidation) on the mass gain after 215 hours at 850°C and their combined effect. DOF: degrees of freedom; SS: sum of squares; MS: mean squares; F: F-ratio...	182
Table 5.3. Comparison between the chemical compositions of Inconel 600 and Inconel 718 superalloys.	184

Table 6.1. Mass gains for unit of surface area collected after the aluminizing test performed at 900 °C for 5 hours.	196
Table 6.2. Mass gains for unit of surface area collected after the aluminizing test performed at 1065 °C for 2 hours.	210
Table 6.3. Mass gains for unit of surface area collected after the aluminizing test performed at 800 °C for 5 hours.	212

List of Figures

Figure 1.1. Weldability map of the nickel superalloys based on the Al and Ti content. The alloys below the red line are considered weldable. From: [15].	10
Figure 1.2. Continuous Cooling Transformation (CCT) curves of Inconel 718 ingot after homogenization treatment at 1180°C for 90 hours. From: [25].	12
Figure 1.3. SEM micrograph showing carbides in Inconel 718 alloy after solution treatment at 1095°C for 1 hour. From: [33].	13
Figure 1.4. Crystal structure of Laves phase. Hexagonal system with MgZn ₂ lattice type and parameters [21] a = b = 0.475-0.495 nm, c = 0.77-0.815 nm.	13
Figure 1.5. Laves phases network on the interdendritic region of the fusion zone of a weld. Higher (a) and lower (b) magnification. From: [36].	14
Figure 1.6. Orthorhombic DO _a crystal structure of δ phase with parameters [18] a = 0.5141 nm, b = 0.4231 nm, c = 0.4534 nm.	14
Figure 1.7. SEM micrograph showing plate-like δ precipitates formed after exposition at 950°C for 50 hours in an Inconel 718 alloy. From: [23].	15
Figure 1.8. TEM micrograph showing plates of δ phase nucleated on γ'' particles in a spray formed Inconel 718 alloy heat treated at 875°C for 6 hours. From: [23].	15
Figure 1.9. Body centered tetragonal DO ₂₂ crystal structure of γ'' phase with parameters [18] a = b = 0.3624 nm, c = 0.7460 nm.	16
Figure 1.10. TEM micrograph showing discoidal γ'' and spherical γ' precipitates on an Inconel 718 alloy aged at 750°C for 100 hours. From: [49].	17

Figure 1.11. Cubic $L1_2$ crystal structure of γ' phase with parameters [18] $a = b = c = 0.3605$.	17
Figure 1.12. Scheme of a dislocation that pass an ordered structure forming an antiphase boundary (left); dislocations are forced to move in pairs in the ordered structure (right). From: [14].	18
Figure 1.13. TEM micrograph showing the co-precipitation of γ' and γ'' particles in an Inconel 718 alloy. From: [24].	19
Figure 1.14. Solute profiles in the solid and liquid phase and path followed in the phase diagram by the mean concentration in the solid according to the Scheil's model in the cases of $k < 1$ and $k > 1$.	21
Figure 1.15. Formation of constitutional undercooling of the liquid ahead the solidification front with consequent destabilization of the planar solid/liquid interface. From: [53].	24
Figure 1.16. Examples of cellular microstructures. Top view of the cells disposed on a hexagonal pattern (A) and lateral view of columnar dendrites without secondary arms (B). From: [58].	24
Figure 1.17. Change in the solidification front morphology and structures size in function of the temperature gradient G and the growth rate R . From: [59].	25
Figure 1.18. Scheme of the fast solidification path for a general Nb-bearing nickel alloy (DuPont's path, adapted from: [63]) and that of Inconel 718 alloy in particular (Knorovsky's path, from: [55]).	27
Figure 1.19. General structure of the standard heat treatment cycle of Inconel 718 alloy.	27
Figure 1.20. Elastic modulus, mean Thermal Expansion Coefficient (CTE), specific heat on thermal conductivity of Inconel 718 alloy in function of the temperature. Data from: [66].	29
Figure 1.21. Tensile properties of a wrought Inconel 718 alloy after double aging. Data from: [69].	30
Figure 1.22. Tensile properties of Inconel 718 alloy at room temperature (left) and at 650°C (right) after the heat treatment cycle in function of the temperature of the preliminary solution step. From: [70].	31
Figure 1.23. Hardness of Inconel 718 alloy after 4 hours of aging at different temperatures (left) and for different times and temperatures of aging (right). The	

hardness measured after the solution annealing and before the aging step is 245 Hv. From: [16].	31
Figure 1.24. Room temperature tensile properties of Inconel 718 alloy after different times of thermal exposure at 593°C and 649°C. From: [71].	32
Figure 1.25. Rupture time at 650°C with an applied load of 730 MPa of Inconel 718 alloy in function of the grain size. From: [72].	33
Figure 1.26. Creep σp vs ε curves at different test temperatures. From: [74].	34
Figure 1.27. Creep curves at 625 MPa and 650°C of Inconel 718 alloy previously submitted to three different heat treatment cycles. From: [33].	35
Figure 1.28. Creep strain and rupture life of Inconel 718 alloy at 625°C with an applied load of 795 MPa in function of the precipitates size (left) and density (right). From: [75].	35
Figure 1.29. Left: fatigue stress vs number of cycle curves at two different test temperatures and two different grain size obtained on wrought Inconel 718 alloy previously submitted to solution annealing at 970°C and double aging according to the standard recipe n.1 (see paragraph 1.3.3), from: [72]. Right: Paris curves at three different test temperatures of wrought Inconel 718 alloy previously submitted to the standard heat treatment cycle n.1 (see paragraph 1.3.3) and with a grain size of 10 μm , from: [77].	36
Figure 1.30. Ellingham diagram relative to the Ni, Cr, Ti and Al oxides. Data from: [80].	38
Figure 1.31. Ternary isothermal diagram showing the compositional borders between the three groups of alloys. The point relative to Inconel 718 alloy is added. Adapted from: [79].	39
Figure 1.32. Phase diagram of the aluminum-nickel system. From: [104].	43
Figure 1.33. Scheme of the reaction chain occurring during the pack aluminization process. From: [109].	44
Figure 1.34. Schemes of the typical coating structures obtained in low activity (left) and high activity (right) pack aluminization processes. From: [110].	44
Figure 1.35. Optical micrographs of aluminized coatings on Udimet 700 alloy. Inward diffusion formed coating obtained with a high activity process before (a) and after (b) the diffusion heat treatment at 1080°C of 4 hours. Outward diffusion formed coating obtained with a low activity process (c). From: [107].	45

Figure 1.36. Intrinsic diffusivity at 1000°C of Al and Ni in β -AlNi in function of the composition. From: [117].	46
Figure 1.37. Scheme of the SLM process.	49
Figure 1.38. Optical micrographs showing the laser tracks on the horizontal plane and the arc-shape melt pool boundaries on the vertical plane of a SLM Inconel 718 alloy. From: [140].	49
Figure 1.39. Scheme showing the main SLM process parameters which determine the Volumetric Energy Density (VED), i.e. laser power P , scan speed v , hatching distance hd and layer thickness d . From: [137].	51
Figure 1.40. SEM micrograph showing some examples of gas porosities and lack of fusion porosities on a SLM Inconel 718 alloy. From: [144].	51
Figure 1.41. Examples of typical defects of the SLM products: keyhole geometry and porosity (left) and balling (right). From: [143].	52
Figure 1.42. Inverse Pole Figure (IPF) maps showing the crystallographic texture of Inconel 718 alloy produced by SLM. In this picture the building direction corresponds to the z axis. From: [154].	55
Figure 1.43. Three-dimensional composition of optical micrographs showing the sub-granular structure of columnar dendrites on a SLM Inconel 718 alloy. From: [159].	55
Figure 1.44. SEM micrographs showing the horizontal plane (top, from: [154]) and the vertical plane (bottom, from: [175]) of the cellular microstructure of an Inconel 718 alloy produced through SLM process. Arrow 1 indicates a γ + Laves eutectic, arrow 2 indicates a divorced eutectic, arrow 3 indicates a MC carbide.	56
Figure 1.45. EDS analysis of the γ matrix in comparison with the eutectic products, i.e. carbides and Laves phases. From: [158].	56
Figure 1.46. Scheme of the evolution of the Inconel 718 alloy microstructure caused by the thermal cycles during a laser powder injection AM process (top) and SEM micrographs showing the eutectic products and the γ'' precipitates in the intracellular zone (bottom). From: [177].	57
Figure 1.47. Heat treated SLM Inconel 718. Top: SEM micrograph of the vertical plane showing the formation of δ precipitates at the interdendritic boundaries after heat treatment at 850°C for 2 hours, the arrow indicates the building direction. From: [179]. Bottom: SEM micrographs of the horizontal plane showing carbides after solution annealing at 1100°C for 1 hour (a) and 7 hours (b). From: [183].	61

Figure 2.1. Optical micrographs showing the cross sections of the Inconel 718 powders used for this study. Not etched (A and B) and etched with Kalling's n.2 etchant (C).....	66
Figure 2.2. SEM micrograph showing the morphology of the Inconel 718 powders used for this study (A) and relative size distribution obtained with laser diffraction technique (B). First published in [186].....	66
Figure 2.3. Schematic representation of the scan strategy adopted in this study: bidirectional scanning path with rotation of 67° at each layer. From: [187].....	67
Figure 2.4. Example of porosity evaluation through image analysis of an optical micrograph. The lower and higher estimations are represented in the magnified figure by the red areas and the blue areas respectively.....	70
Figure 2.5. Module with internal channels of triangular section produced by SLM.	81
Figure 2.6. Scheme of the cuts performed on the aluminized modules for the cross section examination.	81
Figure 2.7. Summary diagram collecting all the thermal histories of the SLM Inconel 718 samples which characterization is reported in this thesis. Starting from a square, representing the as built (gray) or a solution annealing condition (blue), each subsequent step of a thermal history can be reached by following the arrows. Green points represent the first (dark green) and second (light green) aging treatments; orange points represent the thermal treatments performed to investigate the aging response; red bars represent all the short, middle and long oxidation isotherms; yellow points represent the pack aluminization treatments. T: treatment temperature; t: treatment time.....	82
Figure 2.8. Representation of the edge effect and secondary electrons yield in function of the tilt angle of the specimen surface. From: [193].	84
Figure 2.9. Example of image analysis of a FESEM micrograph collected on the sample solutioned at 1065°C for 2 hours and the derived size distribution with average volume fractions and cumulative volume fractions of the precipitates. First published in [194].	85
Figure 2.10. Backscattered electron fraction in function of the atomic number Z on the spot illuminated by the primary beam. From: [193].	86
Figure 2.11. Nomogram for evaluate the diffusion range of the electron in the Scanning Electron Microscopy in function of the specimen density and the used voltage. Adapted from: [195].....	87

Figure 2.12. Scheme of the EBSD set up and an example of the Kikuchi diffraction bands, detected on a single spot on the examined surface, which allow to obtain the orientation of the local UVW coordinate system respect to the XYZ sample coordinate system in term of the Euler angles φ , θ , ψ	88
Figure 2.13. Scheme explaining the criterion used to establish the position of the grain boundaries. A grain boundary is present between two spots when their highest mis-orientation θ_{mis} between them is higher than a threshold value θ_{th}	89
Figure 2.14. Stereographic projection of a direction r in the 3D space on the 2D unitary circle.	90
Figure 2.15. Representation of the $\{100\}$, $\{110\}$ and $\{111\}$ crystallographic directions through pole figures.	90
Figure 2.16. Representation of the orientation of the lattice cell through inverse pole figures.	91
Figure 2.17. Ewald construction. The Ewald sphere radius is equal to $1/\lambda$, where λ is the wavelength of the incident radiation. The origin O of the reciprocal lattice lays on the Ewald sphere, $\mathbf{s0}$ and \mathbf{s} are the unit vectors along the directions of the incident and the diffracted beams respectively (A), for each point G of the reciprocal lattice laying on the Ewald sphere, a beam is diffracted (B). Case of electron diffraction (C), the curvature of the Ewald sphere is exaggerated for clarity. From: [199].....	93
Figure 2.18. Thermic ramps measured during DSC and TMA analysis at different set heating rates.....	97
Figure 3.1. Apparent density measurements of the SLM samples produced for each set of process parameters combination in comparison with the theoretical density values. Data published in [186].	101
Figure 3.2. Optical micrograph of sample n.18 ($P = 185$ W, $v = 900$ mm/s, $hd = 0.09$ mm) as example of the general porosity condition of the SLM samples with presence of small pores (blue ellipses) and some bigger rounded pores (red ellipse).	102
Figure 3.3. Porosity area fraction ranges obtained on the SLM samples produced for each set of process parameters combination. Data published in [186].	103
Figure 3.4. Sample n.15 ($P = 175$ W, $v = 600$ mm/s, $hd = 0.07$ mm) as example of the porosity condition (red ellipses indicate gas porosities) in most of the samples obtained with $v = 600$ mm/s (A) and sample n.11 ($P = 195$ W, $v = 900$ mm/s, $hd =$	

0.07 mm) obtained with the highest VED between the samples produced with $v > 600$ mm/s (B).	103
Figure 3.5. Sample n.4 ($P = 175$ W, $v = 1200$ mm/s, $hd = 0.11$ mm) obtained with the smallest VED value (A) and sample n.16 ($P = 195$ W, $v = 1200$ mm/s, $hd = 0.11$ mm) obtained with a higher value of laser power (B). The red ellipses indicate some lack of fusion voids.....	104
Figure 3.6. Main and interaction effects of the SLM process parameters on the Brinell hardness of Inconel 718 alloy. Data published in [186].	104
Figure 3.7. Micrographs on the horizontal plane of the samples produced with $v = 600$ mm/s. The red ellipses indicate gas porosities and other defects. Kalling's n.2 etchant.....	106
Figure 3.8. Micrographs on the horizontal plane of the samples produced with $v = 1200$ mm/s. The red ellipses indicate some lack of fusion voids between laser tracks. Kalling's n.2 etchant.....	106
Figure 3.9. Optical micrograph of the horizontal plane of the SLM as built material showing the typical laser tracks. Electrochemical etching.	108
Figure 3.10. Optical micrographs collected on the horizontal plane of the as built sample showing the grain boundaries, the laser tracks boundaries and the sub-granular structure. Kalling's n.2 etchant.	109
Figure 3.11. Optical micrographs collected on the vertical plane of the as built sample showing the melt pool boundaries (A), the grains crossing the deposited layers and the sub-granular columnar dendrites (B). Kalling's n.2 etchant.	110
Figure 3.12. Grain maps obtained through EBSD analysis of the as built material on the horizontal plane (A) and vertical plane (B). The grains, defined here as the regions completely delimited by high-angle boundaries, are shown in the maps on the left. In the maps on the right, different color shades are used for indicating the sub-grain domains, the high-angle boundaries (mis-orientation of at least 10°) are marked in dark blue and the low-angle boundaries (maximum mis-orientation angle between 10° and 4°) are marked in lighter blue. First published in [186].....	111
Figure 3.13. Experimental pole figures relative to the EBSD analysis on the horizontal plane, each colored square represent the mean orientation of the respective grain of figure 3.12-A respect to the sample coordinate system. The small circles represent the mean orientation of the sub-granular domains. Simulated pole figures for a material without preferential orientation with the same number of grains are also reported. First published in [186].	112

Figure 3.14. Experimental pole figures relative to the EBSD analysis on the vertical plane, each colored square represent the mean orientation of the respective grain of figure 3.12-B respect to the sample coordinate system. The small circles represent the mean orientation of the sub-granular domains. First published in [186].	113
Figure 3.15. Inverse Pole Figure (IPF) charts relative to the three axes on both the horizontal and vertical planes. First published in [186].	113
Figure 3.16. Paths of the representative point on the IPF charts during the rotation of a crystal around the [001] direction oriented at a low angle to the building direction (R_1 axis). This example is referred to the horizontal plane, the paths relative to the vertical plane are analogous.	114
Figure 3.17. IPF maps on both the Horizontal plane (H. p.) and the vertical plane (V. p.) relative to the three axes. The IPF-Z maps have been previously published in [186].	115
Figure 3.18. Argus image and higher resolution IPF maps on the horizontal plane of the areas marked by the green box. First published in [186].	116
Figure 3.19. Argus image and higher resolution IPF maps on the vertical plane of the areas marked by the green box. Note the zig-zag features of the slightly mis-oriented intragranular zones and the columnar intragranular structure (black circle in the IPF-Z map). First published in [186].	116
Figure 3.20. FESEM micrograph of the horizontal plane showing the sub-granular dendrite structure. Sets of dendrites grown parallel and perpendicular to the Building Direction (BD) are visible.	117
Figure 3.21. FESEM micrographs of the vertical plane. Most of the columnar dendrites are parallel to the Building Direction (BD), but some changes in the growth direction are visible along the melt pool boundaries (an example is indicated by the ellipse in the higher magnification micrograph).	118
Figure 3.22. FESEM micrograph of the vertical plane showing the abrupt change of the dendrite arm spacing across a melt pool boundary.	119
Figure 3.23. FESEM micrographs of the vertical plane showing the abrupt change of the dendrite arm spacing and growth direction (indicated by the arrows in the higher magnification micrograph) across a melt pool boundary. First published in [186].	119
Figure 3.24. FESEM micrographs of the horizontal plane on zones in which the dendrites grew parallel (A) and perpendicular (B) to the building direction. Green	

and brown ellipses indicate some rounded and smaller precipitates and coarser precipitates of irregular shape, respectively.	120
Figure 3.25. FESEM micrographs of the horizontal plane showing the formation of a continuous intercellular network of second phases along the laser track boundaries.	121
Figure 3.26. FESEM micrograph of the vertical plane. Green and brown ellipses indicate some rounded and smaller precipitates and coarser precipitates of irregular shape, respectively.	121
Figure 3.27. FESEM micrographs of the horizontal plane in a zone in which very small particles (blue ellipses) precipitate in the core of the cells in addition to the other two kinds of precipitates (green and brown ellipses, see figures 3.24 and 3.26). First published in [194].	122
Figure 3.28. STEM images at the dendrite length scale showing the dislocations around a interdendritic precipitate. First published in [186].	122
Figure 3.29. EDS analysis: line analysis across the dendrite showing the microsegregation of the alloying elements, point analysis on the matrix (point 3) and on the precipitates (carbides, points 1 and 4, and Laves, point 1). First published in [186].	123
Figure 3.30. TEM image showing the matrix γ phase (dark contrast, area 1) and an interdendritic precipitate (bright contrast, area 2). Selective Area Electron Diffraction (SAED) patterns taken along the [001] Zone Axis of the γ phase. First published in [186].	124
Figure 3.31. SAED pattern on area 2 of figure 3.30 showing the spots given by the γ phase, circled in red, and the ones supposed to be due to the Laves phase, circled in green (A). Construction of the second pattern by translating the repetitive unit drawn in blue and extra spots marked with red crosses (B). Indexed calculated pattern at the [112] Zone Axis of the Laves structure (C).	125
Figure 3.32. Scheme of the domain boundary along a slip and respective displacement vector Dm (A). Domains formed by a sequence of s slips (B) and by a slips sequence $s's's'ss$ (C). The configuration in B causes the kinematic extinction of the spots with l odd in the strong rows and of all the spots with $h + k \neq 3N$; the configuration in C restore the weaker spots.	127
Figure 3.33. Scheme illustrating the possible ways in which the solidification of a new melt pool can occur depending on the crystallographic orientation of the dendrites with respect to the local thermal fluxes (orange arrows).	130

Figure 3.34. Schematic representation of the solidification process and consequent distribution of the eutectic products (carbides and Laves phases) in the dendrite structure.	131
Figure 4.1. DSC analysis across the melting/solidification range. The detected peaks are indicated by the arrows.	136
Figure 4.2. DSC curves of heating and cooling relative to the horizontal samples. The arrows indicate the detected peaks.	138
Figure 4.3. Comparison of the DSC curves of vertical and horizontal samples at the heating rate of 5°C/min and 20°C/min.	139
Figure 4.4. TMA heating curves of horizontal and vertical samples at the heating rate of 5°C/min and 20°C/min.	139
Figure 4.5. Comparison between the collected DSC and TMA curves at the heating rate of 5°C/min and 20°C/min. Dotted boxes indicate the overlapping signal peaks.	140
Figure 4.6. Scheme illustrating the not uniform expansion during the dissolution of the interdendritic phases in the SLM material. The expansion is lower of a Δ along the transversal direction of the interdendritic boundaries.	142
Figure 4.7. Optical micrographs of the horizontal plane after solution annealing at 980°C for 1 hour and 2 hours. Dotted ellipses indicate small recrystallized grains at the laser track boundaries.	144
Figure 4.8. Optical micrographs of the vertical plane after solution annealing at 980°C for 1 hour and 2 hours. Dotted ellipses indicate small recrystallized grains at the laser track boundaries. The higher magnification micrographs show the interdendritic and intradendritic plate-like δ precipitates.	145
Figure 4.9. SEM micrograph of the vertical plane after solution annealing at 980°C for 1 hour showing the columnar dendrite texture still visible due to the formation of interdendritic δ precipitates.	145
Figure 4.10. SE FESEM micrographs of the horizontal plane after solution annealing at 980°C for 1 hour and 2 hours. Newly formed plate-like δ precipitates and residuals of the eutectic products are the main present second phases.	146
Figure 4.11. Size distributions relative to the samples solutioned at 980°C (A). Contributions of the precipitates with plate-like morphology and without plate-like morphology after 1 hour (B) and 2 hours (C) of treatment at 980°C. First published in [194].	147

Figure 4.12. Optical micrographs of the horizontal plane after solution annealing at 1065°C for 1 hour and 2 hours.....	147
Figure 4.13. Optical micrographs of the vertical plane after solution annealing at 1065°C for 1 hour and 2 hours.....	148
Figure 4.14. SEM micrograph of the vertical plane after solution annealing at 1065°C for 1 hour showing the grain boundaries decorated with newly formed precipitates. The columnar structure is no more visible.	148
Figure 4.15. SE FESEM micrographs of the horizontal plane after solution annealing at 1065°C for 1 hour and 2 hours. Newly formed intergranular carbides and intragranular precipitates are the main present second phases.	149
Figure 4.16. Size distributions relative to the samples solutioned at 1065°C. First published in [194].	150
Figure 4.17. Optical micrographs of the horizontal and vertical planes after solution annealing at 1200°C for 1 hour and 2 hours. First published in [194].	150
Figure 4.18. SEM micrograph of the vertical plane after solution annealing at 1200°C for 1 hour showing the carbides clusters along the previous positions of the grain boundaries and a new grain boundary unconstrained by the carbides after recrystallization (compare with figure 14). EDS point analysis on a Nb-rich carbides cluster (point 1) in comparison to the intragranular matrix zone (point 2).	151
Figure 4.19. SE FESEM micrographs of the horizontal plane after solution annealing at 1200°C for 1 hour and 2 hours. Note the grain boundaries free from precipitates and the presence of residuals of the interdendritic precipitates inside the grains (higher magnification images).	152
Figure 4.20. Size distributions relative to the samples solutioned at 1200°C. First published in [194].	152
Figure 4.21. Size distributions: comparison between different solution temperature after 1 hour (A) and 2 hours (B) of heat treatment. First published in [194].	153
Figure 4.22. Correlation between the Vickers microhardness and the average volume fraction of precipitates in the as built sample (the volume fraction of the as built sample is obtained considering the eutectic products and neglecting eventual very small intradendritic precipitates as those in figure 3.27) and the solutioned samples. The vertical error bars refer to 95% confidence intervals on HV _{0.01} , the horizontal error bars refer to standard deviations of the volume fractions. The	

regression line with relative 95% confidence band is obtained excluding the points of the samples solutioned at 1200 °C. First published in [194].	154
Figure 4.23. Brinell hardness (HB10) and Vickers microhardness (HV _{0.01}) in function of the temperature (T _{sol}) and time (t _{sol}) of the solution annealing.	155
Figure 4.24. Optical micrographs of the horizontal plane of samples solutioned at 980°C and 1065°C for 4 and 8 hours.	156
Figure 4.25. SEM micrographs of the horizontal plane of the samples solutioned for 8 hours at 980°C and 1065°C showing the different intergranular precipitates.	156
Figure 4.26. Comparison between the DSC heating curves collected on the as built material and on the previously solutioned samples. Heating rate: 20°C/min. The as built and the 1065°C/2h solution annealing curves have been previously published in [186].	157
Figure 4.27. Comparison between the DSC and TMA heating curves collected on the samples previously solutioned at 980°C and 1065°C for 8 hours. Heating rate: 20°C/min. Dotted boxes indicate the overlapping signal peaks.	158
Figure 4.28. Mean Vickers microhardness obtained on the samples solutioned at 1065°C for 2 hours and then aged at the characteristic temperatures of the alloy. The bars indicate the 95% confidence ranges. Data published in [186].	160
Figure 4.29. X-ray diffractograms of the as built sample and the sample solutioned at 1065°C for 2 hours. First published in [186].	161
Figure 4.30. X-ray diffractograms of the samples aged at the characteristic temperatures of the alloy with magnification on the γ (200) peak in order to observe the shift respect to as solutioned state. First published in [186].	162
Figure 4.31. Values of the lattice parameter of γ phase with different thermal histories obtained from the XRD analyses. Data published in [186].	162
Figure 4.32. FESEM micrographs of the samples aged at 565°C. The micrographs acquired on the sample aged for 24 hours have been already published in [186].	163
Figure 4.33. FESEM micrographs of the samples aged at 740°C. Formation of discoidal γ'' after longer aging time.	164
Figure 4.34. FESEM micrographs of the samples aged at 800°C. Formation of intergranular δ and further coarsening of discoidal γ'' .	165

Figure 4.35. FESEM micrographs of the samples aged at 870°C. Intergranular and intragranular plate-like δ precipitates form and grow during aging.	166
Figure 4.36. Effects on the Brinell hardness of the heat treatment factors, the solution treatment temperature (A) and time (B) and the aging treatment temperature (C) and time (D), and their most significant interactions.	166
Figure 4.37. Brinell hardness (HB10) and Vickers microhardness (HV _{0.01}) in function of the aging temperature after solution annealing at 1065°C for 2 hours and 8 hours of aging.....	167
Figure 4.38. Brinell hardness (HB10) and Vickers microhardness (HV _{0.01}) as function of the solution treatment time after aging at 720°C for 8 hours.	168
Figure 4.39. Brinell hardness at different aging condition without preliminary solution annealing (direct aging) and with solution annealing at 1065°C for 2 hours.	170
Figure 4.40. FESEM micrographs of single aged samples in different solution conditions.....	171
Figure 4.41. Brinell hardness (HB10) and Vickers microhardness (HV _{0.01}) in function of the second aging temperature and time after preliminary solution annealing at 1065°C for 2 hours and first aging at 720°C for 8 hours.	172
Figure 4.42. FESEM micrographs of double aged samples after preliminary solution annealing at 1065°C for 2 hours and first aging at 720°C for 8 hours. .	172
Figure 4.43. Mean Brinell hardness after each step of the optimized treatment cycle and relative microstructure. The error bars refer to 95% confidence ranges.....	174
Figure 5.1. Mass gain ($\Delta m/A$) vs time (t) plots for the as built samples and the solutioned samples at the oxidation temperatures of 900°C (orange) and 850°C (blue) and relative fitting power laws.	177
Figure 5.2. Mass gain squares vs time plots for the as built samples and the solutioned samples at the oxidation temperatures of 850°C. The first nine points are fitter with a zero-intercept regression line (initial transient oxidation), the others are fitted with a line with lower slope (stationary oxidation). The error bars indicate the measurement uncertainties.....	179
Figure 5.3. Mass gain squares vs time plots for the as built samples and the solutioned samples at the oxidation temperatures of 900°C. The error bars indicate the measurement uncertainties.....	180

Figure 5.4. Mass gains collected after 215 hours in both cycled (red bars) and isothermal (blue bars) oxidation at 850°C on the as built and the solutioned samples used in the middle term test (the error bars indicate the measurement uncertainties). Solution annealing was performed at 1065°C for 2 hours. The average mass gains of the samples solutioned in air and in vacuum and oxidized in isotherm or via thermal cycles are also compared (the error bars indicate 95% confidence ranges).	181
Figure 5.5. Mass gain squares vs time plots for the as built sample and the solutioned samples oxidized via thermal cycles during the middle term test. The error bars indicate the measurement uncertainties.....	182
Figure 5.6. Backscattered electrons (BSE) SEM images of the cross section of samples pretreated in air (A and B) and in vacuum (C and D) and oxidized at 850°C through thermal cycles (A and C) and in isotherm (B and D) for 215 hours.	183
Figure 5.7. Mass gain squares vs time plot of solutioned SLM Inconel 718 and Inconel 600 oxidized at 850°C with relative zero-intercept linear regressions lines. The dotted lines indicate 95% confidence ranges, the error bars indicate the measurement uncertainties. First published in [194].....	185
Figure 5.8. Optical micrographs of the cross section of the oxide scales grown on Inconel 718 and Inconel 600 alloys after 908 hours of isothermal oxidation. BD indicates the Building Direction of the Inconel 718 sample.....	186
Figure 5.9. Oxide thickness vs mass gain plots for Inconel 718 and Inconel 600 alloys in comparison with the theoretical value of equation 5.2. The dotted lines indicate 95% confidence ranges.	187
Figure 5.10. Backscattered electrons (BSE) FESEM image of the cross section of the oxide scale grown on SLM Inconel 718 after 908 hours of isothermal exposure at 850°C. The sample was previously solutioned at 1065°C for 2 hours in vacuum. BD indicates the Building Direction of the sample. First published in [194].	188
Figure 5.11. Backscattered electrons (BSE) FESEM images showing in greater details the morphology and structure of the oxide scale on SLM Inconel 718 after 908 hours of isothermal exposure at 850°C. First published in [194].....	189
Figure 5.12. Sample of Inconel 718 oxidized for 160 hours at 850°C. Spot EDS analysis on: superficial oxide layer (spectrum 1); particles embedded in it (spectrum 2); thin interlayer at metal/oxide interface (spectrum 3); internal oxides rich in Ti (spectrum 4); deeper internal oxides rich in Al (spectrum 5); intergranular precipitate (spectrum 6). First published in [194].....	190

Figure 5.13. Backscattered electrons (BSE) FESEM image of the cross section of the oxide scale grown on Inconel 600 alloy after 908 hours of isothermal exposure at 850°C. Spot EDS analysis on an isolated superficial oxide (point 1), the continuous oxide layer (point 2) and an internal oxide (point 3).....	192
Figure 6.1. Optical micrographs of the cross sections of the coatings developed on the samples during the intermediate temperature test (900°C for 5 hours).	197
Figure 6.2. SEM micrographs of the cross sections of the coatings developed on the samples during the intermediate temperature test (900°C for 5 hours). BE: Backscattered Electrons mode; SE: Secondary Electrons mode.	198
Figure 6.3. BSE FESEM image of the coating on sample A2 showing the layered structure (A). Higher magnification of the interdiffusion layer (B) and the passage between the dense layer and the porous one (C).	199
Figure 6.4. Spot EDS analyses on the porous superficial layer (point 1) and on the intermediate dense layer (point 2) of sample A2.	200
Figure 6.5. EDS line analysis showing the profile of the chemical elements present along the intermediate layer of the coating (sample A2). Black arrows indicate the peaks of the Cr, Fe, Nb, Mo and Ti signals and the valleys of the Al and Ni signals in presence of a precipitate on the intermediate layer.	201
Figure 6.6. Schematic representation of the coating formation mechanism.....	202
Figure 6.7. Aluminide coating on sample A2 after oxidation for 72 hours at 850°C.	204
Figure 6.8. Schematic representation of the coating degradation mechanism.....	205
Figure 6.9. Spot EDS analyses on the oxidized zone (point 1) and on the intermetallic part (point 2) of the superficial layer of the coating on sample A2 after thermal exposure for 72 hours at 850°C in air.....	206
Figure 6.10. BSE FESEM micrograph showing the spalling of the coating on sample A2 observed after exposition at 850°C for 72 hours.	206
Figure 6.11. Optical micrographs of the cross sections of the coatings developed on the totally embedded part of the bars (dotted ellipse in the schematic drawing).	207
Figure 6.12. Optical micrographs showing the spalling of the aluminide coating formed in the middle of bar B1 and at the not embedded end of bar B2.....	207
Figure 6.13. Optical micrographs showing the coating formed on bar B1 in different positions respect to the powder pack.	208

Figure 6.14. Coating thickness in function of the pack composition (contents of Al and activator) after aluminization at 900°C for 5 hours. The degraded fraction, i.e. porous layer thickness/(porous layer + dense layer thicknesses) ratio, are also shown in function of the activator content for the samples treated with 15% of Al in the pack.	210
Figure 6.15. Optical micrographs of the cross sections of the coatings developed on the samples during the high temperature test (1065°C for 2 hours).	211
Figure 6.16. Intergranular corrosion about 250 µm in deep beneath the coating on sample H4.	212
Figure 6.17. Optical micrographs of the cross sections of the coatings developed on the samples during the low temperature test (800°C for 5 hours).	213
Figure 6.18. SEM micrographs of the cross sections of the coating developed on the sample L1 showing the superficial isolated protrusions. BSE: Backscattered Electrons mode; SE: Secondary Electrons mode. Spot EDS analysis on a protrusion.	213
Figure 6.19. Optical micrographs showing the coating on the external surface of module n.1 from the deeper embedded end to the surface of the pack.....	215
Figure 6.20. Optical micrographs showing the coating formed in the internal surfaces. A zone in which the typical structure forms (A) and a zone in which only a degraded layer forms (B).	216
Figure 6.21. Properly formed aluminide coating on an external surface of module n.2 before the thermal cycles (A) and after five thermal cycles at 850°C (B).....	216
Figure 6.22. Oxidation/degradation of the aluminide coating on an external surface of module n.2 in a zone in which the coating is unstable during the thermal cycles at 850°C.	217
Figure 6.23. Optical micrographs showing the cross section of the coating on the internal surface of the channels in module n.2 before the thermal cycles and after 2 and 4 cycles at 850°C.....	218

Chapter 1

Literature review

1.1 The superalloys

Superalloys are a class of metallic materials developed in 1940-50s to meet the demand for materials capable of maintaining high mechanical performance at elevated operating temperatures typical of gas turbine applications components for jets and aircrafts. Nowadays, superalloys are still used in the aeronautical field, but they also find applications in power generation systems, chemical, petrochemical and nuclear plants, heat exchangers. In this kind of applications, it is required not only a high resistance to static load at high temperature, but also good creep and fatigue resistance as well as a high stability in aggressive environmental conditions, for example in presence of highly oxidizing hot or corrosive gases. The characteristic feature of the superalloys is the capability to maintain almost unchanged the mechanical properties even at temperatures close to their melting point T_m , typically they can be applied up to $T/T_m = 0.8$, that is a prohibitive condition for most of the other classes of metallic materials of engineering interest. For this reason, superalloys can be used to bridge the gap between advanced ceramic materials and stainless steels. The former materials are characterized by very high thermal and oxidation resistance, but also by brittleness and poor formability. On the contrary, the latter materials have good ductility and toughness, but they cannot be used at temperatures higher than 800-900°C due to an excessive reduction of the mechanical properties and high oxidation occurring at higher temperatures.

1.1.1 Production techniques

The conventional production processes for superalloys can be divided in three categories: casting, wrought and powder metallurgy. In the following the main features of the products obtained with these conventional techniques are described briefly [1] [2] [3] [4] [5].

1.1.1.1 Casting

Cast products are obtained in near-net shape form through special molds and shapes. During casting, the control of the solidification conditions, in particular the cooling rate and the direction and extent of the thermal gradients that are established, has a great importance as they deeply affect the solidification mode and the consequent defects introduced on the final product. The typical defects present in the casting products are voids and gas porosities, cracks due to thermal stresses established in the solidification and cooling step, microstructural heterogeneity, segregation of alloy elements and the formation of brittle phases that decrease the toughness and ductility of the material. A precise control of the thermal flows during solidification also allows to obtain directionally solidified polycrystalline products (DS), in which the grains assume a predominantly elongated shape along a fixed direction. This grains conformation is useful in high temperature applications in which the material is subjected to tensile stress along the major axis of the grains. In fact, removing the grain boundaries perpendicular to the load axis allows to obtain substantial reduction of the creep deformation.

The modern casting techniques allow also to obtain single crystal products, in which the grain boundaries are completely absent with consequent high increase in the creep resistance. DS and single crystal products are largely used in the production of components, in particular blades and vanes, which work in the hottest zones of turbine engines.

1.1.1.2 Wrought

The wrought parts are obtained starting from cast ingots usually produced through vacuum induction melting (VIM) and subsequently submitted to one or more re-melting cycles through electro-slag re-melting (ESR) and / or vacuum arc re-melting (VAR). The re-melting cycles have the aim of reducing the impurities content and the segregation patterns. Typically, a long homogenization heat treatment is also performed to further reduce the level of segregation and microstructural heterogeneity. These preliminary operations of re-melting and homogenization are necessary to obtain the required alloy workability in view of the following mechanical processing. Then, bars or billets are obtained through one or more hot plastic deformation steps. During the thermomechanical processing cycles, the material undergoes dynamic recrystallisation and other important microstructural modification. The typical defects of the cast material, in particular the compositional segregation, the microstructural inhomogeneity and the porosity, are largely reduced through this manufacturing route. For this reason, the ductility, mechanical properties and low-cycle fatigue strength at low or medium temperature (up to about 700-750 °C) of the wrought material are generally higher with respect to the cast one. However, the grain size of the wrought products is generally lower with respect to the cast condition because of the recrystallization phenomenon. Therefore, the high temperature performances (creep resistance and rupture life) are

lower. For this reason, the wrought products are usually applied for turbine disks or other components subjected to high mechanical loads but working at a not too high temperature.

1.1.1.3 Powder metallurgy and HIP

There are some superalloys that are not suitable for the mechanical processing. They are usually alloys with a high content of refractory alloying elements such as Ti, Ta, W, Mo, Nb; some examples of them are Rene 95, IN-100 and Astroloy. These alloys are more prone to cracking during the mechanical processing steps because of the high level of segregation, the high required flow stress and the development of thermally induced stresses.

The powder metallurgy techniques allow to manage this type of alloys that are not suitable for the mechanical processing in the applications in which the performances obtainable with the cast methods cannot guarantee the minimum requirements. However, this kind of production techniques are usually more expensive. The powders are usually produced by gas atomization of a VIM ingot and then sieved and cleaned, low size powders are generally preferable but result in a higher cost. The powders are then sealed in a container, usually in steel, degassed and consolidated, usually through hot extrusion or Hot Isostatic Pressing (HIP) technique. The obtained product has a higher homogeneity degree with respect to the cast ingots and a lower defects and inclusions content. Therefore, it can be submitted to thermomechanical processing with a much lower risk of cracking.

Typical defects of the powder metallurgy products are the presence of prior particle boundaries (PPB) and residual porosities filled with gas coming from the atomization process. The PPBs are the residues of the powder particles surfaces and are usually characterized by a high level of segregation with formation of embrittling phases such as oxides and carbides. On the contrary, the gas entrapped in the pores expands during the subsequent heat treatment steps leading to an enlargement of the pore and to increased crack risk.

The Hot Isostatic Pressing (HIP) is a very common technique in the superalloys field [6] [7] [8]. It consists in subjecting the working piece to a high hydrostatic pressure, in the 10^8 Pa magnitude order, and to a heat treatment, usually at around 1200°C for 3-5 hours, at the same time.

The combined effects of the triggered plastic flow and the diffusion phenomena causes the bonding and consolidation of powders leading to a dense final product. HIP can also be used to produce near-net-shape components, saving the cost of the forging step, or as post process for cast products obtained by VIM [9] or for metallic parts produced through Additive Manufacturing (AM) techniques, in particular Selective Laser Melting (SLM) [10] [11]. The HIP process after SLM production allows to increase the degree of densification and homogeneity of the material and to reduce the technique related defects as porosities, cracks, anisotropy, internal

stresses and the presence of unwanted brittle second phases. The HIP process was also used as a joining technique [12].

1.1.2 Superalloys categories

Superalloys can be classified on the base of their base metal: the three main superalloys categories are based on iron, nickel and cobalt, respectively [2] [3].

1.1.2.1 Iron-based superalloys

The iron-based superalloys are the most economical and they can be considered as an evolution of the austenitic stainless steel. These alloys possess high mechanical properties and wear resistance at room temperature, furthermore they are characterized by good mechanical properties at high temperature, creep, oxidation and corrosion resistance. The matrix is mainly constituted by iron and nickel, the latter is present in quantities above 25% in order to stabilize the close packed Face Centered Cubic (FCC) austenitic phase. The other alloying elements are added to provide a solid solution reinforcement (Cr, Mo), promote the formation of strengthening precipitates (Al, Ti, Nb) or increase the oxidation and corrosion resistance (Cr, La, Y).

The Ni content determines the stability of the austenitic phase. A low Ni content allows the occurring of the martensitic transformation, therefore the strengthening is given by the formation of martensite and so this kind of alloys can only be used at low temperatures (up to about 500 °C). Martensitic-type alloys suffer of a greater crack sensitivity, which reduces their workability and weldability and requires an annealing pre-treatment or a post-stress relieving treatment. Conversely, if the Ni content is high enough to stabilize the austenitic phase in the entire window between room temperature and the melting point, the reinforcement is obtained through work hardening or precipitation hardening, in this latter case it is possible to use the alloy at higher temperatures. The chemical compositions of some Fe-based alloys are shown in table 1.1.

Table 1.1. Nominal compositions of some Fe-based superalloys. Data from: [2].

	Cr	Ni	Co	Mo	W	Nb	Ti	Al	Fe	C	Others
<i>Solid solution strengthened alloys</i>											
Alloy N-155	21	20	20	3	2.5	1	-	-	32.2	0.15	0.15 N, 0.2 La, 0.02 Zr
Haynes 556	22	21	20	3	2.5	0.1	-	0.3	29	0.1	0.50 Ta, 0.02 La, 0.002 Zr
Incoloy 800	21	32.5	-	-	-	-	0.38	0.38	45.7	0.05	-
Incoloy 801	20.5	32	-	-	-	-	1.13	-	46.3	0.05	-
Incoloy 802	21	32.5	-	-	-	-	0.75	0.58	44.8	0.35	-
<i>Precipitation hardened alloys</i>											
A-286	15	26	-	1.25	-	-	2	0.2	55.2	0.04	0.005 B, 0.3 V
Discaloy	14	26	-	3	-	-	1.7	0.25	55	0.06	-
Incoloy 903	<0.1	38	15	0.1	-	3	1.4	0.7	41	0.04	-
Incoloy 907	-	38.4	13	-	-	4.7	1.5	0.03	42	0.01	0.15 Si
Incoloy 909	-	38	13	-	-	4.7	1.5	0.03	42	0.01	0.4 Si
Incoloy 925	20.5	44	-	2.8	-	-	2.1	0.2	29	0.01	1.8 Cu

1.1.2.2 Nickel-based superalloys

Nickel-based alloys are the most diffused and studied superalloys. They are made by a highly stable austenitic FCC phase containing a large number of dissolved alloying elements which have different functions including, mainly, solid solution strengthening (Cr, Fe, Mo, W), formation of reinforcing second phases (Al, Ti, Nb), grain size control (C, B, Zr, Hf), increase of the oxidation and corrosion resistance (Cr, Al, Mo), increase of the creep resistance (B, Ta). Because of their high temperature resistance, the main applications of Ni-based alloys are: gas turbine components for aircraft or power generation systems, furnaces, vessels, reactors and other devices for the chemical and petrochemical industry and for nuclear plants, heat exchangers and rocket components in the aerospace field. The large quantities of expensive alloying elements and the requirement of long and complex heat treatment cycles, necessary to obtain the suitable microstructure, are the main causes of the high cost of these alloys, which limits its use to high value-added applications. The chemical compositions of some of the most important Ni-based superalloys, classified on the base of the production process for which they were developed, are reported in table 1.2.

Table 1.2. Nominal compositions of some Ni-based superalloys.

	Cr	Ni	Co	Mo	W	Nb	Ti	Al	Fe	C	Others	Source
<i>Cast alloys</i>												
CMSX-10	2	Bal.	3	0.4	5	0.1	0.2	5.7	-	-	8 Ta, 6 Re, 0.03 Hf	[3]
IN-713LC	12	Bal.	-	4.5	-	2	0.6	5.9	-	0.05	0.01 B, 0.1 Zr	[3]
IN792	12.6	Bal.	9	1.9	4.3	-	4	3.4	-	0.09	4.3 Ta, 1 Hf, 0.02 B, 0.06 Zr	[3]
Mar-M246	8.3	Bal.	10	0.7	10	-	1	5.5	-	0.14	3 Ta, 1.5 Hf, 0.02 B, 0.05 Zr	[3]
Nasair 100	9	Bal.	-	1	10.5	-	1.2	5.75	-	-	3.3 Ta	[1]
Renè 80	14	Bal.	9.5	4	4	-	5	3	-	0.17	0.02 B, 0.03 Zr	[3]
Renè N6	4.2	Bal.	12.5	1.4	6	-	-	5.8	-	0.05	7.2 Ta, 5.4 Re, 0.15 Hf, 0.01 Y	[3]
TMS-138	2.8	Bal.	5.8	2.9	6.1	-	-	5.8	-	-	5.6 Ta, 5.1 Re, 0.05 Hf	[1]
TMS-162	2.9	Bal.	5.8	3.9	5.8	-	-	5.8	-	-	5.6 Ta, 4.9 Re, 0.09 Hf, 6 Ru	[1]
<i>Wrought alloys</i>												
Astroloy	15	56.5	15	5.25	-	-	3.5	4.4	<0.3	0.06	0.03 B, 0.06 Zr	[2]
Hastelloy X	22	49	<1.5	9	0.6	-	-	-	15.8	0.15	-	[2]
Haynes 230	22	55	<5	2	14	-	-	0.35	<3	0.1	<0.015 B, 0.02 La	[2]
Incoloy 901	12.5	42.5	-	6	-	-	2.7	-	36.2	<0.1	-	[2]
Inconel 600	15.5	76	-	-	-	-	-	-	8	0.08	0.25 Cu	[2]
Inconel 625	21.5	61	-	9	-	3.6	0.2	0.2	2.5	0.05	-	[2]
Inconel 718	19	52.5	-	3	-	5.1	0.9	0.5	18.5	<0.08	<0.15 Cu	[2]
Nimonic 80A	19.5	73	1	-	-	-	2.25	1.4	1.5	0.05	<0.10 Cu	[2]
Renè 41	19	55	11	10	-	-	3.1	1.5	<0.3	0.09	0.01 B	[2]
Udimet 720	18	55	14.8	3	1.25	-	5	2.5	-	0.035	0.03 Zr	[2]
Waspaloy	19.5	57	13.5	4.3	-	-	3	1.4	<2	0.07	0.006 B, 0.09 Zr	[2]
<i>Alloys for powder metallurgy</i>												
IN100	12.4	Bal.	18.4	3.2	-	-	4.3	4.9	-	0.07	0.02 B, 0.07 Zr	[3]
N18	11.2	Bal.	15.6	6.5	-	-	4.4	4.4	-	0.02	0.5 Hf, 0.015 B, 0.03 Zr	[3]
Renè 88 DT	16	Bal.	13	4	4	0.7	3.7	2.1	-	0.03	0.015 B	[3]
Renè 95	13	Bal.	8	3.5	3.5	3.5	2.5	3.5	-	0.065	0.013 B, 0.05 Zr	[3]

The Ni-based superalloys will be further deepened at paragraph 1.2. Inconel 718 alloy, on which the research work reported in this thesis has been performed, will be described in greater details at paragraph 1.3.

1.1.2.3 Cobalt-based superalloys

Cobalt-based superalloys possess the highest strength at elevated temperature and thermal shock resistance, therefore they are used in applications with service temperatures of 1000-1100°C, beyond the operability field of the nickel-based superalloys. Examples of similar applications are the components of the combustion chambers. Because of the low hot cracking sensitivity, the cobalt-based alloys have a high workability and weldability. They are strengthened mainly by highly stable carbides of refractory elements (Mo, W), the formation of these carbides along the grain boundaries determines a high creep resistance. The chemical compositions of some cobalt-based superalloys are shown in table 1.3.

Table 1.3. Nominal compositions of some Co-based superalloys.

Alloy	Cr	Ni	Co	Mo	W	Nb	Ti	Al	Fe	C	Others	Source
Co 6	29	<3	Bal.	<1.5	5.5	-	-	-	<3	1.1	0.8 Si	[3]
F-75	28	<1	Bal.	6	<0.2	-	-	-	<0.75	0.25	0.5 Mn. 0.8 Si	[3]
FSX-414	29.5	10	Bal.	-	7.5	-	-	-	<2	0.35	0.5 Mn. 0.9 Si	[3]
Haynes 188	22	22	37	-	14.5	-	-	-	<3	0.1	0.90 La	[2]
Haynes 25	20	10	Bal.	-	15	-	-	-	<3	0.1	1.2 Mn. 0.8 Si	[3]
Haynes 25 (L605)	20	10	50	-	15	-	-	-	3	0.1	1.5 Mn	[2]
Haynes Ultimet	25	9	Bal.	5	2	-	-	-	3	0.06	0.8 Mn. 0.3 Si	[3]
MAR-M 509	23.5	10	54.5	-	7	-	0.2	-	-	0.6	3.5 Ta. 0.5 Zr	[2]
MAR-M 918	20	20	52	-	-	-	-	-	-	0.05	7.5 Ta. 0.1 Zr	[2]
Stellite B	30	1	61.5	-	4.5	-	-	-	1	1	-	[2]
UMCo-50	28	-	49	-	-	-	-	-	21	0.12	-	[2]
WI-52	21	-	Bal.	-	11	-	-	-	2	0.45	0.4 Mn. 0.4 Si	[3]
X-40	25	10	Bal.	-	7.5	-	-	-	<2	0.5	0.5 Mn. 0.9 Si	[3]
X-40 (Stellite alloy 31)	22	10	57.5	-	7.5	-	-	-	1.5	0.5	0.5 Mn. 0.5 Si	[2]
X-45	25	10	Bal.	-	7.5	-	-	-	<2	0.25	0.5 Mn. 0.9 Si	[3]

1.2 Categories and features of nickel-based superalloys

The main reasons that justify the use of nickel as a base metal for the development of this category of superalloys are listed below [1]:

- it can be easily strengthened through solid solution mechanism due to its ability to dissolve a high amount of Cr and Fe;
- it has an FCC structure that involves greater ductility and toughness, furthermore it also does not suffer from ductile/brittle transition;
- it does not undergo allotropic transformations that can cause instability and volume variations with consequent development of deleterious tension states;
- it has a high activation energy for self-diffusion (285 kJ/mol [13]), which determines a low creep rate of the matrix;
- it has good intrinsic resistance to hot oxidation and corrosion
- it has an acceptable specific weight and cost compared to other FCC materials such as Pd, Pt, Rh and Ir.

Nickel is the solvent of the γ solid solution, which constitutes the continuous austenitic matrix. In addition to nickel, superalloys contain a large number, usually

more than ten, of other alloying elements, which can be divided into three main groups:

- the elements of the first group tend to dissolve into the γ solid solution: Fe, Cr, Co, W, Ru, Mo and Re;
- the elements of the second group tend to form second ordered phases, called γ' and γ'' , with stoichiometry Ni_3M (where M represents a generic metallic atom): Al, Ti, Nb and Ta;
- the elements of the third group tend to segregate at the grain boundary: C, B, Zr and Hf; the interstitials C and B tend to form intergranular carbides and borides with Cr, Mo, W, Nb, Ta, Ti and Hf.

In the first group, Cr is usually added to achieve oxidation resistance through the formation of Cr_2O_3 passivating layer (see paragraph 1.3.6), but it can also form carbides that enhance the high temperature resistance. The presence of Al has two purposes, i.e. to further increase the oxidation resistance through the formation of highly stable Al_2O_3 protective scale and to cause the formation of γ' - Ni_3Al phase, which can be even strengthened by partial substitution of Al with Ti and Nb. Furthermore, Nb is added also to form the strengthening γ'' phase and carbides. Fe can improve the strength of the matrix through the solid solution mechanism, but it is detrimental for the oxidation resistance because it reduces the adherence of the protective scale. Co gives solid solution strengthening and it reduces the solubility of Al and Ti in the γ matrix leading to an increase of the solvus point of the γ' phase and, therefore, increase the retaining of the mechanical performances at high temperature. The mechanical strength is increased by the presence of Mo, W, Ta both because of the solid solution mechanism and of the formation of carbides. In the third group, B and Zr are added to increase the ductility and to form intergranular carbides which enhance the creep resistance. However, an excessive amount of these elements is detrimental for the weldability of the alloy.

The alloy composition determines the predominant strengthening mechanism, which can occur mainly due to the presence of a large amount of different dissolved solutes in the γ phase or because of the formation of second reinforcing phases, in particular γ' and/or γ'' , finely dispersed in the matrix phase.

Table 1.4. Tensile properties of some solid solution strengthening superalloys.

Alloy	Yield Strength (MPa)			Ultimate Tensile Strength (MPa)			Elongation to failure (%)			Source
	at	at	at	at	at	at	at	at		
	21°C	540°C	760°C	21°C	540°C	760°C	21°C	540°C	760°C	
Hastelloy S	455	340	310	845	775	575	49	50	70	[2]
Hastelloy X	360	290	260	785	650	435	43	45	37	[2]
Haynes 230	390	275	285	870	720	575	48	56	46	[2]
Incoloy 800	310	-	-	585	-	-	40	-	-	[14]
Incoloy 800H	275	-	-	585	-	-	45	-	-	[14]
Incoloy 800HT	275	-	-	585	-	-	40	-	-	[14]
Incoloy 825	345	-	-	655	-	-	35	-	-	[14]
Inconel 600	285	220	180	660	560	260	45	41	70	[2]
Inconel 625	490	415	415	965	910	550	50	50	45	[2]
Monel 400	345	-	-	585	-	-	35	-	-	[14]
Nimonic 75	285	200	160	745	675	310	40	40	67	[2]

On the base of this criterion, it is possible to divide the nickel-based superalloys into two main categories: solid solution strengthening and precipitation hardening alloys. A list of the main alloys of the two classes is reported in tables 1.4 and 1.5, respectively, together with an indication of the main mechanical properties.

Table 1.5. Tensile properties of some precipitation hardening superalloys.

Alloy	Yield Strength (MPa)			Ultimate Tensile Strength (MPa)			Elongation to failure (%)			Source
	at 21°C	at 540°C	at 760°C	at 21°C	at 540°C	at 760°C	at 21°C	at 540°C	at 760°C	
Astroloy	1050	965	910	1415	1240	1160	16	16	21	[2]
Inconel 706	1005	910	660	1310	1145	725	20	19	32	[2]
Haynes 263	638 ± 53	-	-	1035 ± 65	-	-	40 ± 5	-	-	[14]
Incoloy 909	1035	-	-	1275	-	-	15	-	-	[14]
Incoloy 925	760	-	-	970	-	-	18	-	-	[14]
Incoloy 945	968 ± 68	-	-	1170 ± 70	-	-	25 ± 5	-	-	[14]
Inconel 713	-	-	-	830	-	-	5	-	-	[14]
Inconel 725	900 ± 70	-	-	1238 ± 73	-	-	30 ± 5	-	-	[14]
Inconel X750	815	725	-	1200	1050	-	27	26	-	[2]
Inconel X-750	863 ± 173	-	-	1240 ± 140	-	-	23 ± 8	-	-	[14]
M-252	840	765	720	1240	1230	945	16	15	10	[2]
Monel K500	790	-	-	1100	-	-	20	-	-	[14]
Nimonic 105	830	775	740	1180	1130	930	16	22	25	[2]
Nimonic 115	865	795	800	1240	1090	1085	27	18	24	[2]
Nimonic 80A	620	530	505	1000	875	600	39	37	17	[2]
Nimonic 90	810	725	540	1235	1075	655	33	28	12	[2]
Pyromet 860	835	840	835	1295	1255	910	22	15	18	[2]
Renè 41	1060	1020	940	1420	1400	1105	14	14	11	[2]
Renè 95	1310	1255	1100	1620	1550	1170	15	12	15	[2]
Udimet 500	840	795	730	1310	1240	1040	32	28	39	[2]
Udimet 520	860	825	725	1310	1240	725	21	20	15	[2]
Udimet 630	1310	1170	860	1520	1380	965	15	15	5	[2]
Udimet 700	965	895	825	1410	1275	1035	17	16	20	[2]
Udimet 710	910	850	815	1185	1150	1020	7	10	25	[2]
Udimet 720	1195	-	1050	1570	-	1455	13	-	9	[2]
Waspaloy	795	725	675	1275	1170	650	25	23	28	[2]

1.2.1 Solid solution strengthened alloys

Solid solution strengthened alloys contain substitutional alloying elements such as Cr, Fe, Co, W, Mo dissolved in the γ solid solution. The strengthening is given by the crystallographic distortion due to the difference in the atomic radius of the solute atoms with respect to Ni; this crystallographic distortion hinders the dislocations motion and increases the mechanical resistance of the austenitic phase consequently. Solid solution strengthened alloys are usually submitted to a solution annealing at a temperature between 1000 and 1200°C with the aim of dissolving any embrittling second phases eventually present and enriching the solid solution with all the potential alloying elements contents. The yield strength and ultimate tensile strength values of these kind of nickel-based superalloys can reach respectively 450 MPa and 830 MPa [14]. Precipitation hardening alloys should be used when higher levels of mechanical strength are required. However, solid solution strengthened alloys have generally a higher corrosion resistance and, therefore, find applications in power generation, chemical and petrochemical plants. Furthermore, since the mechanical properties of these alloys are not based on the formation of strengthening second phases, their service temperature is not limited by the respective solvus temperatures of these phases. The elements dissolved in the solid solution affect not only the mechanical properties, but also

other important features of the alloy such as the oxidation resistance and weldability. Mo and W also allow to improve the creep resistance of the alloy due to their low diffusivity in the γ matrix. Depending on the present alloying elements and the heat treatments cycle at which they are submitted, the solid solution strengthened alloys may contain carbides, mainly of the MC type, formed by Nb, Ti, W, Mo, and Ta, and of the $M_{23}C_6$ type, formed by Cr, Mo and W. Carbides tend to form along the grain boundaries and so they can be used to control grain size, avoiding the coarsening of them during heat treatment, and to improve the creep resistance by hindering the intergranular sliding. The discrete blocky or globular carbides morphology is preferable for these purposes, instead of intergranular film of Cr carbides that causes the sensitization of the alloy to intergranular corrosion. Because of this mix of pros and contra, the quantity and morphology of carbides must be carefully controlled through suitable heat treatments.

1.2.2 Precipitation hardening alloys

Precipitation hardening alloys contain larger amounts of Al, Ti and Nb, which allow the formation of strengthening second phases during an appropriate heat treatment cycle. The strengthening second phases consist mainly in the coherent γ' and γ'' intermetallic compounds, which allow to maintain high mechanical properties even at high temperatures, i.e. up to about $0.5T_m$ where T_m is the melting point of the alloy. Therefore, these alloys combine high mechanical performances with good oxidation and corrosion resistance. The yield strength and ultimate tensile strength values are 1035 MPa and 1380 MPa, respectively [14]. These alloys usually require heat treatment cycles consisting of a high temperature solutioning step, in which the unwanted coarse second phases are dissolved and the content of solute elements in the matrix is increased. The solute elements, released in solid solution during the solution annealing, form the strengthening compounds during the controlled cooling and the aging step, which usually consists of one or more thermal cycles designed to obtain the size, morphology and distribution of precipitates that optimize the mechanical properties of the alloy. The mechanical strength can be retained at high temperature as long as the reinforcing precipitates remain stable. If the coarsening of these precipitates occurs, the coherency with the matrix is progressively lost with consequential decrease of the mechanical properties. The evolution of the reinforcing precipitates population strongly affects also the weldability of the alloy and its sensitivity to hot cracking.

1.2.3 Weldability

The weldability of solid solution strengthened alloys is influenced by the formation of second phases formed due to the microsegregation phenomenon of the alloy elements which occurs during the fast solidification of the fusion welds [14]. Typically, these second phases consist of carbides and Topologically Closed Packed (TCP) intermetallic compounds such as σ , μ and P. They have a negative

effect on toughness, ductility and mechanical properties of the alloy. Furthermore, their formation can lead to a local reduction of the melting point with consequent increase in the solidification cracking susceptibility of the alloy. The segregation of Cr and Mo can also cause a reduction in the oxidation and corrosion resistance of the alloy. In some cases, solid solution strengthened alloys can be used in the as-welded condition, otherwise it may be necessary to perform a suitable Post-Weld Heat Treatment (PWHT). PWHT helps to reduce the microsegregation, to dissolve the undesirable second phases, which form from the liquid during the welding process or through precipitation in the Heat Affected Zone (HAZ), and to restore the correct microstructure in view of the mechanical properties and the oxidation and corrosion resistance. PWHT has also the aim of reducing the residual stresses induced by the welding and, therefore, it guarantees a better dimensional stability.

The high complexity of the chemical composition that characterizes the precipitation hardening alloys implies even more severe welding problems deriving from microsegregation, liquation and formation of undesired second phases both during solidification and subsequent heat treatments. In particular, the alloys whose strengthening is obtained through an extensive precipitation of γ' phases, for example René 41, René 80, CM247LC, Udimet 700, Inconel X-750 and Waspaloy, are very prone to the strain-aging cracking mechanism [15], which occurs because of the overheating in the HAZ which causes an extremely rapid precipitation of γ' with consequent drastic reduction of the alloy ductility. The internal stresses, related to the fast formation of γ' precipitates, may cause the nucleation of cracks, usually where an inclusion or a microstructural defect, for example a void or an intergranular carbide, is present, and subsequent cracks propagation favored by the embrittlement of the alloy. Strain-age cracking can also occur after the welding process during the PWHT. The strain-aging cracking phenomenon is a serious limitation on the weldability of these kind of alloys; a high content of the γ' forming elements, i.e. Ti and Al, and brittle carbides forming elements, for example Cr and Co, make the alloy extremely hard to weld. The plot in figure 1.1 classifies the main nickel-based precipitation hardening superalloys in alloys considered as weldable (below the red line) and difficult to weld alloys (above the red line) on the base of the Ti and Al content and the consequent susceptibility to strain-age cracking.

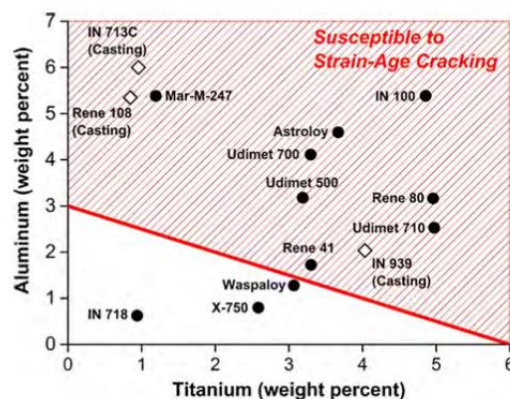


Figure 1.1. Weldability map of the nickel superalloys based on the Al and Ti content. The alloys below the red line are considered weldable. From: [15].

The typical approach followed to reduce the strain-aging cracking problem is to strongly decrease the content of Al and Ti in the alloy composition in order to avoid an excessive formation of γ' . The reduction of Al and Ti can be compensated by the increase of the Nb content, which leads to strengthening due to the precipitation of γ'' -Ni₃Nb phase rather than γ' phase. The coherency strain between γ'' and the matrix γ is much higher with respect to the one between γ' and γ , for this reason the nucleation of γ'' occurs slower than γ' [1] [16]. Consequently, the risk of a significant alloy embrittlement and cracking due to an excessively rapid precipitation during heating and cooling cycles is strongly reduced. This is the followed solution in the case of Inconel 718 alloy, which in fact is characterized by an extremely high weldability. However, Inconel 718 is particularly sensitive to the intergranular micro-fissuring in the HAZ [17]. The micro-fissuring phenomenon occurs due to the plastic strain that develops in the HAZ when this strain cannot be accommodated because of the formation of liquid at the grain boundaries, on its turn caused by the presence of segregations, impurities or low melting second phases as the Nb-rich Laves phases. Decreasing the Al and Ti contents in order to reduce the strain-cracking problem has also the effect of decreasing the γ' solvus temperature. Therefore, the service temperature of Inconel 718 is lower with respect to the one of the superalloys which are strengthened by an extensive precipitation of the γ' phase because the strengthening due to the γ' and γ'' phases vanishes at lower temperatures.

1.3 Inconel 718 alloy

Inconel 718 is a nickel-based superalloy belonging to the precipitation hardening alloys category, it is based on the Ni-Cr-Fe ternary system and it finds applications in the aerospace fields and in the chemical, petrochemical and nuclear plants. The chemical composition of Inconel 718 is reported in table 1.2.

Inconel 718 possesses high mechanical properties at service temperatures of 700°C, but can also be used at cryogenic regime. Furthermore, it has good creep and fatigue resistance and excellent hot oxidation and corrosion resistance. As already discussed at paragraph 1.2.3, Inconel 718 is characterized by a very good weldability due to its low sensitivity to the strain-age cracking.

1.3.1 Microstructure and phases

Inconel 718 consists of a γ austenitic matrix with face-centered cubic (FCC) crystallographic system and a lattice parameter $a = 0.3616$ nm. The main strengthening phases are γ' and γ'' , both of which form a coherent interface with the matrix. Plenty of other types of second phases can be found dispersed in the matrix depending on the production cycle and the heat treatments at which the alloy is submitted (see the CCT curves in figure 1.2). These second phases affect the features of the alloy, in particular the high temperature mechanical performances and the ductility and toughness. In the follow, a description of the main types of

precipitates that can be found most frequently in Inconel 718 is given [1] [18] [19] [20] [21] [22] [23] [24].

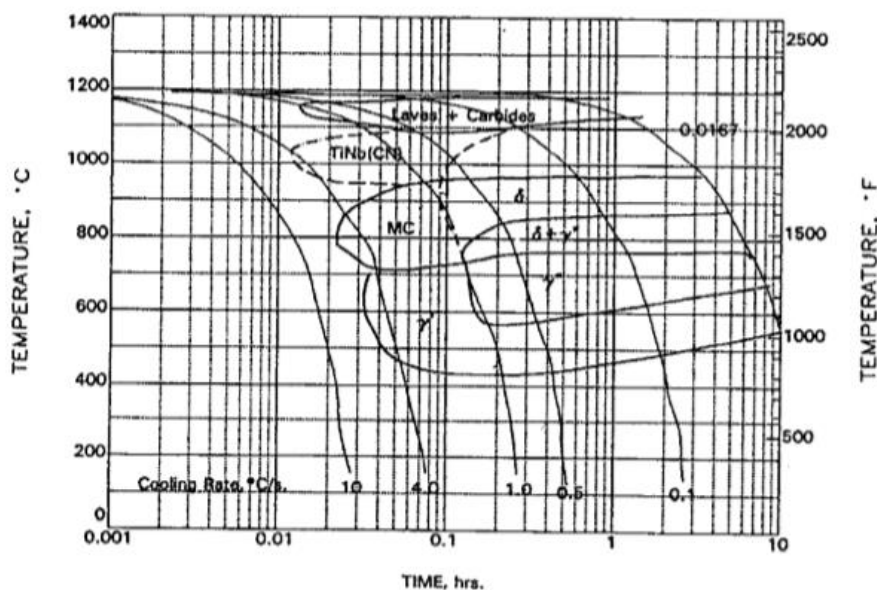


Figure 1.2. Continuous Cooling Transformation (CCT) curves of Inconel 718 ingot after homogenization treatment at 1180°C for 90 hours. From: [25].

1.3.1.1 Carbides

Because of the presence of a carbon content up to 0.08% wt. in the nominal composition of Inconel 718, carbides of the alloying elements which have higher affinities with C, i.e. Nb, Ti and Mo, may form. In Inconel 718 alloy, the observable carbides are mainly of the MC type and are rich in Nb or Ti. MC carbides form during solidification due to the microsegregation of Nb and Ti in the interdendritic zones (see paragraph 1.3.2.3) and they are sufficiently stable to do not modify during the heat treatments at low temperature. Partial dissolution of carbides can occur during the heat treatment at temperatures around 1100°C (see figure 1.3). The carbides formed at the grain boundaries allow to avoid the grain coarsening during the heat treatments. The decomposition of MC carbides after prolonged exposure at temperatures around 750-900°C [26] through reaction with the matrix is reported for some superalloys as Waspaloy [27], Renè 80 [28] [29] [30], CM 247 LC [31]: $MC + \gamma \rightarrow M_6C$ or $M_{23}C_6 + \gamma'$.

The $M_{23}C_6$ carbides are richer in Cr, whereas M_6C carbides have a greater content of Ni, Co, W and Cr [30]. These carbides tend to form along grain boundaries (see figure 3) and their amount and morphology should be carefully controlled in order to avoid embrittlement due to nucleation and propagation of intergranular cracks and sensitization to intergranular corrosion. The presence of $M_{23}C_6$ carbides in Inconel 718 alloy is reported in the HAZ of welds [32], however secondary carbides arising from the decomposition of MC does not tend to form in this alloy even after prolonged thermal exposure [18].

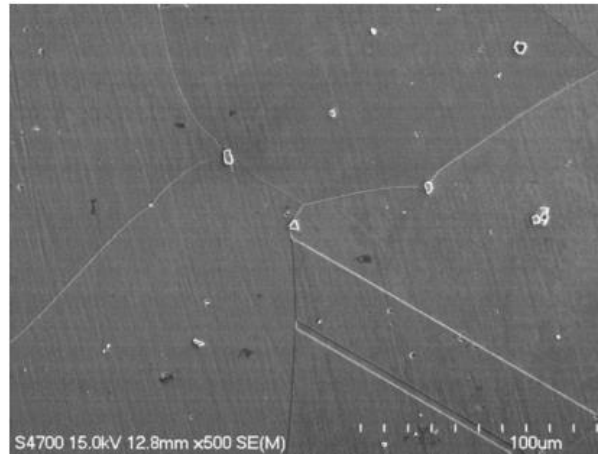


Figure 1.3. SEM micrograph showing carbides in Inconel 718 alloy after solution treatment at 1095°C for 1 hour. From: [33].

1.3.1.2 Topologically Close Packed (TCP) phases

The TCP phases form generally in the final stage of the solidification through eutectic reaction because of the microsegregation of the alloying elements in the remaining liquid in the interdendritic zones (see paragraph 1.3.2.3). TCP phases can also form along the grain boundaries during a prolonged exposure at temperatures of about 800-900°C [21], typically in the form of needles or plates. These compounds should be avoided in the service microstructure because they are very brittle and detrimental to the mechanical properties, ductility and weldability of the alloy. Furthermore, the sequestration of Cr and Mo within these phases may affect the corrosion resistance. The most frequently reported TCP phases in superalloys are σ (tetragonal), μ (hexagonal) and P (orthorhombic) [21] [34] [35].

In Inconel 718, the main observed TCP compounds are the Laves phases, which are mostly found in the interdendritic zones [36] [37] [38] [39] due to the strong microsegregation of Nb and Mo in the final liquid or formed after prolonged exposure to high temperatures. Laves phases are metastable intermetallic compounds with the following stoichiometry $(\text{Ni, Fe, Cr})_2(\text{Nb, Mo, Ti})$ which crystallize in the hexagonal system with a MgZn_2 lattice type (figure 1.4); they typically form as large globular or irregularly shaped precipitates.

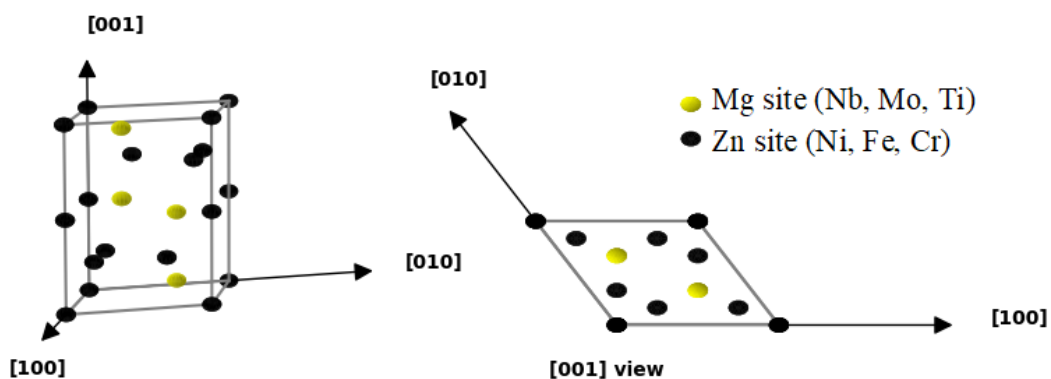


Figure 1.4. Crystal structure of Laves phase. Hexagonal system with MgZn_2 lattice type and parameters [21] $a = b = 0.475\text{-}0.495$ nm, $c = 0.77\text{-}0.815$ nm.

The presence of the Laves phase in the alloy microstructure is strongly unwanted because they lead to embrittlement (these precipitates act as cracks nucleation sites) [40] and reduce the availability of Nb and Ti for the formation of the strengthening γ' and γ'' precipitates. Furthermore, they reduce the local melting temperature with consequent increase in the liquation cracking susceptibility. The presence of Laves phases requires a long homogenization heat treatment or a HIP treatment in order to reduce the segregation level of the alloy [41].

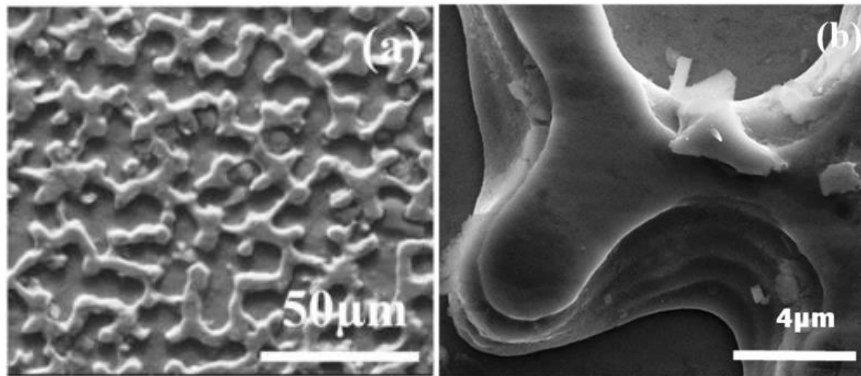


Figure 1.5. Laves phases network on the interdendritic region of the fusion zone of a weld. Higher (a) and lower (b) magnification. From: [36].

1.3.1.3 Delta phase

The δ phase is a thermodynamically stable compound with Ni_3Nb stoichiometry which tends to form in Inconel 718 during exposure to temperatures between 800 and 1010°C [23]. The δ phase crystallizes in the DO_a orthorhombic system, the unit cell is represented in figure 1.6.

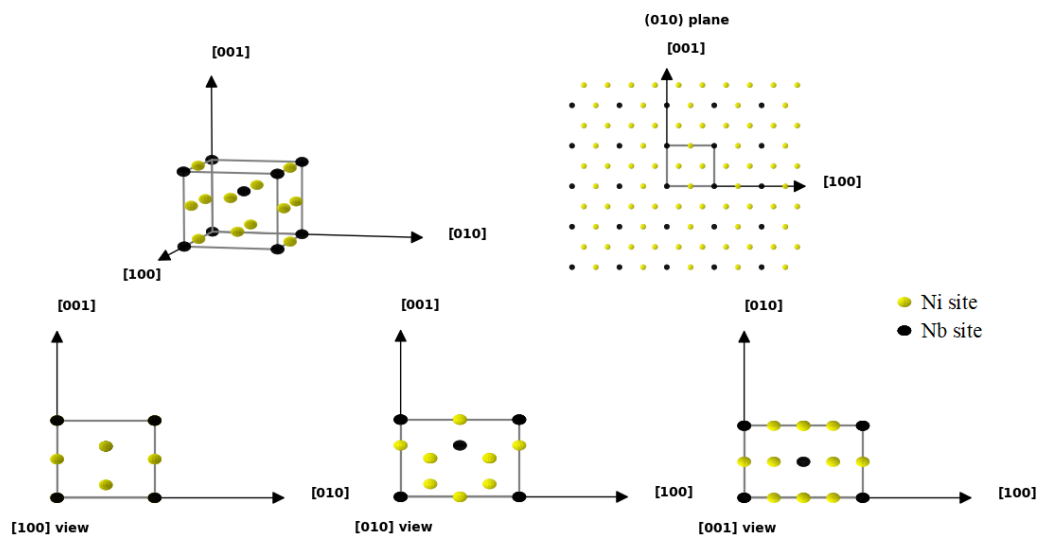


Figure 1.6. Orthorhombic DO_a crystal structure of δ phase with parameters [18] $a = 0.5141$ nm, $b = 0.4231$ nm, $c = 0.4534$ nm.

The high mismatch between the unit cells of δ and γ phases involves the formation of an incoherent γ/δ interface, therefore the δ type precipitates are not

suitable to perform an effective reinforcing function. Furthermore, the δ precipitates have typically a plate-like morphology with thickness that fall between 200 nm and 1 μm (see figure 1.7) and because of this shape they can act as stress concentrators with consequent embrittlement of the alloy and increase of susceptibility to the hot cracking. The δ phase is usually unwanted also because it reduces the availability of Nb for the formation of the strengthening phase γ'' , with consequent reduction of the mechanical properties that can potentially be achieved with the aging treatment.

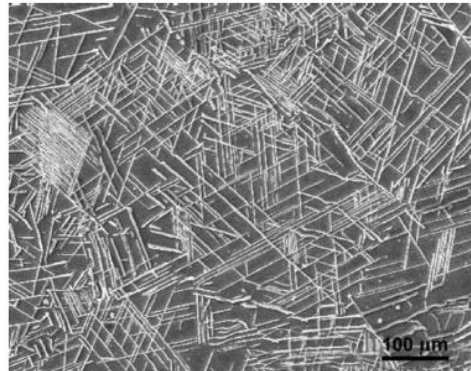


Figure 1.7. SEM micrograph showing plate-like δ precipitates formed after exposition at 950°C for 50 hours in an Inconel 718 alloy. From: [23].

The plate morphology can be corrected by a thermomechanical treatment in which the plates are fragmented to form spherical particles or slightly elongated precipitates [42]. The formation of globular δ is also reported in the literature [43] [44]. The δ phase starts to form at about 800-850°C and the higher precipitation rate is reached at about 900°C [45], the solvus temperature can vary between 1005°C, when the Nb content is 5.06%, to 1015°C, when the Nb content is 5.41% [23]. The δ phase can form both along the grain boundaries and inside the grains; the intragranular δ precipitates have usually a lower size and grow according to a precise crystallographic relationship with the matrix [19] [44] [46] [47]: $(010)_\delta \parallel \{111\}_\gamma$, $[100]_\delta \parallel \langle 1\bar{1}0 \rangle_\gamma$.

Intragranular precipitation occurs through nucleation at the stacking fault defects present in the γ'' phase (figure 1.8) [19]. At temperatures above 900°C, the γ'' phase does not form and δ nucleates directly in the matrix.

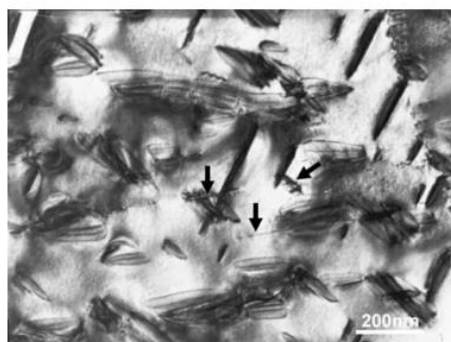


Figure 1.8. TEM micrograph showing plates of δ phase nucleated on γ'' particles in a spray formed Inconel 718 alloy heat treated at 875°C for 6 hours. From: [23].

The intragranular δ precipitates tend to form clusters of parallel plates, instead intergranular δ precipitates are usually isolated and they grow with a random orientation [45] [48]. These two kinds of δ precipitates have different effect on the properties of the alloy. A great amount of intragranular δ precipitates can lead to a loss in the ductility [45], instead the intergranular δ phase can also be beneficial in certain situations because it allows to control the grain size, avoiding coarsening during the heat treatment [23]. Furthermore, the intergranular precipitates with plate-like morphology may hinder the reciprocal motion of the grains, with consequent increase in the creep resistance, and improve the high temperatures stress rupture properties because of a crack deflection mechanism from the grain boundaries [22].

1.3.1.4 Gamma double prime phase

The γ'' phase represents the main strengthening constituent in Inconel 718 alloy. γ'' phase is an ordered intermetallic phase with Ni_3Nb stoichiometry that crystallize in the DO_{22} body centered tetragonal (BCT) system. The disposition of the atoms in the γ'' unit cell is shown in figure 1.9, the unit cell can be approximately obtained by stacking two γ cubic cells. The low mismatch between the γ and γ'' lattices allows the formation of a coherent interface with the matrix, which can guarantee the stress transfer from the matrix to the γ'' precipitates avoiding the stress concentration effect.

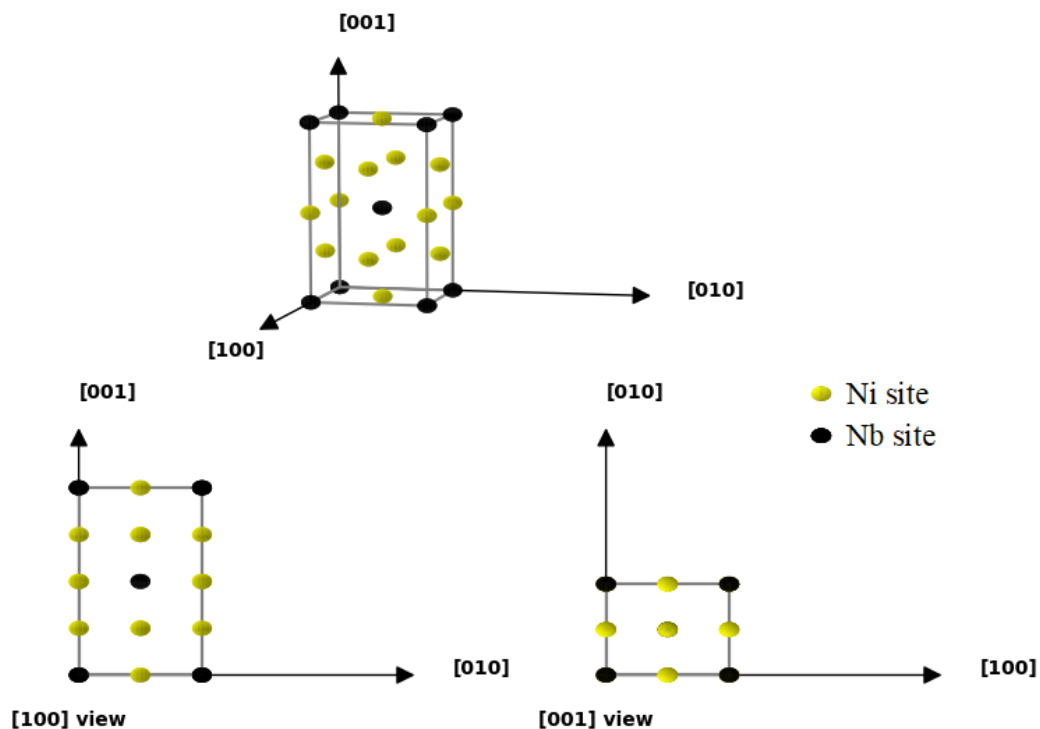


Figure 1.9. Body centered tetragonal DO_{22} crystal structure of γ'' phase with parameters [18] $a = b = 0.3624$ nm, $c = 0.7460$ nm.

The γ'' phase forms in the temperature range between about 700°C and 900°C. It tends to precipitate with a discoidal morphology with an aspect ratio between the diameter and the thickness of about 5-6. If the precipitation occurs at a low temperature, the formed γ'' particles have an extremely small size and their uniform dispersion in the matrix (see figure 1.10) allows to obtain a high improvement of the mechanical properties. However, the γ'' precipitates can undergo coarsening due to the exposure to high temperature during heat treatment or in service with consequent reduction of their strengthening effect [24] [49] [50]. Furthermore, the γ'' phase is not stable and so, after prolonged thermal exposure, it tends to transform into the incoherent δ phase, which has the same chemical composition but different crystallographic arrangement [16], with consequent reduction of the mechanical properties.

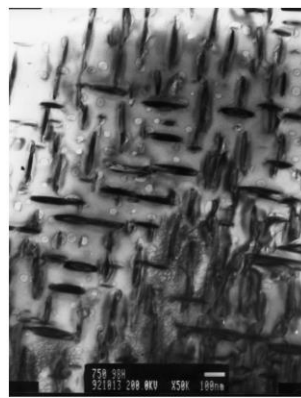


Figure 1.10. TEM micrograph showing discoidal γ'' and spherical γ' precipitates on an Inconel 718 alloy aged at 750°C for 100 hours. From: [49].

1.3.1.5 Gamma prime phase

The ordered γ' phase has $\text{Ni}_3(\text{Ti}, \text{Al})$ stoichiometry and crystallize in the $L1_2$ cubic system. The unit cell of γ' phase is represented in figure 1.11.

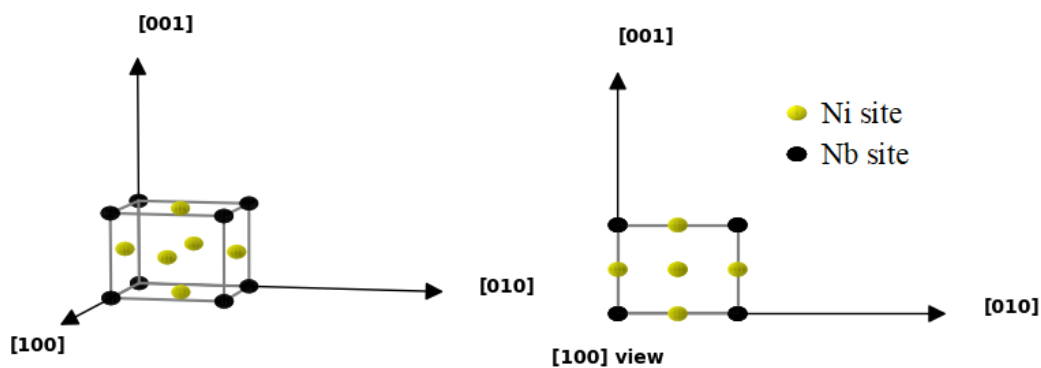


Figure 1.11. Cubic $L1_2$ crystal structure of γ' phase with parameters [18] $a = b = c = 0.3605$.

In Inconel 718 alloy, Nb can partially occupy the Ti and Al sites in the unit cell with consequent reinforcement of the γ' phase through the substitutional mechanism. The intermetallic γ' - Ni_3Al compound possesses a peculiar mechanical behavior characterized by an increase in the tensile properties with the temperature

up to about 800°C. Because of the ordered structure, the passage of a dislocation in the $L1_2$ type lattice causes the formation of a two-dimensional defect called antiphase boundary (APB). The APB is a plane along which the arrangement of atoms is not the correct one, as shown in figure 1.12, this results in a high energy surplus with respect to the minimum energy condition of perfect disposition of the atoms in the theoretical lattice. The movement of a single dislocation is strongly hindered in Ni_3Al because of the formation of the high energy APB, however the dislocations can still move in pairs, forming the so-called “super dislocations”. The passage of the second dislocation of the pair re-establishes the correct order in the atoms arrangement in the lattice, in this way the APB is limited to the area between the two dislocations of the pair. The atypical behavior of Ni_3Al is ascribed to the thermally activated cross slip mechanism occurring when the temperature is increased, causing the cross slip of some segments of the super dislocations from a $\{111\}$ octahedral slip plane to a $\{001\}$ cube slip plane. The segments where the cross slip has occurred cannot move without extending the APB, therefore their motion is hindered and the resistance to plastic deformation is consequently increased. This microstructural constraint is called Kear-Wilsdorf lock [1] [15] [51].

The γ' phase forms a coherent interface with the γ matrix, therefore the dislocations in γ can cross the γ' lattice where their motion is hindered by the formation of the APB (figure 1.12). As a consequence, the alloy is strengthened even at high temperature by the presence of many γ' particles.

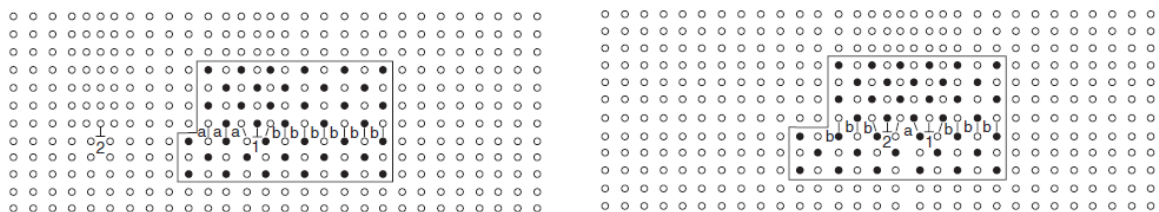


Figure 1.12. Scheme of a dislocation that pass an ordered structure forming an antiphase boundary (left); dislocations are forced to move in pairs in the ordered structure (right). From: [14].

The γ' phase is usually present in Inconel 718 alloy in the form of globular precipitates with a size lower than 20 nm that form in the temperature range of about 595°C and 700°C. Coalescence of the γ' particles of can occur during exposure to high temperatures with consequent increase of their size and reduction of the obtainable reinforcing effect for the alloy. During the coarsening process, the coherency with the matrix is progressively lost and the morphology of the γ' particles change from spherical to cubic [5] [15] [52].

In Inconel 718 alloy, the γ' and γ'' phases can sometimes form together by co-precipitation (figure 1.13), forming the so-called compact morphology [24].

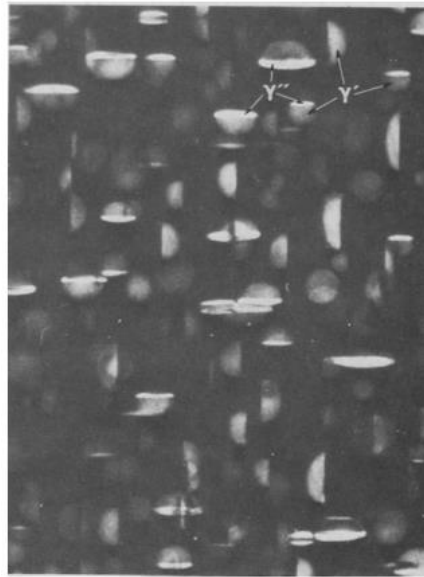


Figure 1.13. TEM micrograph showing the co-precipitation of γ' and γ'' particles in an Inconel 718 alloy. From: [24].

1.3.2 Solidification

The solidification modality of a metal alloy determines its microstructural features and the distribution and size of the eventually formed second phases, therefore it has a deep influence on the final performances of the alloy and on its response to the subsequent heat treatments. Therefore, the comprehension of the phenomena occurring during solidification and the effects on the microstructural characteristics of the conditions in which it occurs, in particular the type and quantity of solute present, the rate of cooling and the extent of the established thermal gradients, is of fundamental importance.

1.3.2.1 Microsegregation: partition coefficient and Scheil's model

When the solidification occurs in thermodynamic equilibrium conditions, i.e. when the rate R of the solidification front tends to zero, the solute concentrations in the liquid C_L and in the solid C_S phases are uniform and equal, at each temperature, to the equilibrium value indicated by the phase diagram. The ratio $k = C_S/C_L$, approximately independent from the temperature in the solidification range, is called the partition coefficient of the solute, therefore k is a measure of the solute tendency to segregate in the solid phase during the solidification: the solute tends to dissolve more in the solid when $k > 1$, instead it will be more present in the liquid until the end of the solidification if when $k < 1$. However, in most of the technological processes of industrial interest, the alloys solidification is too fast and the thermodynamic equilibrium conditions cannot be maintained. In these cases, the solute concentrations corresponding to the thermodynamic equilibrium can be established only locally at the solid/liquid interface and the establishment of a certain grade of compositional microsegregation cannot be avoided because there is no time for the solute diffusion to uniform the concentration in the system.

This situation can be described through the Scheil's model [53], that is based on the follow simplifying assumptions:

1. perfect mixing in the liquid, i.e. the solute concentration C_L is uniform in the liquid domain;
2. the solute diffusion in the solid phase does not occur or it is negligible;
3. local equilibrium at the solid/liquid interface, in other words the solute concentrations C_S and C_L respectively in the solid and in the liquid in reciprocal contact are the ones reported by the phase diagram at each temperature;
4. the difference between the molar volumes of the liquid and the solid can be neglected;
5. the partition coefficient k is constant with the temperature;
6. the solid/liquid interface is planar or it has a curvature sufficiently low that the Gibbs-Thomson effect can be neglected.

At the beginning of the solidification, the liquid has the nominal solute concentration C_0 , therefore the first solid is formed at the temperature T_1 with the solute concentration $C_S(T_1) = kC_0$. In the case of $k < 1$, the formed solid has a solute concentration lower than the liquid, therefore the solute must be rejected in the remaining liquid as the solidification process proceeds. Conversely, in the case $k > 1$, the liquid is progressively depleted in the solute. During the temperature decreasing, the solute concentration $C_L(T)$ of the liquid phase remain uniform over all the liquid volume at the corresponding value indicated by the phase diagram because of the assumptions N.1 and N.3. Conversely, in the solid phase the equilibrium solute concentration value $C_S(T) = kC_L(T)$ is established only at the solid/liquid interface, instead the solid formed previously between T_1 and the current temperature T has a lower or higher solute concentration respect to the equilibrium value if k is minus or major to 1 respectively. Therefore, a compositional gradient is formed in the solid that cannot be reduced by the solute diffusion because of the assumption N.2. The trend of the mean value $C_{S,mean}(T)$ of the solute concentration in the solid phase does not follow the solidus curve of the phase diagram, as in the case of a quasi-static solidification, but it traces a curve placed below or above it in the case of $k < 1$ or $k > 1$, respectively, as shown in figure 1.14.

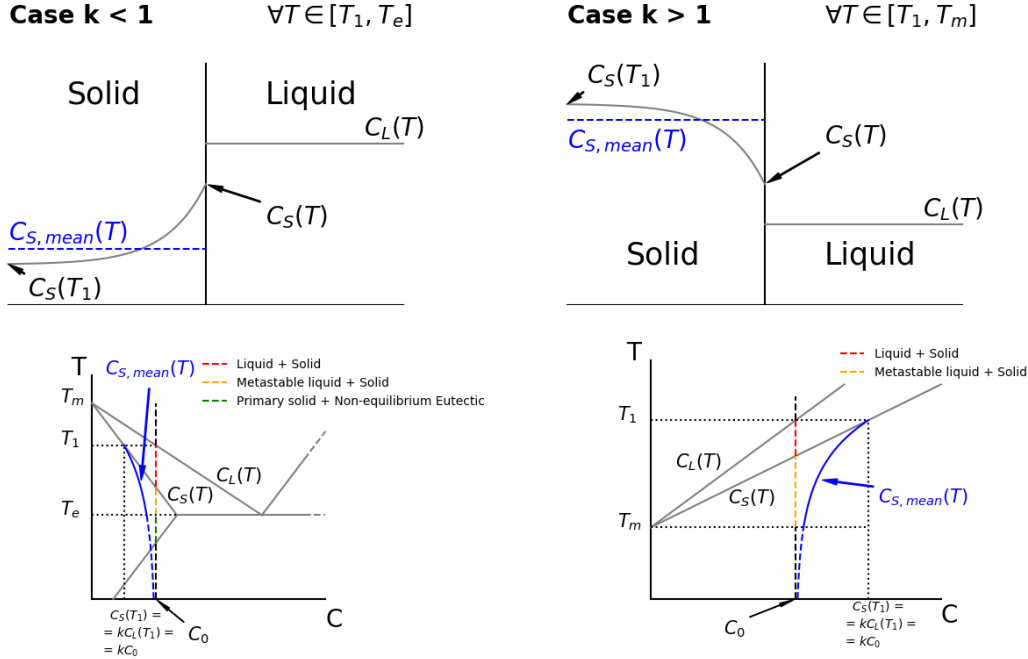


Figure 1.14. Solute profiles in the solid and liquid phase and path followed in the phase diagram by the mean concentration in the solid according to the Scheil's model in the cases of $k < 1$ and $k > 1$.

At each reduction dT of the system temperature, an infinitesimal liquid volume dV_L solidifies. The difference between the solute quantity $C_L(T) \cdot dV_L$ in the infinitesimal volume before the solidification and the solute quantity $C_S(T) \cdot dV_S$ after the solidification corresponds to the solute rejected to (if $k < 1$) or removed from (if $k > 1$) the liquid. This difference is equal to:

$$C_L(T)dV_L - C_S(T)dV_S = C_L(T)dV_L - kC_L(T)dV_S = (1 - k)C_L(T)dV_S \quad \text{eq. 1.1}$$

where the last equality is justified by the assumption N.4, for which it is possible to neglect the volume variation associated to the solidification, i.e. $dV_S \cong dV_L$. The solute rejected to or removed from the liquid during the solidification of dV_L leads to an infinitesimal variation of the solute concentration in the liquid equals to:

$$V_L[C_L(T - dT) - C_L(T)] = V_L dC_L \quad \text{eq. 1.2}$$

By equating the last terms of equations 1.1 and 1.2 and dividing by the total volume V of the system:

$$(1 - k)C_L(T)df_S = f_L dC_L \Rightarrow (1 - k) \frac{df_S}{1 - f_S} = \frac{dC_L}{C_L(T)} \quad \text{eq. 1.3}$$

with $f_S = V_S/V$ and $f_L = V_L/V$ the volume fractions of the solid and the liquid, respectively. By integrating equation 1.3 between the temperature T_1 , at which

corresponds $f_S = 0$ and $C_L = C_0$, and a generic temperature T in the solidification range using the assumption N.5:

$$\begin{aligned} \int_{f_S=0}^{f_S} (1-k) \frac{df_S}{1-f_S} &= \int_{C_0}^{C_L} \frac{dC_L}{C_L(T)} \Rightarrow (k-1) \ln(1-f_S) = \ln\left(\frac{C_L}{C_0}\right) \Rightarrow \\ \Rightarrow f_L &= 1-f_S = \left(\frac{C_L}{C_0}\right)^{\frac{1}{k-1}}, \\ \Rightarrow C_L &= C_0 f_L^{k-1}, \\ \Rightarrow C_S &= kC_0 (1-f_S)^{k-1} \end{aligned} \quad \text{eq. 1.4}$$

The Scheil's equation 1.4, also called non-equilibrium lever rule, predicts that, in the case of $k < 1$, the solute concentration in the liquid diverges when f_L go to zero independently from the solute quantity present in the system. In other word, when $k < 1$ and the solute diffusion in the solid cannot occur, the solidification always ends with an eutectic transformation in presence of an arbitrary low quantity of solute.

The Scheil's model can be modified in order to include an eventual not negligible solute diffusion in the solid during the solidification, the Brody-Flemings equation 1.5 is obtained in this way [14]:

$$C_S = kC_0 \left[1 - \frac{f_S}{1 + \frac{D_S t_f}{L^2} k} \right]^{k-1} \quad \text{eq. 1.5}$$

where D_S is the solute diffusivity in the solid, t_f is the local solidification time, i.e. the period during which both the liquid and solid phases are present, and L is the length scale of the microsegregation, usually half the arm dendrite spacing is used as L .

In Inconel 718 alloy, there are both elements with a partition coefficient $k < 1$, they are Nb, Mo and Ti, and elements with $k > 1$, i.e. Fe and Cr. The partition coefficients of the alloying elements of Inconel 718 are reported in table 1.6. According to the Scheil's model, a certain grade of segregation is expected to occur during a fast solidification: the Fe and Cr contents tend to be higher in the zones where the solidification has started, i.e. the cores of the dendrites, instead Nb, Mo and Ti prevail where the last liquid solidified, i.e. the interdendritic zones. As it can be observed in table 1.6, the highest microsegregation level is expected with the niobium. At first approximation, it is possible to describe the solidification of Inconel 718 as a binary alloy by considering only the role of the Nb solute [54] [55].

Table 1.6. Partition coefficients k of the alloying elements of Inconel 718 alloy. From: [56].

Element	Ni	Cr	Fe	Nb	Mo	Ti	Al	C
Experimental k value	1.03	1.09	1.20	0.28	0.73	0.41	0.79	0.12

1.3.2.2 Morphology of the solidification front

The progress of the solidification front depends on the eventual presence of undercooled liquid, that is a liquid at a temperature lower than the liquidus T_L at which the liquid phase is in thermodynamic equilibrium with the solid one. An eventual protrusion of the solid casually formed on the solidification front can advance only in presence of an undercooled liquid ahead the solid/liquid interface. In fact, if an undercooled liquid is not present, any random protrusion would approach a zone in which $T > T_1$ and so its growth would stop, therefore a planar solid/liquid interface is stable. However, the local speed of the solidification front on a random protrusion is higher in presence of undercooled liquid and so the further development of this protrusion occurs. In these conditions, destabilization of the planar front and formation of dendrites occurs.

In a binary alloy, the destabilization of the planar front can occur in presence of a temperature gradient G in liquid phase [53]. In fact, in the case of $k < 1$, the solute is continually rejected from the forming solid to the liquid and, therefore, a solute concentration gradient can form in the liquid in contact with the solidification front if the solidification is sufficiently fast to prevent the solute diffusion to uniform the composition in the liquid. Obviously, if a compositional gradient is present in the liquid, then the Scheil's model is no more valid because the assumption N.1 does not hold anymore. In turns, the compositional gradient determines a relative gradient of the local liquidus temperature T_L in the liquid ahead the solidification front. Constitutional undercooling, so called because it is related to the solute concentration, is present where the liquid temperature is lower than T_L . If the thermal gradient G in the liquid is higher than a certain critical value (see figure 1.15), a constitutional undercooled zone cannot form and so the planar solid/liquid interface remains stable. However, if the value of G decreases under the critical threshold, a zone in which the liquid is constitutionally undercooled form ahead the solidification front. This causes the destabilization of the planar front.

Therefore, the solid/liquid interface morphology is related to the G/R ratio between the thermal gradient in the liquid and the rate of the solidification front. High G/R values determine a planar interface, but if G/R decreases under the critical value written in equation 1.6, parallel dendrites form growing along the direction of the thermal gradient without developing of secondary branches.

$$\left. \frac{G}{R} \right|_{\text{planar to cellular}} = \frac{\Delta T}{D_L} \quad \text{eq. 1.6}$$

where D_L is the diffusivity of the solute in the liquid and ΔT is the solidification range, i.e. the difference between the liquidus and solidus temperatures at the nominal composition [53] [57] [58]. This solidification modality leads to the so called cellular structure, whose name is due to the observable aspect on the cross-section perpendicular to the dendrites (figure 1.16).

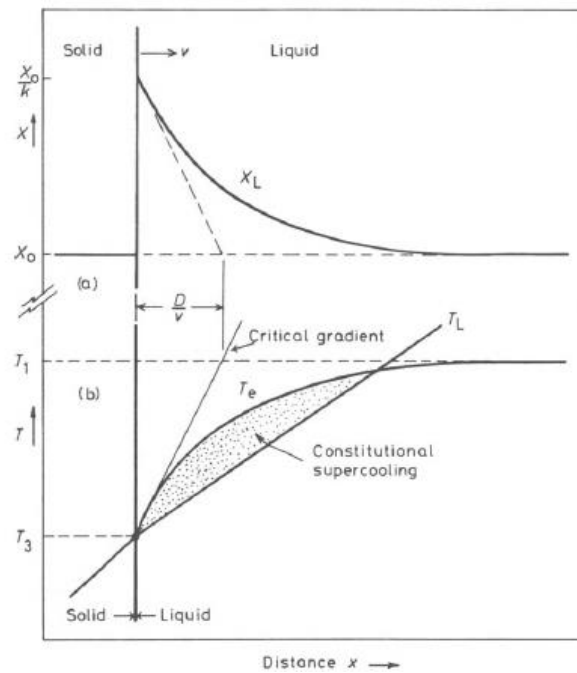


Figure 1.15. Formation of constitutional undercooling of the liquid ahead the solidification front with consequent destabilization of the planar solid/liquid interface. From: [53].

The crystallographic orientation of the cells is virtually the same because they originate from the same initial grain. Therefore, the boundaries between cells and dendrites are also called Solidification Sub-Grain Boundary (SSGB), because they form due to the alloying elements microsegregation on the base of the k partition coefficient during the solidification.

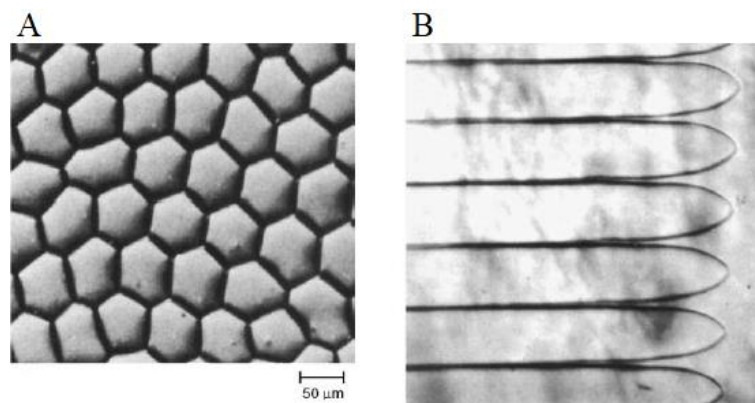


Figure 1.16. Examples of cellular microstructures. Top view of the cells disposed on a hexagonal pattern (A) and lateral view of columnar dendrites without secondary arms (B). From: [58].

If the G/R ratio is further decreased, the extension of the undercooled liquid increases and secondary branches start to form from the walls of the parallel dendrites. Eventually, also tertiary branches can form from the secondary ones. In the metals with a cubic crystallographic system, the dendrites develop along the $\langle 100 \rangle$ type crystallographic axes because of the energetically favorable growth [59]. Therefore, the grains with a $\langle 100 \rangle$ axis aligned to the thermal gradient are favored and they develop with the formation of columnar dendrites. The secondary branches form along the other two $\langle 100 \rangle$ axes, that are orthogonal to the growth

direction of the primary branch from which they originate [57]. Equation 1.7 shows the threshold value of the G/R ratio for the transition from the cellular to the dendrite microstructure [57] [60].

$$\left. \frac{G}{R} \right|_{\text{cellular to dendritic}} = \frac{k\Delta T}{D} \quad \text{eq. 1.7}$$

where k is the solute partition coefficient.

A further reduction of the G/R ratio leads to a solidification that occurs predominantly by nucleation of new grains in the undercooled liquid volume. In these conditions, the so called equiaxed dendrites form (see figure 1.17): the low G value can no more affect the growth direction of the dendritic branches, therefore the growth is only controlled by the orientation of the $\langle 100 \rangle$ crystallographic axes.

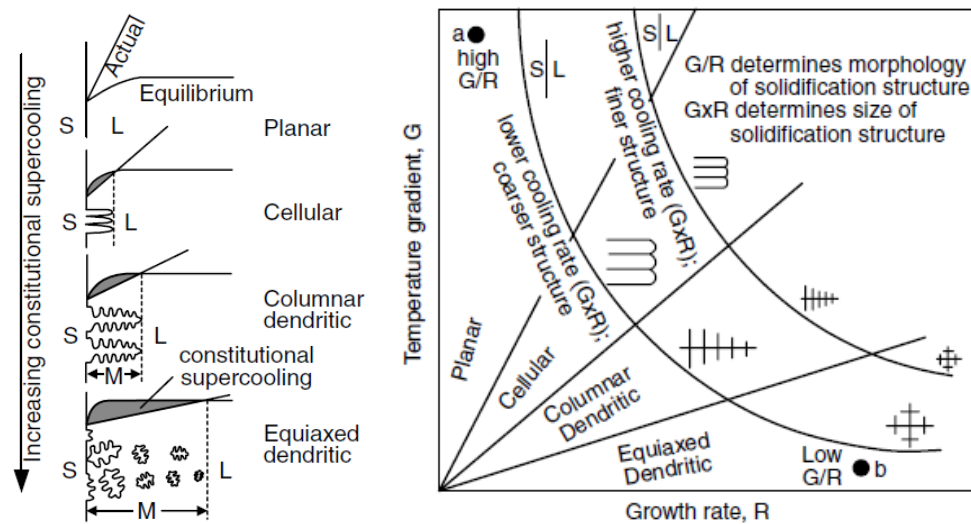


Figure 1.17. Change in the solidification front morphology and structures size in function of the temperature gradient G and the growth rate R . From: [59].

1.3.2.3 The fast solidification path

In most of the cases of practical interest, the establishing of a stable planar solid/liquid interface during the solidification of Inconel 718 alloy is very rare, therefore dendritic structure is almost always obtained. The morphology of the formed dendrites is determined by the G/R ratio as explained at paragraph 1.3.2.2. On the contrary, the characteristic size of these structure, i.e. the primary arm spacing and, if ramifications are present, the secondary and tertiary arm spacing, depend on the cooling rate, that is the $G \cdot R$ product: high values of the cooling rate decrease the solute diffusion length and determines lower interdendritic distances as a consequence making the microstructure finer.

During the formation of the dendrites, the remaining liquid in the interdendritic space is progressively enriched in Nb, so the liquidus temperature is reduced consequently until the eutectic conditions are reached. Although the Scheil's model cannot hold in this description because of the violation of the assumptions N.1 and N.6, the fact that the solidification must end with the eutectic transformation

remains valid. This is true because the solute cannot diffuse in the solid phase, no matter how low the initial solute quantity. However, the solute content in the system determines the volume of the formed eutectic. The final result is a heterogeneous structure characterized by a certain degree of microsegregation: the cores of the dendrites have a higher content of the elements with $k > 1$, i.e. Cr and Fe, instead the eutectic products, rich in the elements with $k < 1$, in particular Nb, are concentrated at the boundaries between the dendrites.

DuPont et al. investigated the fast solidification path of Nb-bearing nickel-base alloys through the liquidus projection of the Ni-Nb-C system at the Ni-rich corner providing a pseudo-ternary solidification diagram [61] [62] [63]. The effect of Fe, Cr and Si, which are stabilizers of the Laves phase, is indirectly considered by substituting the Ni_3Nb compound of the Ni-Nb-C system with the Laves phase [61]. In their study, these researchers observed the presence of two distinct γ/NbC and γ/Laves eutectic structures and they concluded that the solidification does not terminate with a ternary $\gamma/\text{NbC}/\text{Laves}$ eutectic transformation, which would lead to an intimate mixture of the three constituents. Actually, they argued that solidification ends rather through two non-invariant binary eutectic transformations: $L \rightarrow L + \gamma + \text{carbides}$ and $L \rightarrow \gamma + \text{Laves phases}$ (where L indicates the liquid phase). According to this description, dendrites of γ phase form and grow at the first stage of the solidification rejecting C and Nb in the liquid phase that is progressively enriched in these elements, consequently. The diffusion of Nb in the solid phase during the solidification at a high cooling rate, as the one established in the welding processes, is negligible, therefore its distribution can be modeled with the Scheil's law, instead the lever rule can be used for C because of its fast diffusion [62] [63]. In the pseudoternary diagram reported in figure 1.18, the liquid composition follows the arc drawn in the γ field during the first stage of the solidification, then the $L \rightarrow \gamma + \text{NbC}$ eutectic transformation starts as soon as the liquid composition reaches the line between the γ and NbC fields. This reaction causes a depletion of C and an enrichment of Nb in the liquid, therefore the representative point of the liquid phase composition follows the arrow towards the Ni-Nb edge of the diagram. When the liquid composition reaches the junction point between the three phases, i.e. γ , NbC and Laves, a transition from the $L \rightarrow \gamma + \text{NbC}$ reaction to the $L \rightarrow \gamma + \text{Laves}$ eutectic reaction occurs and then the solidification ends at the Ni-Nb edge. DuPont et al. also observed that Fe, Cr and Si tend to increase the Laves precipitation, instead Nb tends to increase the volume fraction of NbC at the end of the solidification if the content of C in the alloy composition is high, otherwise its primary effect is to further increase the volume fraction of the Laves phase [61].

The study on the fast solidification of Inconel 718 alloy performed by Knorovsky et al. is quite in agreement with the above reported description that involves two separate binary eutectic transformations. In the case of Inconel 718 alloy, which is a Nb-bearing alloy with a very low content of C, the $L \rightarrow L + \gamma + \text{carbides}$ transformation occurs at about 1230-1260°C and the $L \rightarrow \gamma + \text{Laves}$

transformation occurs at about 1200°C [55]. The solidification path obtained by the authors is also reported in figure 1.18. The only notable difference with DuPont work is that in the Knorovsky's description the first eutectic depletes the liquid both from C and Nb and it ends as soon as the C content in the liquid is completely consumed. Then an intermediate step, in which γ dendrites restart to grow according to the $L \rightarrow L + \gamma$ reaction and the liquid is again enriched in Nb, occurs prior to the last $L \rightarrow \gamma + \text{Laves}$ eutectic transformation [55]. Note that a non-equilibrium γ/Laves interdendritic eutectic can form even if the nominal Nb content of the alloy does not exceed the solubility of Nb in the γ matrix because of the suppression of the Nb diffusion in the solid [64].

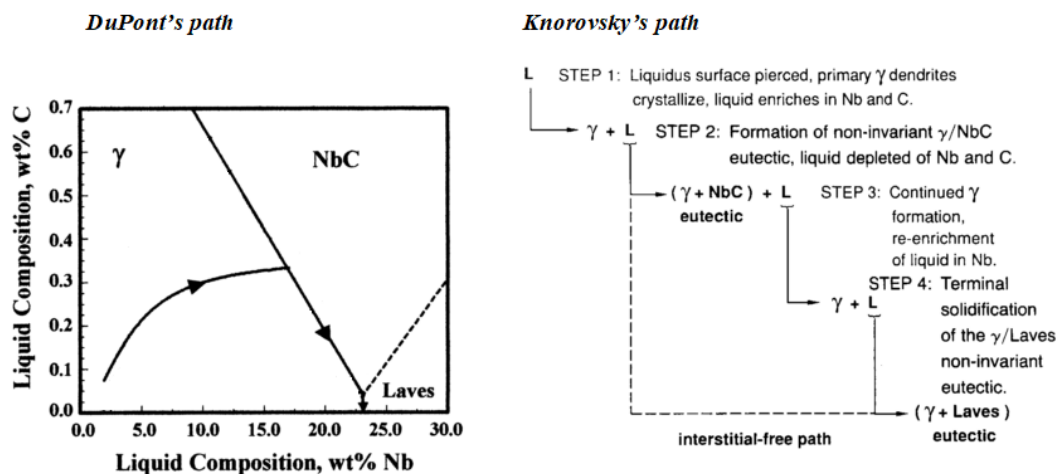


Figure 1.18. Scheme of the fast solidification path for a general Nb-bearing nickel alloy (DuPont's path, adapted from: [63]) and that of Inconel 718 alloy in particular (Knorovsky's path, from: [55]).

1.3.3 The standard heat treatments

The generic heat treatments cycle at which Inconel 718 is usually submitted consists of a solution annealing run and two aging steps. The general structure of the standard heat treatments cycle is reported in figure 1.19.

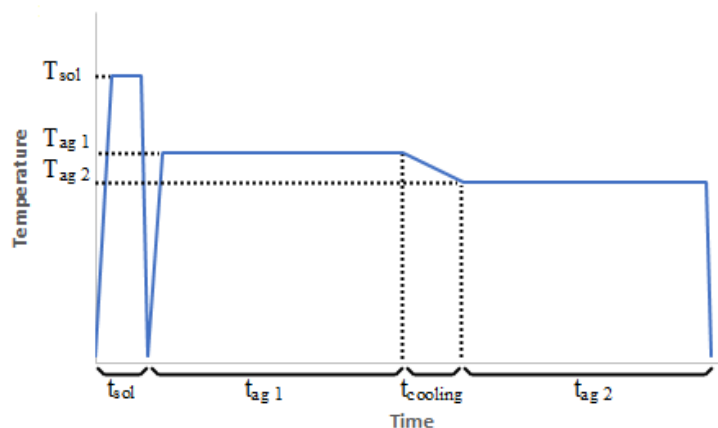


Figure 1.19. General structure of the standard heat treatment cycle of Inconel 718 alloy.

The solution annealing has the purpose to reduce the microsegregation levels and dissolve the unwanted second phases that formed during the solidification and subsequent cooling, in particular the Laves phases and the eventual δ phases. A high temperature homogenization treatment at 1100-1200°C may be required to dissolve the as-cast γ /Laves interdendritic eutectic [64].

During the solution annealing, the alloying elements that will be necessary for the formation of the strengthening precipitates during the following aging steps are transferred in the γ solid solution. This is particularly true for Nb, Ti and Al. The solution treatment is concluded with a rapid cooling at room temperature through water or air quenching, that has the aim to avoid re-precipitation of unwanted second phases during the cooling step.

During the subsequent aging cycles, the strengthening γ' and γ'' phases precipitate in form of small particles finely dispersed throughout the volume of the γ matrix. The temperature and duration of the aging treatments are chosen in order to obtain the formation of a large number of precipitates avoiding the coarsening of them or the formation of unwanted phases, for example δ .

The two main alternative heat treatments for Inconel 718 alloy are:

1. solution annealing between 920°C and 1010°C followed by water or air quench, aging at 720°C for 8 hours, furnace cooling for 2 hours until 620°C and soaking at this temperature for 8 hours, then air cooling (AMS 5662-3);
2. solution annealing between 1040°C and 1070°C followed by water or air quench, aging at 760°C for 10 hours, furnace cooling for 2 hours until 650°C and soaking at this temperature for 8 hours, then air cooling (AMS 5664).

Anbarasan et al. [65] found that the solution treatment at 1066°C for 1 hour may lead to grain coarsening, while the grain size remains unchanged after solution annealing at 980 ° C for 1 hour. They also observed that the δ phase can form during the treatment at 980°C because the solvus temperature of this phase is higher, about 1000°C, instead the precipitation of NbC carbides along the grain boundaries can occur at 1066°C. Because of the finer granulometry, generally the heat treatment n.1 allows to obtain higher mechanical properties at room temperature and higher fatigue resistance. Instead, the heat treatment n.2 optimizes the ductility and the impact resistance of the alloy.

1.3.4 Physical and mechanical properties

The typical values of the main physical properties of Inconel 718 alloy are reported in table 1.7.

Table 1.7. Physical properties of Inconel 718 alloy. Data from: [66].

<i>Property</i>	<i>State</i>	<i>Value</i>
Density (g/cm ³)	Annealed	8.19
	Annealed and aged	8.22
Elastic modulus at 21°C (GPa)	-	200
Melting range (°C)	Cast	1205-1345
	Wrought	1260-1335
Mean thermal expansion coefficient from 20°C to 93°C (10 ⁻⁶ K ⁻¹)	-	12.2
Specific heat at 21°C (J/kg·K)	-	430
Thermal conductivity at 21°C (W/m·K)	-	11.4
Electrical resistivity at 21°C (10 ⁻⁶ Ω·m)	Annealed	1.25
	Annealed and aged	1.21

The elastic modulus, thermal expansion coefficient (CTE), specific heat and thermal conductivity in function of the temperature are reported in figure 1.20. Variations from the values reported here can be due to differences in the composition or in the state (cast, wrought, heat treatment condition, etc.) of the alloy.

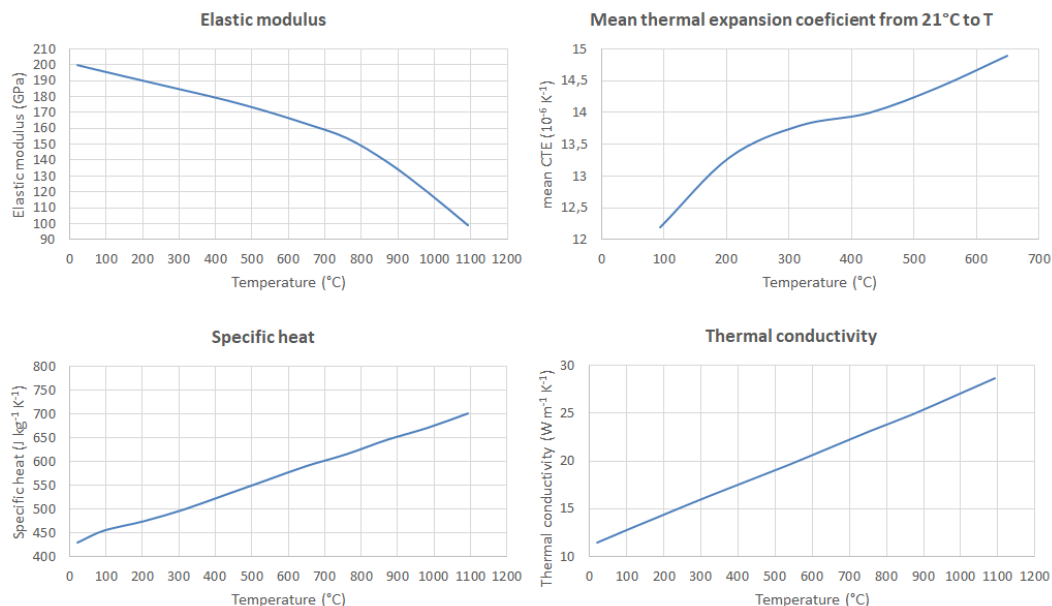


Figure 1.20. Elastic modulus, mean Thermal Expansion Coefficient (CTE), specific heat on thermal conductivity of Inconel 718 alloy in function of the temperature. Data from: [66].

The mechanical properties are strongly related to the process and the thermal history of the material. Some indicative values of the tensile properties at room

temperature in the cast state and at various temperatures in the wrought state are provided in table 1.8.

Table 1.8. Tensile properties of Inconel 718 alloy. Data from: [66].

<i>State</i>	<i>Test temperature (°C)</i>	<i>Yield Strength (MPa)</i>	<i>Ultimate Tensile Strength (MPa)</i>	<i>Elongation to failure (%)</i>
Cast	21	915	1090	11
Wrought (bars)	21	1125	1365	21
Wrought (bars)	538	1020	1195	20
Wrought (bars)	649	965	1105	20
Wrought (bars)	760	800	855	30

The variation of the tensile properties with the temperature until 700°C is shown in figure 1.21 for a forged Inconel 718 alloy submitted to double aging at 720°C for 8 hours and 620°C for 8 hours. From these plots it is possible to observe a reduction in ductility within about 500°C and 600°C. The intermediate temperature embrittlement, i.e. the reduction in elongation, is a quite common phenomenon in the nickel-based superalloys [51] [67] [68].

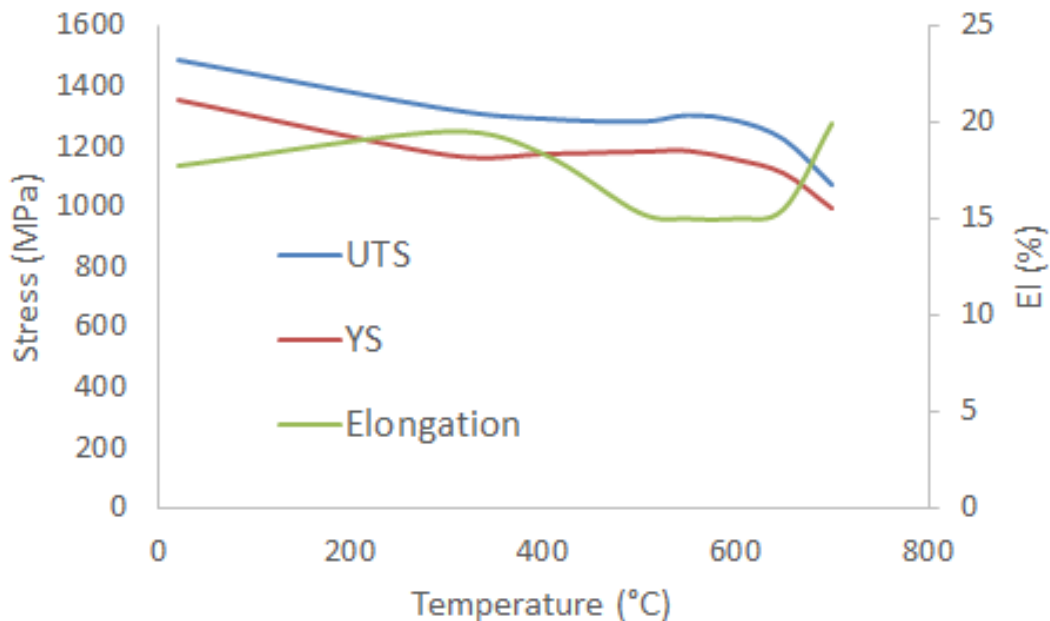


Figure 1.21. Tensile properties of a wrought Inconel 718 alloy after double aging. Data from: [69].

The tensile properties of wrought Inconel 718 alloy at room temperature and at 650°C are shown in figure 1.22 as a function of the solution treatment temperature and after double aging at 720 and 620°C. The formation of intergranular δ precipitates during the solution treatment below the δ solvus temperature prevents grain coarsening, which instead may occur above 1000°C. YS and UTS increase and the elongation decreases until the solution temperature of 990°C because of the greater dissolution of the δ phase, but for higher solution temperature the tensile properties get worse because of the grain coarsening [70].

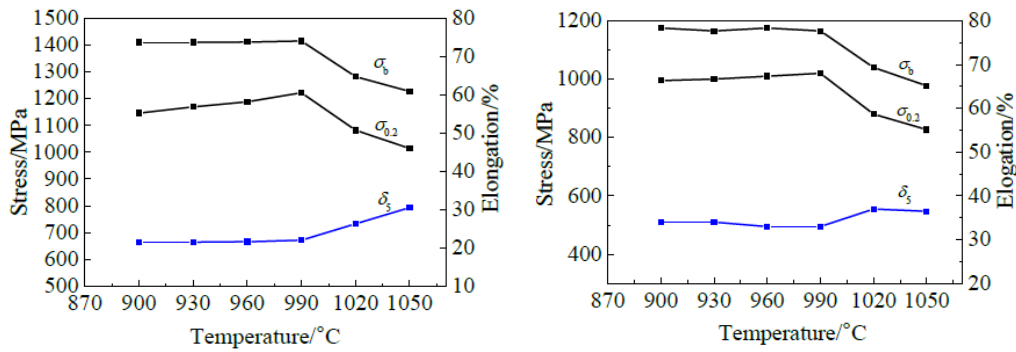


Figure 1.22. Tensile properties of Inconel 718 alloy at room temperature (left) and at 650°C (right) after the heat treatment cycle in function of the temperature of the preliminary solution step. From: [70].

The hardening during the aging step is given by the formation of fine γ' and γ'' precipitates. The effect of the aging temperature and time on the development of these strengthening precipitates and on the Vickers hardness of wrought Inconel 718 alloy, previously submitted to solution annealing at 990°C for 30 minutes and water quenched, was investigated by Slama et al. [16]. From the plots in figure 1.23 it is possible to observe that the hardness increases slowly at aging temperatures lower than 600°C, because of the precipitation of γ' , and that the hardening rate increases with the temperature. Between 600 and 650°C, the hardening is faster and the maximum achieved hardness value increases with the aging temperature. A fast hardening is observed at 680°C due to the precipitation of γ' , then a second hardening occurs with the aging time starting from about 20 hours because of the formation of the γ'' precipitates. A further extension of the aging leads to a reduction of the hardness starting from about 50 hours because the δ phase progressively replaces the γ'' phase. The peak of the hardness is reached at 750°C after 4 hours of aging, then a softening is observed because of the excessive coarsening of the γ' and γ'' particles. A further increase of the aging temperature leads to lower hardness because the precipitation of δ prevails on the formation of γ' and γ'' . Finally, at the aging temperature of 850°C, γ' doesn't form and the formed γ'' is progressively replaced by δ with consequent lack of hardness.

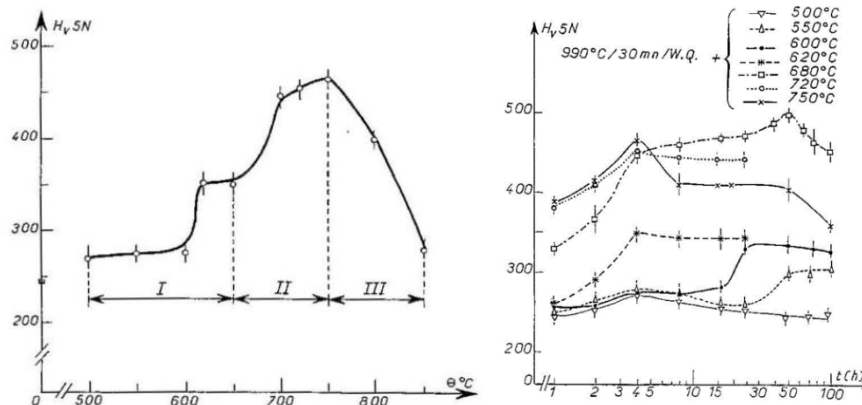


Figure 1.23. Hardness of Inconel 718 alloy after 4 hours of aging at different temperatures (left) and for different times and temperatures of aging (right). The hardness measured after the solution annealing and before the aging step is 245 Hv. From: [16].

Table 1.9 compares the tensile properties of cast Inconel 718 alloy, previously heat treated at 980°C for 1 hour, nitrogen quenched and double aged following the recipe n.1 reported at paragraph 1.3.3, before and after a HIP treatment at 1180°C at a pressure of 175 MPa for 4 hours. The HIP allows not only to reduce the porosity and the segregation level of the cast, but also to refine the grain size and favor the formation of intergranular discontinuous carbides and γ'' precipitates.

Table 1.9. Hardness, porosity and tensile properties of heat treated (as-HT) and heat treated and HIPed (HIP) cast Inconel 718 alloy. Heat treatment: solution annealing at 980°C for 1 hour, nitrogen quench, double aging at 720°C for 8 hours and 620°C for 8 hours: HIP treatment at 1180°C and 175 MPa for 4 hours. Data from: [9].

State	Hardness (HRC)	Porosity (%)	Average grain size (μm)	Test temperature (°C)	Yield Strength (MPa)	Ultimate Tensile Strength (MPa)	Elongation to failure (%)
As-HT	36.3	0.612	91.9	25	806.1	903.3	2.5
				540	732.6	782.2	2.8
				650	694.1	736.2	4.2
HIP	43.7	0.086	74.8	25	1130.3	1185.4	5.1
				540	960.7	993.5	6.4
				650	887.6	909.8	6.7

Another fundamental quality factor for a superalloy is the microstructure stability for long time of thermal exposure at high temperature. The effect of the thermal exposure at two different temperatures on the room temperature tensile properties of a heat treated wrought Inconel 718 alloy is illustrated in the plots at figure 1.24 [71]. It is possible to observe that the alloy strengthens and its ductility is slightly modified during the exposition at 593°C, instead the tensile properties increase during the initial step at 649°C, but softening occurs after very long time of exposure caused by the coarsening of the γ'' precipitates and the progressive replacement of them by the δ phase.

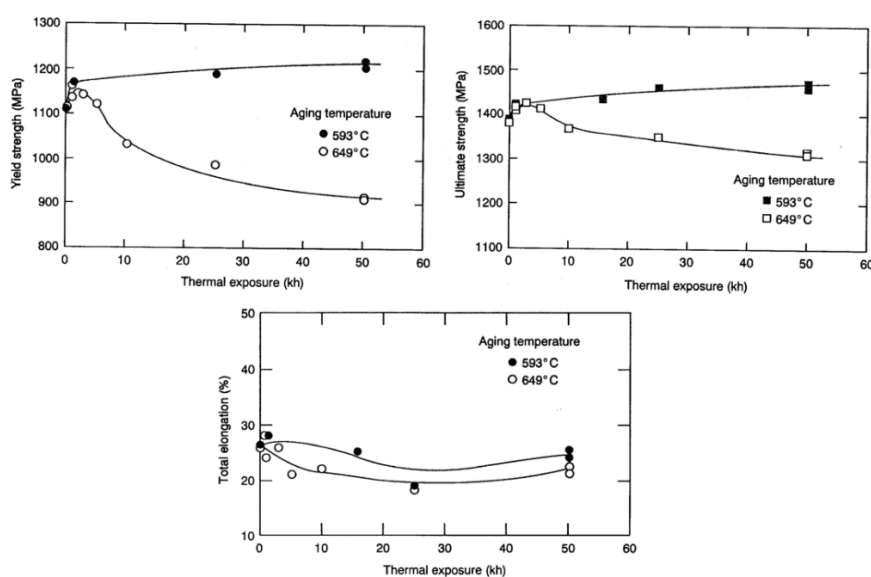


Figure 1.24. Room temperature tensile properties of Inconel 718 alloy after different times of thermal exposure at 593°C and 649°C. From: [71].

1.3.5 Creep and high temperature fatigue resistance

The creep performances are influenced by the heat treatment and the thermal history of the alloy, which determines the type and distribution of the present second phases. The creep is particularly affected by the grain size (see the influence on the rupture life shown in figure 1.25) [72] and by the morphology, size and distribution of the eventually present δ precipitates. A limited content of intergranular δ phase is reported to improve the creep performances, but the amount of it should be sufficiently low to not affect significantly the γ'' precipitation with consequent negative effect on the mechanical properties [70].

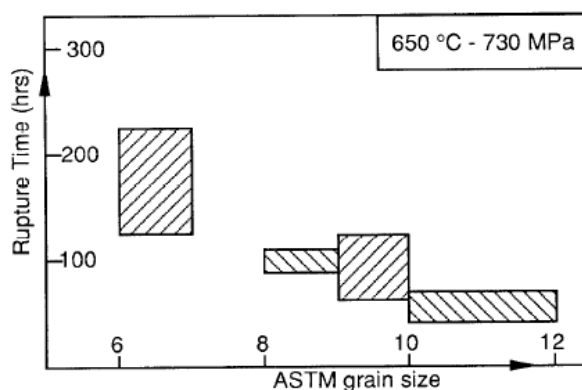


Figure 1.25. Rupture time at 650°C with an applied load of 730 MPa of Inconel 718 alloy in function of the grain size. From: [72].

The relationship between the creep strain rate, temperature and stress can be modeled with the hyperbolic sine constitutive equation 1.8 [73]:

$$\dot{\epsilon} = A \sinh^n(\alpha\sigma) e^{-\frac{Q}{RT}} \quad \text{eq. 1.8}$$

where $\dot{\epsilon}$ is the strain rate, σ is the flow stress (in stress-controlled tests) or the peak stress (in strain-controlled tests), Q is the activation energy for the creep, R is the gas constant ($8.314 \text{ J mol}^{-1} \text{ K}^{-1}$), T is the absolute temperature, n is the creep exponent and A and α are material related constants.

The peak stress vs strain rate curves at different temperatures for an Inconel 718 alloy homogenized at 1080°C for 1 hour are reported in the plots with log-log scale of figure 1.26: the creep exponent n is approximately constant with the temperature except at 900°C, where some hardening caused by dynamical precipitation occurs [74].

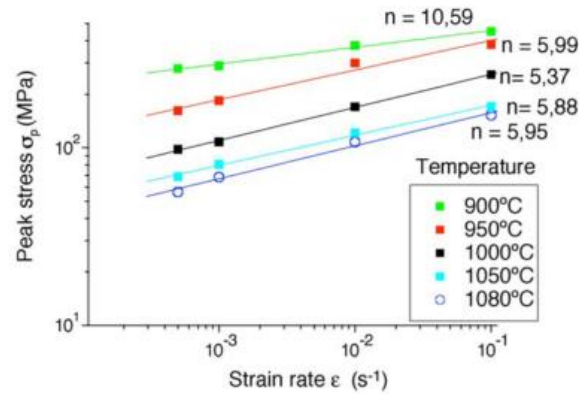


Figure 1.26. Creep σ_p vs $\dot{\epsilon}$ curves at different test temperatures. From: [74].

Kuo et al. have studied the effect of 3 different heat treatment cycles on the creep properties of Inconel 718 alloy [33]. All the heat treatment cycles include a solution annealing at 1095°C for 1 hour and a double aging following the recipe n.1 reported at paragraph 1.3.3. The first cycle (HT1) includes a further step, between the solution annealing and the double aging, performed at 955°C for 1 hour. The second cycle (HT2) does not include the step at 955°C, whereas in the third one (HT3) that step lasts for 3.5 hours. Precipitation of δ phase at the grain boundary occurs during the exposition at 955°C. The presence of the intergranular δ precipitates increases the resistance to the reciprocal slide of the grains with consequent reduction of the steady state creep rate, as it can be observed from the creep curves at figure 1.27 and the values reported in table 1.10 [33].

Table 1.10. Creep data reported by Kuo et al. on Inconel 718 alloy after different heat treatment cycles (see text for the heat treatment recipes). Data from: [33].

Heat treatment	Stress rupture life (hours)	Elongation to failure (%)	Steady state creep rate (1/s)
HT1	160 ± 19	1.15 ± 0.06	0.96 ± 0.05 · 10 ⁻⁴
HT2	331 ± 29	5.36 ± 0.27	1.42 ± 0.02 · 10 ⁻⁴
HT3	197 ± 16	1.49 ± 0.07	1.04 ± 0.03 · 10 ⁻⁴

From such clues one can also ascertain that the stress rupture life of the samples that contain δ phase is lower. The sample previously submitted to HT2, i.e. without δ phase, shows a higher creep elongation to failure up to 5.6%. In this sample, the carbides that remain undissolved during the solution annealing can hinder the grain sliding. Kuo et al. also report that the fracture of the sample submitted to HT2 is mainly of ductile or mixed transgranular/intergranular type. The structural damage due to creep starts at the interface between the intergranular carbides and the matrix, then the formed defects coalesce leading to transgranular fracture [33]. Instead, the presence of the intergranular δ phase leads to a much more limited grain sliding, in fact the authors report a creep elongation to failure of about 1-1.5%, furthermore the final fracture is mainly of intergranular type and it occurs because of the detachment along the δ/γ incoherent interface [33].

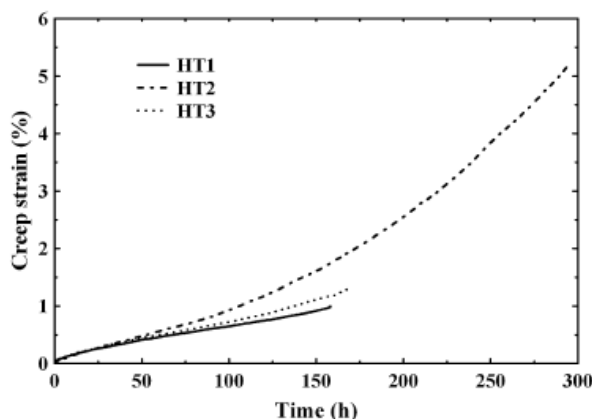


Figure 1.27. Creep curves at 625 MPa and 650°C of Inconel 718 alloy previously submitted to three different heat treatment cycles. From: [33].

The size and the distribution density of the intergranular precipitates affect the creep performances (figure 1.28) [75]. At low distribution density of precipitates, the fracture occurs through propagation of wedge-like cracks that nucleate at the triple points of the grain boundaries. Under these conditions, an increase in the density of precipitates causes a reduction of the time to rupture and of the creep deformation. Conversely, when the distribution density of intergranular precipitates is high, the rupture occurs predominantly by propagation of cracks that form from voids originating by the creep deformation at the grain boundaries placed in the normal direction with respect to the applied load. In this situation, the time to rupture and creep deformation increase with the density of precipitates.

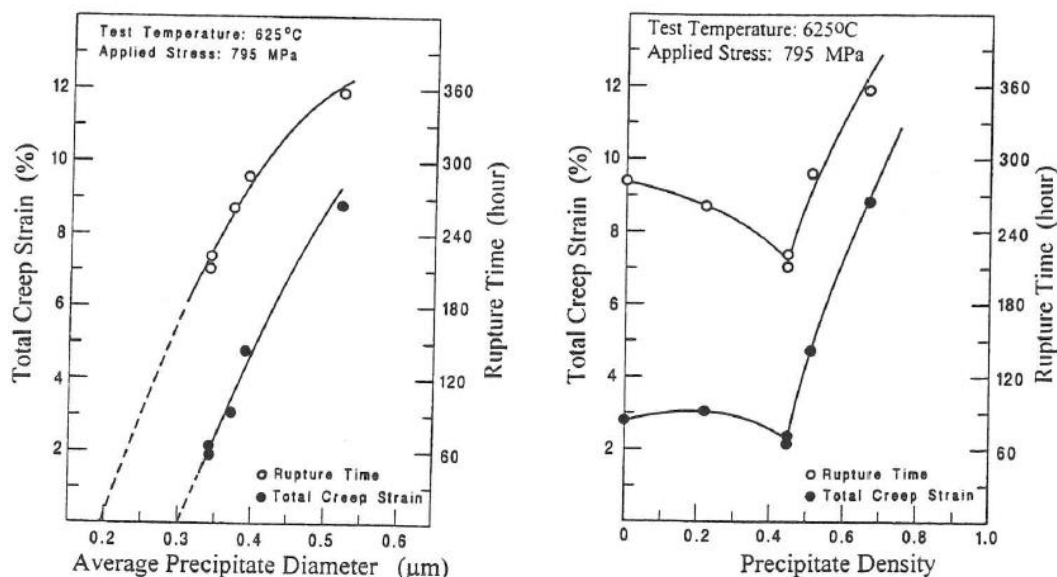


Figure 1.28. Creep strain and rupture life of Inconel 718 alloy at 625°C with an applied load of 795 MPa in function of the precipitates size (left) and density (right). From: [75].

The fatigue resistance is mainly influenced by the exposure temperature [76] [77], the grain size [72], the preliminary applied heat treatment [70] and the load vs time profile [77]. In general, an increase in the exposure temperature reduces the fatigue life and increases growth rate of the fatigue crack, whereas a lower grain

size determines a higher fatigue resistance at the same exposure temperature (see figure 1.29).

The complex interactions between the precipitates dispersed in the γ matrix and the cyclic stress field may give rise to microstructural modifications with not negligible consequences in the mechanical properties of the alloy and its fatigue performance. In particular, large precipitation of intragranular δ phase is reported to occur at 700°C, because of the synergetic effect of the temperature and the strain, with consequent reduction of the fatigue strength [78].

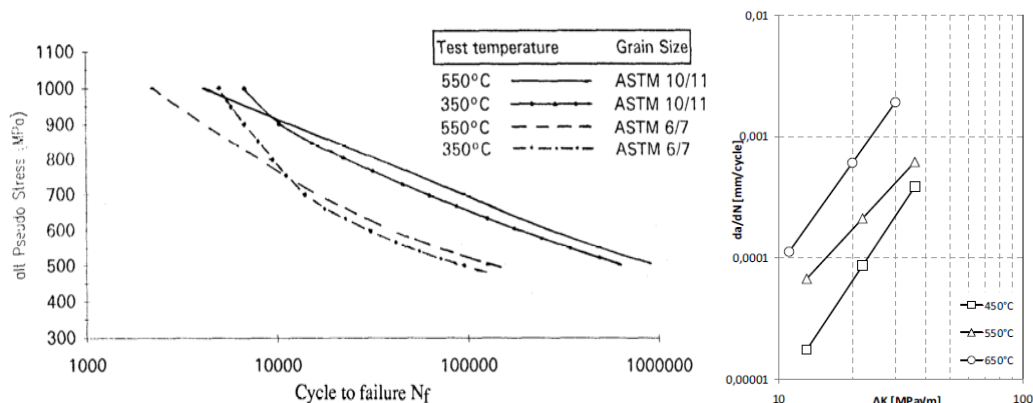


Figure 1.29. Left: fatigue stress vs number of cycle curves at two different test temperatures and two different grain size obtained on wrought Inconel 718 alloy previously submitted to solution annealing at 970°C and double aging according to the standard recipe n.1 (see paragraph 1.3.3), from: [72]. Right: Paris curves at three different test temperatures of wrought Inconel 718 alloy previously submitted to the standard heat treatment cycle n.1 (see paragraph 1.3.3) and with a grain size of 10 μm , from: [77].

1.3.6 Hot oxidation resistance

The hot oxidation resistance of nickel-based superalloys is determined by the formation of a passivating oxide layer on the surface. This layer should be dense and well adherent to the metal substrate in order to provide an adequate protection against further oxidation. Therefore, the hot oxidation resistance is mainly determined by the Cr and Al contents in the alloy, which are the two main passivating oxide formers. In oxidizing environment, Cr and Al form respectively chromia Cr_2O_3 and Alumina Al_2O_3 , both with the lattice structure of the corundum type.

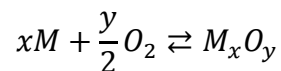
Giggins and Pettit studied the response of Ni-Cr-Al alloys to exposition at high temperatures, between 1000°C and 1200°C, in oxidizing environment [79]. These alloys can be considered as the base prototype of the more complex superalloys for what concerns the oxidation behavior. On the base of the nature of the superficial oxide scale formed during the oxidation, the alloys belonging to the Ni-Cr-Al system can be classified in three groups:

1. the alloys belonging to the group I form a superficial scale mainly made by NiO oxide;

2. the alloys belonging to the group II form a superficial scale mainly made by Cr_2O_3 oxide;
3. the alloys belonging to the group III form a superficial scale mainly made by Al_2O_3 oxide.

Giggins and Pettit [79] observe that a transient oxidation period is present at the beginning of the exposition, during this period the oxide scale formation on the surface occurs in an inhomogeneous manner and its structure is not constant. At the end of the transient oxidation step, the effective duration of which depends on the exposition temperature and the chemical composition of the alloy, a stable oxide scale has formed with a structure that remains almost unchanged for long exposure time. This stage of the oxidation is referred as steady-state oxidation regime.

The alloys belonging to the group I has a Cr and Al contents too low for a continuous chromia or alumina superficial scale to form at the end of the transient oxidation step. Therefore, an external continuous oxide scale of NiO and a subscale made of discontinuous oxides of Cr_2O_3 , Al_2O_3 and $\text{Ni}(\text{Cr}, \text{Al})_2\text{O}_4$ develops on these alloys. The discontinuous oxides form internally because of the oxygen inward diffusion through the superficial NiO layer. The oxidation of a metal M can proceed as long as the oxygen partial pressure p_{O_2} in the environment is higher than the $p_{\text{O}_2,eq}(T)$ value at which the equilibrium is established at the exposure temperature:



A low value of $p_{\text{O}_2,eq}(T)$ indicates a high affinity of the metal M with the oxygen, this means a greater tendency to oxidizing. During the thermal exposure at T, the local oxygen content decreases moving in deep from the surface of the alloy. The alloying elements can oxidize as long as the oxygen concentration remains higher than the equilibrium value $p_{\text{O}_2,eq}(T)$, but their oxidation stops as soon as the oxygen content drops below such threshold. Therefore, the alloying elements with a lower oxygen affinity stop oxidizing earlier than those with a higher oxygen affinity, which instead tend to form internal oxides at greater depth. The oxygen affinity of Ni is lower than that of Cr, which in turn is lower than that of Al (see the Ellingham diagram in figure 1.30). Therefore, internal oxidation of Cr and Al along a certain thickness can occur under the superficial layer of NiO in the alloys of the group I.

The alloys of the group II have a higher Cr content and a limited Al content. In this case the developing of Cr_2O_3 is sufficient to form a superficial continuous layer that prevail on NiO at the end of the transient oxidation. Instead, the Al oxidation leads only to the formation of discontinuous internal oxides. In this situation, the higher oxygen affinity of Al allows the oxidation of this element below the continuous Cr_2O_3 layer.

The alloys of the group III have a higher Al content, therefore the formation of Al_2O_3 alumina prevails on Cr_2O_3 and on NiO at the end of the transient oxidation step. The final result is a superficial scale formed by a single continuous and dense Al_2O_3 layer without internal oxides formed below it.

The alloys with an intermediate composition between two groups are characterized by a longer transient oxidation and by a mixed oxidation behavior with consequent developing of a heterogeneous superficial scale [79].

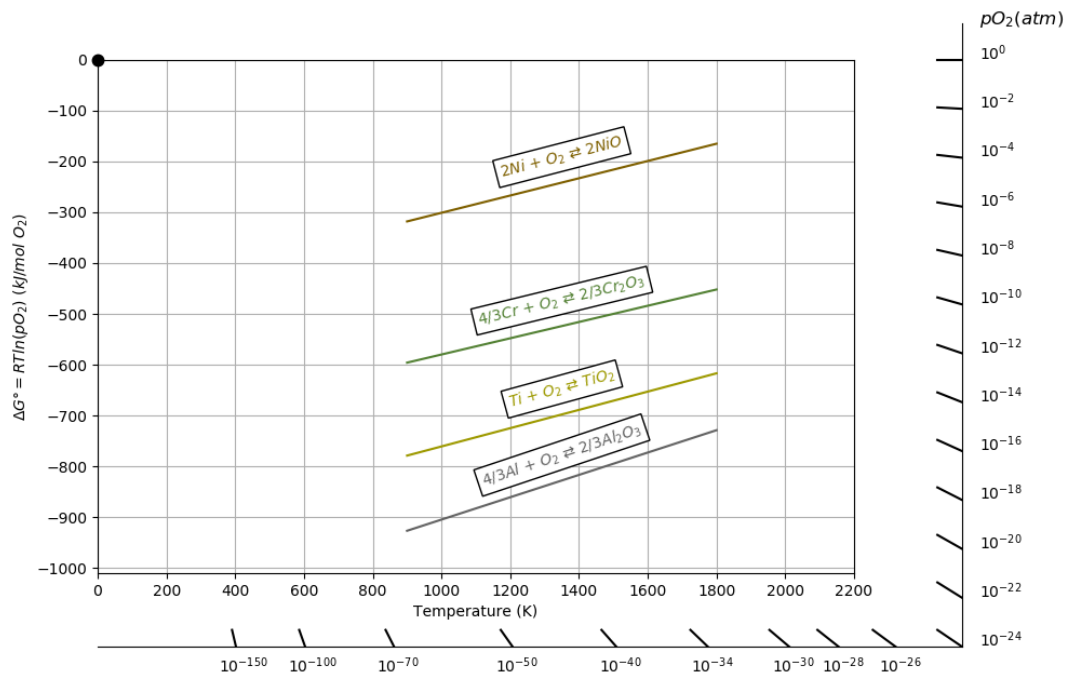


Figure 1.30. Ellingham diagram relative to the Ni, Cr, Ti and Al oxides. Data from: [80].

During the steady-state oxidation, the only time-dependent feature is the thickness of the external scale, which increases with the thermal exposure time. When the protective oxide layer is dense and well adherent to the substrate, the growth rate of the scale is adequately described by a parabolic law (equation 1.9):

$$\left(\frac{\Delta m}{A}\right)^2 = k_p t \quad \text{eq. 1.9}$$

where Δm is the mass gain recorded on the oxidized sample due to the insertion of oxygen atoms during the growth of the oxide, A is the exposed area of the alloy, t is the total time of exposure in temperature and k_p is the parabolic rate constant. A low value of k_p indicates a high hot oxidation resistance of the alloy, as it determines a slow growth of the oxide and, therefore, a limited consumption of the oxide forming alloying elements and a lower risk of spalling due to the development of thermal stresses in the layer. Under these conditions, the alloy can remain stable in an oxidizing environment for long periods. The parabolic growth is observed whenever on the surface of the alloy a protective passivating layer forms whose stationary growth is controlled by the diffusion, through this layer, of the O^{2-} anions from the atmosphere/oxide to the oxide/metal interfaces and of the oxide forming metallic cations M^{Y+} along the inverse path [81]. The parabolic law was first obtained by Tammann, Pilling and Bedworth without taking into account the electrical charge of the ionic species and, therefore, assuming that the diffusion of these species through the oxide layer can be approximately described by the first

Fick's law. Afterwards, Wagner formulated a more elaborated model, that take into account the effect of the electric field in the oxide layer on the transport of the charged species, i.e. cations, anions and electrons [81] [82].

Giggins and Pettit [79] report that the oxidation of Ni-Cr-Al type alloys at 1000°C, 1100°C and 1200°C respects the parabolic law in most of the cases and that the parabolic constant of the alloys of group I is higher than that recorded in the alloys of group II, while alloys of group III have the lowest values of the parabolic constant.

Inconel 718 alloy has a high Cr content (between 17 and 21% wt.) and a relatively low Al content (between 0.2 and 0.8% wt.), therefore it belongs to group II (see figure 1.31) and so it tends to form a continuous surface layer of chromia and internal discontinuous alumina oxides.

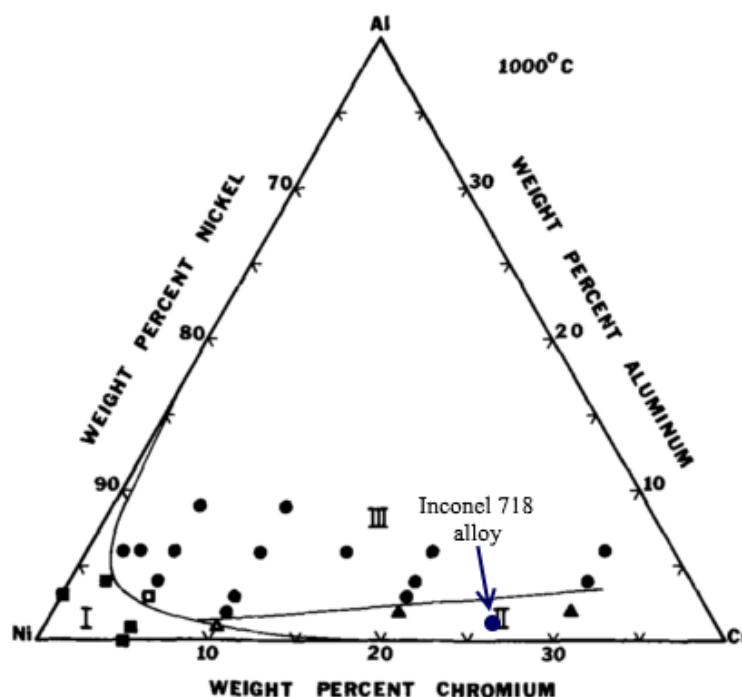


Figure 1.31. Ternary isothermal diagram showing the compositional borders between the three groups of alloys. The point relative to Inconel 718 alloy is added. Adapted from: [79].

Greene and Finfrock report three oxidation regimes for Inconel 718 alloy based on the exposure temperature [83]:

- at temperatures below 900°C, oxidation is characterized by a first transient oxidation period of about 24 hours during which the surface oxide scale is formed, then the further stationary growth of the oxide proceeds following a parabolic trend with a very low k_p value (under 800°C, the oxidation rate is so low that a mass gain between the first 24 hours and 15 days of thermal exposition cannot be measured);
- at temperatures falling between 900 and 1250-1300°C, the oxidation behavior follows a parabolic law and the parabolic constant k_p increases exponentially with the oxidation temperature;

- starting from 1265°C, the oxide becomes unstable and tends more and more to spall from the substrate as the temperature increases; therefore the scale is no longer able to adequately protect the surface; furthermore at these temperatures and for long periods of exposure the evaporation of the chromia can occur according to the $Cr_2O_3(s) + 3/2 O_2(g) \rightleftharpoons 2CrO_3(g)$ reaction [84] [85].

The oxide scale structure formed on Inconel 718 alloy is affected by the numerous alloying elements present. In addition to Cr and Al, also other oxide forming elements, such as Fe, Ti, Mn and Si, can play a role in the scale formation. Therefore, the composition and structure of the formed protective oxide are very complex and heterogeneous. Delaunay et al. investigated the oxide formed on Inconel 718 alloy after oxidation at 900°C until 48 hours through XPS and SEM analysis [86], revealing a particularly complex structure consisting of an outer layer, made of Cr, Ti, Ni, Fe, Mn oxides, mixed oxides and spinels, and a more homogeneous internal layer of chromia containing Fe substitutional impurities. The authors have also noted the presence of internal Ti and Al oxides below the continuous layers, mainly present along the grain boundaries, and a quasi-continuous layer of Ni₃Nb intermetallic phase placed at the oxide/alloy interface [86].

The Ni₃Nb intermetallic layer forms in the early stages of the oxidation and it can act as a second barrier to the diffusion of the anionic and cationic species through the protective scale with consequent reduction of the k_p constant of the parabolic trend [86]. The presence of a layer rich in Nb at the oxide/alloy interface is also reported by Al-Hatab et al. in Inconel 718 alloy subjected to cyclic oxidation at 750°C, 850°C and 950°C [87]. At these test temperatures, the thermally grown scale is well adherent and adequately performs its protective function. However the authors [87] found some deviations from the parabolic behavior of the oxidation rate during the first exposure period due to the complex interactions between the different alloying elements and to the variation in the oxidation kinetics caused by the formation of the above mentioned intermetallic layer.

Grain boundaries can also play an important role in the oxidation behavior, as they are zones in which the diffusivity of the ionic species is greater. Trindade et al. have shown that the reduction of the grain size, hence the increase of the grain boundaries, may lead to an increase in the parabolic constant k_p [88]. Along to the grain boundaries, the greater outward flow of Cr leads to the formation of a greater thickness of the superficial oxide with respect to the intragranular zones [88]. On the other hand the inward flow of oxygen leads to the formation of internal oxides along grain boundaries [86] [87] [88].

Some values of the k_p constant of the parabolic law obtained on Inconel 718 alloy at different oxidation temperatures are reported in table 1.11. The dispersion of the results of the oxidation tests is usually large because of the high sensitivity to the particular conditions at which they are performed (for example the surface

finishing of the analyzed samples); this is even more true at low oxidation temperatures (below 900°C).

Table 1.11. Values of the parabolic constant k_p reported after oxidation tests at different temperature and exposure time.

<i>Oxidation temperature (°C)</i>	<i>Total exposure time (hours)</i>	k_p ($mg^2 cm^{-4} h^{-1}$)	<i>Source</i>
750	~ 170	$2.4 \cdot 10^{-4}$	[87]
800	2000	$2.01 \cdot 10^{-5}$	[89]
850	~ 170	$7.7 \cdot 10^{-4}$	[87]
850	between 25 and 2000	$8.78 \cdot 10^{-5}$	[89]
850	100	$1.6 \cdot 10^{-2}$	[90]
900	between 25 and 2000	$4.13 \cdot 10^{-3}$	[89]
900	24	$9.6-22.6 \cdot 10^{-3}$	[83]
900	48	$2.8 \cdot 10^{-3}$ *	[86]
950	~ 170	$7.4 \cdot 10^{-3}$	[87]
950	between 25 and 2000	$6.21 \cdot 10^{-3}$	[89]
1000	between 25 and 2000	$4.08 \cdot 10^{-2}$	[89]
1000	24	$1.681 \cdot 10^{-1}$	[83]
1000	100	$3.74 \cdot 10^{-1}$	[88]
1050	between 25 and 2000	$3.27 \cdot 10^{-2}$	[89]
1100	25	$2.15 \cdot 10^{-1}$	[89]
1100	24	$3.456 \cdot 10^{-1}$	[83]
1200	24	$6.984 \cdot 10^{-1}$	[83]
1300	24	8.712	[83]

* thickness converted in mass assuming a density of the oxide scale of 5.22 g/cm³

1.3.7 Pack aluminization

At high service temperatures the oxidation rate of Inconel 718 increases drastically and the continuous surface layer of chromia fails in its protective function due to spalling or evaporation after prolonged exposure periods. For this reason, a surface coating may be necessary in applications in which the alloy must operate at temperatures higher than 1000°C, in an aggressive environment or when the formation of CrO₃ vapor should be avoided. A typical example of an application of this type is found in the SOFC systems, where the evaporation of the chromia formed on the metal interconnector can cause the poisoning of the components of the cell with consequent loss of its efficiency [91].

Pack aluminization is a simple and economic technique of surface modification that it is used to increase the service temperature of steels [92] [93] [94], titanium [95] and nickel-based superalloys [96] [97] [98] through the conversion of the superficial layer of the substrate into an aluminate intermetallic product. Usually, the surface modification affects a zone of a few tens of micrometers in depth. In an oxidizing environment, the intermetallic aluminate coating is able to form a dense passivating layer of highly stable alumina able to protect the metal substrate [99] and to avoid the development of chromium oxide vapors. The pack aluminization

technique consists in embedding the piece to be coated in a powders mixture containing at least three main constituents:

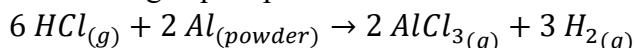
1. an aluminum source, usually consisting of pure aluminum powders or Al-Si or Al-Fe alloy powders;
2. an activator, usually fine grains of a halide salt as NaF, NH₄Cl, NH₄F or AlF₃;
3. inert powder, usually in alumina.

The powder pack with the metallic substrate embedded in it is submitted to a heat treatment at a temperature usually between 700 and 1100 ° C. As soon as the pack is heated to the treatment temperature, the activator decomposes forming a gaseous reactant which activates the aluminization reactions cycle. When e.g. ammonium chloride is used as activator the basic sequence of reactions occurring during the treatment of a nickel-based alloy is reported below:

1. decomposition of the activator:



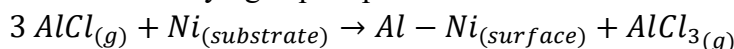
2. formation of aluminizing vapor species:



3. Al transfer from the Al source to the carrying vapor species:



4. Al transfer from the carrying vapor species to the metallic substrate:



During the aluminization process, the aluminum flow towards the substrate is guaranteed by the aluminizing vapor species through the continuous loop of reactions n.3 and n.4. For this reason, the pack aluminization technique can be classified as a Chemical Vapor Deposition (CVD) process, in which the aluminizing vapor species are produced in situ by the reactions n.1 and n.2. An important advantage of the pack aluminization processes is the absence of the line-of-sight problem [100], which represents a strong limitation of other deposition processes such as the thermal spray or galvanic deposition techniques. For this reason, pack aluminization is a potentially good candidate for covering topologically complex or hard to access surfaces such as the internal surfaces of pipes, holes or cavities. For example, the pack aluminization technique can be used to coat or completely convert nickel-based metal foams [101] [102] [103]. The reaction n.4 between the aluminizing vapor species and the metallic substrate leads to an increase in the superficial Al content of the alloy, which causes the formation of the intermetallic compounds present in the Ni-Al phase diagram shown in figure 1.32.

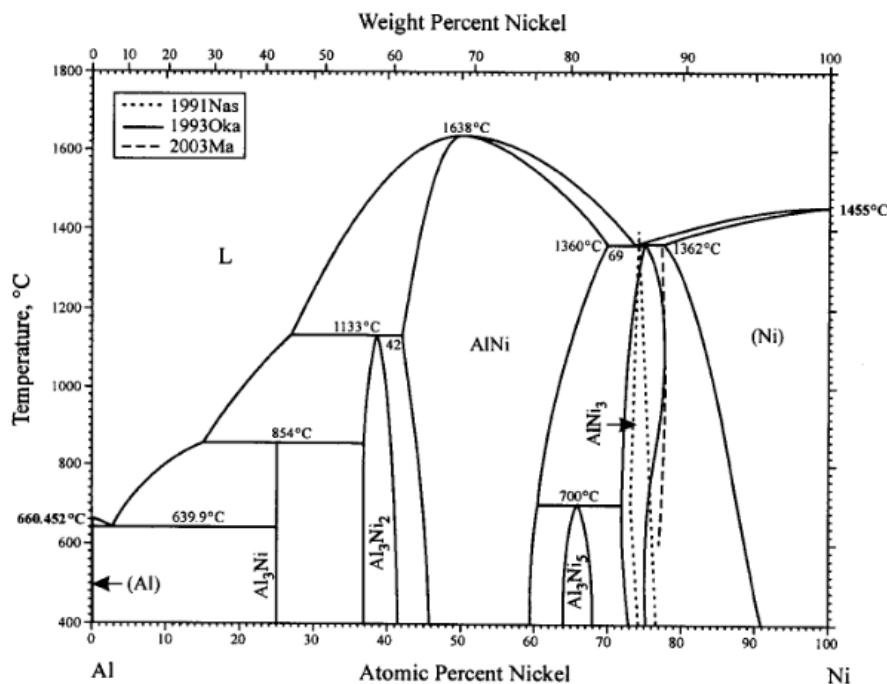


Figure 1.32. Phase diagram of the aluminum-nickel system. From: [104].

The intermetallic compounds whose formation is more often reported after a pack aluminization process are δ -Al₃Ni₂ and β -AlNi [105]. δ -Al₃Ni₂ is a diffusionally unstable compound, moreover it is more brittle and so more sensitive to cracking with consequent fail in its protective function. Therefore, the formation of β -AlNi is usually the aim of the process [106] because of its stability in a wide compositional range as seen in the phase diagram (figure 1.32).

After the formation of a continuous superficial intermetallic layer, the further thickening of the coating during the aluminization process is controlled by the solid state diffusion through this layer. The aluminum coating growth can occur by outward Ni diffusion from the substrate to the surface or by the inward Al diffusion along the reverse path, in the more general case the development of the coating occurs with a mixed mechanism [98] [107]. According to the ASTM standard [108], the pack aluminization processes can be classified into two main categories on the base of the adopted process parameters and the prevailing coating formation mechanism: High Temperature Low Activity (HTLA) aluminization and Low Temperature High Activity (LTHA) aluminization process. The HTLA processes are characterized by a low Al content in the pack and are usually performed at temperature between 900 and 1150°C. Instead, in the LTHA processes, the Al content in the pack is higher and the heat treatment is carried out at relatively low temperatures, usually between 700 and 900°C. In a HTLA process, the coating tends to form outward [109] and, therefore, it occurs mainly through the Ni diffusion from the metal substrate to the coating/atmosphere interface, where the reaction with the aluminizing vapor species occurs (figure 1.33). In this kind of processes, a coating almost entirely made of β -AlNi compound tends to form. The depletion of Ni at the interface between the forming coating and the substrate causes the solubility limit of the alloying elements to be reached with consequent

formation of interfacial precipitates, the region in which this occurs is called Interdiffusion Layer (IDL). The presence of the IDL is characteristic of the aluminization processes which are entirely or partially controlled by the outward Ni diffusion (figures 1.33 and 1.34).

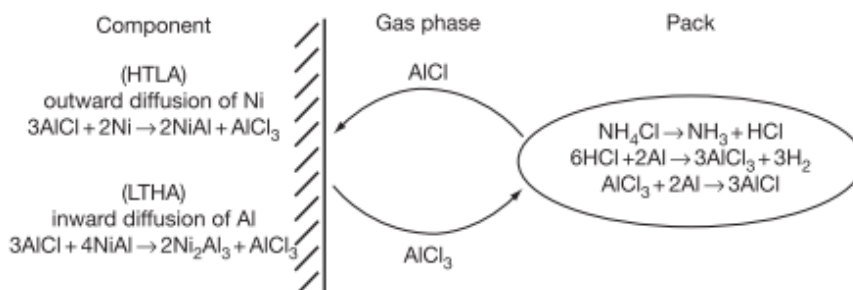


Figure 1.33. Scheme of the reaction chain occurring during the pack aluminization process. From: [109].

Conversely, in the LTHA process, the coating tends to develop inwardly [109] through the conversion of the metal alloy into an intermetallic compound. This occurs though the Al diffusion from the surface in contact with the aluminizing atmosphere towards the substrate. During a low activity aluminization process, δ - Al_3Ni_2 tends to form on the surface [97] because of the reaction between AlNi and the aluminizing vapor species. Therefore, the typical final product is a bilayer coating consisting of an outer layer of Al_3Ni_2 and an inner AlNi layer. Because of the brittleness and instability of the Al_3Ni_2 layer, a high temperature diffusion treatment is usually required after a LTHA process. The diffusion treatment is usually performed around 1000°C and it has the aim to convert all the Al_3Ni_2 layer into an AlNi compound. This transformation occurs with an increase in coating thickness [97]. The inward Al diffusion occurring during a high activity aluminization process and the consequent conversion of the metal matrix lead to the precipitation of the alloying elements which are not soluble in the intermetallic compound. Therefore, the presence of precipitates dispersed in the coating indicates that the formation of the layer occurred predominantly through inward Al diffusion (figure 1.34 and 1.35).

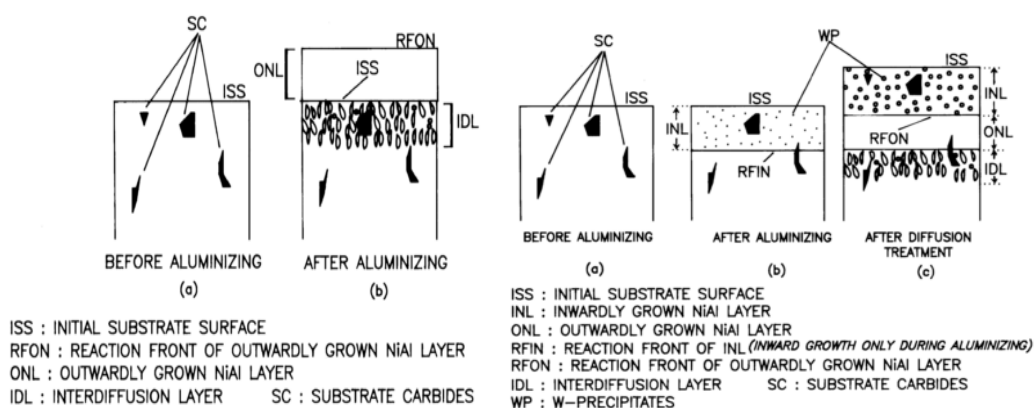


Figure 1.34. Schemes of the typical coating structures obtained in low activity (left) and high activity (right) pack aluminization processes. From: [110].

The coating formation mechanism is determined by the diffusion of Ni and Al in the β -AlNi compound, which in turn is strongly dependent on the composition of the diffusing media itself. The β -AlNi phase has a B2 crystalline structure of the CsCl type made by two interpenetrating simple cubic sublattices respectively constituted by Ni and Al atoms. The β -AlNi is stable in a wide range of compositions around the 1:1 stoichiometric one, in fact the deviations from the stoichiometric ratio can be accommodated by the presence of two main kinds of crystalline defects, which are the antisite defects and the structural vacancies in the Ni sublattice [111]. The antisite defects consist of Ni atoms which occupy the reticular positions of the Al sublattice; when antisite defects are present, the intermetallic compound is poorer in Al and richer in Ni with respect to the stoichiometric composition and it is therefore designated as hypostoichiometric AlNi. Conversely, when Ni vacancies are present, the phase is richer in Al and poorer in Ni respect to the stoichiometric composition and it is therefore designated as hyperstoichiometric AlNi.

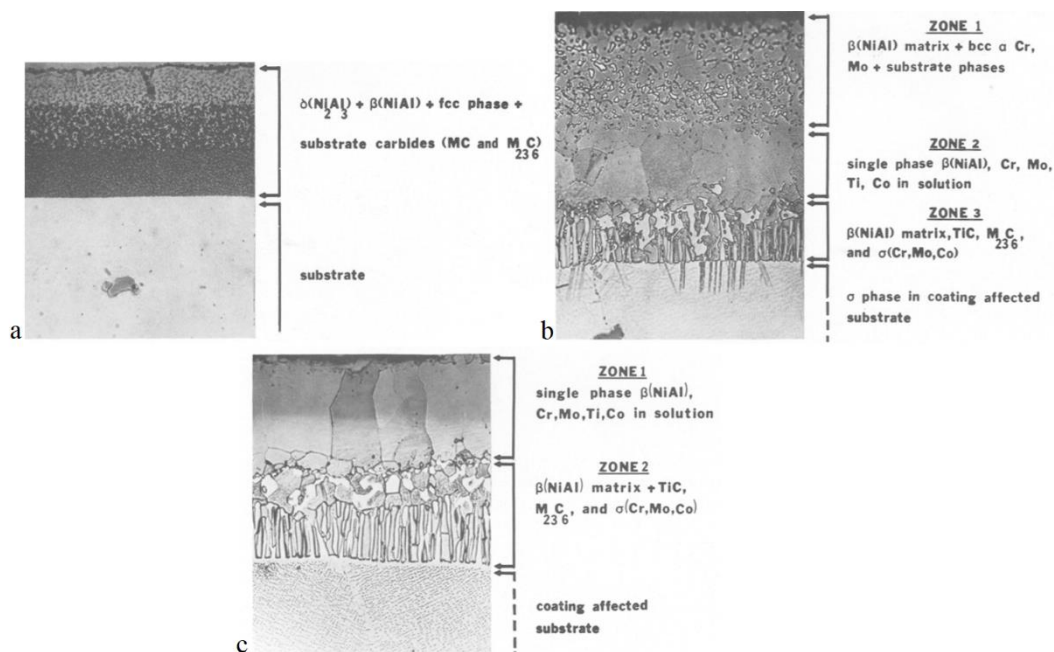


Figure 1.35. Optical micrographs of aluminized coatings on Udimet 700 alloy. Inward diffusion formed coating obtained with a high activity process before (a) and after (b) the diffusion heat treatment at 1080°C of 4 hours. Outward diffusion formed coating obtained with a low activity process (c). From: [107].

The intrinsic diffusivities of Ni and Al species in β -AlNi is reported in figure 1.36 as a function of the composition of the phase. It is possible to observe that the diffusivities of both the species have a minimum near the stoichiometric composition. Furthermore, the Ni diffusion strongly prevails in the hypostoichiometric AlNi, instead the Al diffusion prevails in the hyperstoichiometric side (note the log scale in the plot of figure 1.36). Similar results on the interdiffusion of Al and Ni in β -AlNi compound are also reported in other studies [111] [112] [113] [114]. This peculiar behavior is due to the complex diffusion mechanisms that are established in the long range ordered structure, in

particular the migration of triple defects and the anti-structure bridge (ASB) mechanism [115] [116].

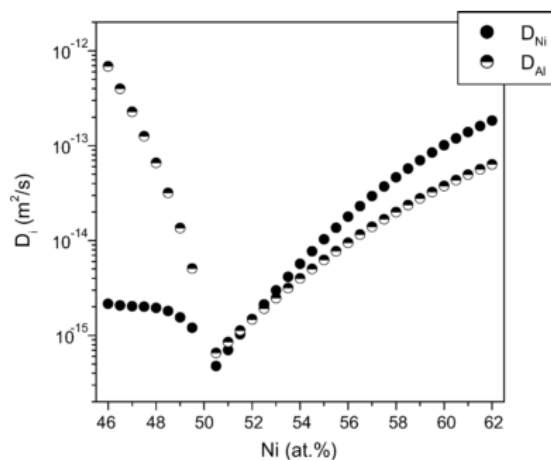


Figure 1.36. Intrinsic diffusivity at 1000°C of Al and Ni in β -AlNi in function of the composition. From: [117].

During a HTLA process, hypostoichiometric AlNi forms to allow the outward Ni diffusion. Instead, in a LTHA process, the formed product is mainly hyperstoichiometric AlNi through which the inward Al diffusion can occur.

In most of the practical situations, the coating development occurs through a mixed process, therefore an inner layer of hypostoichiometric AlNi and an external layer of hyperstoichiometric AlNi can form. In these cases, the coating growth occurs both inwardly and outwardly and the final obtained structure has the characteristics features of both the coating typologies [97] [110]. The effect of the constituents concentration in the powder mixture in a high-activity process on nickel-based superalloys, during which the coating growth occurs mainly by inward Al diffusion, has been investigated by Xiang et al. [118]. They observed that the coating structure (bilayer or monolayer) and its thickness is strongly influenced by the Al amount in the pack and that the activator type and the process temperature affect the growth rate of the coating because they determine the partial pressure of the aluminizing vapors during the process [118] [119]. Furthermore, the authors observed that the coating growth by Ni diffusion starts to be prevalent with an Al content in the pack lower than 2% wt. and a process temperature higher than 950°C [118]. Tong et al. also observed that in a LTHA process, performed at 700°C for 8 hours, the increase in the Al amount in the pack has the effect to increase the obtained coating thickness until reaching a saturation level above 20 wt%. On the contrary the content of the NH_4Cl activator is reported to do not affect significantly the final coating thickness [120].

1.4 Additive manufacturing

The “additive manufacturing” expression indicates a wide set of production techniques that have in common the basic concept of obtaining the final part through the progressive addition of material. Initially introduced in the field of rapid prototyping [121], the additive processes, also known as 3d printing techniques, are nowadays sufficiently mature to allow the production from the digital model of near-net shape pieces which are directly usable. The Computer Aided Design (CAD) model is subdivided into thin sections which are then consecutively produced to obtain the final product. The additive techniques can be classified on the base of the category used as a feedstock, i.e. polymeric [122], metallic [123], ceramic [124] or composite materials [125].

Focusing on the additive manufacturing techniques for the production of metal components [126] [127], a further sub-classification can be made on the base of the starting feedstocks, which is usually metallic powders, but also wires, as in the Laser Metal Wire Deposition (LMWD) technique [128], or thin sheets, as in the Laminated Object Manufacturing (LOM) [129] and Ultrasonic Consolidation (UC) [130] techniques. Finally, the additive techniques that use metal powders as feedstock are subdivided into two main categories: powder bed and injected powder techniques; in both of them, the product is obtained in consecutive steps in each of which a single section is built supported by the material previously deposited. In the powder bed processes, a thin layer of metal powder is firstly spread out at each step and then it is scanned with an energy beam, typically a laser radiation (Selective Laser Sintering, SLS [131] [132], or Selective Laser Melting, SLM [133]) or an electronic beam (Electron Beam Melting, EBM [134]), according to the profile of the section currently in construction. The energy beam causes the consolidation of the powders by triggering their sintering, in the case of SLM process, or by complete melting and subsequent re-solidification of the molten pool, as in the SLM process. At the end of each scan, there is a region in which the powders are consolidated into a massive material, while the remaining part still contain loose powders. When the production is complete, the finished piece is buried in the unused powder and it has to be extracted and cleaned. In the injected powder techniques, the powders are sprayed toward the substrate through nozzles coaxial to the energy beam system, therefore the new material is added directly into the fusion bath generated by the beam. The Laser Engineered Net Shaping (LENS) technique belongs to this category [135] [136].

The main advantages and disadvantages of the Additive Manufacturing (AM) techniques are reported below.

The advantages of AM are:

- geometrical freedom, that allows the production of components with complex shape that would be hard to obtain with the conventional techniques;
- high flexibility;

- high automation;
- very low waste of material with respect to the subtractive techniques;
- no expensive molds or dies are required and the wear of tools is avoided.

The current disadvantages of AM are:

- limited dimensional accuracy;
- high surface roughness requiring a finishing post treatment;
- geometrical constraints related to structural issues and to the difficulties in the removal of the powders from internal cavities or hard to access zones after the production;
- long process time for the production of each piece;
- necessity of post heat treatments or HIP to relieve the thermal stresses induced during the process and to correct the intrinsic defects introduced by the production technique (commonly voids and porosities, anisotropy, microstructural instabilities, presence of embrittling second phases);
- high costs deriving from the equipment and powders.

Because of the above reported limitations, the additive techniques are not suitable for large series productions nowadays, however they represent an interesting solution when the production of few highly customized components are required for specific applications, as in the biomedical and aerospace fields.

1.4.1 SLM: general process features and most common defects

The research on Selective Laser Melting (SLM) is mainly focused on the production of stainless steels, titanium, aluminum and nickel alloys. The technique find application in all the industrial fields in which the production of specially designed high-tech components is required; some examples are dental and medical applications, heat exchangers, light structures for the robotic and aeronautical field, components for aircraft engines as rotors and gas turbine blades [137].

The SLM technique allows to produce a tridimensional object through the deposition and consolidation of consecutive powder layers (see the scheme in figure 1.37). The first powder layer is spread out on a metallic support plate, then a high energy laser beam scans the powder bed and causes the selective fusion of some areas of it. At each subsequent step, a thin layer of powders is spread out on the previous deposited powders and then is scanned along the current section profile by the laser beam. The laser beam irradiation causes both the local melting of the powder and the partial remelt of the adjacent material and the previously deposited layer; then the consolidation of the added material and the formation of strongly bond with the previous layer occur through the solidification of the molten pool when the laser beam moves out [138]. The deposition and laser scan steps are repeated until the object, which at the end of the manufacturing process is buried in the loose powders, is complete. At this point, it is necessary to remove the unused powder and detach the piece from the support plate, this is usually done with electrical discharge machining (EDM).

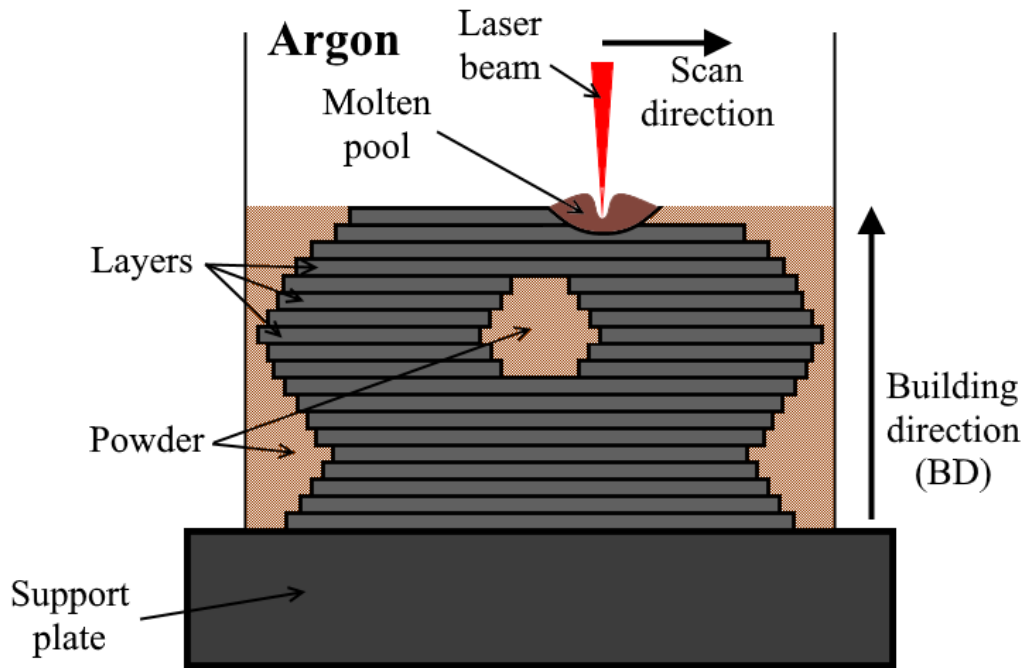


Figure 1.37. Scheme of the SLM process.

The general production procedure described above determines the typical laser related features in the parts produced through SLM. These characteristic features are the “laser tracks”, visible on the plane of the deposited layers and that keep track of the path followed by the laser beam during the scan of each layer, and the so-called “melt pools”, visible on the planes perpendicular to the deposition plane and that are due to the formation of the molten pools and the penetration of these into the underlying layers. The boundaries between laser tracks and melt pools become clearly visible at the optical microscope after chemical etching, some examples of them are shown in figure 1.38. These boundaries, sometimes referred as track-track and layer-layer molten pool boundaries (MPB), can affect the plastic deformation and the fracture mode of the sample and, therefore, represent a source of anisotropy in the mechanical behavior [139].

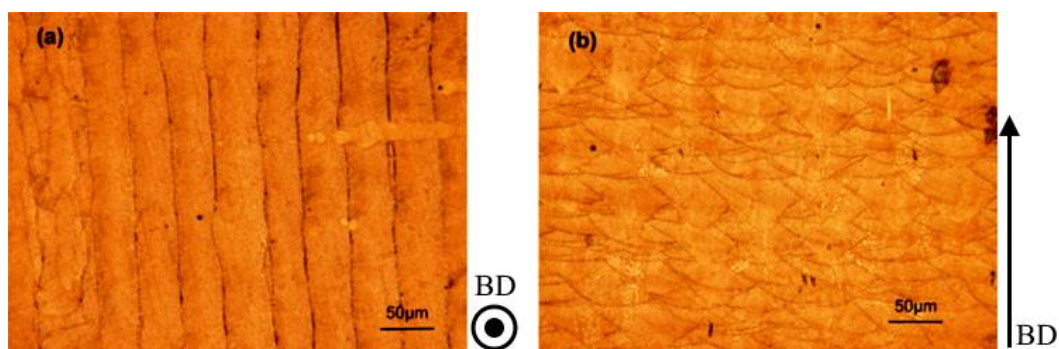


Figure 1.38. Optical micrographs showing the laser tracks on the horizontal plane and the arc-shape melt pool boundaries on the vertical plane of a SLM Inconel 718 alloy. From: [140].

Actually, the products obtained by SLM technique are inevitably characterized by a certain anisotropy deriving from the asymmetric process conditions between the Building Direction (BD), along which the forming piece grows through the

progressive addition of the layers (BD is indicated in figures 1.37 and 1.38) and the directions laying on the deposition plane, i.e. orthogonal to BD. The production of a metallic component through SLM technique is a complex process characterized by a large number of parameters whose optimization determines the final quality of the product. The main SLM process parameters are listed below:

- laser radiation parameters:
 - radiation wavelength
 - laser power
 - wave form (continuous or pulsed)
- laser scan parameters:
 - scan speed of the beam
 - hatching distance between consecutive scanning lines
 - scanning strategy:
 - scanning path (unidirectional, bidirectional, spiral, etc.)
 - scanning scheme (parallel stripes, square areas, etc.)
 - scanning orientation between layers (rotation of an angle of 0°, 45°, 67°, 90° or 180°)
 - eventual scanning repetition
- system parameters:
 - powder layer thickness
 - chamber atmosphere (nitrogen or argon inert gas to avoid oxidation)
 - eventual pre-heating of the support plate
- material parameters:
 - physical properties: elastic modulus and density
 - thermal properties: heat capacity, latent heat of fusion, thermal conductivity, Coefficient of Thermal Expansion (CTE)
 - mechanical and thermomechanical properties: Ultimate Tensile Strength (UTS), Yield Strength (YS), fracture toughness, thermal shock resistance
- powder parameters:
 - absorbance to the laser radiation
 - particle shape
 - size distribution
 - flowability

The amount of energy absorbed by the powders depends firstly on their absorbance, which can also be much greater with respect to the bulk material for the same laser wavelength due to multiple reflections and absorptions of the radiation on the surface of the powders [132]. Furthermore, the absorbed energy is also related to the imposed Volumetric Energy Density (VED) given by equation 1.10:

$$VED = \frac{P}{vh_d d} \quad \text{eq. 1.10}$$

where P is the laser power, v the scan speed, h_d the hatching distance and d the powder layer thickness. A schematic representation of these parameters is shown in figure 1.39.

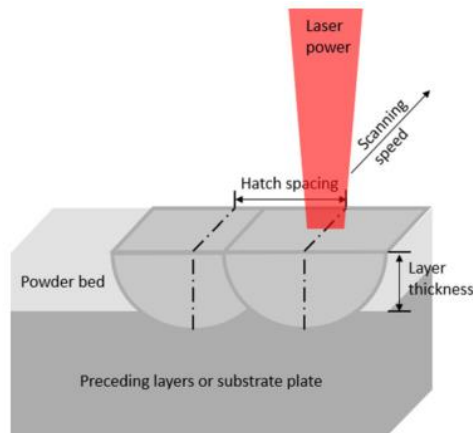


Figure 1.39. Scheme showing the main SLM process parameters which determine the Volumetric Energy Density (VED), i.e. laser power P , scan speed v , hatching distance h_d and layer thickness d . From: [137].

These process parameters have to be optimized with the aim to obtain a suitable amount of energy absorbed by the powder bed [141]. Actually, a too low absorbed energy determines the formation of defects and porosity due to lack of fusion, which can be due to an insufficient penetration of the molten pool into the substrate or to an excessive hatching distance that doesn't allow the overlap between the subsequent laser tracks. Furthermore, a low absorbed energy favors the balling phenomenon [133] [142] [143], which is due to a poor wettability of the liquid formed by melting of the powders on the platform or on the previously deposited material surface. In these conditions, the liquid surface tension causes the formation of spherical drops resulting in a poor consolidation of the added material and formation of voids.

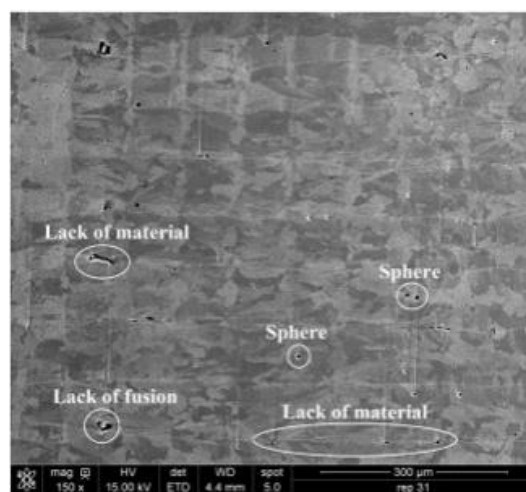


Figure 1.40. SEM micrograph showing some examples of gas porosities and lack of fusion porosities on a SLM Inconel 718 alloy. From: [144].

On the other hand, also an excessive absorbed energy can lead to the formation of defects as melt pools with keyhole shape [143], caused by too deep penetration, porosities due to the trapping of bubbles formed due to vaporizing of the too overheated material (see figures 1.40 and 1.41) and formation of cracks in the solidifying molten pool [145]. Trapped gas can also derive from not well packed powders or from porosities already present in the initial powder feedstock [146].

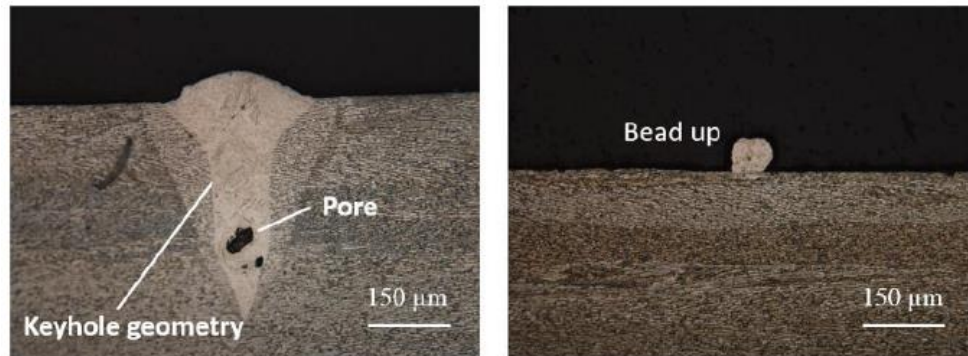


Figure 1.41. Examples of typical defects of the SLM products: keyhole geometry and porosity (left) and balling (right). From: [143].

Further defects that can be found in the components produced by SLM are cracks and delamination between layers due to thermal stresses developed in the material and caused by the high temperature gradients and solidification shrinkages which occur during all the laser-based processes, in particular SLM [147]. Internal stresses and cracks can also be due to phase transformations that occurs during the heating and cooling cycles at which the material is submitted during the SLM process [148]. The thermal stresses can be reduced through the pre-heating of the support plate, which allows to reduce the thermal gradients arising during the process, or by performing a second scan at lower laser power and higher scan speed after the deposition of each layer in order to induce stress release [147] [149].

The choice of the scan strategy has also an important role in the formation of residual stresses and the anisotropy of the produced sample [150]. The correct choice of the scan strategy allows to balance the energy input applied on the powder layer and to accommodate the introduced thermal stresses. It also allows to avoid to accumulate defects systematically in the same zones, typically at the beginning and at the end of the scan lines [146]. Furthermore, the scan strategy affects the grain structure, the material texture and the crack formation because it determines the direction and the intensity of the heat fluxes arising during the process [151]. Therefore, it could be even convenient to vary its effect depending on the size and the geometry of the produced part [152].

During the SLM process, the extremely fast solidification of the molten pools generates the formation of non-equilibrium microstructures characterized by the presence of second metastable phases. The cooling rates and thermal gradients have also an important effect on the size and the directionality of the grains and, therefore, they strongly affect the mechanical properties and the anisotropy level of the as-built material. It is very hard to correctly predict the microstructure arising

from the SLM process because of the complex solidification conditions, but also for the remelting, which occurs in the overlap region between laser scans and between consecutive layers, and the heterogeneous thermal histories that each portion of the material undergoes. Actually, whenever a new layer is added to the stack, the heat generated during the laser scan is partially transferred to the substrate by conduction, therefore the previously deposited material is submitted to a sequence of thermal cycles of decreasing intensity [148] which can cause microstructural alterations [153].

1.4.2 SLM applied to Inconel 718 alloy

The manufacturing of nickel-based superalloys products through the use of the SLM technique represents a very interesting solution because of the unique possibility to obtain components with complex shape and specifically designed for applications requiring high mechanical strength and high temperature stability. This is particularly interesting whenever the use of the conventional production techniques results too complex, long or expensive. The microstructure of the nickel-based superalloys arising from the SLM technique is particularly complex and heterogeneous due to the effect of the large number of alloying elements present in these systems and the consequent different microstructural features and second phases that can form as a consequence of the not-equilibrium phenomena that occurs during the additive process. Similar conditions, characterized by high heat inputs, thermal gradients and cooling rates, are also encountered in the welding processes, during which it is possible to introduce defects and cracks in the Heat Affected Zone (HAZ). The occurrence of such defects is due to the development of thermal stresses, incipient melting in presence of low melting second phases in the interdendritic zones or to the precipitation of brittle second phases (see paragraph 1.2.3). For this reason, at a first glance the most weldable superalloys are also the most suitable to be used in the SLM process as they avoid excessive formation of cracks, voids and other defects [145]. Therefore, the weldability map shown in figure 1.1 represents a useful tool to perform an initial selection of the most potentially appropriate nickel-based superalloys.

Because of its very low sensitivity to the strain-cracking mechanism and consequent good weldability, Inconel 718 alloy represents one of the most interesting candidates among the nickel-based superalloys for the use in the SLM process. For this reason, a lot of research efforts were focused on this alloy in the last years in order to determine the process conditions that allow to obtain the highest densification of the material and to investigate the resulting microstructure and properties.

1.4.2.1 Porosity and microstructure of SLM Inconel 718

Jia et al. has studied the effect of the laser energy density on the porosity, microstructure and oxidation properties of SLM Inconel 718 [142]. They found out that the relative density of the alloy increases as the adopted energy density increases. Actually, the balling phenomenon and the poor level of consolidation between laser tracks deriving from the low energy density lead to the formation of large cavities in the material. Porosities can progressively be reduced by increasing the energy density until to obtain a near full dense material and the mechanical properties and the oxidation resistance are improved consequentially [142]. In another study [90], Jia et al. have deeply characterized the oxidation behavior at 850°C in air of Inconel 718 samples produced through SLM and tested at the as built state. They found that low values of energy density (70 J/mm^3) determines a rapid and irregular oxidation rate because of the occurring of the severe spallation, instead the parabolic trend is followed with samples obtained at higher energy density. The parabolic constant values reported in this study are $7.6 \cdot 10^{-2} \text{ mg}^2\text{cm}^{-4}\text{h}^{-1}$, when an energy density of 110 J/mm^3 is used, and $1.6 \cdot 10^{-2} \text{ mg}^2\text{cm}^{-4}\text{h}^{-1}$ at 130 J/mm^3 . The authors explain the greater stability of the oxide scale grown in the samples obtained by increasing the energy density with the reduction of the porosity and the formation of a finer and uniform dendritic microstructure [90]. The effect of the scan speed on the porosity and microstructure of SLM Inconel 718 alloy was investigated by Choi et al. [154]. In this study low scanning speeds result in a high heat absorption providing the vaporization of the material and the formation of pores due to trapping of vapor. On the contrary, voids due to incomplete consolidation between laser tracks and unmelted particles are observed at excessively high speed values. An almost complete densification can be obtained by operating between these boundaries of scanning speeds. Once established the correct set of process parameters that allows to obtain the highest densification level, the study analyzed the microstructural features of Inconel 718 arising from the SLM process and their effects on the alloy performances. These microstructural features strongly depend on the local solidification conditions and, therefore, they are affected by the adopted process parameters and by the choice of the scanning strategy. The most frequently reported features are [155] [156] [157] [158] [159] [160]:

- epitaxial growth through several melt pools of elongated grains along the Building Direction (BD);
- crystallographic texture, i.e. a non random crystallographic orientation of the grains characterized by the tendency to align one of the $\langle 100 \rangle$ crystallographic axis at a low angle respect to BD;
- fine sub-granular structure consisting of columnar dendrites;
- microsegregation of the alloying elements at the length scale of the dendrites with consequent formation of eutectic products near and along the interdendritic boundaries;

- high microstructural heterogeneity level.

The directional growth of the grains and the relative crystallographic texture of Inconel 718 alloy produced by SLM can be detected through EBSD analysis, a typical example being shown in figure 1.42.

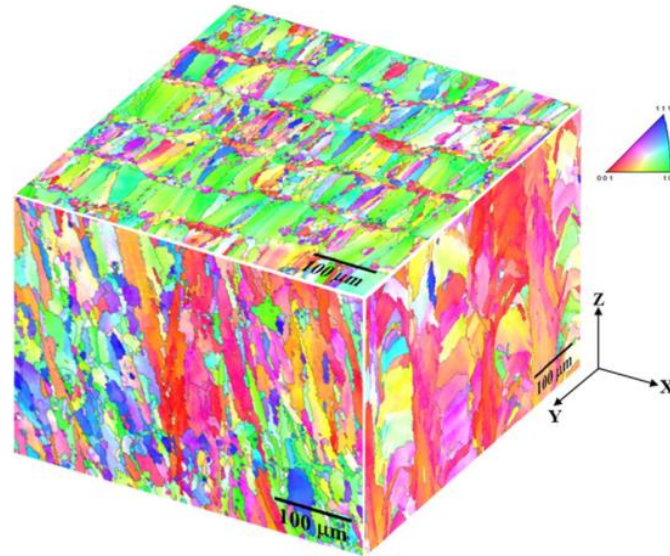


Figure 1.42. Inverse Pole Figure (IPF) maps showing the crystallographic texture of Inconel 718 alloy produced by SLM. In this picture the building direction corresponds to the z axis. From: [154].

In terms of microstructural features, the typical sub-granular dendritic structure that is observable in the as built material after SLM process is shown in figures 1.43 and 1.44.

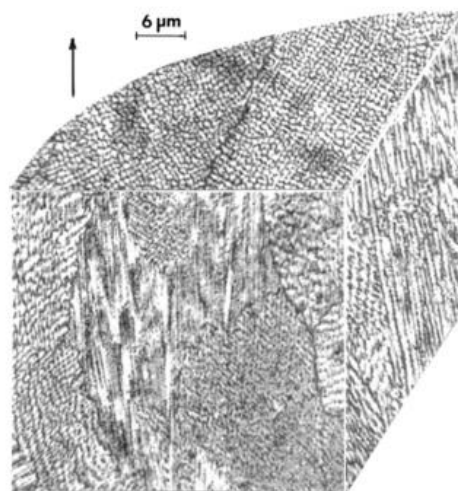


Figure 1.43. Three-dimensional composition of optical micrographs showing the sub-granular structure of columnar dendrites on a SLM Inconel 718 alloy. From: [159].

The formation of the γ dendrites is driven by the directions of the thermal gradients in the molten pools. At each laser passage, the last deposited layer is submitted to a partial melt, then the resolidification occurs through epitaxial growth of the sub-granular dendrites at the solid/liquid interface. The occurrence of

epitaxial growth in SLM and other laser based additive manufacturing technique is extensively reported in the literature [139] [142] [156] [161] [162] [163] [164] [165] [166]. A competitive growth between the dendrites is established, in which the dendrites with a $\langle 100 \rangle$ crystallographic axis aligned to the thermal gradient are favored and so prevail on the differently oriented ones. This determines the strong $\langle 100 \rangle$ crystallographic texture also reported in other nickel base superalloys produced through additive techniques [167] [168] [169] [170] [171] [172] [173] [174].

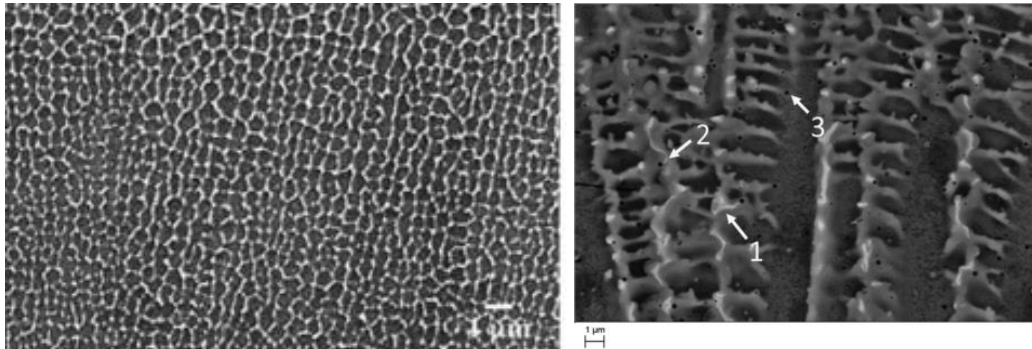


Figure 1.44. SEM micrographs showing the horizontal plane (top, from: [154]) and the vertical plane (bottom, from: [175]) of the cellular microstructure of an Inconel 718 alloy produced through SLM process. Arrow 1 indicates a γ + Laves eutectic, arrow 2 indicates a divorced eutectic, arrow 3 indicates a MC carbide.

During the rapid solidification (see paragraph 1.3.2.3), the alloying elements with a partition coefficient $k < 1$, in particular Nb, are rejected in the liquid and accumulate in the interdendritic zones [176] where they cause the formation of eutectic products, i.e. Nb carbides (NbC) and Laves phases (figure 1.45) [158], which can sometimes form a dense network at the interdendritic boundaries (figure 1.44).

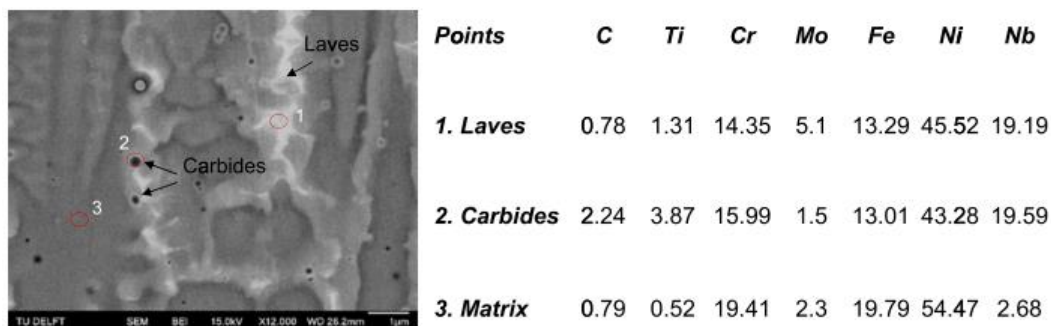


Figure 1.45. EDS analysis of the γ matrix in comparison with the eutectic products, i.e. carbides and Laves phases. From: [158].

Tian et al. have investigated the evolution of the microstructure during a laser powder injection AM process and they have observed that the heating peaks at decreasing temperature, experienced by the material in correspondence of the deposition of each new layer, may cause firstly a partial dissolution of the interdendritic network. In a second stage the redistribution of the Nb solute through diffusion towards the cores of the dendrites and finally the formation of a population

of γ'' precipitates distributed with a decreasing density as the core of the cell is approached [177] occur. Such sequence of events is described in the micrographs and scheme reported in figure 1.46.

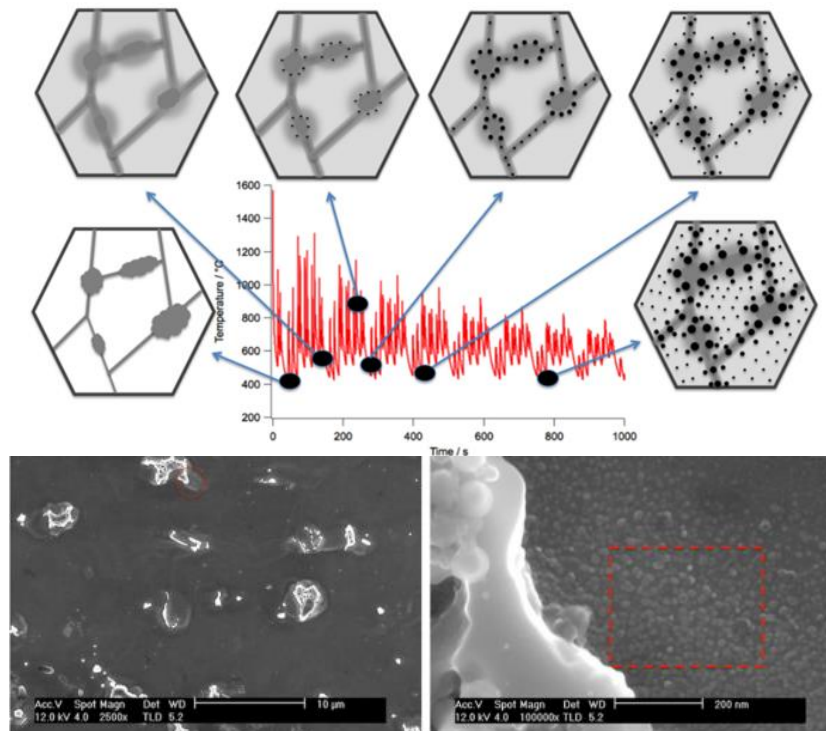


Figure 1.46. Scheme of the evolution of the Inconel 718 alloy microstructure caused by the thermal cycles during a laser powder injection AM process (top) and SEM micrographs showing the eutectic products and the γ'' precipitates in the intracellular zone (bottom). From: [177].

The interesting issue in the study of Tian et al. [177] is that the second phases, as γ' , γ'' and δ , which are not theoretically expected to form during the consolidation step as a consequence of the too rapid cooling during solidification process, can potentially form heterogeneously during the deposition of the successive layers. In a similar way, precipitation of columnar arrays of γ'' precipitates are also reported by Amato et al. [159].

A certain microstructural heterogeneity is also reported by Wang and Chou [157], which have ascertained a difference in the dendrites size between the bottom of the produced piece, in contact with the support plate, and the top of it, i.e. the last deposited layer. Close to the bottom the directionality of the dendrites is lower and their size is about $0.51 \mu\text{m}$, whereas close to the top they are coarser, about $0.84 \mu\text{m}$, and the directionality along the building direction is marked. This occurs because of the different solidification conditions that are established. An important role is, in particular, played by the direction of thermal fluxes and by the local cooling rate, which is higher during the first depositions because of the high thermal conductivity of the support plate and of its progressive reduction with the height of the part. The authors have also observed that the thermal cycles suffered by the deposited material determine a different distribution and morphology of the interdendritic Laves phases at different distance from the support plate [157]. The

morphology of the melt pools can also vary along the height of the forming piece as a consequence of the different cooling rates even if the nominal process parameters are not varied [178]. Table 1.12 collects some indicative values of the mechanical properties reported in the literature for Inconel 718 alloy produced by SLM as well as the related sets of process parameters. It is possible to observe a certain anisotropy of the as built material, in fact the elastic modulus and the tensile properties tend to be higher along the directions perpendicular to the building one, i.e. on the horizontal built specimens. The mechanical anisotropy is related to the directionality of the grains and the crystallographic texture.

Table 1.12. Mechanical properties of SLM Inconel 718 varying the process parameters, the specimen orientation and the test temperature. The specimen orientation is given as the angle between the building direction of the tensile specimen and the load axis. The sets of SLM parameters are listed in the table below. RT: Room Temperature; P: laser power (W), v: scan speed (mm/s), hd: hatching distance (mm), PLT: Powder layer thickness (μm), OR: overlap ratio (%).

Test temperature ($^{\circ}\text{C}$)	Specimen orientation ($^{\circ}$)	n. set of SLM parameters	Elastic modulus (GPa)	Yield Strength (MPa)	Ultimate Tensile Strength (MPa)	Elongation to failure (%)	Reference
RT	0	1	-	737 ± 4	1010 ± 104	20.6 ± 2.1	[176]
	0	2	173 ± 13	668 ± 16	1011 ± 27	22 ± 2	[179]
	0	3	113 ± 3	531 ± 9	866 ± 33	21 ± 5	[179]
	0	4	162 ± 18	572 ± 44	904 ± 22	19 ± 4	[175]
	45	4	200 ± 23	590 ± 15	954 ± 10	20 ± 1	[175]
	54.73*	4	208 ± 48	723 ± 55	1117 ± 45	16 ± 3	[175]
	90	5	204	898 ± 9	1142 ± 6	22.5 ± 3.4	[140]
	90	4	193 ± 24	643 ± 63	991 ± 62	13 ± 6	[175]
	90	6	-	849	1126	22.8	[180]
	90	1	-	816 ± 24	1085 ± 11	19.1 ± 0.7	[176]
650	0	2	-	650 ± 11	845 ± 9	28 ± 4	[179]
	0	3	-	543 ± 2	782 ± 6	31 ± 6	[179]

* the load axis of this specimen is aligned to the (1, 1, 1) vector in the cartesian coordinate system where the (0, 0, 1) unit vector is aligned to the building direction.

n. set of SLM parameters	Parameters	Reference
1	PLT = 20	[176]
2	P = 250, v = 700, hd = 0.12, PLT = 50, chess-board scanning strategy 10 x 10 mm	[179]
3	P = 950, v = 320, hd = 0.50, PLT = 100, chess-board scanning strategy 20 x 20 mm	[179]
4	P = 100, v = 85.7, hd = 0.16, PLT = 50, zig-zag scanning and 90° rotation	[175]
5	P = 170, v = 417, OR = 30, PLT = 20, bidirectional scanning and 90° rotation	[140]
6	v = 1200, OR = 30	[180]

1.4.2.2 Post process: heat treatments and HIP

The microstructural features of the as built material determine also the response to the post heat treatments or to the exposition to the service temperature. The post thermal treatments or the HIP process on the as built material can have different functions, e.g. to eliminate the porosities, to release the residual stresses, to reduce the level of microsegregation of the alloying elements, to homogenize the microstructure and to reduce the anisotropy by causing a partial or total recrystallization. Furthermore, the nature and the distribution of the second phases typically obtained in the as built state are rarely the optimal one from the point of view of the mechanical performances. Therefore a solution annealing treatment may be necessary in order to dissolve the embrittling metastable phases, in particular the interdendritic Laves phases, which can easily act as a preferential site for the nucleation of cracks [181]. Then, one or more aging cycle are performed to obtain a homogeneous distribution of γ' and γ'' strengthening precipitates to optimize the mechanical properties.

After proper heat treatment, the mechanical properties of Inconel 718 alloy produced through SLM process become comparable to those of the conventional wrought alloy [140] [182].

Zhang et al. observe a partial recrystallization of the as built material, but the permanence of Laves phases and carbides after a heat treatment at 980°C, whereas a complete recrystallization and a greater dissolution of the Laves phases can be achieved with a preliminary homogenization treatment at 1080°C [180]. The HIP treatment increases the ductility of the as built material and modifies the microstructure arising from the SLM process by generating equiaxed and coarser grains and reducing the preferential crystallographic orientation [161]. Although HIPing can drastically reduce the porosity related to SLM process, it is ineffective in removing the pores filled with argon gas coming from the chamber during the manufacturing process [11].

Popovich et al. have obtained zones with different granulometry, texture and microstructure in the same sample by varying the SLM process parameters (reported in table 1.12) and they studied corresponding response to different post-treatment cycles [179]. They found that an annealing treatment at 850°C for 2 hours maintains the columnar structure and causes the formation of needle like δ precipitates along the grain boundaries and along the interdendritic boundaries because of the release of Nb due to the partial dissolution of the Laves phases. Instead, the HIP treatment causes a better homogenization of the microstructure and the complete dissolution of the Laves phases, but the recrystallization, the grain growth and the reduction of the preferential crystallographic orientation occur in a different measure depending on the initial microstructure. The porosity values measured by the authors are reported in table 1.13, the HIP treatment allows to reduce the porosity level of one order of magnitude. HIP can also be used to fix the cracking occurred during the SLM process [145].

Chlebus et al. report the formation of needle-like δ precipitates and the presence of residual Laves phases after solubilization of 1 hour at 980°C and 1040°C [175]. Actually, the complete dissolution of these compounds is hindered by the low Nb diffusivity in nickel. On the contrary, at the temperature of 1100°C, the authors observed partial recrystallization, almost complete dissolution of the Laves phases and formation of Nb rich MC carbides at the grain boundaries, which prevent grain coarsening. However the elongated shape of the grains and the crystallographic texture, with the consequent anisotropy of the mechanical properties, are not completely eliminated by the heat treatment [175]. If the aging treatment is performed directly on the as built material (direct aging) without a preliminary solution annealing, the strengthening γ' and γ'' phases tend to form mainly along the interdendritic boundaries. Conversely the homogenization achieved with the solution treatment allows to obtain a uniform distribution of γ' and γ'' phases during the subsequent aging cycles. Precipitation of MC type carbides along the grain boundaries may occur during the HIP post-treatment and the high temperature (above 1000°C) homogenization [178].

Table 1.13. Porosity of SLM Inconel 718 alloy at the as built state and after different post treatments. HT: solution annealed at 850°C for 2 hours; HIP: HIPed at 1180°C for 3 hours at 150 MPa; HIP + HT: HIPed + solution annealed at 1065°C for 1h + aged at 760°C for 10 hours + aged at 650°C for 8 hours. Source: ref. [179].

<i>SLM parameters</i>	<i>State</i>	<i>Porosity (%)</i>
P = 250, v = 700, hd = 0.12, PLT = 50	As built	0.11
	HT	0.15
	HIP	0.02
	HIP + HT	0.04
P = 950, v = 320, hd = 0.50, PLT = 100	As built	0.27
	HT	0.29
	HIP	0.06
	HIP + HT	0.07

The formation and growth of relatively coarse intergranular carbides of about 1 μm during the heat treatment at high temperatures, i.e. 1100°C and 1250°C, are also reported by Tucho et al. (figure 1.47) [183]. These extremely stable carbides are formed as a result of the release of carbide forming elements previously entrapped in the eutectic products along the sub-grain boundaries in the as-built state. The precipitation of new phases during the heat treatment, in particular MC carbides at high temperatures (above 1000°C) and δ phase at lower temperatures (800-1000°C), should be controlled to avoid excessive Nb sequestration with consequent lack of formation of the strengthening γ'' precipitates during the aging step. However, the formation of precipitates along grain boundaries may be desirable because they hinder the grain coarsening through a pinning effect during heat treatment.

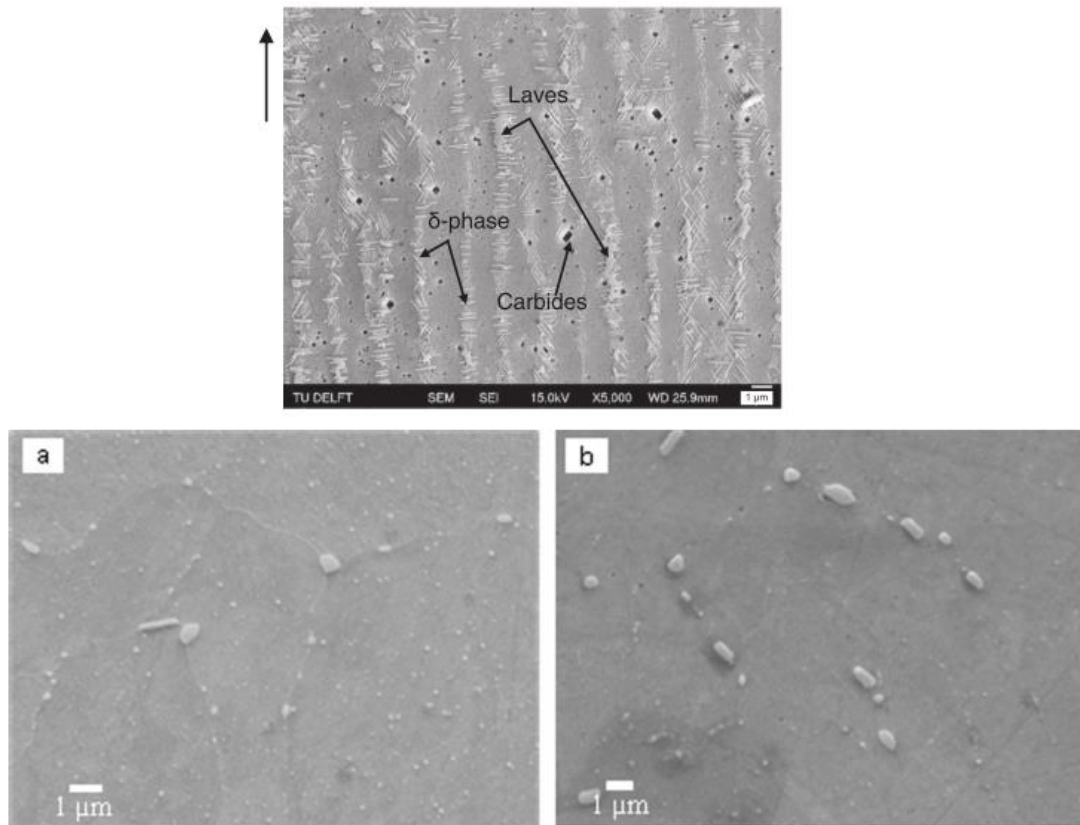


Figure 1.47. Heat treated SLM Inconel 718. Top: SEM micrograph of the vertical plane showing the formation of δ precipitates at the interdendritic boundaries after heat treatment at 850°C for 2 hours, the arrow indicates the building direction. From: [179]. Bottom: SEM micrographs of the horizontal plane showing carbides after solution annealing at 1100°C for 1 hour (a) and 7 hours (b). From: [183].

Some indicative values of the mechanical properties of SLM Inconel 718 after different post processes, i.e. heat treatments and/or HIP, are reported in table 1.14 in comparison with the cast and wrought alloy. After the complete heat treatment cycle, the tensile properties of the SLM material become comparable to these in the wrought state, the HIP treatment tends to increase the ductility of the alloy due to a general homogenization of the microstructure. Note that a certain grade of anisotropy persists even after post processing.

Table 1.14. Mechanical properties of SLM Inconel 718 in different post processing condition (heat treatment and eventual HIP) in comparison with the conventional wrought and cast alloy. The specimen orientation is given as the angle between the building direction of the tensile specimen and the load axis. T: testing temperature; HIP: Hot Isostatic Pressing; sol.: solution annealing; ag.: double aging.

T (°C)	Specimen orientation (°)	State	Elastic modulus (GPa)	Yield Strength (MPa)	Ultimate Tensile Strength (MPa)	Elongation to failure (%)	Reference
RT	-	wrought	-	1125	1365	21	[66]
RT	-	wrought	-	1192	1380	19.1	[184]
450	-	wrought	-	1055	1177	17	[184]
649	-	wrought	-	965	1105	20	[66]
650	-	wrought	-	1061	1061	13.9	[184]
RT	-	cast	-	915	1090	11	[66]
RT	-	cast	-	940	950	23.1	[184]
450	-	cast	-	750	766	10.9	[184]
650	-	cast	-	517	576	13.7	[184]
RT	0	SLM* + sol. 850°C/2h	190 ± 11	875 ± 11	1153 ± 4	17 ± 2	[179]
RT	0	SLM** + sol. 850°C/2h	138 ± 5	668 ± 7	884 ± 80	7 ± 2	[179]
RT	0	SLM + sol. 954°C/1h + ag. 718°C/8h, 50°C/h, 621°C/8h	165	1215	-	-	[161]
RT	0	SLM + sol. 980°C/1h + ag. 718°C/8h, 621°C/8h	-	1180	1400	20.4	[184]
RT	0	SLM + sol. 980°C/1h + ag. 760°C/10h, 55°C/h, 650°C/8h	-	1136 ± 16	1357 ± 5	13.6 ± 0.2	[176]
RT	0	SLM + sol. 1065°C/1h + sol. 980°C/1h + ag. 760°C/10h, 55°C/h, 650°C/8h	-	1186 ± 23	1387 ± 12	17.4 ± 0.4	[176]
RT	0	SLM + sol. 1100°C/1h + ag. 720°C/8h, 100°C/h, 620°C/10h	163 ± 30	1074 ± 42	1320 ± 6	19 ± 2	[175]
RT	0	SLM + sol. 982°C/0.5h + HIP at 1163°C/4h/100MPa	-	850	1140	28	[159]
RT	0	SLM* + HIP at 1180°C/3h/150MPa	188 ± 8	645 ± 6	1025 ± 14	38 ± 1	[179]
RT	0	SLM** + HIP at 1180°C/3h/150MPa	183 ± 19	481 ± 11	788 ± 12	34 ± 3	[179]
RT	0	SLM* + HIP at 1180°C/3h/150MPa + sol. 1065°C/1h + ag. 760°C/10h, 55°C/h, 650°C/8h	190 ± 6	1145 ± 16	1376 ± 14	19 ± 1	[179]
RT	0	SLM** + HIP at 1180°C/3h/150MPa + sol. 1065°C/1h + ag. 760°C/10h, 55°C/h, 650°C/8h	188 ± 20	1065 ± 20	1272 ± 12	15 ± 4	[179]
RT	54.73	SLM + sol. 1100°C/1h + ag. 720°C/8h, 100°C/h, 620°C/10h	209 ± 44	1241 ± 68	1457 ± 55	14 ± 5	[175]

continued

RT	45	SLM + sol. 954°C/1h + ag. 718°C/8h, 50°C/h, 621°C/8h	215	1305	-	-	[161]
RT	45	SLM + sol. 980°C/1h + ag. 718°C/8h, 621°C/8h	-	1190	1450	16.9	[184]
RT	45	SLM + sol. 1100°C/1h + ag. 720°C/8h, 100°C/h, 620°C/10h	188 ± 19	1152 ± 24	1371 ± 5	15 ± 5	[175]
RT	90	SLM + sol. 954°C/1h + ag. 718°C/8h, 50°C/h, 621°C/8h	195	1290	-	-	[161]
RT	90	SLM + sol. 980°C/1h + ag. 718°C/8h, 621°C/8h	-	1186	1440	18.5	[184]
RT	90	SLM + sol. 980°C/1h + ag. 720°C/8h, 620°C/8h	201	1131 ± 30	1319 ± 39	16 ± 6	[140]
RT	90	SLM + sol. 980°C/1h + ag. 720°C/8h, 55°C/h, 620°C/8h	-	1084	1371	10.1	[180]
RT	90	SLM + sol. 980°C/1h + ag. 760°C/10h, 55°C/h, 650°C/8h	-	1227 ± 1	1447 ± 10	10.1 ± 0.6	[176]
RT	90	SLM + sol. 1065°C/1h + 980°C/1h + ag. 760°C/10h, 55°C/h, 650°C/8h	-	1222 ± 26	1417 ± 4	15.9 ± 1	[176]
RT	90	SLM + sol. 1080°C/1.5h + 980°C/1 sol. h + ag. 720°C/8h, 55°C/h, 620°C/8h	-	1046	1371	12.3	[180]
RT	90	SLM + sol. 1100°C/1h, ag. 720°C/8h, 100°C/h, 620°C/10h	199 ± 15	1159 ± 32	1377 ± 66	8 ± 6	[175]
RT	90	SLM + sol. 982°C/0.5h + HIP at 1163°C/4h/100MPa	-	890	1200	28	[159]
RT	-	SLM + sol. 954°C/1h + ag. 718°C/8h, 50°C/h, 621°C/8h + HIP at 1163°C/4h/100 MPa	200	1125	-	-	[161]
450	0	SLM + sol. 980°C/1h + ag. 718°C/8h, 621°C/8h	-	1026	1160	15.9	[184]
450	45	SLM + sol. 980°C/1h + ag. 718°C/8h + 621°C/8h	-	1080	1255	12.8	[184]
450	90	SLM + sol. 980°C/1h + ag. 718°C/8h, 621°C/8h	-	1033	1216	12.4	[184]
650	0	SLM* + sol. 850°C/2h	-	-	-	-	[179]
650	0	SLM** + sol. 850°C/2h	-	-	-	-	[179]
650	0	SLM + sol. 980°C/1h + ag. 718°C/8h, 621°C/8h	-	860	992	14.2	[184]
650	0	SLM* + HIP at 1180°C/3h/150MPa	-	626 ± 8	857 ± 14	29 ± 1	[179]
650	0	SLM** + HIP at 1180°C/3h/150MPa	-	479 ± 5	665 ± 7	28 ± 2	[179]

continued

650	0	SLM* + HIP at 1180°C/3h/150MPa + sol. 1065°C/1h + ag. 760°C/10h, 55°C/h, 650°C/8h	-	942 ± 11	1078 ± 8	20 ± 2	[179]
650	0	SLM** + HIP at 1180°C/3h/150MPa + sol. 1065°C/1h + ag. 760°C/10h, 55°C/h, 650°C/8h	-	872 ± 13	1005 ± 12	17 ± 4	[179]
650	45	SLM + sol. 980°C/1h + ag. 718°C/8h, 621°C/8h	-	855	1074	5.8	[184]
650	90	SLM + sol. 980°C/1h + ag. 718°C/8h, 621°C/8h	-	870	1011	3.6	[184]

* produced at P = 250 (set of process parameters n.2 in table 1.12)

** produced at P = 950 (set of process parameters n.3 in table 1.12)

Chapter 2

Materials and characterization methods

2.1 Starting powders

The gas atomized Inconel 718 powders used as a feedstock material to produce the samples were supplied by EOS GmbH. The nominal composition of the powders is reported in table 2.1.

Table 2.1. Nominal composition (%) of the Inconel 718 powders used in this study. Provided by EOS: [185].

Ni	Cr	Nb	Mo	Ti	Al	Fe
50- 55	17-21	4.74-5.5	2.8-3.3	0.65-1.15	0.2-0.8	balance
Co	Cu	C	Si + Mn	P + S	B	
<1	<0.3	<0.08	<0.35	<0.015	<0.006	

The feedstock powders should have a suitable shape, as spherical as possible in order to guarantee a sufficient flowability to allow the deposition of the layers at each deposition step without difficulties. Eventual internal porosities are unwanted because the gas trapped in them can cause the formation of bubbles and consequent voids and cavities in the produced material during the SLM process [146]. Monomodal and narrow size distribution of the powders are usually preferred to facilitate a uniform deposition of the powder layer. A large powder size limits the obtainable resolution, the dimensional accuracy and the surface finish of the part. Conversely, a too low powder size is also unwanted because the small particles tend to form agglomerates with consequent reduction of the flowability.

The cross sections shown in figure 2.1 demonstrate that the used powders have a quite regular and spherical shape, furthermore they have substantially no or very limited internal porosities. The micrograph in figure 2.1-C, obtained after Kalling's etching (1 g CuCl₂ in 20 ml HCl and 20 ml of ethanol), shows an equiaxed dendritic

structure that is formed due to the extremely fast cooling and solidification during the powder production through atomization process.

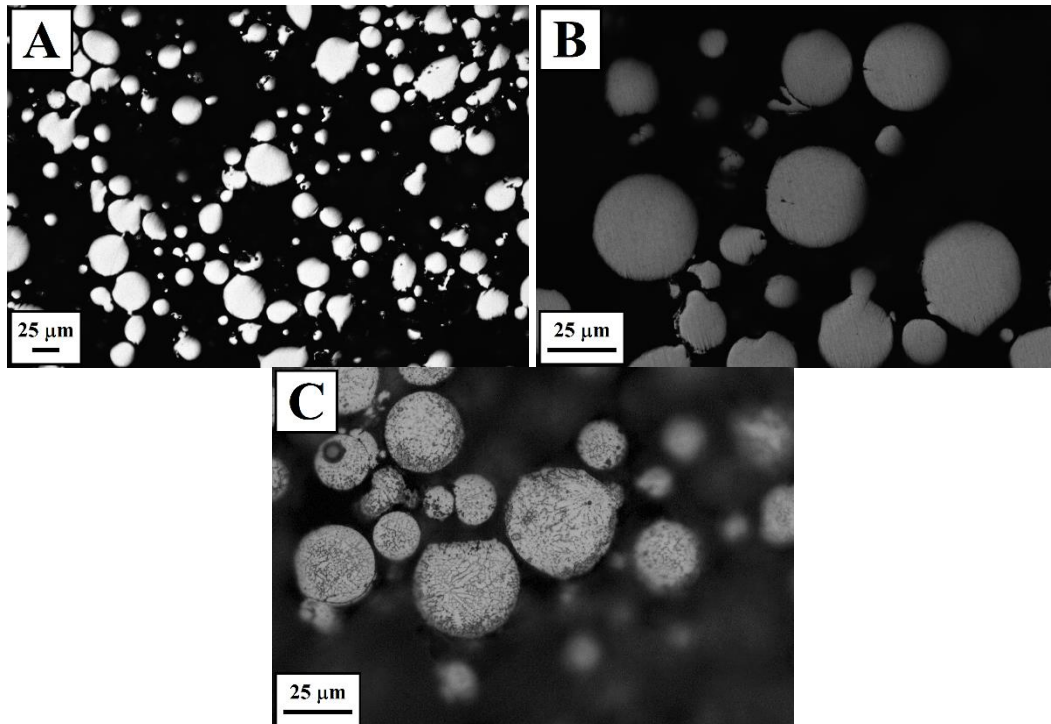


Figure 2.1. Optical micrographs showing the cross sections of the Inconel 718 powders used for this study. Not etched (A and B) and etched with Kalling's n.2 etchant (C).

The SEM micrograph shown in figure 2.2-A confirms the spherical morphology of the powder particles and reveals the presence of some small satellite particles agglomerated on the surface of the bigger ones. The powder size distribution, obtained through laser diffraction with a Fritsch model Analysette 22 Compact system, is also reported in figure 2.2-B. It is possible to observe that the size distribution is monomodal with a median value of about 25 μm .

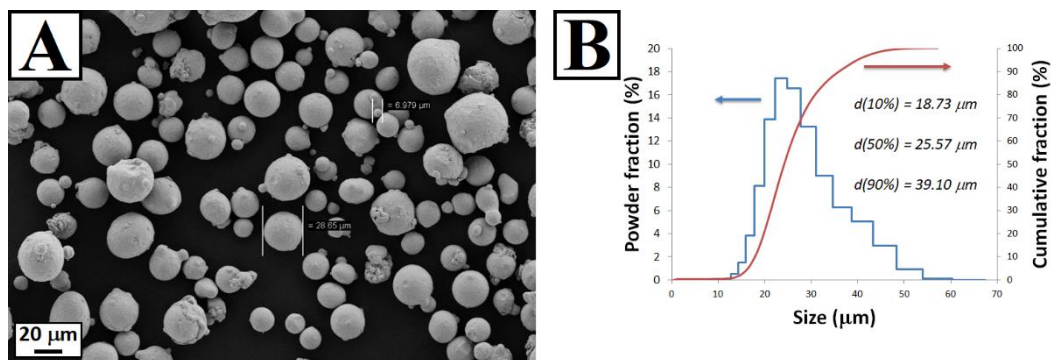


Figure 2.2. SEM micrograph showing the morphology of the Inconel 718 powders used for this study (A) and relative size distribution obtained with laser diffraction technique (B). First published in [186].

2.2 SLM equipment and procedure

All the samples used in this thesis were produced through Selective Laser Melting (SLM) technique using an EOSINT M270 Dual mode machine equipped with a fiber continuous Yb laser system with nominal power 200 W and wavelength 1060-1100 nm. The pieces are produced based on a digital 3D CAD model, some support structures are included in the digital drawing when required by the geometry of the part.

Before the production step, the powders are sieved and loaded on the dispenser. The chamber is fill with Ar inert gas, the oxygen level in the atmosphere is kept below 0.1% to avoid oxidation of the powders and of the produced part during the process. After this preliminary step, the procedure of additive production is completely automatized. At each deposition step, a powder layer with a thickness of 200 μm is spread with a blade, after that the laser beam with a spot size of 100 μm scans the layer with the process parameters set by the user: laser power, scan speed and hatching distance. The EOS recommended parameters for the used feedstock powders are:

- Laser power: 195 W
- Scan speed: 1200 mm/s
- Hatching distance: 0.09 mm

The first layer is spread on a stainless steel support plate, which has to subtain the powder and the piece under construction during the SLM process and to dissipate the heat generated during the laser scan. The scan of every single layer is performed following a bidirectional scanning path and between each layer the scanning direction is rotated of 67° (figure 2.3). This scan strategy prevents the incidence of periodic repetitions in the scan direction between neighbor layers with the aim to reduce the anisotropy of the produced piece on the plane of the deposited layers.

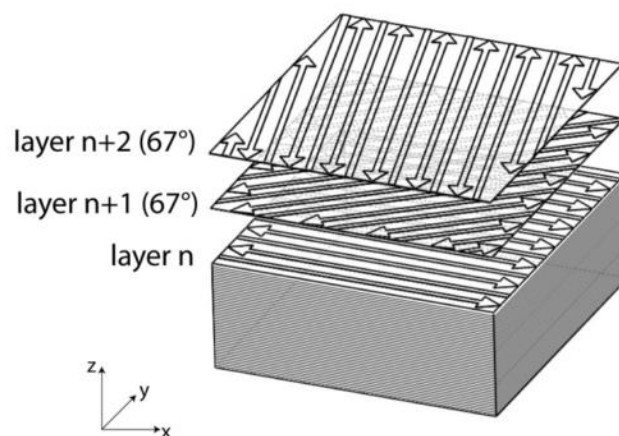


Figure 2.3. Schematic representation of the scan strategy adopted in this study: bidirectional scanning path with rotation of 67° at each layer. From: [187].

After the scanning of each layer, the laser beam performs a second rapid scan along the contours of the current section in order to improve the tolerance of the geometry on the base of the starting CAD model. After that, the base platform moves down for a length equal to the layer thickness and a new powder layer is deposited. The above described steps are repeated until the product is completed.

It is possible to produce the metal part directly on the support plate or, alternatively, on support structures produced on the stainless steel platform during the first depositions. This latter strategy allows more easily removing the piece from the platform at the end of the process. If the support structures are used, the pieces can be removed manually from the platform, otherwise the electrical discharge machining (EDM) is necessary to remove the pieces from the support plate.

Some of the produced samples were submitted to a stress relieving heat treatment at 450°C for 2 hours before to remove them from the support plate. This heat treatment step reduces the risk of deforming the piece after the detachment related to the internal stresses developed in the material during the SLM production.

2.3 Preliminary study on the effects of the SLM process parameters

The effects of the process parameters, in particular of the laser power, the scan speed and the hatching distance, on the density, the porosity level and the hardness of the produced material were investigated as a starting point for the subsequent characterizations. This preliminary study was performed according to a 3^3 factorial experimental plane, in which three levels for each of the three process factors are taken into account. The factorial plane allows to evaluate efficiently both the effect of each single factor and the eventual interaction between them [188]. The adopted level values of the three factors of the plan and the relative 27 combinations are reported in table 2.2.

Table 2.2. Factors and respective levels of the 3³ factorial plane on the study of the SLM process parameters and set of all the performed combinations of them.

Factors	Level		
	<i>low</i>	<i>medium</i>	<i>high</i>
P (W)	175	185	195
v (mm/s)	600	900	1200
hd (mm)	0.07	0.09	0.11

ID Sample	P (W)	v (mm/s)	hd (mm)	VED (J/mm³)
1	175	600	0.09	162.04
2	195	600	0.09	180.56
3	175	900	0.07	138.89
4	175	1200	0.11	66.29
5	175	1200	0.07	104.17
6	185	600	0.09	171.30
7	185	1200	0.11	70.08
8	185	900	0.07	146.83
9	175	1200	0.09	81.02
10	185	900	0.11	93.43
11	195	900	0.07	154.76
12	185	600	0.07	220.24
13	195	600	0.07	232.14
14	195	1200	0.09	90.28
15	175	600	0.07	208.33
16	195	1200	0.11	73.86
17	195	900	0.09	120.37
18	185	900	0.09	114.20
19	185	1200	0.07	110.12
20	185	1200	0.09	85.65
21	175	900	0.09	108.02
22	175	600	0.11	132.58
23	195	600	0.11	147.73
24	195	1200	0.07	116.07
25	185	600	0.11	140.15
26	195	900	0.11	98.48
27	175	900	0.11	88.38

One sample of about 15x15x10 mm in size was produced for each of the parameter combination reported in table 2.2. The apparent density of each sample was evaluated through Archimede's method [189] using a precision balance with resolution 0.1 mg. The apparent density ρ_{ap} is calculated through equation 2.1:

$$\rho_{ap} = \rho_{H_2O} \frac{w}{w - w_{H_2O}} \quad \text{eq. 2.1}$$

where w is the weight of the sample, w_{H_2O} is the weight of the sample immersed in distilled water and ρ_{H_2O} is the density of the water at room temperature, equals to $0.997 \pm 0.001 \text{ g/cm}^3$.

The surface of samples used for such measurements was lapped with SiC abrasive paper before the measurement in order to reduce the high surface roughness arising from the SLM process, which would lead to difficulties in the weigh measurements due to the trapping of air and the consequent formation of bubbles on the surface of the sample.

An estimation of the porosity level of each sample was also obtained through image analysis of optical micrographs. For this analysis, one face of each sample was polished with diamond pastes with decreasing grade until $1 \mu\text{m}$. Each collected optical image covers an area of $1.8 \times 1.4 \text{ mm}$ and for each sample a total of 28 images were collected, therefore a total area of about 73.6 mm^2 was examined. The images were binarized by setting a threshold value of grey, then the porosity value was obtained in terms of percentage coverage of the observed voids on the total area of the image. Figure 2.4 reports an example of the applied procedure. A lower and higher boundaries estimations of the porosity were derived for each treated image using two different threshold values.

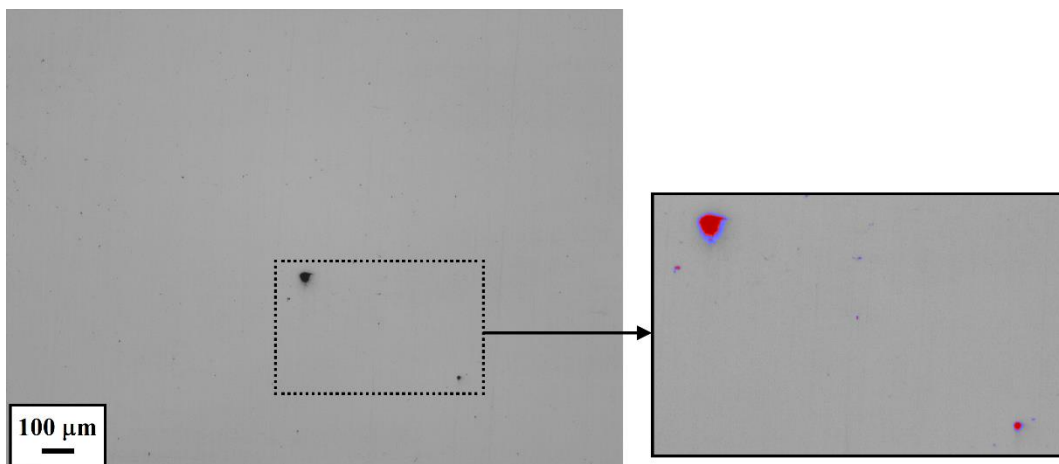


Figure 2.4. Example of porosity evaluation through image analysis of an optical micrograph. The lower and higher estimations are represented in the magnified figure by the red areas and the blue areas respectively.

The Brinell hardness was measured by performing five indentations on each sample. For the Brinell hardness measurements an EMCO TEST M4U instrument (see paragraph 2.10.1) was used.

The results of the preliminary study on the effect of the main SLM process parameters, listed at paragraph 2.3, has confirmed the EOS recommended values of P , v and hd (reported at paragraph 2.2) as suitable to obtain high densification level. Therefore, all the subsequent characterizations were performed on samples produced by adopting these parameters.

2.4 Heat treatment study

In a second stage of the research the effect of the solution annealing treatment on Inconel 718 samples was investigated. In particular, the influence of the heat treatment on the microstructure and the distribution of second phases, as well as their impact on the hardness and microhardness and oxidation resistance of the material was evaluated. Furthermore, an optimization study of the complete cycle of heat treatment, consisting of a solutioning step and a double aging step, was performed and the effect of each heat treatment step on the hardness and microhardness was assessed.

2.4.1 Solutioning

Samples obtained from a bar produced through SLM and submitted to stress relieving were used for the study of the solution heat treatment. The samples were inserted in the preheated chamber of a BICASA mod B.E. 35 muffle furnace and exposed at a temperature T_{sol} for a definite soaking period of t_{sol} . After this holding time, the samples were rapidly cooled through water quench. In order to evaluate the effect of the solutioning parameters on the microstructure, three temperature levels T_{sol} and 2 durations t_{sol} were adopted; the resulting combinations used for the microstructural study are reported in table 2.3.

Table 2.3. Set of all the recipes used for the investigation of the effect of the solution treatment on the microstructure of the SLM produced Inconel 718 alloy.

Solution treatment temperature (°C)	Solution treatment time (hours)
980	1
980	2
1065	1
1065	2
1200	1
1200	2

In addition to the standard solution temperatures, i.e. 980°C and 1065°C, the effect of a high solution temperature (1200°C) was also tested to promote an extremely high level of homogenization. Actually, this is the operability limit of the alloy as using higher solution temperature is not possible due to the risk of incipient melting.

The solution treatment was performed also on some samples as a preliminary treatment before the oxidation tests. The solution treatment performed before the short-term oxidation tests were conducted with the Bicasa muffle furnace using the parameters reported in table 2.3, but excluding the treatments at 1200°C. Some of the samples used for the study of the oxidation behavior in the middle and long term tests were previously submitted to solutioning at 1065°C for 2 hours in vacuum (10^{-2} mbar) using a TAV minijet HP oven. After the solution treatment in vacuum, the samples were quenched in nitrogen gas.

The samples used for the study of the complete cycle of heat treatment were obtained from bars produced through SLM and not stress relieved. Each heat treatment was performed by inserting the samples in the preheated chamber of a Nabertherm RHTC 80-710/15/P330 horizontal tubular programmable furnace. At the end of each heat treatment, the samples were removed from the tube and cooled in calm air. In the first step of the study, the effect of the temperature T_{sol} and the soaking time t_{sol} of solutioning on the Brinell hardness of the alloy was investigated. The parameters used for this study are reported in table 2.4.

Table 2.4. Set of all the recipes used for the investigation of the effect of the solution treatment on the Brinell hardness of SLM Inconel 178 alloy.

T_{sol} (°C)	t_{sol} (hours)
980	1
980	2
980	4
980	8
1065	1
1065	2
1065	4
1065	8

2.4.2 Study of the aging response

In order to evaluate the response of the solutioned samples to the successive heat treatments, some samples were solutioned and then analyzed through DSC and TMA techniques (see paragraph 2.8), which allow to determine the characteristic temperatures of the alloy at which the main phenomena of precipitation and dissolution of second phases occur.

On the base of the results derived by the thermal analysis, a deepening on the microstructural modifications provided to the material by progressive exposure to the characteristic temperatures was performed. The samples used in this study were submitted to a preliminary solution annealing at 1065°C for 2 hours followed by air quenching and then exposed at a definite aging temperature T_{ag} . After a first exposition period t_{ag1} , the samples were removed from the furnace and cooled in calm air. After this aging step these samples were cut and one of the two halves was exposed again at the same temperature T_{ag} for a second period t_{ag2} . At this stage, some samples were submitted to a further exposition period t_{ag3} according to the same strategy applied as before. Table 2.5 summarizes temperatures and times of the whole heat treatment runs performed for this study.

Table 2.5. Set of all the heat treatments performed for the investigation of the aging response of SLM Inconel 718 alloy previously solution annealed at 1065°C for 2 hours.

T_{ag} (°C)	t_{ag1} (hours)	t_{ag2} (hours)	t_{ag3} (hours)	$t_{tot} = t_{ag1} + t_{ag2} + t_{ag3}$
565	4	20	-	24
740	2	6	16	24
800	4	20	-	24
870	4	4	16	24

The durations of each exposition step were chosen on the base of the thermal phenomena occurring at the specific temperature studied T_{ag} . Justifications about these aspects will be given in the result and discussion section.

2.4.3 Optimization of the aging cycle

Based on the outcome of thermal analysis and the observation of the material response to the aging treatment reported above, a systematic study of the heat treatment cycle until the first aging step was carried out by investigating the following parameters:

- solution annealing temperature (T_{sol}) varied between 980°C and 1065°C
- solution annealing time (t_{sol}) varied between 1 and 2 hours
- first aging temperature (T_{ag1}) varied between 650°C and 720°C
- first aging time (t_{ag1}) varied between 4 and 8 hours

A complete 2^4 factorial design was used for this study containing all the possible combination of the above listed values of the heat treatment parameters. Furthermore, also samples submitted to direct aging from the as built condition, i.e. not submitted to preliminary solution annealing, were prepared. Table 2.6 summarizes all the 20 samples treated for this study.

Table 2.6. Set of all the heat treatments performed for the optimization study until the first aging step.

T_{sol} (°C)	t_{sol} (hours)	T_{ag1} (°C)	t_{ag1} (hours)
-	0	650	4
-	0	650	8
-	0	720	4
-	0	720	8
980	1	650	4
980	1	650	8
980	1	720	4
980	1	720	8
980	2	650	4
980	2	650	8
980	2	720	4
980	2	720	8
1065	1	650	4
1065	1	650	8
1065	1	720	4
1065	1	720	8
1065	2	650	4
1065	2	650	8
1065	2	720	4
1065	2	720	8

All the samples prepared for this optimization study were preliminary heat treated in the tubular Nabertherm furnace.

In addition to the heat treatments reported in table 2.6, the extra cycles reported in table 2.7 were also performed in order to evaluate the effects of a prolongation of the preliminary solution annealing and of an increase of the aging temperature on the determined optimal condition.

Table 2.7. Additional heat treatments performed to evaluate the effect of prolonging the solution annealing step or increasing the aging temperature.

T_{sol} (°C)	t_{sol} (hours)	T_{ag1} (°C)	t_{ag1} (hours)
980	8	720	8
1065	8	720	8
1065	2	760	8

Once the heat treatment recipe until the first aging step was frozen, the complete HT cycle optimization was concluded by adding a second aging step. Four samples, previously submitted to solution annealing at 1065°C for 2 hours and air quenched, were used for this last part of the optimization study. The samples were submitted to a double aging following the procedure described below:

- the sample is inserted in the tubular Nabertherm furnace preheated at 720°C;
- holding at temperature for 8 hours;
- furnace cooling from 720°C at the second aging temperature T_{ag2} in 2 hours;

- holding at the temperature T_{ag2} for a time t_{ag2} ;
- removal of the sample from the furnace and cooling in calm air.

Two values of T_{ag2} , 520°C and 630°C, and two durations, 4 and 8 hours, were tested. Table 2.8 summarizes the combination of parameters used for the investigation of the second aging step and the total time of aging for each sample.

Table 2.8. Set of the second aging recipes performed on samples previously submitted to solution annealing at 1065°C for 2 hours and first aging at 720°C for 8 hours. t_{tot} indicate the total duration of the aging step (including the cooling time).

T_{ag2} (°C)	t_{ag2} (hours)	t_{tot} (hours)
520	4	14
520	8	18
630	4	14
630	8	18

2.5 Oxidation tests

The oxidation behavior of SLM Inconel 718 was investigated through short, medium and long term runs at high temperature in oxidative environment.

The short term oxidation tests were performed using plate 25x25x2 mm sample with a total superficial area A between 14.75 and 15.15 cm². Some of the tested samples were previously submitted to solution annealing in the Bicasa furnace and then quenched in water. Before to start the oxidation test, the surfaces of the samples were lapped with SiC abrasive papers with progressive grade until 1200 in order to reduce the excessive roughness of the as built samples, remove the superficial oxide scale formed on the solutioned samples during the heat treatment and obtain uniform surface finishing for all the tested samples.

Short-term tests were performed at two exposition temperatures, T_{ox} , of 850°C and 900°C, respectively. In both the tests, 5 plate like samples were used: one sample was tested in the as built metallurgical state, the others were previously solutioned at 980°C for 1 and 2 hours and at 1065°C for 1 and 2 hours, respectively. The samples were previously weighed using a precision balance with guaranteed resolution of 0.1 mg and then submitted to cyclic oxidation. After each thermal cycle, the mass variation of all the samples was recorded. Each thermal cycle was performed by inserting the samples together in the preheated chamber of the Bicasa furnace and leaving them exposed to the temperature T_{ox} in simple air for a definite time, then the samples were removed and cooled in calm air. The durations of all the performed oxidation cycles of the short-term tests are summarized in table 2.9.

Table 2.9. Durations (t_{cycle}) of the cycles performed during the short term oxidation tests and total oxidation time (t_{ox}) after each thermal cycle.

n. cycle	1	2	3	4	5	6	7	8	9	10	11	12	13	14
t_{cycle} (hours)	0.5	0.5	0.5	0.5	1	1	1	1	2	2	6	8	16	16
t_{ox} (hours)	0.5	1	1.5	2	3	4	5	6	8	10	16	24	40	56

The middle-term oxidation test was performed at 850°C in simple air for a total exposition time of 215 hours using samples cut from SLM specimens. During this test the effect of the following two factors on the oxide growth rate were investigated:

- the oxidation mode, i.e. isothermal and oxidation via thermal cycling;
- the atmosphere used during the preventive solutioning heat treatment, in particular the difference that arises by performing solutioning in air or in vacuum (10^{-2} mbar).

Actually, a negligible superficial oxide scale is formed during solution annealing in vacuum due to the low oxygen partial pressure. However, a darkening of the surface of the Inconel 718 samples was observed after thermal exposure in vacuum because of the formation of a very thin superficial layer. This phenomenon is already reported by other authors [190] [191] and it is explained as the result of the oxidation of the niobium segregated at the surface. This thin Nb-rich layer can play a role in the growth of the passivating oxide scale during the following thermal exposure. In order to evaluate this effect, a direct comparison between the growth rate of samples pre-treated respectively in air and in vacuum was performed during the middle term oxidation test.

A total of 14 samples were used with a superficial area that falls between 2.97 and 3.90 cm². They were oxidized under the conditions reported below and summarized in table 2.10:

- 1 reference sample wasn't submitted to heat treatment and was oxidized in isothermal condition;
- 1 reference sample wasn't submitted to heat treatment and was oxidized via thermal cycling;
- 3 samples were submitted to a preventive solubilization treatment at 1065 °C for 2 hours in air atmosphere, then quenched in water and post oxidized in isothermal condition;
- 3 samples were submitted to a preventive solubilization treatment at 1065 °C for 2 hours in air atmosphere, then quenched in water and post oxidized via thermal cycling;
- 3 samples were submitted to a preventive solutioning treatment at 1065 °C for 2 hours in vacuum, then quenched in nitrogen gas and post oxidized in isothermal condition;

- 3 samples were submitted to a preventive solutioning treatment at 1065 °C for 2 hours in vacuum, then quenched in nitrogen gas and post oxidized via thermal cycles.

Table 2.10. Set of the samples used during the middle term oxidation test with the atmosphere of the preliminary solution annealing at 1065°C for 2 hours (air or vacuum) and the oxidation mode (isothermal or cycled oxidation).

		Oxidation mode	
		<i>Isothermal oxidation</i>	<i>Cycled oxidation</i>
Preliminary solution annealing	<i>Not solubilized</i>	1 sample	1 sample
	<i>Solutioned in air</i>	3 samples	3 samples
	<i>Solutioned in vacuum</i>	3 samples	3 samples

The samples subjected to solutioning treatment in vacuum were previously lapped with SiC abrasive paper until 1200 grid and no further surface preparation was done after the heat treatment. On the contrary, the samples subjected to solubilization treatment in air were lapped after the quench to remove the oxide scale formed during the heat treatment. All the samples were finally cleaned and weighted before to start the oxidation test. The thermal cycled samples were subjected to a total of 6 cycles: each of the first four cycles had a duration of 23 hours, the fifth cycle has lasted 70 hours, the last cycle was of 53 hours. The mass variation per unit of exposed area was recorded after each cycle. The samples submitted to isothermal oxidation were exposed in the furnace for a total time of 215 hours without interruptions.

The long-term oxidation test was performed on nine Inconel 718 samples obtained from a bar produced through SLM and with an area falling between 3.7 and 4.4 cm². These samples were exposed to the temperature of 850°C in air for different times of isothermal oxidation. The SLM Inconel 718 samples were previously solution treated at 1065°C for 2 hours in vacuum (10⁻² mbar) and then cooled in nitrogen gas. Then, the samples were lapped with SiC abrasive papers with progressive grade until 1200 to remove the oxide scale and obtain the same superficial finish of the samples used for the previous tests. For comparison, also twelve samples of Inconel 600, with an area falling between 4.4 and 5 cm², were exposed to oxidizing environmental test together with Inconel 718 ones. All the samples were heated to 850°C and isothermally oxidized at this temperature, then at fixed steps an Inconel 718 sample and an Inconel 600 one were removed at the same time from the furnace chamber. After each predetermined time, samples were cooled in air and then weighted to annotate the mass variation after the oxidation period. After 351 hours, the remaining samples (2 of Inconel 718 and 5 of Inconel 600, were all removed at the same time and cooled). After collecting the mass gain of all the samples submitted to isothermal oxidation and fitting the obtained data

with a parabolic curve, a second oxidation run was performed: the samples exposed for the complete period of 351 hours during the first run were heated again at 850°C. The second oxidation run was done in order to confirm that the parabolic trend determined during the first run can be extrapolated for longer oxidation time. The last samples (one of Inconel 718 and one of Inconel 600) were removed after 557 hours from the beginning of the second run, therefore these samples were submitted to a total oxidation time of 908 hours. The oxide scale formed on the tested samples were examined in cross section at the optical and electronic microscopes to determine its thickness, morphology and structure. The chemical composition of the oxide scale was also evaluated through EDS analysis.

2.6 Pack aluminization tests

The aluminization tests were performed on samples obtained from a bar produced through SLM with the optimized parameters and then submitted to stress relieving at 450°C for 2 hours before detaching from the support plate. The generic aluminization process consists in embedding the sample to be coated in a powder mixture, containing an aluminum source, an activator and an inert component, and then performing an appropriate heat treatment. The powders used for the aluminization mixtures are:

- Alfa Aesar Aluminum powder, -325 mesh, chemical composition given in table 2.11;
- Sigma-Aldrich Ammonium Chloride (NH₄Cl), 99.99%;
- Alfa Aesar Aluminum Oxide powder (Al₂O₃), 99%, 32-63 Micron APS Powder, S.A. 200 m²/g.

Table 2.11. Nominal composition (%) of the aluminum powder used in this study. Provided by Alfa Aesar: [192].

Al	Fe	Si	Cu	Mn	Cr	Ni	Zn	Ti	Ga
99.78	0.11	0.04	0.01	< 0.01	< 0.01	< 0.01	< 0.01	0.02	0.01

The general procedure for the pack aluminization tests followed in this study is reported below. The mixtures of powder are prepared by adding at the Al₂O₃ inert a definite amount of Al and of NH₄Cl activator salt powder, measured through a balance with a resolution of 1 mg. Once prepared, the powder packs were inserted in ceramic crucibles and a sample was completely embedded in the powder in each of them. All the surfaces of the samples were preliminary polished with SiC abrasive paper until 1200 grade in order to remove the roughness arising from SLM process and to obtain the same surface finishing. The crucibles with samples embedded in powder packs were submitted to a series of degassing cycles in a glove box. At each degassing cycle, vacuum is made in the glove box and then flushing with nitrogen gas is applied. After degassing cycles, the crucibles were placed in a stainless steel foil bag (Nabertherm). The folding and consequent plastic deformation of the edges of the stainless steel foil bag guarantees its hermetic closure. The use of stainless steel foil bag is twofold: it avoids direct exposure of

the packs to the air during the heat treatment and it prevents the aluminizing vapors produced during the process to diffuse in the furnace chamber, thus avoiding damages at the electrical resistors and the refractory walls. The heat treatment consists of a heating step at ca. 7-8 °C/min up to the process temperature, followed by a holding step for a predetermined period of time. Finally, the cooling step at room temperature is carried out inside the furnace chamber at about 2-3 °C/min. After the heat treatment, the powder of the pack becomes lumpy and agglomerated, therefore the flowability of the powder mixture is drastically reduced. The samples were weighted with a precision balance with a resolution of 0.1 µg before and after the aluminization tests in order to evaluate the mass gain during the coating process.

A first pack aluminization test was carried out at 900 °C for 5 hours in order to study the influence of the amount of Al and activator in the pack. The mass compositions of the trial packs used in this test, that will be referred in the follows as the “intermediate temperature test”, are reported in table 2.12.

Table 2.12. Set of the pack compositions used for the aluminizing test performed at 900 °C for 5 hours.

Samples	Pack composition (wt. %)	Al source/activator ratio
A1	10% Al, 5% NH ₄ Cl, 85% Al ₂ O ₃	2
A2	15% Al, 5% NH ₄ Cl, 80% Al ₂ O ₃	3
A3	10% Al, 10% NH ₄ Cl, 80% Al ₂ O ₃	1
A4	15% Al, 10% NH ₄ Cl, 75% Al ₂ O ₃	1.5

The morphology and structure of the coatings produced in the intermediate temperature test were investigated in cross section view using optical microscopy, SEM and FESEM. Chemical analysis of the layer constituents was performed through EDS. Standard polishing procedure using SiC abrasive paper and diamond paste until 1 µm was followed to prepare the samples for the microscopy analysis.

A possible modification of the procedure consists in placing the sample over the pack instead of putting it embedded in the powder mixture [109]. This is referred as over-pack aluminizing mode. In order to evaluate the results that can be achieved in such over-pack mode, an aluminizing test was performed by adopting the same heat treatment parameter, i.e. at 900°C for 5 hours, and using two short bars (about 30.7 mm in length) as substrates. The bars were immersed only half in the powder mixtures leaving the other half in over-pack condition. The composition of the powder packs used to coat the bars are reported in table 2.13.

Table 2.13. Set of the pack compositions used for the aluminization of the bars half embedded in the powder mixture.

Samples	Pack composition (wt. %)	Al source/activator ratio
B1	15% Al, 3% NH ₄ Cl, 85% Al ₂ O ₃	5
B2	15% Al, 7% NH ₄ Cl, 80% Al ₂ O ₃	~ 2

After the aluminization process, the structure of the coatings was observed via optical microscope in the different zones of the bars, i.e. on the embedded part, near the pack surface and far from the pack surface.

Two further aluminization test types were carried out in different temperature regimes. In the following, these tests will be referred as the “high temperature test”, performed at 1065°C for 2 hours, and the “low temperature test”, performed at 800°C for 5 hours. The compositions of the powder pack sets used in high and low temperature tests are reported in table 2.14 and 2.15, respectively. In both the tests, the samples were totally embedded in the powder packs.

Table 2.14. Set of the pack compositions used for the aluminizing test performed at 1065 °C for 2 hours.

Samples	Pack composition (wt. %)	Al source/activator ratio
H1	9% Al, 3.0% NH ₄ Cl, 88.0% Al ₂ O ₃	3
H2	9% Al, 4.5% NH ₄ Cl, 86.5% Al ₂ O ₃	2
H3	15% Al, 5.0% NH ₄ Cl, 80.0% Al ₂ O ₃	3
H4	15% Al, 7.5% NH ₄ Cl, 77.5% Al ₂ O ₃	2

Table 2.15. Set of the pack compositions used for the aluminizing test performed at 800 °C for 5 hours.

Samples	Pack composition (wt. %)	Al source/activator ratio
L1	15% Al, 3.75% NH ₄ Cl, 81.25% Al ₂ O ₃	4
L2	15% Al, 5.00% NH ₄ Cl, 80.00% Al ₂ O ₃	3
L3	20% Al, 5.00% NH ₄ Cl, 75.00% Al ₂ O ₃	4
L4	20% Al, 6.67% NH ₄ Cl, 73.33% Al ₂ O ₃	3

The developed coatings were studied in terms of microstructure and stability, so as to identify the optimal aluminization recipe. Once the optimized recipe was defined, the possibility to apply the pack aluminization technique for the coating of hard accessible surfaces was evaluated. In particular, the possibility to coat internal surfaces of narrow channels for heat exchanger application was investigated. To this purpose, modules with channels of triangular section produced via SLM were used. The geometry and size of the channels are shown in figure 2.5.

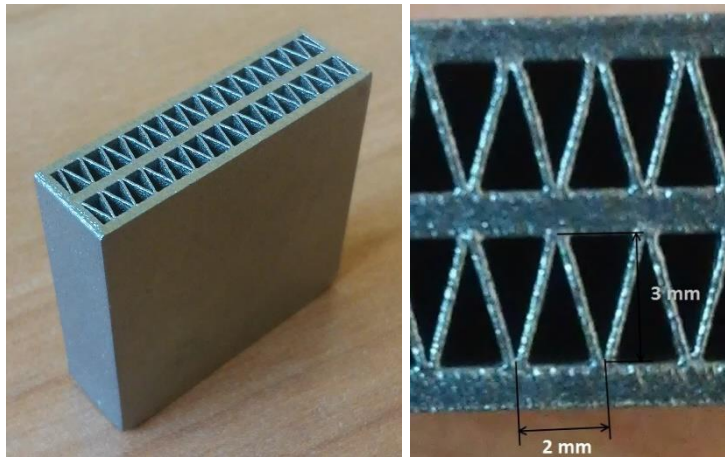


Figure 2.5. Module with internal channels of triangular section produced by SLM.

The same procedure as described above was used for the aluminization of these modules. The external surfaces of the modules were lapped with SiC abrasive paper until the 1200 grade, instead the as built surface finishing of the internal surfaces of the channel was not altered. The composition of the packs used for the aluminization of the modules is the same used for sample A2 in table 2.12 (15% Al, 5% NH_4Cl , 80% Al_2O_3), on which the best coating quality was observed as discussed at paragraph 6.1. Modules were embedded in the pack with their channels placed in vertical position. Also, the channels were filled with the powder mixture. The aluminization process was carried out at 900°C for 5 hours. As a consequence of the loss in flowability of the powder pack, after the aluminization process, some difficulty was encountered for the complete removal of powders from the channels. Actually, mechanical coupling can form between the compacted powders and the superficial asperities of the rough internal surfaces of the channels.

The cross section of the coatings formed on both the external and the internal surfaces of the modules were examined via optical microscope along the cut lines shown in figure 2.6.

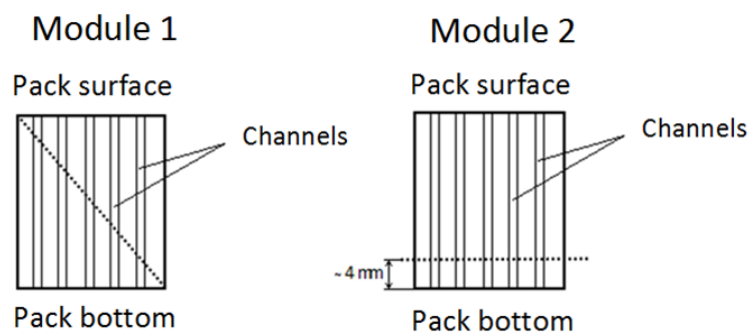


Figure 2.6. Scheme of the cuts performed on the aluminized modules for the cross section examination.

The diagonal cut on module n.1 allows to evaluate the variation of the microstructural features of the coating moving from the bottom part of the module towards the top part of it, being such locations respectively representative of the deepest embedded portion and the shallowest one within the pack.

The bottom of module n.2, shown in figure 2.6, was used to perform a cyclic oxidation test with the aim to evaluate the stability of the obtained coating in oxidizing environment and the consequent level of protection that it can guarantee. The modification of the aluminide coating after each thermal cycle were observed with the optical microscope. The thermal cycles were performed by inserting the sample in the muffle furnace chamber preheated at 850°C and leaving it exposed in simple air. At the end of every thermal cycle, the sample was removed from the furnace and cooled in calm air, then the cross section was polished so as to perform the optical microscope examination. A total of 5 thermal cycles were carried out on the aluminized piece, whose duration was of 1, 2, 4, 6 and 15 hours, respectively.

The graph in figure 2.7 summarizes all the thermal histories investigated in this thesis and described in the previous paragraphs, including all the heat treatment cycles and the oxidation and aluminization tests.

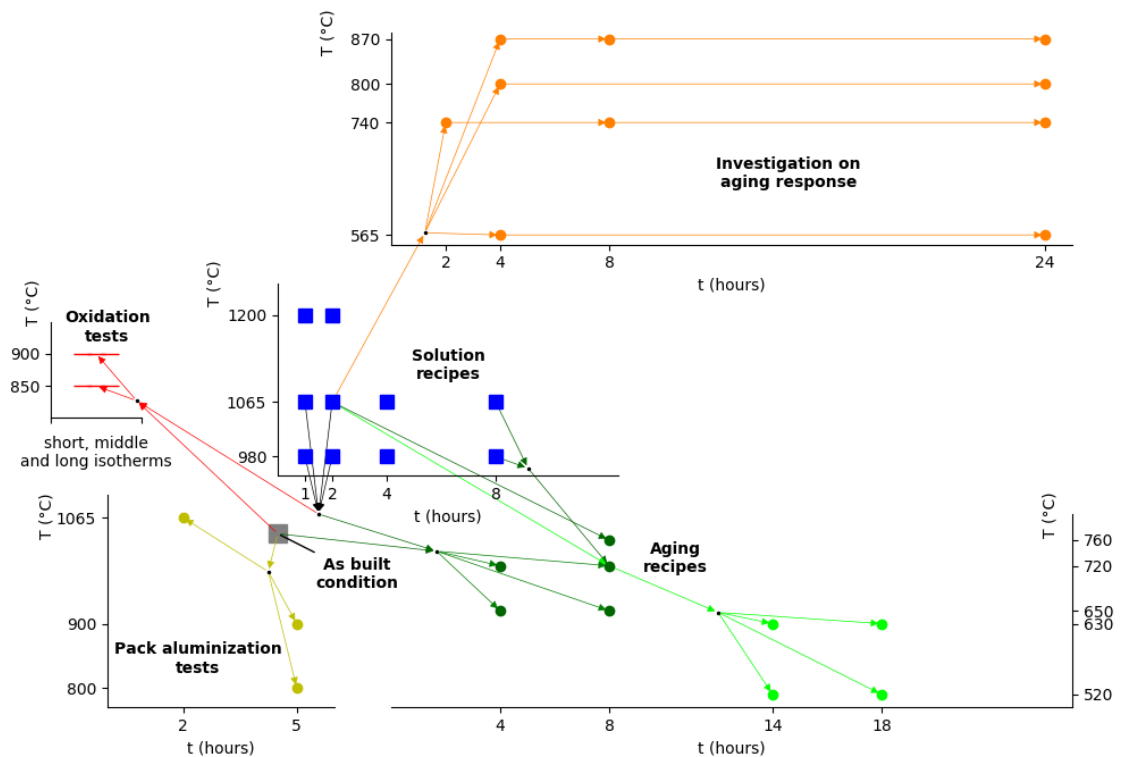


Figure 2.7. Summary diagram collecting all the thermal histories of the SLM Inconel 718 samples which characterization is reported in this thesis. Starting from a square, representing the as built (gray) or a solution annealing condition (blue), each subsequent step of a thermal history can be reached by following the arrows. Green points represent the first (dark green) and second (light green) aging treatments; orange points represent the thermal treatments performed to investigate the aging response; red bars represent all the short, middle and long oxidation isotherms; yellow points represent the pack aluminization treatments. T: treatment temperature; t: treatment time.

2.7 Microscopy

2.7.1 Metallographic preparation

The samples analyzed through optical and electronic microscopy were submitted to the standard metallographic preparation steps: cutting, eventual mounting in resin, grinding, polishing and etching.

The cutting step is necessary to expose the representative metallographic surface and it must be performed avoiding damages of the surface and alterations of the samples caused by the developed heat. A precision linear cutting machine was used to perform the cuts with abrasive aluminum oxide blades or diamond blades. The surfaces exposed by cutting the sample transversally respect to its building direction will be referred in the following as “horizontal planes”, instead the surfaces obtained with a cut path parallel to the building direction will be referred as “vertical planes”.

Some samples were cold mounted in bi-component acrylic resin or hot mounted in conductive epoxydic resin to make them easier to handle or to avoid introducing damages during the successive preparation steps. During the grinding stage, the surface of the sample was lapped through successive steps using SiC abrasive papers progressively finer up to 2400-2500 grade. At each step the scratches produced during the previous step are removed. Then, the sample is submitted to polishing using short napped polishing cloths and diamond pastes with a decreasing granulometry down to 1 μm . Eventually, 0.3 μm alfa alumina and 0.05 μm gamma alumina suspensions were also used to further improve the surface finish when required.

Two different etching procedures were performed on the as built samples to reveal the microstructure: chemical etching with waterless Kalling's n.2 solution and electrochemical etching in a solution of 100 ml HNO_3 and 10 ml water. The chemical etching was done by soaking or swabbing the metallographic surface for 30-60 seconds at room temperature. The electrochemical etching was performed on samples previously mounted in a cylinder of conductive resin in which a screw that act as electrode was inserted. During the electrochemical etching, the sample is immersed in the acid solution and a voltage of 1-2 V is applied for few seconds. In both the procedures, the etching is interrupted by immersing the sample in fresh water for about 5 seconds, then the metallographic surface is carefully cleaned with ethanol o other alcohol based solvent and dried with a flow of warm air.

2.7.2 Optical microscopy

A Leica DMI 5000 M optical microscope, equipped with a digital camera for the acquisition of the images, was used. The optical microscope was widely used in each part of this study and, in particular, it allowed to evaluate:

- shape and microstructure of the starting powders (paragraph 2.1);

- the porosity of the as built samples obtained at different SLM process parameters (paragraph 2.3);
- the microstructure and the second phases of samples produced through SLM process at the as built state and after different solution treatment (paragraph 2.4.1) on horizontal and vertical planes;
- the thickness and morphology of the thermally grown oxides formed during the oxidation tests (paragraph 2.5);
- the features of the coating obtained with the pack aluminization tests (paragraph 2.6).

2.7.3 SEM - scanning electron microscope

A Leo1450 thermo-ionic scanning electronic microscope (SEM) was used during this study. For finer morphological analysis Field Emission Scanning Electronic Microscopes (FESEM) were used when higher resolution micrographs at high magnification were required: Merlin Zeiss, Zeiss SupraTM 40, Carl Zeiss ULTRA.

Secondary electrons probe was used for the microstructural study of the as built samples and of the heat-treated ones, previously prepared according to the general procedure described at paragraph 2.7.1 and etched with waterless Kalling's n.2 solution. The secondary electrons are emitted due to inelastic scattering between the primary beam and the valence electrons of the specimen atoms. These electrons have an energy lower than 50 keV, therefore only the ones generated in the more superficial layers can escape from the material and be detected. This allows to obtain micrographs with high depth of field and detailed topological information on the examined surface. In the images constructed using the secondary electrons signal, the surface that are tilted with respect to the primary beam appear in bright contrast due to the edge effect (figure 2.8).

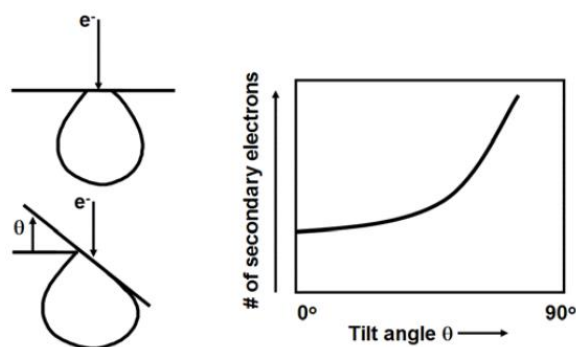


Figure 2.8. Representation of the edge effect and secondary electrons yield in function of the tilt angle of the specimen surface. From: [193].

Secondary electrons (SE) micrographs were collected with the FESEM to evaluate the mean volume fraction of second phases in the alloy in the as built state and after the solution treatments reported in table 2.3. To collect these images the voltage was set to 5 kV, the aperture size to 30 μm and the working distance to 6 mm. The volume fraction of the observed second phases was estimated by

computing the ratio between the area occupied by them and the total image area. The implicit assumption made for this analysis is that the collected data of area fractions are valid estimators of the volume fractions of the detected precipitates in the samples. In particular, 6 SE-FESEM micrographs were collected at different magnifications on the as built samples: two of them have length scale 14.7 nm/pixel and cover an area of 152.1 μm^2 each, other two have length scale 4.9 nm/pixel and cover an area of 16.7 μm^2 each; finally the remaining two have length scale 2.4 nm/pixel and cover an area of 4.2 μm^2 each. Therefore, the total extension of the examined surface on the as built sample is equal to 346 μm^2 . On each solutioned sample, 5 SE-FESEM images with length scale 14.7 nm/pixel covering 152.1 μm^2 each and 5 images with length scale 4.9 nm/pixel covering 16.7 μm^2 each were collected. Therefore, an overall area of 844 μm^2 was examined for each solutioning condition. The image analysis of the collected micrographs also allowed to obtain the size distributions of the detected precipitates on the solutioned samples. Some specific MATLAB routines were used for this analysis, which allows to identify and tag the objects detected in an image on the base of the contrast levels. All the detected precipitates were sub-divided in size classes and the volume fractions of the precipitates in each size class was calculated. The partition in size classes is carried out based on the linear size \mathcal{L} of each precipitate:

$$\mathcal{L} [\text{nm}] = \sqrt{(S [\text{nm}/\text{pixel}])^2 \cdot \mathcal{P}} \quad \text{eq. 2.2}$$

where \mathcal{P} is the number of pixels of the image occupied by the precipitate and S is the length scale of the analyzed image, whose value for all the used images has been reported above. An example of image analysis of a FESEM micrograph acquired on the sample solutioned at 1065°C for 2 hours with the relative obtained size distribution is shown in figure 2.9.

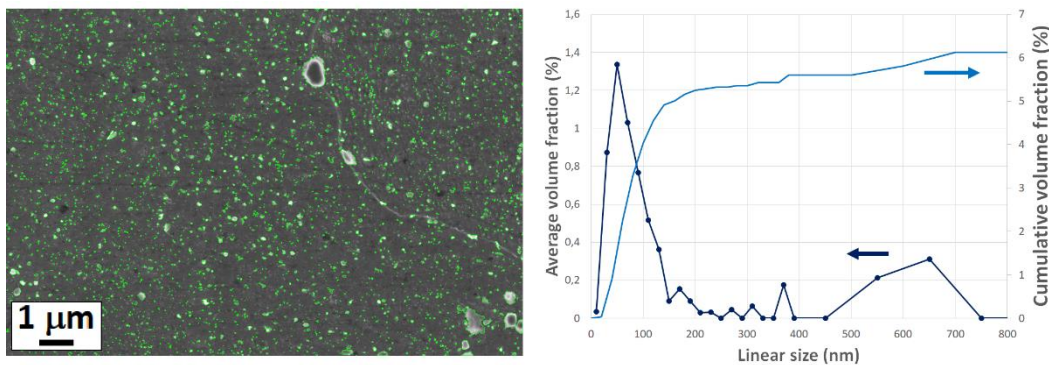


Figure 2.9. Example of image analysis of a FESEM micrograph collected on the sample solutioned at 1065°C for 2 hours and the derived size distribution with average volume fractions and cumulative volume fractions of the precipitates. First published in [194].

The electronic microscope was also used for the cross section examination of the microstructure of the oxide scale thermally grown on the samples submitted to oxidation tests (paragraph 2.5) and of the coatings obtained in the aluminization

tests (paragraph 2.6). During the metallographic preparation, these samples were cold mounted in acrylic resin in order to avoid damaging the superficial scale or coating during the polishing steps. No etching was performed on these samples after polishing. The observation in cross section of the oxide scales and the aluminized coatings were performed using backscattered electrons mode. The backscattered electrons are electrons of the primary beam that are reflected by elastic scattering with the specimen atoms and have a higher energy than the secondary electrons, therefore the information carried by them comes from a deeper region. The backscattered electrons emission is highly sensitive to the atomic number of the constituent atoms of the specimen, therefore they provide compositional information: the zones where lighter elements are present appear in darker contrast in the images obtained with backscattered electrons (figure 2.10).

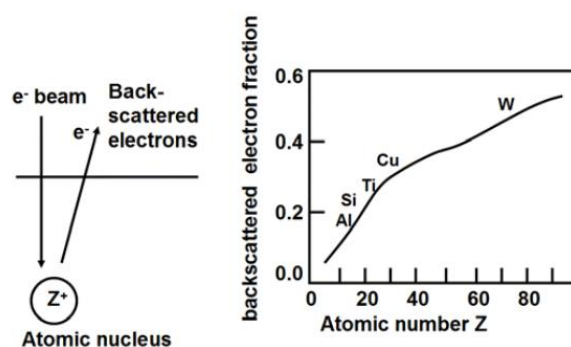


Figure 2.10. Backscattered electron fraction in function of the atomic number Z on the spot illuminated by the primary beam. From: [193].

Energy Dispersive Spectroscopy (EDS) was also used to obtain information on the chemical composition of the oxide scales and the aluminide coatings. The percentage quantities of the elements got with EDS analysis are not very accurate because of the physical limit of the technique, therefore they should be used with care. However, even if EDS analysis cannot provide the exact chemical composition, it can be effectively used to make qualitative and semi-quantitative comparisons between different areas. On the other hand, EDS technique was found to be unsuitable for investigating the microsegregation of the chemical elements at the very fine dendrite scale and the chemical composition of the small precipitates (lower than $1\ \mu\text{m}$) present in the as built and heat treated samples. This limit is caused by the volume of interaction between the electron beam and the analyzed sample, which depends mainly on the imposed voltage and the density of the material. This interaction volume is too large to guarantee the resolution that would be needed. Figure 2.11 shows that the interaction volume on nickel alloy (density of about $8.2\ \text{g/cm}^3$) using a voltage of between 15 and 20 kV, necessary to obtain an adequate signal. One can note that this is included between 0.8 and $2\ \mu\text{m}$, that is to say a size comparable with the length scale of the dendrites and higher than most of the present precipitates.

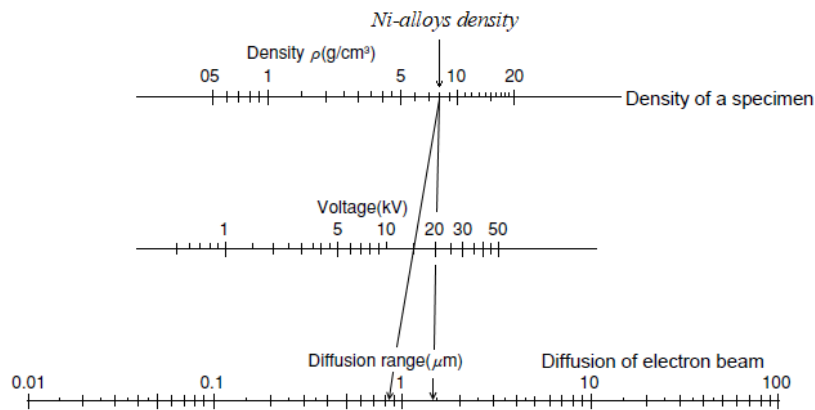


Figure 2.11. Nomogram for evaluate the diffusion range of the electron in the Scanning Electron Microscopy in function of the specimen density and the used voltage. Adapted from: [195].

2.7.4 EBSD analysis

The characterization through Electron BackScattered Diffraction (EBSD) using a Zeiss Supra 40 system equipped with a Bruker detector was performed both on the horizontal and the vertical planes on the as built material produced adopting the optimized SLM parameters in order to investigate the crystallographic texture arising from the SLM process. The EBSD analysis is based on the Bragg diffraction of the backscattered electrons coming from the surface of the specimen and allows to determine the local crystallographic orientation on each zone of the surface. The samples characterized through EBSD analysis were hot mounted in conductive resin and submitted to the polishing procedure described at paragraph 2.7.1. The durations of the final polishing steps must be longer with respect to the normal preparation because EBSD technique requires a very high surface finish [196] [197]. In particular, the samples were polished with 0.3 μm alfa alumina suspension for 15 minutes and with 0.05 μm gamma alumina suspension for about 2 hours in total. Just before the analysis, the samples were further polished for 20-40 minutes with the 0.05 μm gamma alumina suspension in order to remove any eventual thin oxide scale on the surface. After the polishing steps, the surfaces of the samples were carefully cleaned with isopropyl alcohol and a delicate cloth.

Before the EBSD analysis, the so called argus image [198] is acquired using the forescattered and backscattered electrons. The argus image already provides a coarse crystallographic information and it can be obtained rapidly allowing the user to explore the surface of the sample in order to find and select the area of interest on which perform the actual EBSD analysis. Then, the selected area is sub-divided in a square grid of points and each of them is illuminated with the electronic beam for a certain exposure time during which the screen detects the Kikuchi diffraction bands generated by the interaction between the beam and the crystal. The information contained in the Kikuchi bands is automatically elaborated by the software to obtain the crystallographic orientation of each analyzed point. The crystallographic orientation of the crystal with respect to the sample coordinate system is given through the three Euler angles φ , θ , ψ (see figure 2.12).

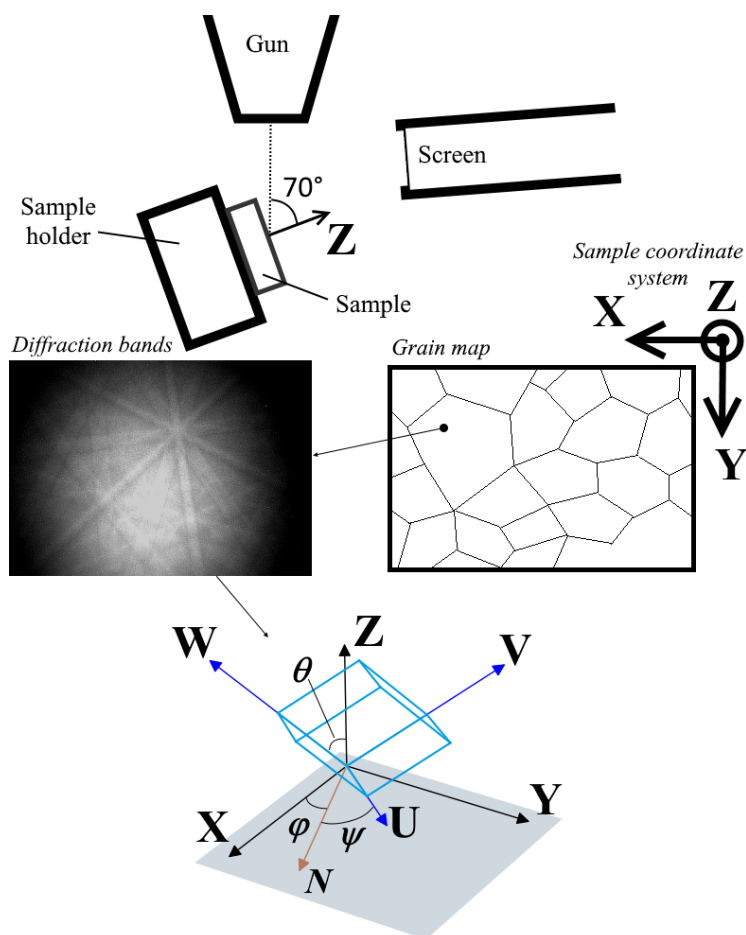


Figure 2.12. Scheme of the EBSD set up and an example of the Kikuchi diffraction bands, detected on a single spot on the examined surface, which allow to obtain the orientation of the local UVW coordinate system respect to the XYZ sample coordinate system in term of the Euler angles φ , θ , ψ .

In the current study, the EBSD characterization was performed imposing a voltage of 20 kV and an exposition time of 150 ms or 200 ms. The sample was placed at an angle of 70° with respect to the electronic beam and at a distance with the detector of about 30 mm. The tilt angle of the detector was regulated before each analysis in order to obtain the best quality of the signal. On the sample cut along a horizontal plane, the building direction is parallel to the Z axis of the sample coordinate system, i.e. it is normal to the analyzed surface. Instead, the sample cut along the vertical plane was oriented in the SEM chamber in such a way to put its building direction parallel to the Y axis of the sample coordinate system. On the horizontal plane, an area of $215 \times 170 \mu\text{m}$ was analyzed imposing a step size between the points of the grid of $1.41 \mu\text{m}$ and a detector tilt angle of 4.52° . A further smaller area of $30 \times 25 \mu\text{m}$ was acquired with higher resolution using a step size of $0.35 \mu\text{m}$ and a detector tilt angle of 4.77° . Instead, on the vertical plane, an area of $150 \times 190 \mu\text{m}$ was analyzed with a step size of $1.41 \mu\text{m}$ and a detector tilt angle of 4.52° and a further area of $60 \times 90 \mu\text{m}$ at higher resolution with a step size of $0.7 \mu\text{m}$ and a detector tilt angle of 3.77° was also acquired.

After the data acquisition step, it is possible to compute the grains present in the analyzed area and the relative grain boundaries positions through a post-processing algorithm of the data. This was done by calculating, for each point, the highest mis-orientation θ_{mis} with respect to the 8 neighbor points. A grain boundary is present between two spots if their mis-orientation is equal or higher than a previously chosen threshold value θ_{th} , usually set to 10° (see figure 2.13) This procedure allows to assign a crystalline grain at each spot, therefore it is possible to determine the number of present grains, their shape and size after the data elaboration step.

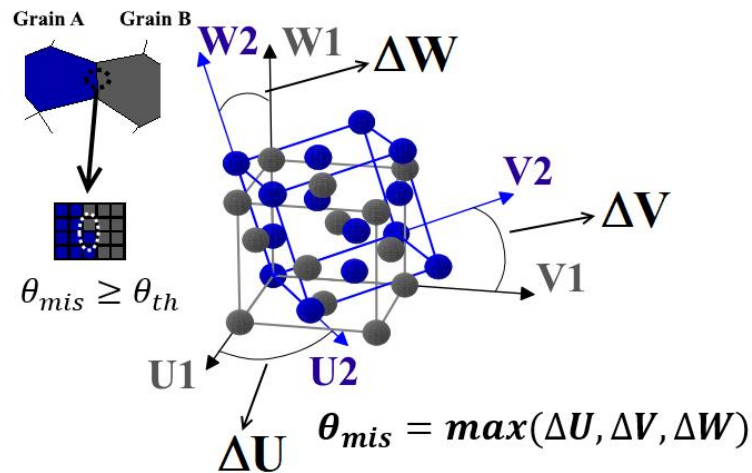


Figure 2.13. Scheme explaining the criterion used to establish the position of the grain boundaries.

A grain boundary is present between two spots when their highest mis-orientation θ_{mis} between them is higher than a threshold value θ_{th} .

The crystallographic texture, i.e. the tendency of the grains of the sample to have a favored orientation rather than to be randomly oriented, can be graphically represented using the pole figures (PF) and the Inverse Pole Figures (IPF). Both the representations allow to visualize a crystallographic direction in the 3D space on a 2D plane through the stereographic projection. Each half line r , that starts from the origin O of the coordinate system, is associated to a point Pr through stereographic projection (see figure 2.14): Pr is the point in which the segment s , that joins the intersection point P between r and the unit sphere S with the south pole of S , intersects the equatorial plane of S . If the direction of r is represented by the unit vector (u, v, w) , then the coordinates of point Pr can be obtained by:

$$x_{Pr} = \frac{u}{w+1}, y_{Pr} = \frac{v}{w+1} \text{ and } z_{Pr} = 0.$$

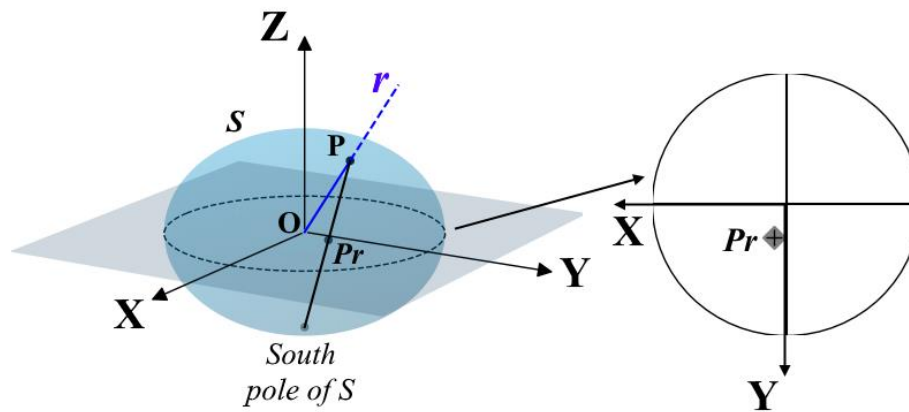


Figure 2.14. Stereographic projection of a direction r in the 3D space on the 2D unitary circle.

A pole figure (PF) is obtained by adopting the sample coordinates system and representing, inside the unit circle, the average orientation of a certain family of crystallographic planes through stereographic projection (see figure 2.15). Each grain detected during the EBSD analysis is associated to a point in the PF. A not uniform distribution of the points indicates a crystallographic texture.

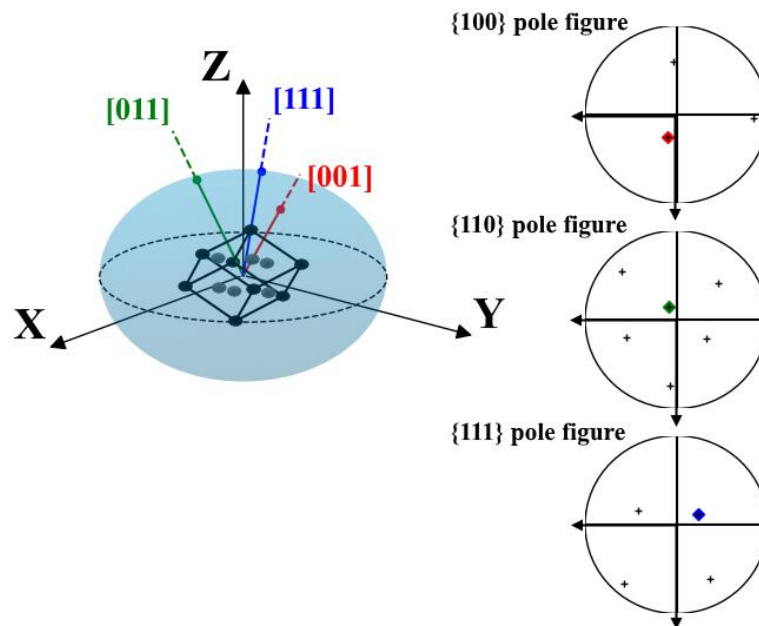


Figure 2.15. Representation of the $\{100\}$, $\{110\}$ and $\{111\}$ crystallographic directions through pole figures.

On the contrary, an inverse Pole Figure (IPF) is obtained by adopting the sample coordinate system of the crystallographic cell and consequentially rotating the axes of the sample coordinate system. After that, the stereographic projection of one of the X, Y or Z axes of the sample coordinate system obtained (see figure 2.16). This procedure is repeated for each spot on the analyzed surface. Because of the symmetries of the cubic cell, the unit circle can be subdivided in equivalent

areas and all the stereographically projected directions can be represented inside the so called standard triangle (see figure 2.16). This representation allows to visualize the overall orientation of the crystallographic directions in the analyzed area with respect to the axes of the sample coordinate system.

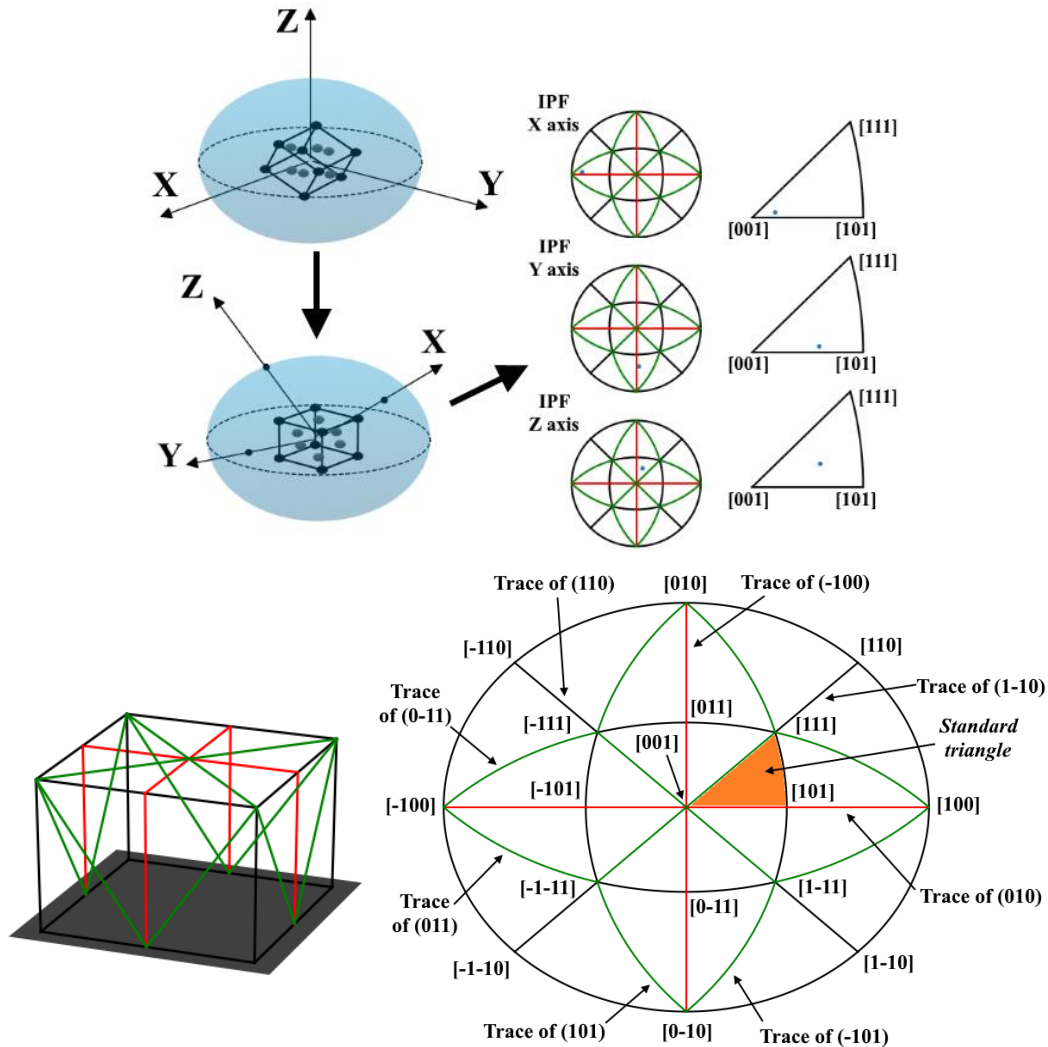


Figure 2.16. Representation of the orientation of the lattice cell through inverse pole figures.

The IPF can be used also to directly show the crystallographic orientation of each grain through the colored IPF maps, in which each analyzed spot is colored on the base of its position in the standard triangle. Examples of IPF maps from the literature are reported in the previously shown figure 1.42.

2.7.5 TEM microscopy and SAED analysis

A FEI Titan scanning/transmission electron microscope (STEM) equipped with energy dispersive X-ray spectrometry (EDS) detector was used to observe the microstructure of the as built material, produced with the optimized parameters, at the length scale of the single dendrite. The Transmission Electron Microscope allows to obtain high resolution images and higher magnification through the

detection of the electrons of the primary beam that cross the sample, that must have a very low thickness. For the preparation of the sample before the STEM observation, a thin lamella of material was prepared using a Carl Zeiss Auriga focused ion beam (FIB) system. The lamella was obtained along a vertical plane of the as built sample, therefore the building direction lays on the plane of the analyzed material.

The transmission electron configuration allows also to perform EDS analysis going beyond the limits, discussed at paragraph 2.7.3, of the technique in the SEM systems and obtaining a close to atomic resolution. However, even in this configuration the EDS analysis can be used only as a semi-quantitative characterization. The EDS technique was used in this study to verify the micro-segregation of each of the main alloying element at the length scale of the single dendrite and to obtain information on the nature of the present inter-dendritic second phases.

The detection of the diffracted beam from the lamella allows also to obtain crystallographic information through the Selected Area Electron Diffraction (SAED) patterns. Each spot in a SAED pattern represents a set of parallel crystallographic planes for which the constructive interference conditions are satisfied allowing the detection of the diffracted beam. The revealed spots depend on the orientation of the crystal with respect to the electronic beam, which determines the establishment of specific diffraction conditions. The SAED patterns reveal the symmetries present in the periodic crystalline structure of the analyzed material, therefore they give indications for the identification of the present phases.

The reciprocal lattice and the Ewald sphere are useful constructions that allow to visualize the angles at which the Laue condition of constructive interference is satisfied.

The reciprocal lattice is defined as the set of vectors \mathbf{R} that satisfied equation 2.3:

$$e^{2\pi i \mathbf{U} \cdot \mathbf{R}} = 1 \quad \text{eq. 2.3}$$

for each vector $\mathbf{U} = u\mathbf{u}_1 + v\mathbf{u}_2 + w\mathbf{u}_3$ of the direct lattice, i.e. the crystalline structure of the irradiated material. Equation 2.3 is satisfied when $\mathbf{U} \cdot \mathbf{R} = N$, where N is an integer. Each reciprocal vector \mathbf{R} can be expressed as equation 2.4:

$$\mathbf{R} = h\mathbf{r}_1 + k\mathbf{r}_2 + l\mathbf{r}_3 \quad \text{eq. 2.4}$$

where h , k and l are integers that correspond to the Miller indices of the set of parallel crystallographic plane in the direct space associated with \mathbf{R} ; the length of \mathbf{R} is equal to $1/d_{\{hkl\}}$, where $d_{\{hkl\}}$ is the interplanar distance of the $\{hkl\}$ planes. The Laue condition states that the scattering vector $\Delta\mathbf{k} = \mathbf{k}_d - \mathbf{k}_i$, where \mathbf{k}_i and \mathbf{k}_d are the wavevectors of the incident and the diffracted beams respectively, belongs to the reciprocal lattice.

The basis vectors of the reciprocal lattice can be determined uniquely from the basis vectors of the crystal lattice through equations 2.5:

$$\begin{aligned} \mathbf{r}_1 &= \frac{\mathbf{u}_2 \wedge \mathbf{u}_3}{\mathbf{u}_1 \cdot (\mathbf{u}_2 \wedge \mathbf{u}_3)} \\ \mathbf{r}_2 &= \frac{\mathbf{u}_3 \wedge \mathbf{u}_1}{\mathbf{u}_2 \cdot (\mathbf{u}_3 \wedge \mathbf{u}_1)} \\ \mathbf{r}_3 &= \frac{\mathbf{u}_1 \wedge \mathbf{u}_2}{\mathbf{u}_3 \cdot (\mathbf{u}_1 \wedge \mathbf{u}_2)} \end{aligned} \quad \text{eq. 2.5}$$

As specific cases, using equations 2.5 is possible to ascertain that the reciprocal lattice of a simple cubic lattice with parameter a is simple cubic too with parameter $1/a$ and that the reciprocal lattice of the hexagonal lattice with parameters $a = b$ and c is a hexagonal lattice rotated of 30° with parameters $2/a\sqrt{3}$ and $1/c$.

The Ewald sphere is centered at the origin of the reciprocal lattice and has a radius equal to $1/\lambda$, where λ is the wavelength of the incident wave (figure 2.17-A). All the points of the reciprocal lattice that lay on the Ewald sphere represent an elastically scattered beam for which the Laue condition is satisfied, as illustrated by figure 2.17-B.

In the case of electron diffraction, the follow two conditions occur:

- the De Broglie wavelength of the electron beam is very short, in the order of 2-4 pm, which leads to a very large radius of the Ewald sphere ($1/\lambda \approx 250\text{-}500 \text{ 1/nm}$) respect to the basis vectors of the reciprocal lattice;
- the irradiated crystal is very thin, about 10-100 nm, which means the zero-dimension points of the ideal reciprocal lattice, obtained by assuming an infinitely extended crystal, become rods elongated along the thickness of the lamella.

Because of the above conditions, the diffraction pattern generated during the SAED analysis corresponds approximately to the reciprocal lattice plane normal to the beam direction (figure 2.17-C).

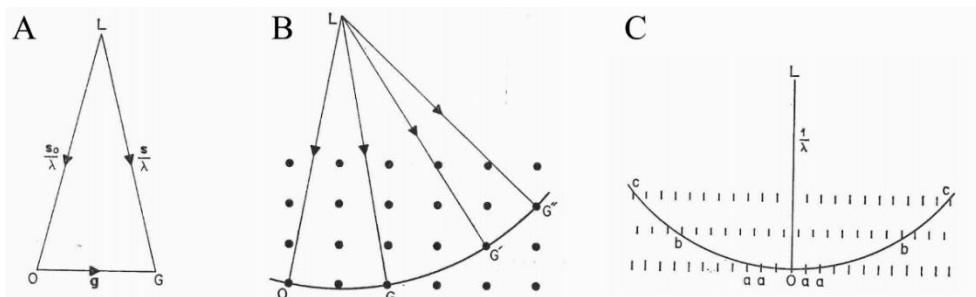


Figure 2.17. Ewald construction. The Ewald sphere radius is equal to $1/\lambda$, where λ is the wavelength of the incident radiation. The origin O of the reciprocal lattice lays on the Ewald sphere, \mathbf{s}_0 and \mathbf{s} are the unit vectors along the directions of the incident and the diffracted beams respectively (A), for each point G of the reciprocal lattice laying on the Ewald sphere, a beam is diffracted (B). Case of electron diffraction (C), the curvature of the Ewald sphere is exaggerated for clarity. From: [199].

The crystallographic direction $[u, v, w]$ that correspond to the line of the incident beam is usually referred as Zone Axis (ZA); the relative electron diffraction pattern contains spots with Miller indices h, k, l that satisfied: $uh + vk + wl = 0$.

The kinematic theory of electron diffraction [199] assumes a negligible attenuation of the incident beam along the specimen thickness, i.e. each atom of the irradiated crystal receives the same wave amplitude and therefore atoms of the same kind scatter waves of the same amplitude. According to the kinematic theory, the diffracted wave $\psi_{\mathbf{R}}$ associated with the scattering vector $\Delta\mathbf{k} = \mathbf{R}$ is given by the summation (equation 2.6) of the electron waves scattered by each atom of the crystal considering the respective phase differences $\phi_n = 2\pi\mathbf{P}_n \cdot \mathbf{R}$ [199]:

$$\begin{aligned}\psi_{\mathbf{R}} \propto F(\mathbf{R}) &= \sum_n f_n e^{-2\pi i \mathbf{P}_n \cdot \mathbf{R}} = \sum_p \sum_{m=1}^M f_m e^{-2\pi i (\mathbf{U}_p + \mathbf{p}_m) \cdot \mathbf{R}} = \\ &= \sum_p e^{-2\pi i \mathbf{U}_p \cdot \mathbf{R}} \sum_{m=1}^M f_m e^{-2\pi i \mathbf{p}_m \cdot \mathbf{R}} = L(\mathbf{R}) \cdot S(\mathbf{R})\end{aligned}\quad \text{eq. 2.6}$$

where f_n is the atomic form factor, depending on the kind of scattering atom, $\mathbf{P}_n = \mathbf{U}_p + \mathbf{p}_m$ is the position vector on n -th atom given by the lattice vector \mathbf{U}_p and the fractional coordinates \mathbf{p}_m of the atom in the p -th unit cell reference. The p summation over all the unit cells in the crystal gives the lattice factor L , the m summation over all the M atoms in each unit cell gives the structure factor S .

The intensity of the diffracted wave is proportional to $F^2 = FF^*$, where F^* indicates the complex conjugate of F . If the irradiated crystal contains only one atom for each lattice point ($M = 1$), then the phases of each scattered waves is equal and so they interfere constructively given the spot signal. The presence of other atoms in position with fractional coordinates can modify the relative intensity of the spots and eventually leads to the kinematic extinction of some spots with $F = 0$ because of the occurring of destructive interference.

As an example, let's consider the face centered cubic structure, which can be described as a simple cubic lattice with four atoms for each lattice point with coordinate:

$$p_0 = (0,0,0), p_1 = (1/2, 1/2, 0), p_2 = (1/2, 0, 1/2), p_3 = (0, 1/2, 1/2).$$

The respective structure factor is:

$$S(h, k, l) = \sum_{m=1}^4 e^{i \mathbf{p}_m \cdot \mathbf{R}} = 1 + e^{2\pi i \frac{h+k}{2}} + e^{2\pi i \frac{h+l}{2}} + e^{2\pi i \frac{k+l}{2}} \quad \text{eq. 2.7}$$

when the indices h, k and l are all odd or all even:

$$S(h, k, l) = 1 + e^{2\pi i N_1} + e^{2\pi i N_2} + e^{2\pi i N_3} = 1 + 1 + 1 + 1 = 4 \quad \text{eq. 2.8}$$

where N_1, N_2 and N_3 are integers. Instead, if h is odd and k and l are even:

$$S(h, k, l) = 1 + e^{\pi i (N_1 + \frac{1}{2})} + e^{\pi i (N_2 + \frac{1}{2})} + e^{2\pi i N_3} = 1 - 1 - 1 + 1 = 0 \quad \text{eq. 2.9}$$

which means that these kinds of reflections are systematically absent.

Analogously, the structure factor S is null each time the rule of the indices h , k and l all odd or all even is not satisfied. Therefore, by cancelling out the above determined forbidden reflections from the simple cubic lattice, a body centered cubic lattice is obtained, which is precisely the reciprocal lattice of the face centered cubic structure.

The above described kinematic theory give a simple and useful tool for the interpretation of the SAED patterns, however it is worth to consider that dynamical effects can determine deviations from the spots intensities evaluated using the kinematic theory for complex structures.

2.8 Thermal analysis

Differential Scanning Calorimetry (DSC) and Thermomechanical analysis (TMA) were carried out in order to study the modifications of the material microstructure during the thermal treatments or the exposition to the service temperature. These analyses allow to reveal the temperature ranges at which the main thermal phenomena occur, usually phase transformation. Both the types of analysis were performed by submitting the analyzed samples to a heating run at a definite heating rate and to a following cooling run. During the cooling, it is not possible to accurately control the cooling rate, therefore the signals collected during this stage should be treated with care. As a consequence, the gathered data during the cooling stage will be omitted when they don't add new substantial information with respect to those already derived by the heating run.

2.8.1 DSC

DSC analysis allows to detect the emitted (exothermic phenomena) or absorbed (endothermic phenomena) heat from the sample during the phase transformations. In this study, the exothermic phenomena of interest are the solidification and the precipitation of second phases, whereas the detected endothermal phenomena are the fusion and the dissolution of second phases. In the plots reported in chapter 5, the exo-up convention is adopted, therefore a peak indicates the occurrence of an exothermic phenomenon conversely, a valley indicates the occurrence of an endothermal phenomenon.

A Thermal analyser Setaram DSC/TGA 92 16.18 was used to perform all the DSC analyses. The ranges of fusion and solidification of the as built alloy was established firstly. A small material sample embedded in alumina powder was used for this analysis. The sample was melted during a heating run until 1400°C at a heating rate of 12°C/min, then the sample was cooled until room temperature with a cooling rate of about 28°C/min. This preliminary analysis was used mainly to establish a maximum safety temperature at which the following analyses were

performed avoiding the melting of the sample and consequently damaging of the measuring equipment.

The DSC analyses performed in the next steps of the research aim at studying the transformations that occur in solid state. Such analysis were performed using cylindrical samples produced with SLM technique using the optimized parameters. Samples with both parallel and perpendicular axis to the building direction were produced. They will be referred in the follow as vertical and horizontal samples, respectively. Three vertical samples were analyzed in the as built state by setting the heating rates at 20°C/min for the first two samples and at 5°C/min for the third. The comparison between the analysis performed with a heating rate of 20°C/min was done to verify the reproducibility. Furthermore, three horizontal samples were also analyzed at the as built state by setting the heating rates at 5°C/min, 10°C/min and 20°C/min, respectively, in order to evaluate the influence of the heating rate on the detected signal. The temperature trends during the DSC analysis with set heating rates at 5°C/min, 10°C/min and 20°C/min are shown in figure 2.18.

Further DSC analyses were performed for the preliminary study of the thermal treatment and the aging response of the material (paragraph 2.4). To the latter purpose, vertical samples solutioned and then air quenched at the following conditions were used: 980°C for 2 and 8 hours, 1065°C for 2 and 8 hours. A fixed heating rate of 20°C/min was used for the analysis of the solutioned samples. As for the cooling rate, all the above mentioned DSC analyses were performed at about 20°C/min, as this parameters was not investigated.

2.8.2 TMA

TMA technique allows to measure the coefficient of thermal expansion (CTE) of the material as a function of temperature (T). When a phase transformation occurs with an expansion or a contraction, a peak or a valley is detected in the CTE vs T curve, respectively. The formation of precipitates in the matrix causes a reduction of the solute content dissolved in the solid solution, this in turn causes a reduction of the reticular distortion. Therefore, the precipitation of second phases occurs with a general contraction of the sample. Conversely, the dissolution of precipitates increases the solute content in solid solution with consequent increase of the reticular distortion, therefore the sample slightly expands.

A TMA-SETSIS Evolution Setaram instrument was used to perform all the TMA analyses in an Argon flow of 50 ml/min. Parallelepiped samples were produced by SLM technique, using the optimized parameters, for the TMA analyses. Both vertical samples, whose measured side during the TMA ramp is parallel to their building direction, and horizontal ones, whose measured side is perpendicular to their building direction, were used. Two vertical samples were analyzed in the as built state by setting the heating rate at 5°C/min and 20°C/min, respectively. Two as built horizontal samples were also analyzed with a heating rate of 5°C/min and 20°C/min, respectively. The temperature trends measured during

the TMA analysis with set heating rates at 5°C/min and 20°C/min are shown in figure 2.18.

In support to the results obtained with the DSC technique, further TMA analyses were performed on two vertical samples previously submitted to solution annealing at 980°C for 8 hours and at 1065°C for 8 hours, respectively, and quenched in air. As for the DSC tests, a fixed heating rate of 20°C/min were adopted for the analysis of solutioned samples.

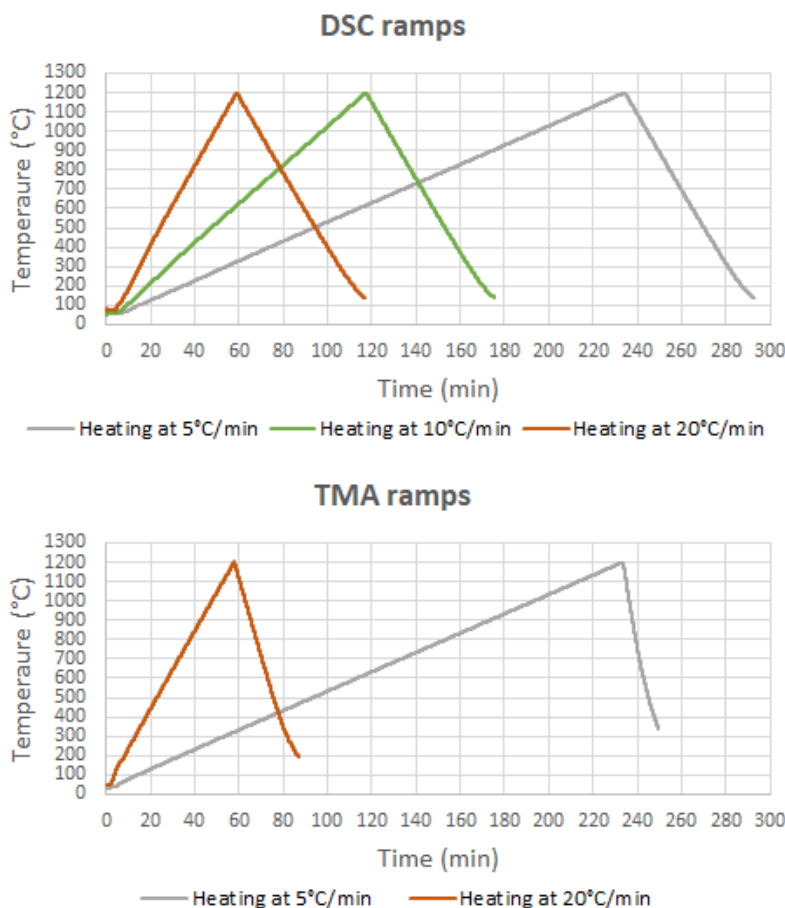


Figure 2.18. Thermic ramps measured during DSC and TMA analysis at different set heating rates.

2.9 XRD analysis

The X-Ray Diffraction (XRD) analysis was used to collect information on the phases constitution in the samples aged at the characteristic temperatures (paragraph 2.4.2) in support to the results obtained with the thermal analysis. An X-Pert Philips diffractometer was used for such characterization using the Cu-K α radiation, a voltage of 40 kV and an anode current of 40 mA being applied. The XRD analyses were carried out by performing a scan between 30° and 100° with a step size of 0.013° and with an exposure time of 25 s in Bragg-Brentano configuration. During the scan, a signal peak is revealed whenever the conditions of constructive interference between the beams reflected by the families of lattice planes are realized, i.e. when the Bragg equation is satisfied:

$$n\lambda = 2d \sin \theta \quad \text{eq. 2.10}$$

where n is an integer number called diffraction order, λ is the wavelength of the incident radiation, d is the inter-planar distance of the lattice planes family that cause the diffraction and θ is the angle at which the diffraction is realized. The diffraction peaks allow to identify the present phases in the analyzed samples, then the reticular parameter of them can be obtained through the Bragg equation.

In this study, the Bragg equation was used to obtain the cell parameter of the γ matrix after the heat treatments listed in table 2.5. The γ phase is identified by five characteristic XRD peaks; sometimes double peaks are recorded due to the presence of the $K\alpha_1$ ($\lambda \cong 0.1541 \text{ nm}$) and $K\alpha_2$ ($\lambda \cong 0.1544 \text{ nm}$) radiations in the incident beam. The peak due to $K\alpha_1$ was used to calculate the cell parameter when a double peak was encountered, otherwise the average value of $K\alpha$ was used ($\lambda \cong 0.1542 \text{ nm}$). The cell parameter was obtained by averaging the values obtained from the first 4 peaks (the fifth is usually too weak).

2.10 Durometers

2.10.1 Brinell tester

The Brinell hardness was measured using an EMCO TEST M4U instrument. All the Brinell indentations reported in this thesis were obtained using a spherical indenter with a diameter D of 2-5 mm and imposing a normal load F and an indentation time of 62.5 kgf ($F/D^2 = 10$) and 15 s, respectively. The Brinell tester was used to evaluate the mechanical properties of the samples of the 3^3 factorial plane during the study on the effects of the SLM process parameters (paragraph 2.3). Five indentations were performed for each of these samples.

Brinell hardness measurements were also collected during the study on the heat treatment cycle: five indentations were performed on each solutioned samples in table 2.4, four indentations were performed on each sample previously submitted to solution annealing and first aging (table 2.6) and each sample submitted to the complete heat treatment cycle (table 2.8). As for samples listed in table 2.7, three Brinell indentations were performed on the those submitted to prolonged solution annealing for 8 hours and four indentations on those aged at 760 °C.

2.10.2 Vickers microhardness tester

The Vickers microhardness was measured using a Tester VMHT with Leica Camera. All the indentations reported in this thesis were obtained using a normal load of 100 gf applied for 15 seconds. The Vickers microhardness of the solutioned samples listed in table 2.3 was evaluated through ten indentations per sample and it was put in correlation with the volume fraction of precipitates obtained with the image analysis of the FESEM micrographs (paragraph 2.7.3).

Vickers microhardness measurements were also collected in support to the Brinell ones during the study for the definition of the heat treatment, in particular ten microindentations were performed on each solutioned sample in table 2.4 and five microindentations on each of the aged samples listed in table 2.7 and doubled aged samples listed in table 2.8.

Finally, the Vickers microhardness of the samples treated at the characteristic temperatures (table 2.5) was measured through a total of ten microindentations for each sample and the obtained results were used together with the XRD and FESEM analysis to infer information about the microstructure. The microhardness modification after the aging treatment was evaluated by comparing the above data with other Vickers measurements collected on a sample in the as built state and on a sample solutioned at 1065°C for 2 hours in the same treatment conditions of the samples listed in table 2.5. A total of 14 and 10 microindentations were performed on the as built and the solutioned samples, respectively.

Chapter 3

Features and microstructure of SLM Inconel 718 alloy

3.1 Study on the SLM parameters process

The first part of the study has the aim to evaluate the influence of the main parameters of the SLM process on the quality of the produced material. Part of this investigation has been previously published in [186]. The process parameters taken into consideration for this study are the laser power (P), the scan speed (v) and the hatching distance (hd). The response of the material at each combination of these parameters is evaluated using two quality indicators: porosity and Brinell hardness. An estimation of the porosity level in the material is evaluated through apparent density measurements with the Archimede's method and image analysis of optical micrographs. The measured apparent densities of each sample are reported in figure 3.1 (see table 2.2 for the SLM process parameters associated at each sample).

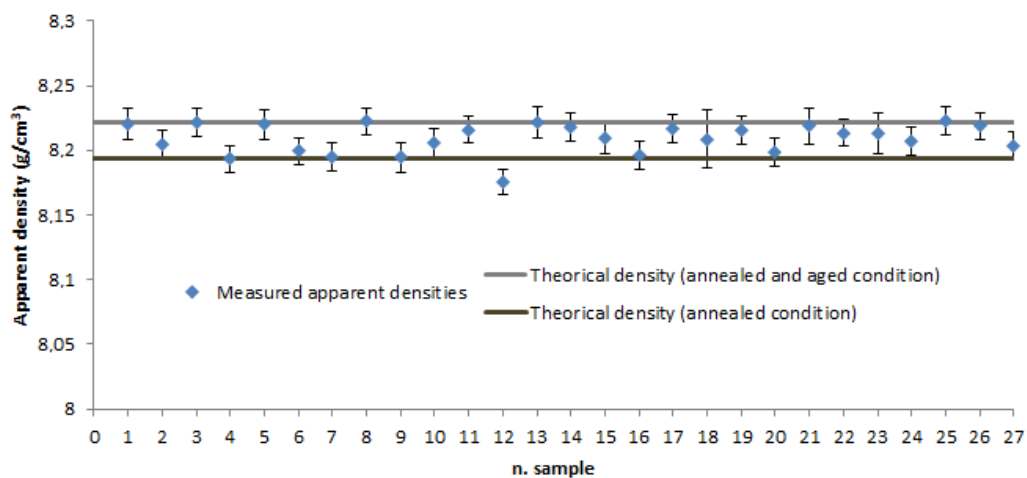


Figure 3.1. Apparent density measurements of the SLM samples produced for each set of process parameters combination in comparison with the theoretical density values. Data published in [186].

It is possible to observe that all the tested samples are near full dense and that the process parameters have not a clear effect on the apparent density of the material in the considered ranges. In general, the presence of small and uniformly distributed pores from 5 to 10 μm in size is observable in figure 3.2 (some examples of them are marked with blue ellipses). Some larger and usually round shaped pores of 20-30 μm (like the one marked with the red ellipse in figure 3.2) are detectable in the collected optical images.

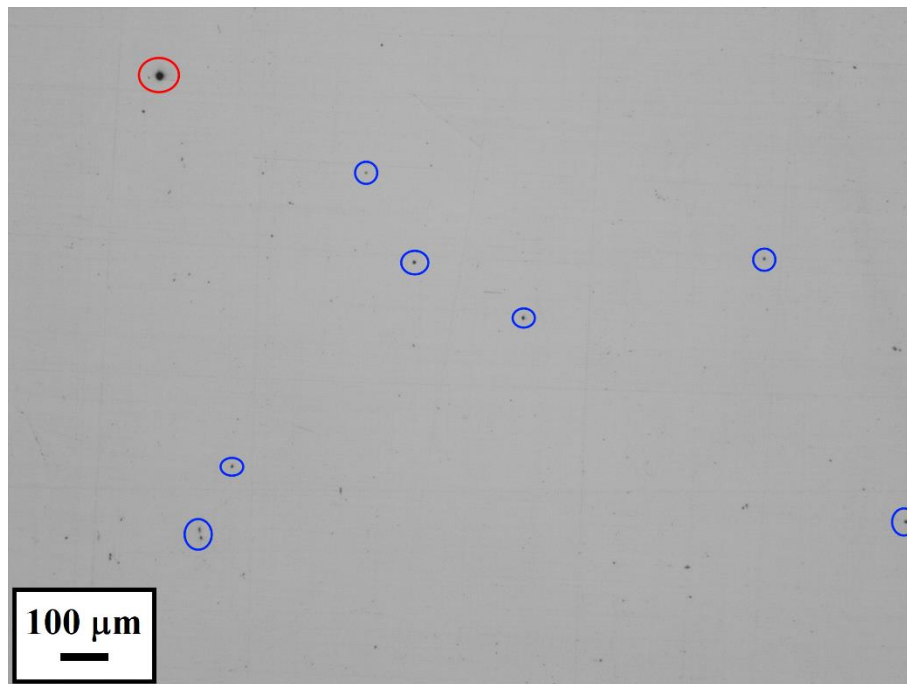


Figure 3.2. Optical micrograph of sample n.18 ($P = 185 \text{ W}$, $v = 900 \text{ mm/s}$, $hd = 0.09 \text{ mm}$) as example of the general porosity condition of the SLM samples with presence of small pores (blue ellipses) and some bigger rounded pores (red ellipse).

The porosities ranges obtained for each tested sample through image analysis are reported in figure 3.3. The results of this analysis confirm that the porosity level of all the sample is very low on average ($< 0.25\%$ apart samples n.4 and n.11). Not evident influence of the SLM process parameters on the overall porosity level can be deduced from the plot in figure 3.3. However, a careful inspection of the collected micrographs reveals that the sample obtained with the lower scan speed ($v = 600 \text{ mm/s}$) tend to have some bigger spherical porosities (red ellipses in figure 3.4-A), probably due to trapped gas. A low scan speed determines a high absorbed energy, which in turn can actually cause partial vaporization of the molten pool leading to the formation of porosities due to the entrapment of the formed vapor. Nevertheless, sample n.22, that is the only one out of those obtained with a scan speed of 600 mm/s that was fabricated applying a low VED, don't exhibit a large number of gas porosities. Therefore, the low value of laser power and the high hatching distance allow to prevent the formation of bubbles even when v is low.

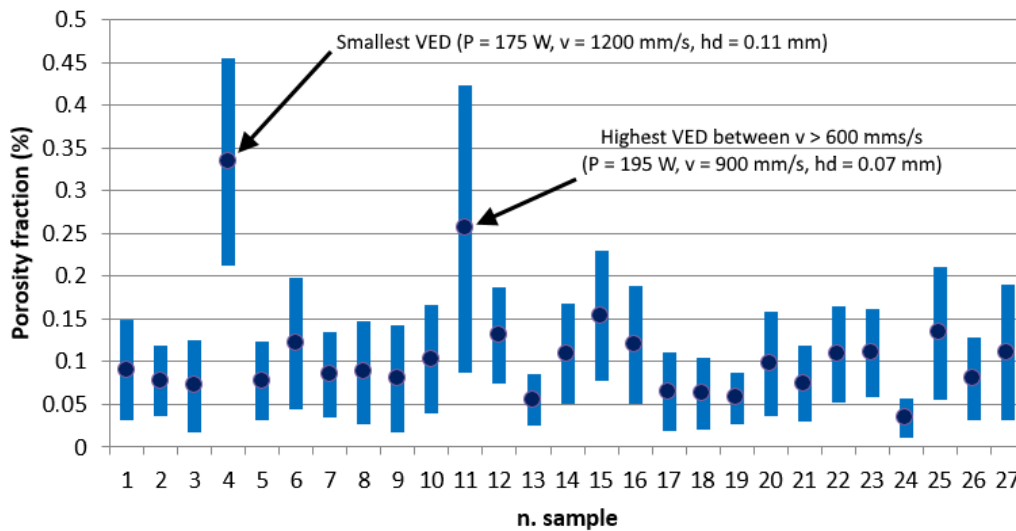


Figure 3.3. Porosity area fraction ranges obtained on the SLM samples produced for each set of process parameters combination. Data published in [186].

On the sample n.11, the revealed porosity is comparable to the general one shown in figure 3.2, however there are some zones, especially near the edges, characterized by an anomalous density of pores (figure 3.4-B). This sample is associated to the highest VED value between the ones obtained with a scan speed higher than 600 mm/s. According to the present analysis such conditions lead to an unstable consolidation process and, as a consequence, they should be avoided.

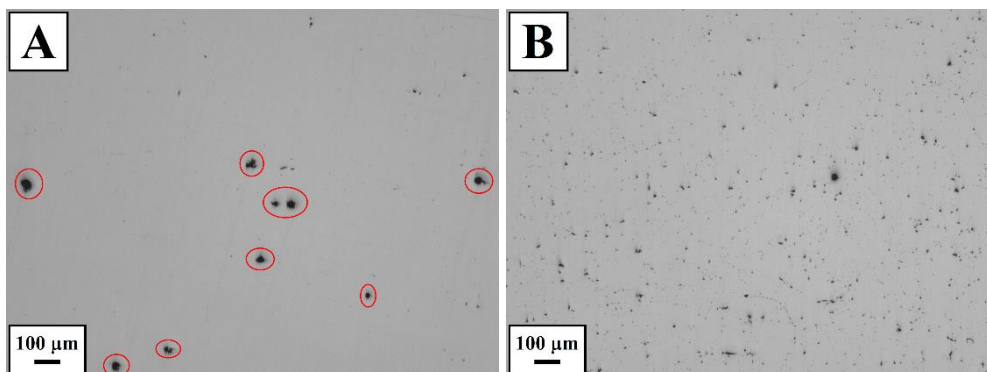


Figure 3.4. Sample n.15 ($P = 175$ W, $v = 600$ mm/s, $hd = 0.07$ mm) as example of the porosity condition (red ellipses indicate gas porosities) in most of the samples obtained with $v = 600$ mm/s (A) and sample n.11 ($P = 195$ W, $v = 900$ mm/s, $hd = 0.07$ mm) obtained with the highest VED between the samples produced with $v > 600$ mm/s (B).

On sample n.4, associated to the lower VED value applied, the porosity level is the highest found. A large number of big voids, mainly irregularly shaped and probably caused by lack of fusion, are present on this sample (some examples of them are marked with red ellipses in figure 3.5-A). This kind of porosity can also be observed on sample n.16, but with a much lower frequency. With respect to sample n.4, the number 16 is fabricated at the same scan speed and hatching distance, but with a higher laser power (195 W). This reduces drastically the problem of lack of fusion (figure 3.5-B).

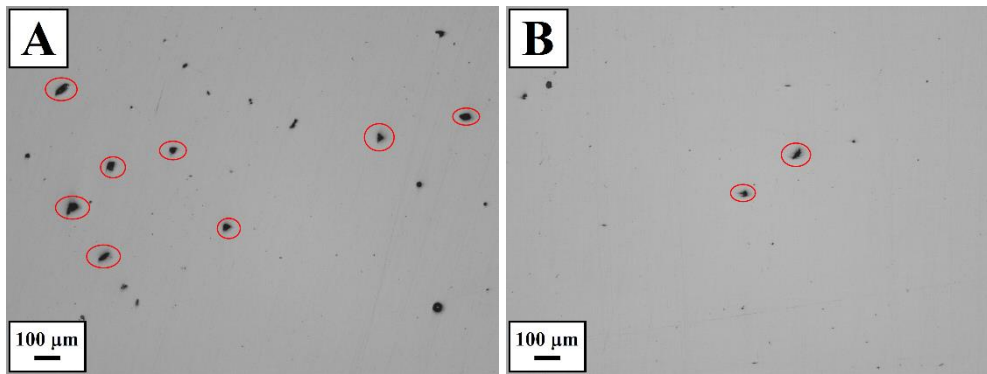


Figure 3.5. Sample n.4 ($P = 175$ W, $v = 1200$ mm/s, $hd = 0.11$ mm) obtained with the smallest VED value (A) and sample n.16 ($P = 195$ W, $v = 1200$ mm/s, $hd = 0.11$ mm) obtained with a higher value of laser power (B). The red ellipses indicate some lack of fusion voids.

In general, abnormal porosity is not found on samples obtained with intermediate VED values.

As far as the Brinell hardness is concerned, all the collected mean values fall between 250 ± 3 HB10 (sample n.12, obtained with $P = 185$ W, $v = 600$ mm/s and $hd = 0.07$ mm) and 266 ± 3 HB10 (sample n.5, obtained with $P = 175$ W, $v = 1200$ mm/s and $hd = 0.07$ mm). The sample produced by adopting the EOS recommended parameters has a mean Brinell hardness of 264 ± 9 HB10, very close to the highest measurement.

The main effects of the SLM process parameters and of the second order interactions between them on the Brinell hardness are shown in the plots reported in figure 3.6.

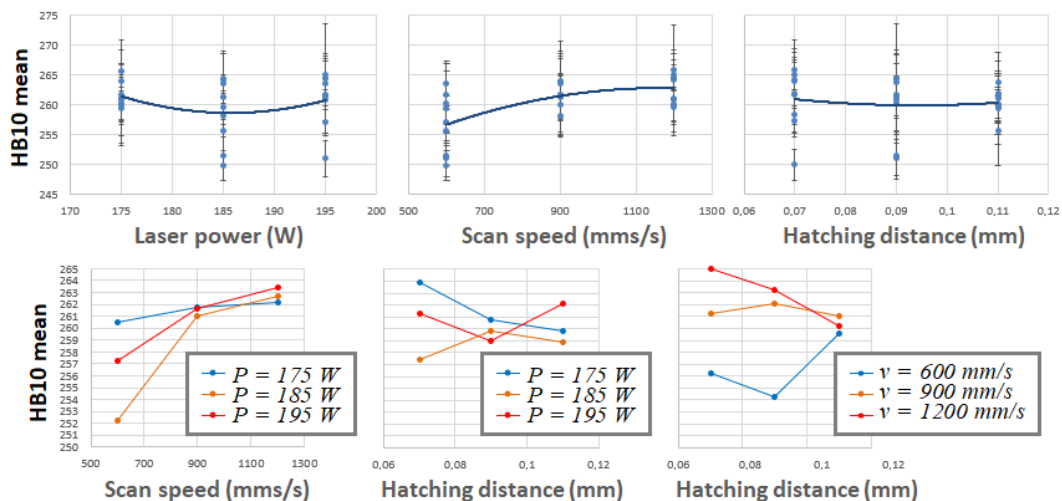


Figure 3.6. Main and interaction effects of the SLM process parameters on the Brinell hardness of Inconel 718 alloy. Data published in [186].

Porosity can affect the hardness, however the observed correlation between the collected data is weak because also concur to this property, for example the microstructure and the development of second phases. Table 3.1 contains the ANOVA treatment relative to the hardness of the tested samples. Linear model based ANOVA is probably not very suitable for describing complex nonlinear

phenomena involved in the SLM process that can influence the final hardness. However, some rules of thumb can be derived from this analysis:

- v is the parameter that mostly affects the hardness, which decreases when v is lower in the analysed range; this is probably again related to the development of gas porosities, as noted on samples produced with v equal to 600 mm/s;
- higher hardness is obtained at higher v and lower values of hd , the latter parameter being effective in reducing the risk to develop voids due to lack of fusion;
- it's better to adopt a higher value of hd when a high P is used and, conversely, a lower value of hd leads to higher hardness when P is lower, the balance between these two parameters allows to obtain an intermediate value of VED and prevents the formation of abnormal porosity;
- intermediate value of P leads to lower hardness, especially if a low scan speed is adopted.

Table 3.1. Analysis of Variance (ANOVA) on the dataset made by 5 Brinell hardness measurements for each sample of the 3^3 factorial plane with the main effects of P , v and hd and their interactions until the second order. DOF: degrees of freedom; SS: sum of squares; MS: mean squares; F: F-ratio.

	<i>DOF</i>	<i>SS</i>	<i>MS</i>	<i>F</i>	<i>p-value</i>
<i>Main effects</i>					
<i>P</i>	2	189.26	94.63	5.66	0.0045
<i>V</i>	2	938.86	469.43	28.08	< 0.0001
<i>Hd</i>	2	22.68	11.34	0.68	0.5094
<i>Second order interactions</i>					
<i>P*v</i>	4	339.32	84.83	5.07	0.0008
<i>P*hd</i>	4	235.90	58.97	3.53	0.0094
<i>v*hd</i>	4	380.30	95.07	5.69	0.0003
<i>Residuals</i>	116	1938.99	16.72		

The optical micrographs of the samples at the vertices of the factorial plane showing the microstructure revealed after etching with Kalling's solution are reported in figures 3.7 and 3.8. The segregation between laser tracks and at grain boundaries appears more intense when the higher value of v is adopted, probably because it determines a faster cooling rate during solidification. Furthermore, some voids between laser tracks are visible on the sample produced with the lower VED value ($P = 175$ W, $v = 1200$ mm/s, $hd = 0.11$ mm).

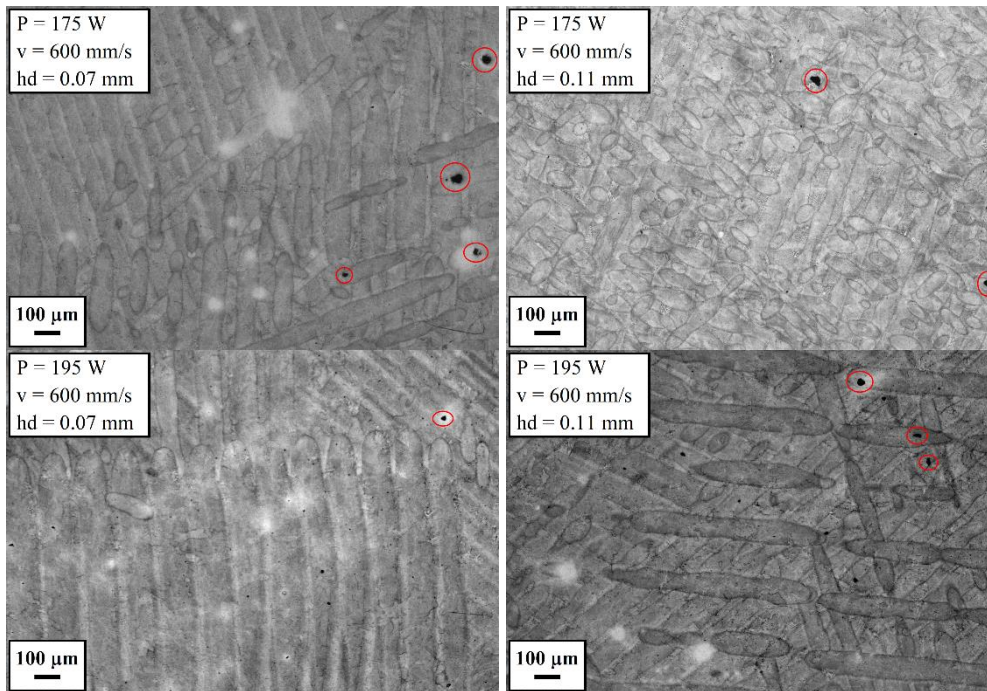


Figure 3.7. Micrographs on the horizontal plane of the samples produced with $v = 600$ mm/s. The red ellipses indicate gas porosities and other defects. Kalling's n.2 etchant.

No further differences in the general microstructural features which could be clearly ascribed to the modulation of the SLM process parameters are detectable at this inspection length scale.

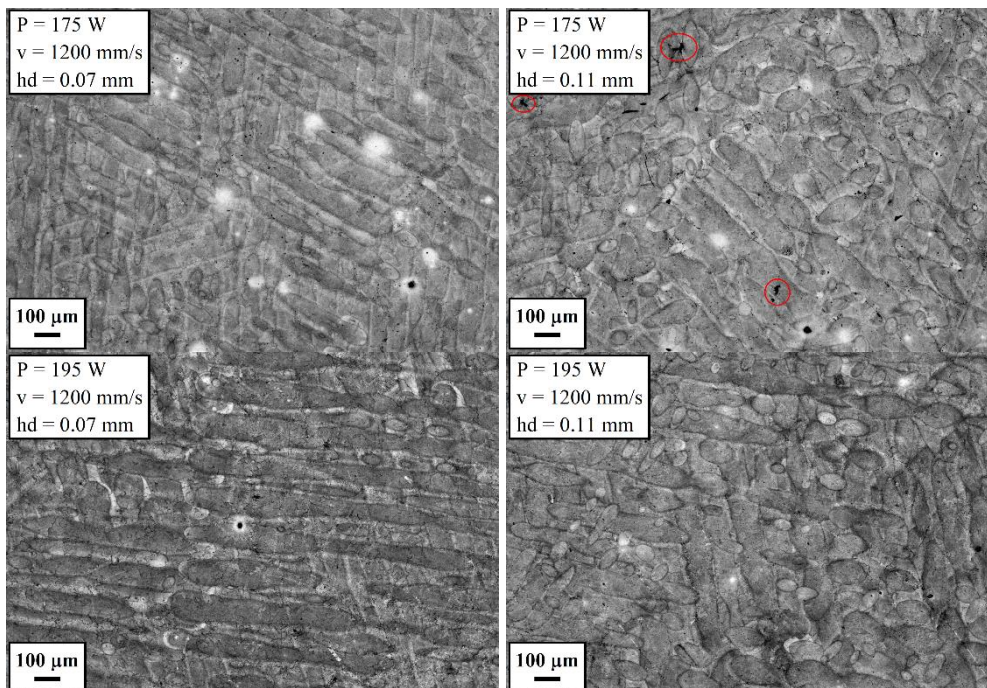


Figure 3.8. Micrographs on the horizontal plane of the samples produced with $v = 1200$ mm/s. The red ellipses indicate some lack of fusion voids between laser tracks. Kalling's n.2 etchant.

The above reported results demonstrate that the production of Inconel 718 through SLM process has a high robustness around the EOS recommended parameters. Near full dense material can be obtained without abrupt changes in

residual porosity level with a limited modification of the main process parameters. This is especially true if extreme value of VED are avoided. Even the Brinell hardness is only slightly affected by parameters values, although in this case some marked effects were detected, especially due to modulation of the scan speed. For these reasons, samples for all the following characterizations reported in this thesis were fabricated through SLM process parameters recommended by EOS, that also according to our investigation were confirmed to be the optimal ones for densification purpose.

3.2 As built microstructure features

After SLM production, Inconel 718 alloy is characterized by a very heterogeneous and complex microstructure which derives from the particular manufacturing conditions. In the following paragraphs, the main microstructural features of the as built material and the interactions between them are presented through the use of different characterization techniques, i.e. optical microscopy, EBSD analysis, SEM and TEM microscopy and EDS analysis. Part of the work concerning the characterization of the alloy at the as built state has been previously published in [186]. The relationship between process conditions and such microstructural features are also discussed.

3.2.1 Grains and laser related boundaries

Due to the directional asymmetry of the SLM process, the microstructural aspect of the as built material appears different on the horizontal and vertical cross sections. In the optical micrograph of figure 3.9, taken on the horizontal plane of an as built sample, nearly perpendicular to the building direction, parallel structures of laser tracks are clearly visible after electrochemical etching. The directions of the laser tracks are a consequence of the adopted scanning strategy using 67° rotation at each layer, that allows to reduce the microstructural anisotropy on the horizontal plane arising from the parallel laser scans.

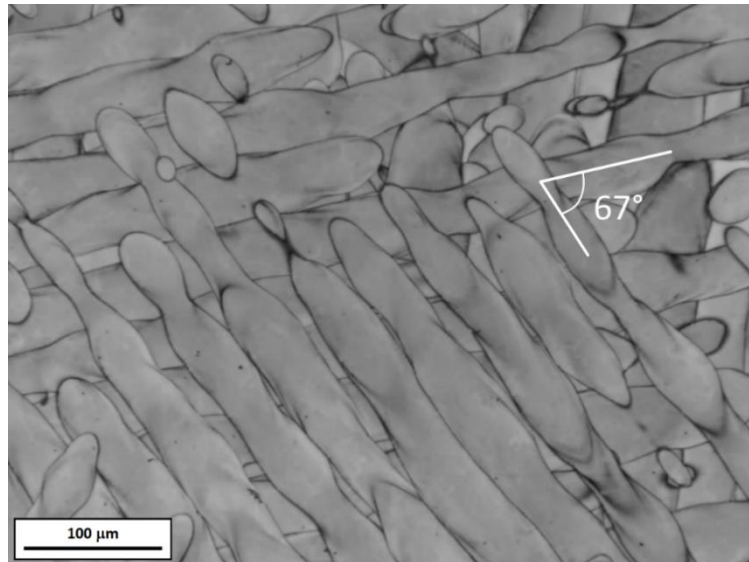


Figure 3.9. Optical micrograph of the horizontal plane of the SLM as built material showing the typical laser tracks. Electrochemical etching.

The optical micrographs of figure 3.10 were collected on the horizontal plane after chemical etching with Kalling's solution. It is possible to note that the grain structure is better revealed by using this etching. Although the grain size on the horizontal plane has the same order of magnitude of the width of the laser tracks, the grains appear not strictly constrained by them. In fact, it is possible to observe that some grains were able to develop across two laser tracks. This feature is a first indication of the occurring of the epitaxial growth during the solidification of the molten pools, which allows to the partially melted grains in the zone of overlapping between consecutive laser scan lines to grow beyond the border of the laser track in which it was formed.

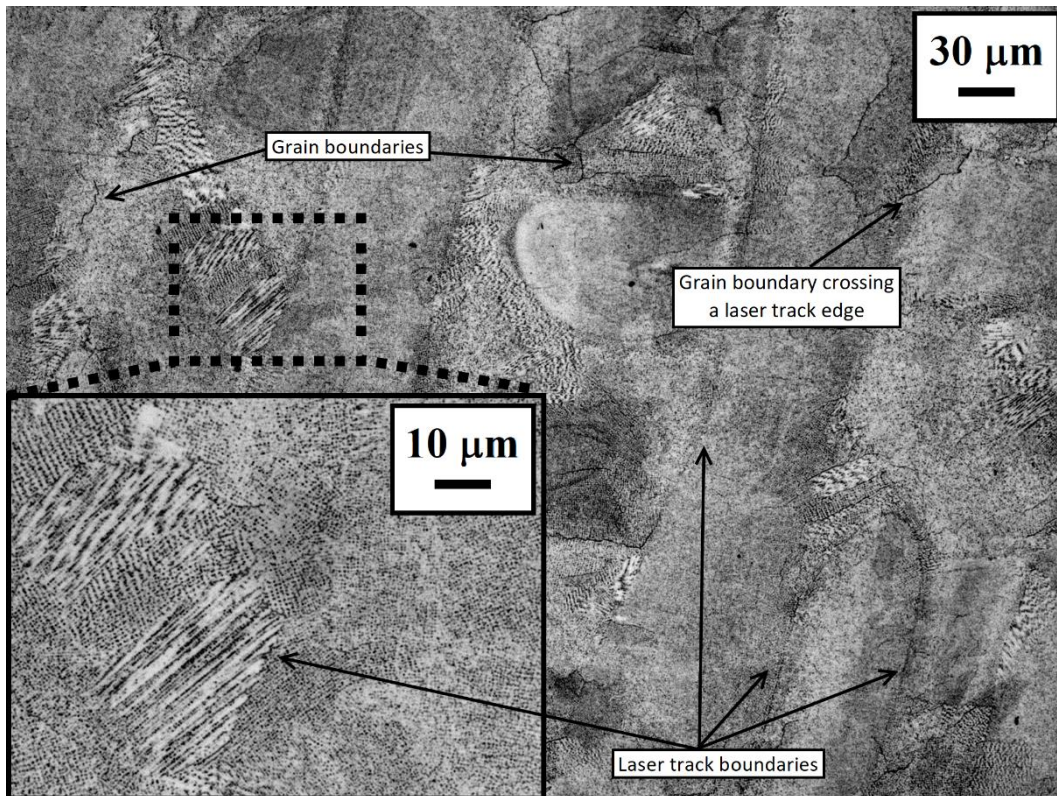


Figure 3.10. Optical micrographs collected on the horizontal plane of the as built sample showing the grain boundaries, the laser tracks boundaries and the sub-granular structure. Kalling's n.2 etchant.

The optical micrographs in figure 3.11 show the general aspect of the as built material on the vertical plane, i.e. nearly parallel to the building direction of the sample. After etching, the laser related boundaries between the arc shaped melt pools become visible. Similarly to what observed on the horizontal plane, the grains are not constrained by the single powder layer thickness and by the boundaries between the melt pools. In fact, the grains assume an elongated shape with their major axis oriented along the building direction and can develop across several melt pools during consecutive depositions.

These observations confirm that, at each laser pass, the released heat causes the partial remelting of the grains grown at the previous pass. After this the solidification of the molten pool occurs through epitaxial growth of these grains.

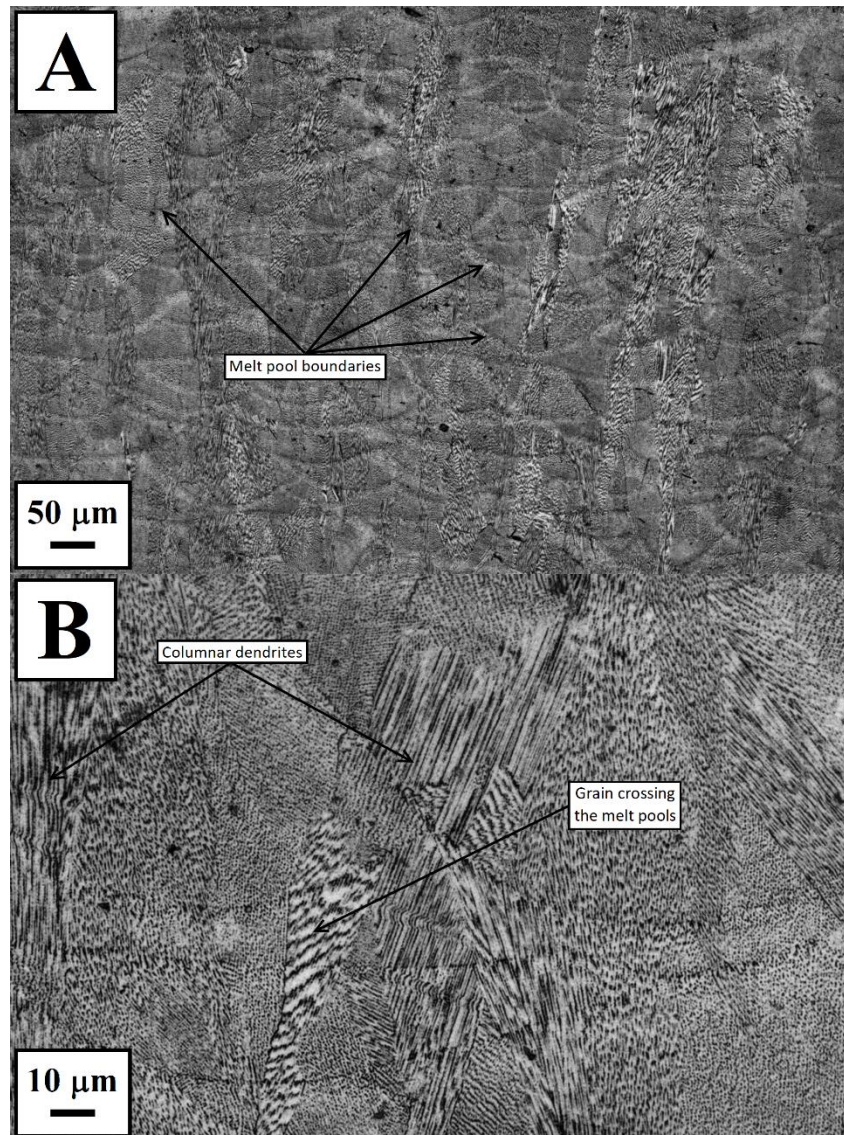


Figure 3.11. Optical micrographs collected on the vertical plane of the as built sample showing the melt pool boundaries (A), the grains crossing the deposited layers and the sub-granular columnar dendrites (B). Kalling's n.2 etchant.

3.2.2 Grain morphology and crystallographic texture

The grain maps obtained through EBSD analysis on both the horizontal and vertical plane of the built sample are shown in figure 3.12. The low-angle boundaries, defined as the boundaries with a maximum mis-orientation angle ranging between 10° and 4° , are shown in the maps of figure 3.12 as lighter blue lines. On the other hand, the high-angle boundaries, with a mis-orientation angle of at least 10° , are marked in dark blue. The grains are here defined as the regions that are completely delimited by high-angle boundaries. Some of the largest grains are composed by sub-grain domains which are delimited also by low-angle boundaries. These domains are depicted in figure 3.12 using different color shades. It's possible to observe that some grains contain up to 11 or even more sub-granular domains.

On the horizontal plane, the grains have substantially equiaxed morphology. In the analyzed area, the mean grain size, expressed as equivalent diameter, is equals

to 11 μm (only the grains that don't touch the edges of the area are considered in this statistic). However, the dispersion on grain sizes is very high (standard deviation: 9 μm) and large grains of 30-50 μm are also present.

In agreement to what observed from the optical micrographs of figure 3.11, the grain map obtained along the vertical plane shows that grains have mostly an elongated shape with their longer axis oriented parallel to the building direction of the part. The calculated average values of the major axis of the grains is 28.5 μm , however a high heterogeneity on the grain size can also be note along the vertical plane (standard deviation: 29.5 μm) with the presence of grains up to 180 μm along the major axis. The ratio between the major and the minor axes of the grains detected on the vertical plane has an average value, weighted on the grain sizes, equal to 5.4.

Laser related boundaries are not evidenced by the grain maps because, as already pointed out, the crystallographic orientation of the grains is independent from the laser scan lines and the deposited layers due to the occurring of epitaxial growth. For this reason, the longer grains can cross up to ten deposited layers leading to a good metallurgical bonding between them.

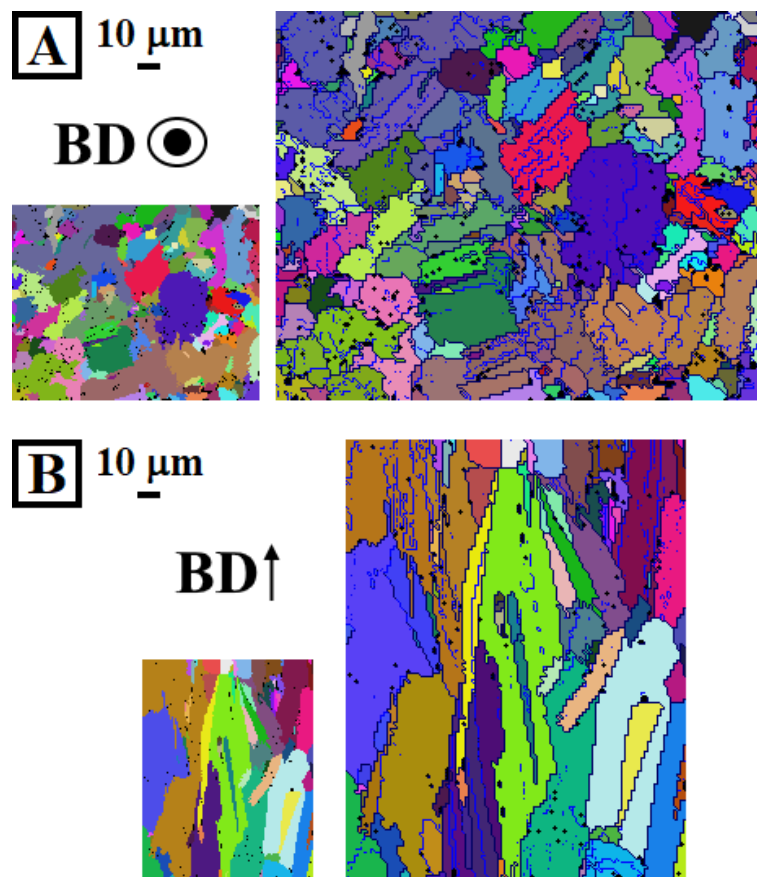


Figure 3.12. Grain maps obtained through EBSD analysis of the as built material on the horizontal plane (A) and vertical plane (B). The grains, defined here as the regions completely delimited by high-angle boundaries, are shown in the maps on the left. In the maps on the right, different color shades are used for indicating the sub-grain domains, the high-angle boundaries (mis-orientation of at least 10°) are marked in dark blue and the low-angle boundaries (maximum mis-orientation angle between 10° and 4°) are marked in lighter blue. First published in [186].

The mean crystallographic orientation of each grain in the maps of figure 3.12 is shown through the $\{100\}$, $\{110\}$ and $\{111\}$ pole figures obtained on the horizontal plane (figure 3.13) and the vertical plane (figure 3.14), respectively. In these figures, the big squares represent the mean orientation of the detected grains with respect to the sample coordinates system. On the contrary, the small circles indicate the mean crystallographic orientation of the respective sub-granular domains.

For comparison, simulated pole figures representing the same number of grains detected on the horizontal plane, but with random orientation, are also reported in figure 3.13. The target of such comparison is to show the aspect of the pole figures if no crystallographic texture would be present.

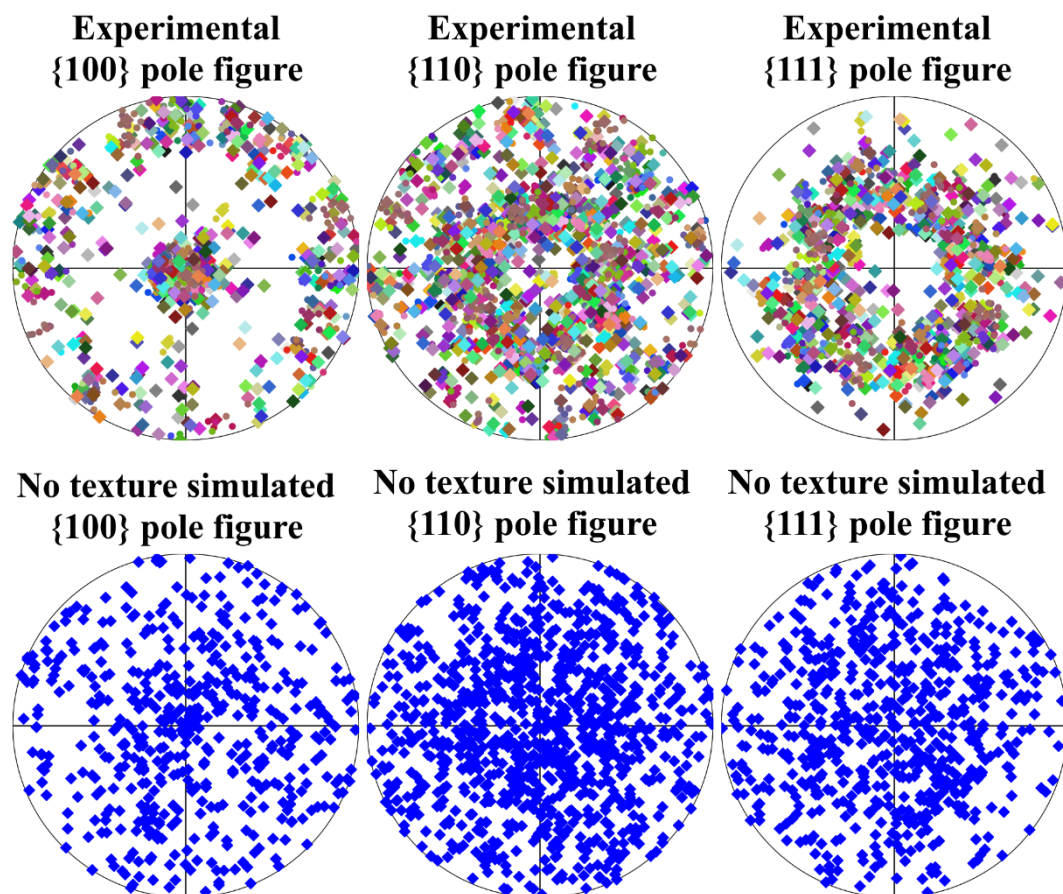


Figure 3.13. Experimental pole figures relative to the EBSD analysis on the horizontal plane, each colored square represent the mean orientation of the respective grain of figure 3.12-A respect to the sample coordinate system. The small circles represent the mean orientation of the sub-granular domains. Simulated pole figures for a material without preferential orientation with the same number of grains are also reported. First published in [186].

This analysis clearly demonstrates that the SLM built material has a strong preferential orientation of the $\{100\}$ lattice planes along the building direction with respect to a material with a random crystallographic orientation.

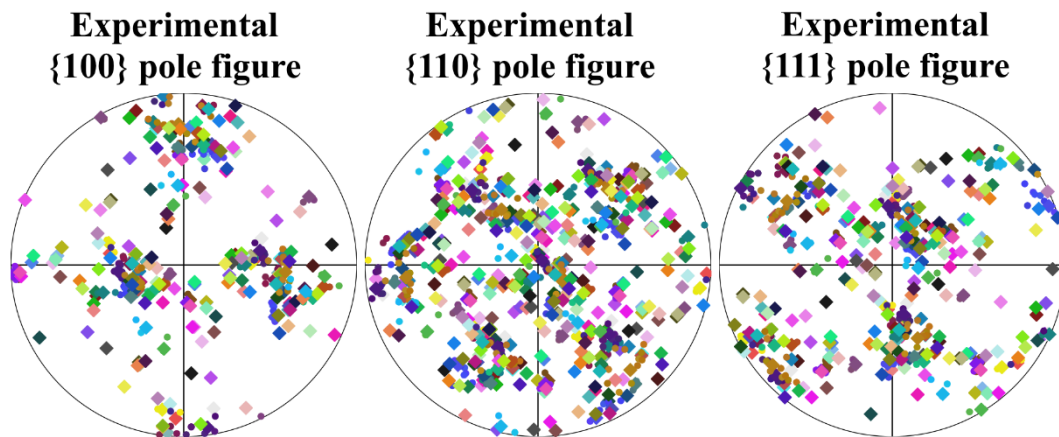


Figure 3.14. Experimental pole figures relative to the EBSD analysis on the vertical plane, each colored square represent the mean orientation of the respective grain of figure 3.12-B respect to the sample coordinate system. The small circles represent the mean orientation of the sub-granular domains. First published in [186].

The crystallographic texture can also be assessed from the Inverse Pole Figure (IPF) charts. In the following discussion, the axis of the sample coordinates system that is parallel to the building direction of the sample will be referred as R_1 axis. Instead, the other two axes will be referred as R_2 and R_3 . It is worthwhile to note that the building direction is represented by Z axis in figures related to samples analyzed on the horizontal plane and by Y axis in figures related to samples analyzed on the vertical plane,

In the IPF chart relative to the R_1 axis of figure 3.15, the density of the points collected on the horizontal plane increase near the $[001]$ vertex of the standard triangle. Instead, the density of the points decreases near the $[111]$ vertex of the IPF charts relative of both the R_2 and R_3 axes. A similar distribution of the points was obtained on the vertical plane.

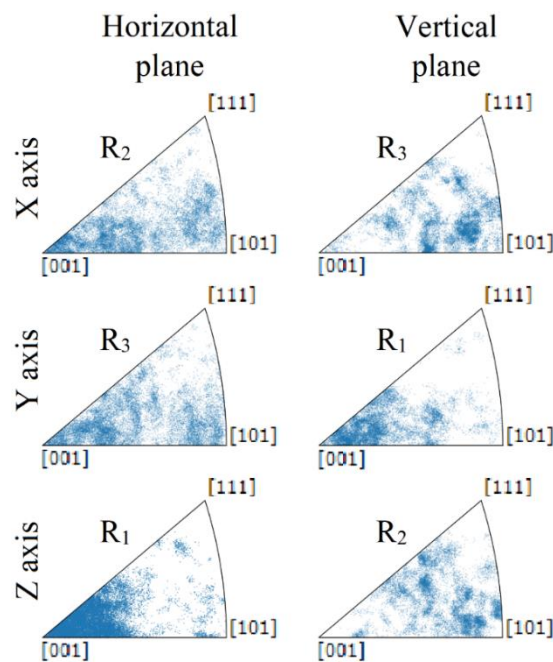


Figure 3.15. Inverse Pole Figure (IPF) charts relative to the three axes on both the horizontal and vertical planes. First published in [186].

These distributions of the points can be understood by observing the path followed by the representative point of the orientation of a cubic cell on the IPF charts during the rotation of this cell around its $[001]$ axis. When the rotation axis has a small inclination with respect to the R_1 axis of the sample coordinate system, the followed path is similar to the ones shown in figure 3.16 as examples. Actually, each of these paths describes a 90 degrees rotation of the cell around its $[001]$ axis, that corresponds to a continuous variation of the ψ Euler angle, during which both the φ and χ angles are kept to a fixed value. The paths of figure 3.16 are referred to the horizontal plane, in which the θ angle represents the inclination of the $[001]$ axis respect the building direction (i.e. the R_1 axis). Similar paths are also followed in the vertical plane.

The example paths of figure 3.16 show that, whenever the angle θ is low and the other Euler angles don't assume preferential values, the points of the IPF charts are disposed along an arch near the $[100]$ vertex of the standard triangle relative to the R_1 axis and, in the meanwhile, they cover the region of the triangle opposite to the $[111]$ vertex on the IPF charts relative to both the R_2 and R_3 axes. This is, precisely, the situation experimentally found and reported in figure 3.15, which therefore denotes both a preferential orientation of the $\langle 100 \rangle$ type axes along the building direction and a uniform random orientation with respect to the other dimensions.

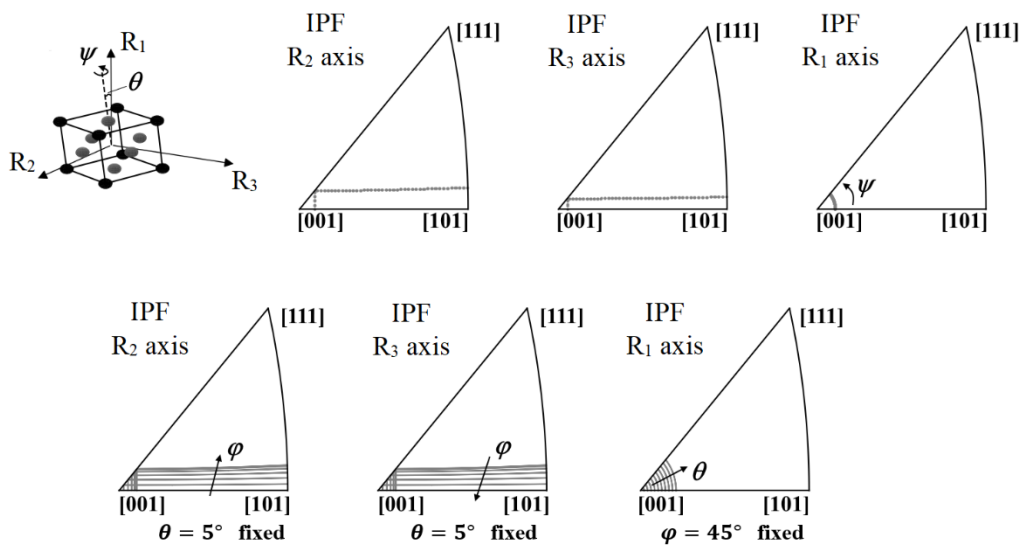


Figure 3.16. Paths of the representative point on the IPF charts during the rotation of a crystal around the $[001]$ direction oriented at a low angle to the building direction (R_1 axis). This example is referred to the horizontal plane, the paths relative to the vertical plane are analogous.

An intuitive representation of the $\langle 100 \rangle$ crystallographic texture of the as built material is given by the IPF maps (figure 3.17) of the horizontal plane and the vertical plane. These maps allow to visualize the crystallographic orientation of each grain detected with the EBSD analysis. A map with balanced color tones denotes an isotropic orientation respect to the reference axis of the map, instead crystallographic a texture is visible as a more uniform colored map. From the IPF

maps relative to the R_1 axis on both the horizontal and vertical planes, it is possible to observe that most of the detected grains has a $\langle 100 \rangle$ crystallographic axis nearly oriented along the building direction. Conversely, the other IPF maps don't reveal a similar texture, as it was expected because the material is substantially isotropic along the other spatial directions as already pointed out in previous discussion.

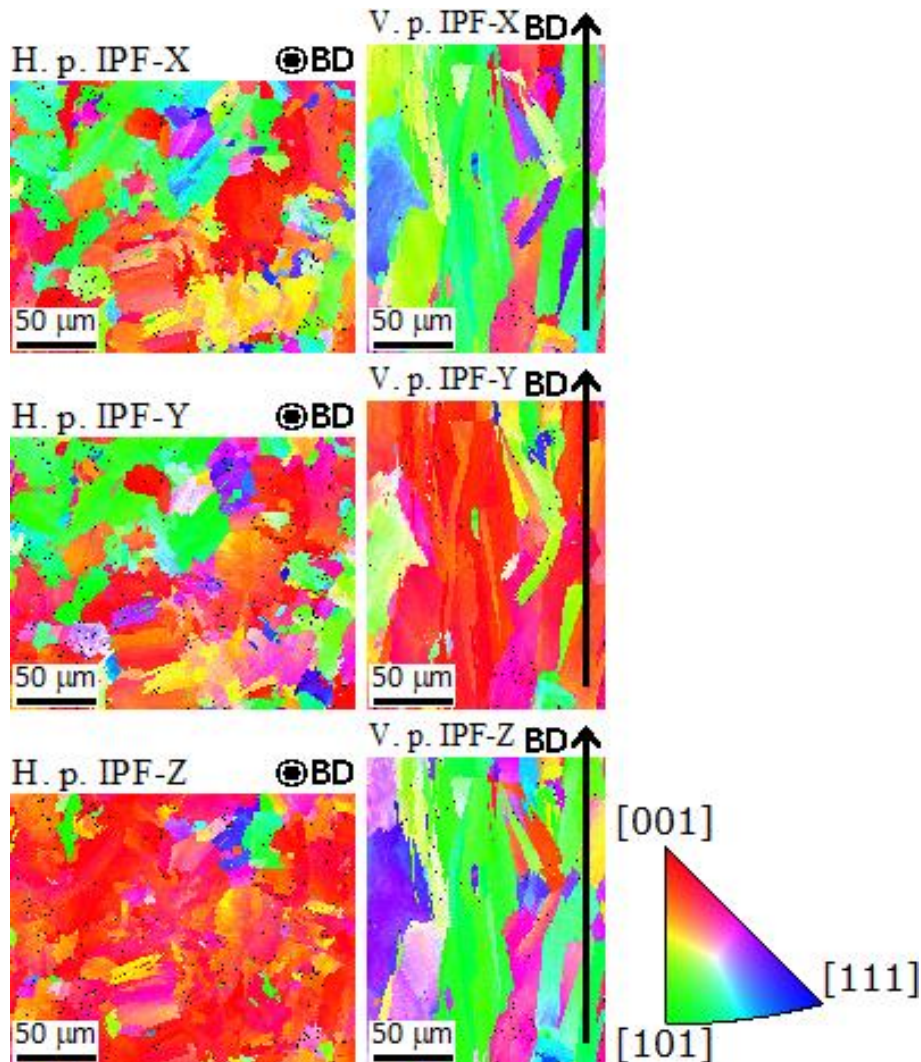


Figure 3.17. IPF maps on both the Horizontal plane (H. p.) and the vertical plane (V. p.) relative to the three axes. The IPF-Z maps have been previously published in [186].

3.2.3 Sub-granular structure

Higher resolution EBSD analysis were also carried out on shorter areas in order to reveal an eventual sub-granular structure. The results of these analysis are reported in figures 3.18 and 3.19 as IPF maps. On the horizontal plane it is possible to note the prevalence of grains with a $\langle 100 \rangle$ texture along the build direction as already discussed in the previous paragraph, but no new noteworthy features are visible. On the contrary the high resolution EBSD analysis on the vertical plane reveals an interesting intragranular structure, in fact it is possible to distinguish distinct regions with a slight mis-orientation ($1-2^\circ$) inside the central grain. These

features indicate a zig-zag growth characterized by abrupt change of 90° in the growth direction.

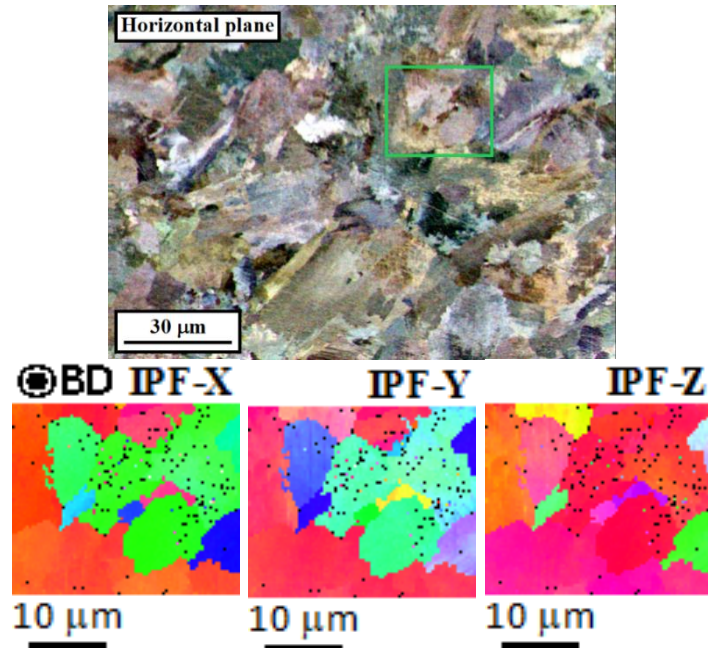


Figure 3.18. Argus image and higher resolution IPF maps on the horizontal plane of the areas marked by the green box. First published in [186].

Furthermore, a columnar intragranular structure (marked by the circle in figure 3.19) oriented along the growth direction can be note on the Z axis IPF map.

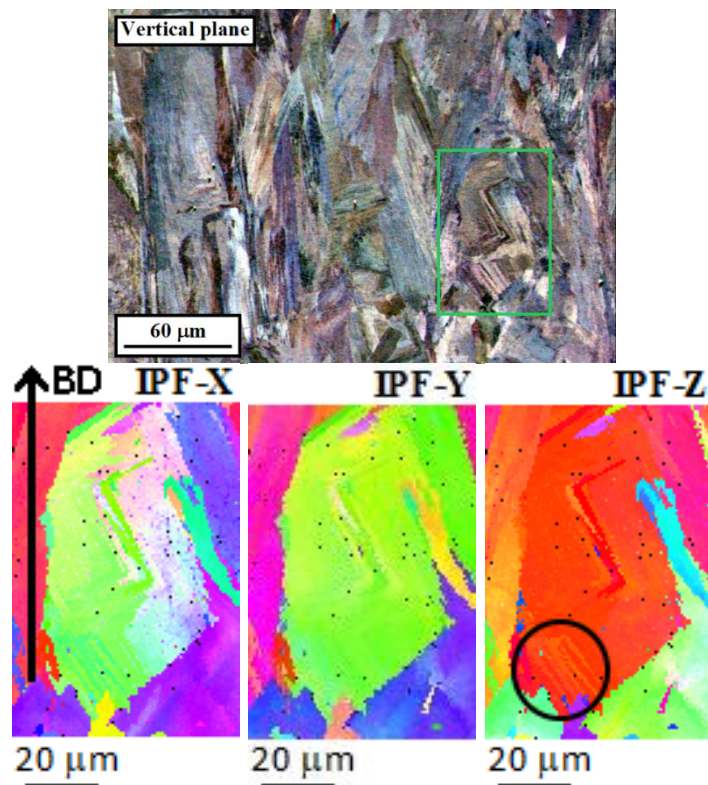


Figure 3.19. Argus image and higher resolution IPF maps on the vertical plane of the areas marked by the green box. Note the zig-zag features of the slightly mis-oriented intragranular zones and the columnar intragranular structure (black circle in the IPF-Z map). First published in [186].

These structures, which can be observed also from the optical micrographs of figures 3.10 and 3.11, are made by sets of parallel columnar dendrites, generally without secondary branches and with an arm spacing in the order of 1 μm . The EBSD analysis shows that the sub-granular dendrites share the same crystallographic orientation, no mis-orientation, or a very small one, exists between them.

The dendritic structure is shown in more detail with FESEM micrographs representative of the horizontal plane (figure 3.20) and of the vertical plane (figure 3.21).

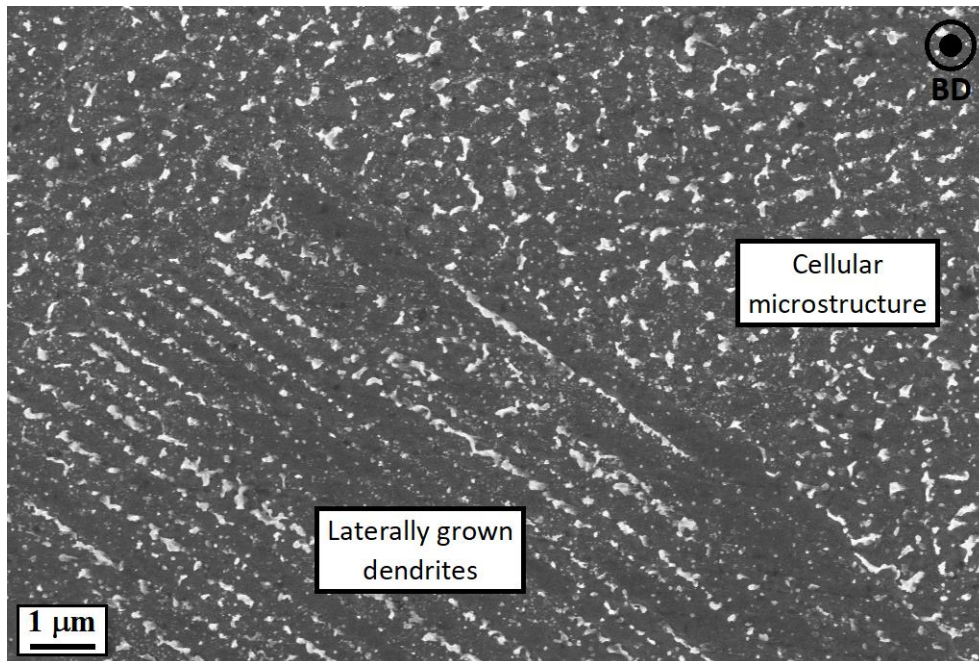


Figure 3.20. FESEM micrograph of the horizontal plane showing the sub-granular dendrite structure. Sets of dendrites grown parallel and perpendicular to the Building Direction (BD) are visible.

From these images, it is possible to note that, generally, the dendrites tend to develop aligned to the building direction of the sample. Therefore, on the horizontal plane most of the colonies of dendrites are cut along their transversal cross section and then the so called cellular microstructure can be observed (figure 3.20). However, it is also possible to find some exceptions to this general rule, that are regions in which the growth axis of the dendrites is not oriented along the building direction. An example of this is clearly visible in figure 3.20, where the lateral side of a set of dendrites can be observed on the horizontal plane.

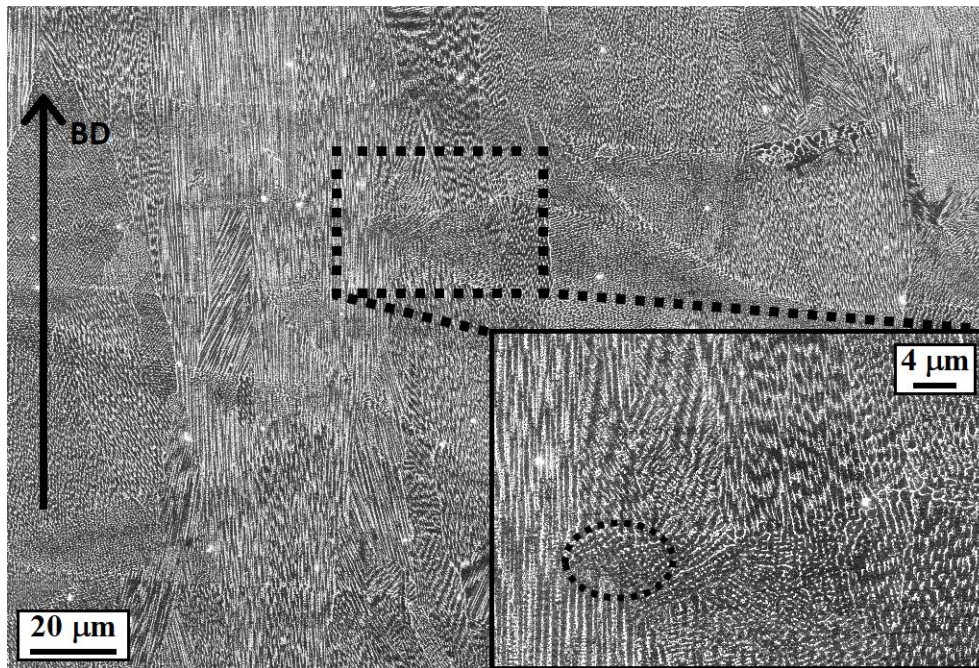


Figure 3.21. FESEM micrographs of the vertical plane. Most of the columnar dendrites are parallel to the Building Direction (BD), but some changes in the growth direction are visible along the melt pool boundaries (an example is indicated by the ellipse in the higher magnification micrograph).

The dendritic sub-granular structure is dependent from the laser related boundaries. Actually, it is possible to observe that abrupt changes of both the arm spacing and the growth direction of the columnar dendrites occurs in correspondence of some boundary between melt pool. Some examples of these abrupt changes are shown in the SEM micrographs of figures 3.22 and 3.23, collected on the vertical plane of the sample. The size of the dendrite tends to increase moving from the bottom of the melt pool toward the top of it, then it suddenly reduce when the boundaries between the next melt pool is crossed. This difference on the size is probably due to a variation of the cooling rate, which is very high at the bottom of the molten pool, where the material solidifies first, and decreases moving toward the top, where the last liquid solidifies.

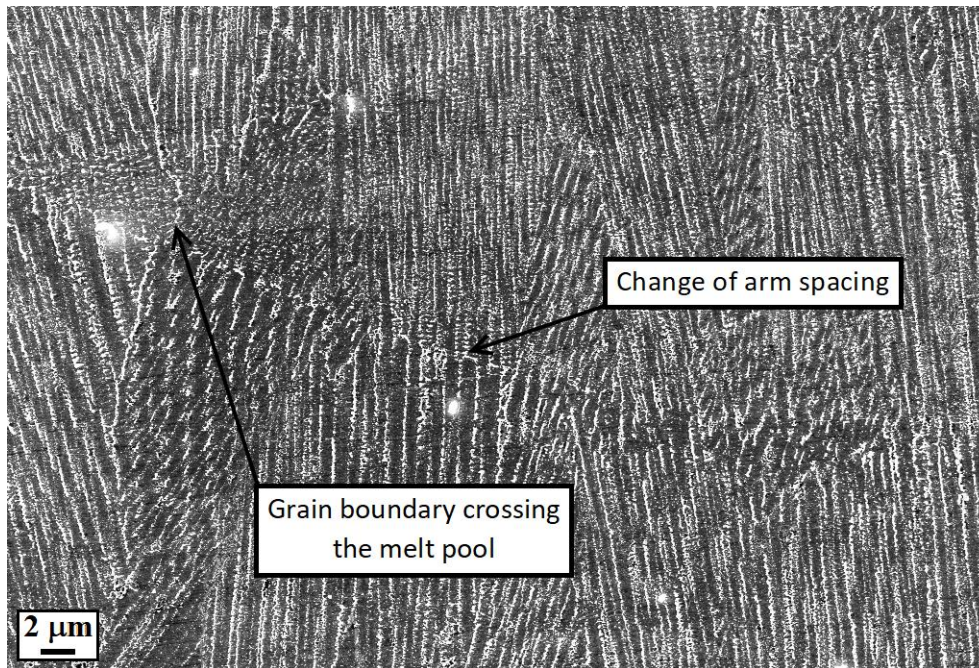


Figure 3.22. FESEM micrograph of the vertical plane showing the abrupt change of the dendrite arm spacing across a melt pool boundary.

The growth direction tends to be aligned with the building direction and it is generally maintained when a melt pool boundary is crossed near the center of the laser track. On the contrary it sometimes rotates by an angle of 90 degrees at laser track boundaries. The 90-degree rotation of the growth direction can also lead to a zig-zag growth of the grain as observed in the argus image of figure 3.19 and in the FESEM micrograph of figure 3.23.

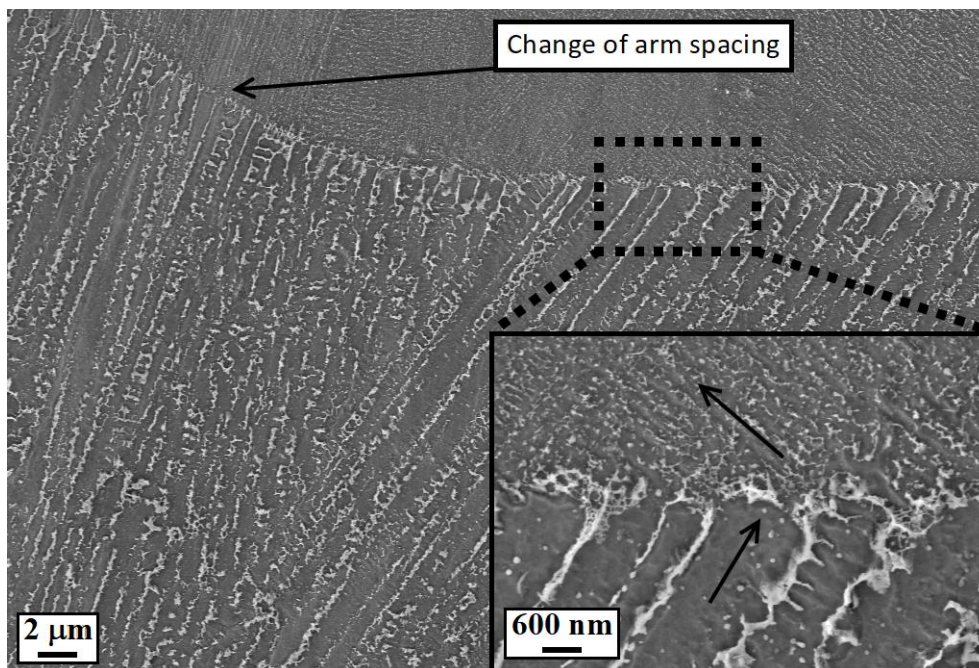


Figure 3.23. FESEM micrographs of the vertical plane showing the abrupt change of the dendrite arm spacing and growth direction (indicated by the arrows in the higher magnification micrograph) across a melt pool boundary. First published in [186].

3.2.4 Sub-dendrite structure

At the dendrite length scale, it is possible to observe the presence of second phases at the interdendritic boundaries that appear in bright contrast in the FESEM micrographs (figure 3.24). Such second phases are formed during the solidification in the SLM process and they can be classified in two categories: 1) small rounded precipitates of about 25-50 nm in size and 2) coarser precipitates of irregular shape of about 100-120 nm in size. The distribution of these precipitates is not uniform. Actually, relatively coarser and irregular ones (some examples are highlighted with brown ellipses in figure 3.24), are located predominantly at the triple points of contact between dendrites. Conversely, the rounded and finer precipitates, marked by green ellipses in figure 3.24, are located mostly near to dendrites boundaries and their density tends to decrease moving towards the core of the dendrites.

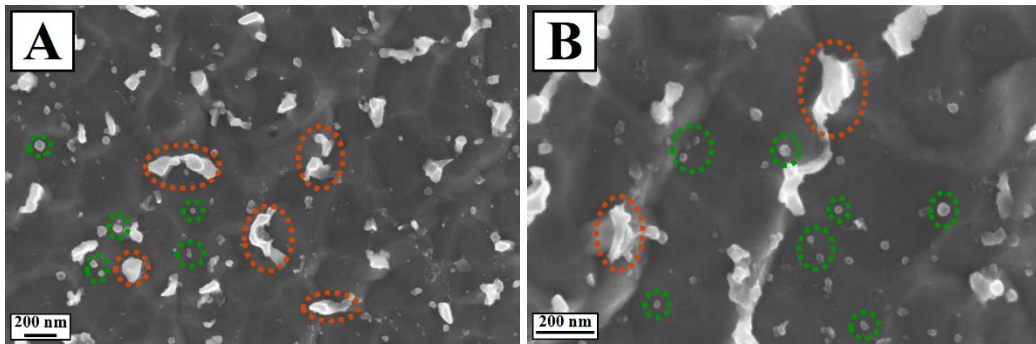


Figure 3.24. FESEM micrographs of the horizontal plane on zones in which the dendrites grew parallel (A) and perpendicular (B) to the building direction. Green and brown ellipses indicate some rounded and smaller precipitates and coarser precipitates of irregular shape, respectively.

The distribution of these second phases is not uniform throughout the material. Actually, isolated precipitates are formed in the internal zones of the laser tracks as reported in figure 3.20, whereas they tend to form a continuous network of second phases between the cells in the zones nearer the boundaries between laser tracks, as shown in the FESEM micrographs of figure 3.25.

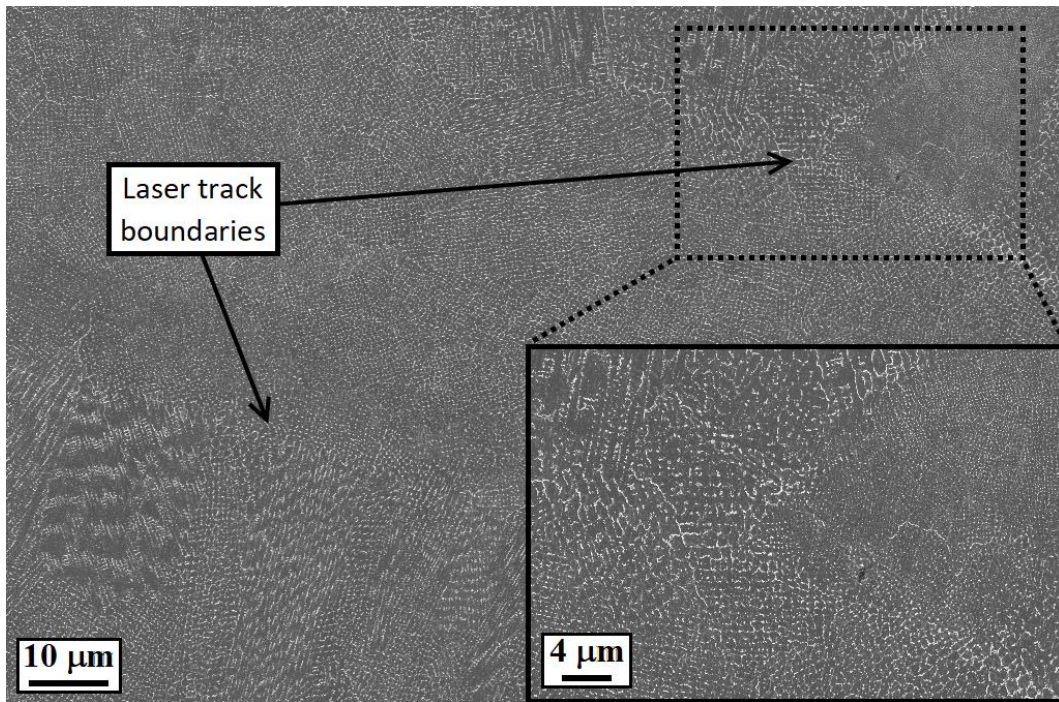


Figure 3.25. FESEM micrographs of the horizontal plane showing the formation of a continuous intercellular network of second phases along the laser track boundaries.

The two detected types of precipitates are also present on the vertical plane of the as built sample. In figure 3.26 it is possible to observe both the fine rounded precipitates (green ellipses), which are predominantly disposed near the edges of the dendrites, and the coarser precipitates (brown ellipses), which tend to assume an elongated shape and to dispose themselves long the interdendritic boundaries.

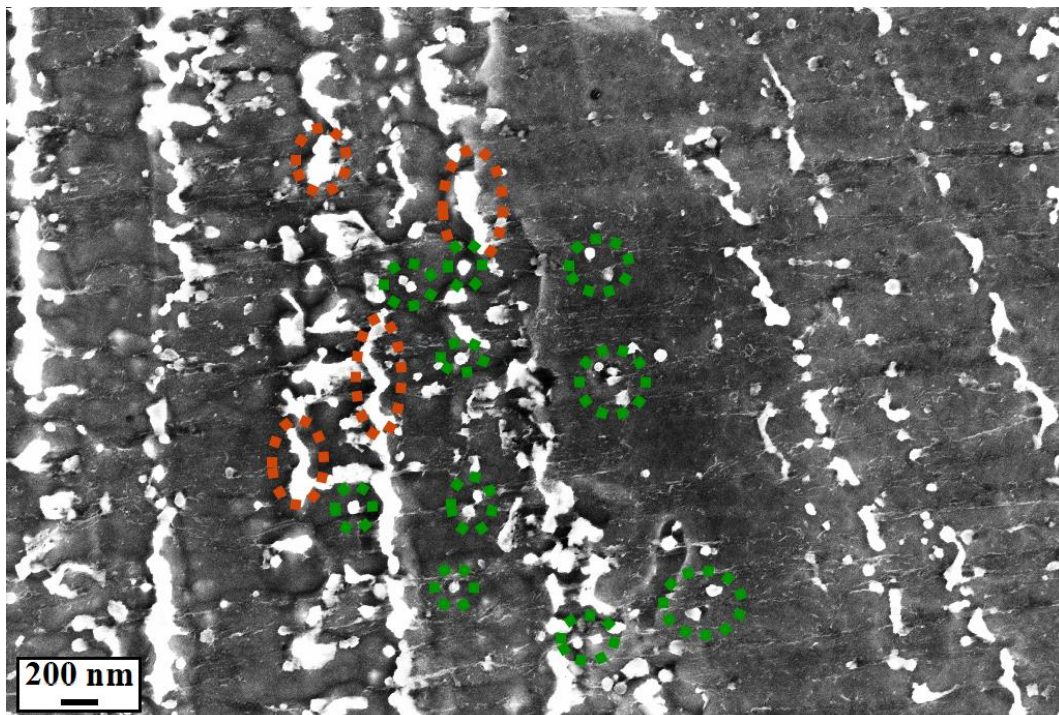


Figure 3.26. FESEM micrograph of the vertical plane. Green and brown ellipses indicate some rounded and smaller precipitates and coarser precipitates of irregular shape, respectively.

Besides the above reported two types of precipitates, a further population of extremely fine precipitates, dispersed inside the core of the dendrites, has been detected on some samples in the as built state. An example of this is given in figure 3.27, in which some of these small particles are highlighted by blue ellipses.

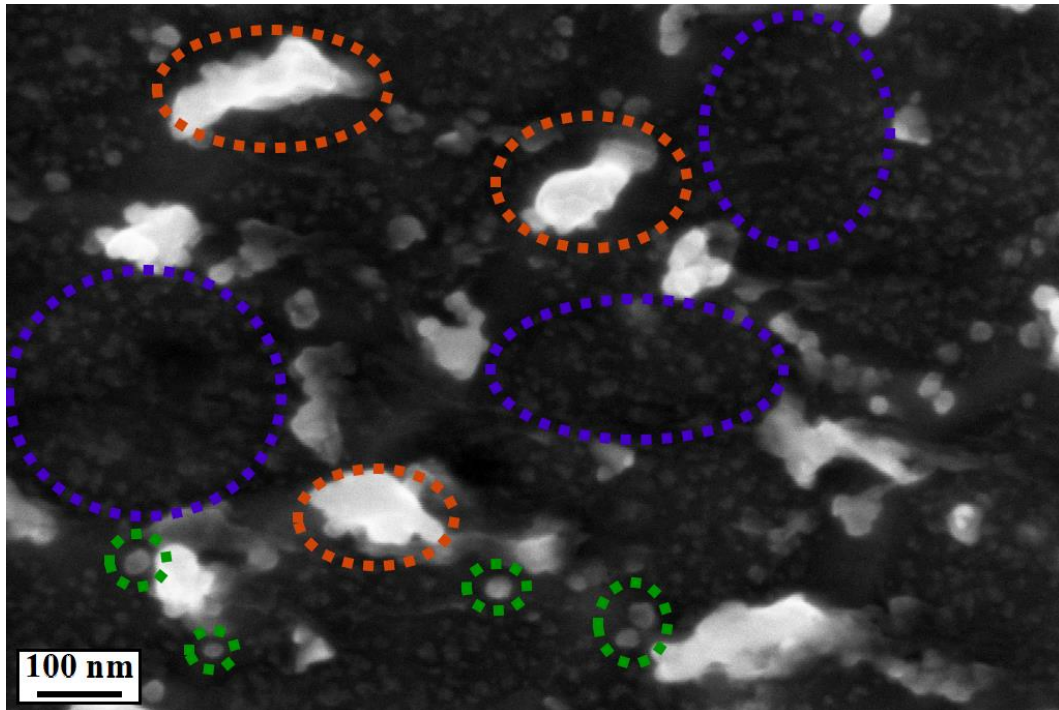


Figure 3.27. FESEM micrographs of the horizontal plane in a zone in which very small particles (blue ellipses) precipitate in the core of the cells in addition to the other two kinds of precipitates (green and brown ellipses, see figures 3.24 and 3.26). First published in [194].

To further deepen the study of these features the structure of a single dendrite was analyzed by TEM. In figure 3.28, STEM images are reported showing the presence of a high density of dislocations which tend to accumulate at the edge of the dendrite and, in particular, around the interdendritic precipitates.

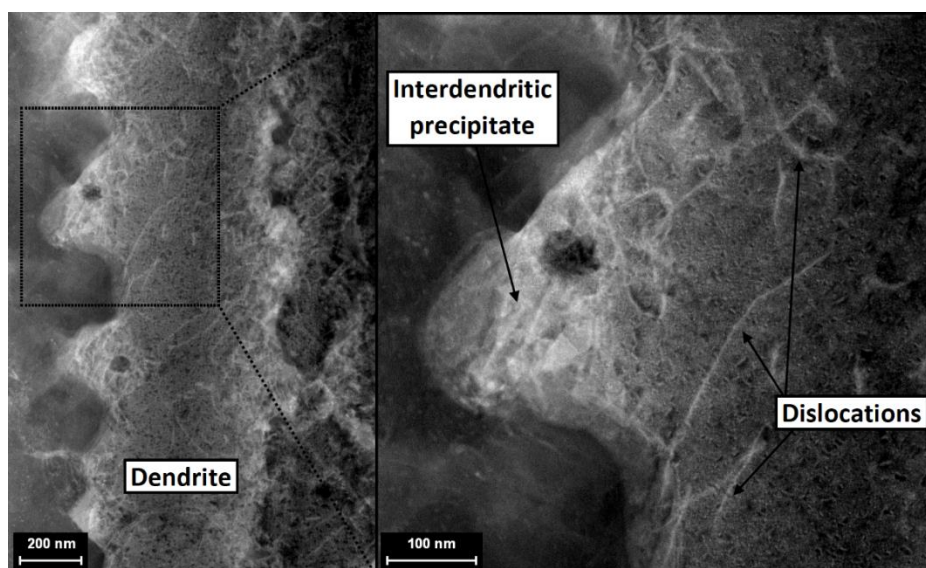


Figure 3.28. STEM images at the dendrite length scale showing the dislocations around a interdendritic precipitate. First published in [186].

The EDS line analysis along the width of the dendrite shows the distribution of the alloying elements at the length scale of a single dendrite. It is possible to observe that Nb and Ti and, to a lesser extent, Mo and Al tend to segregate at the interdendritic boundaries, instead the contents of Ni, Cr and Fe are higher in the core of the dendrite and decrease toward the boundaries. The point EDS analysis reported in figure 3.29 indicates that the detected precipitates are rich in Nb, Mo and Ti, and thus they form at the interdendritic boundaries where these elements tend to preferentially segregate. The elemental composition detected through EDS analysis of these precipitates, together with their morphology and disposition inside the dendrite, suggests that the small rounded precipitates are carbides rich in Nb and Ti, instead the coarser compounds of irregular shape are intermetallic Laves phases.

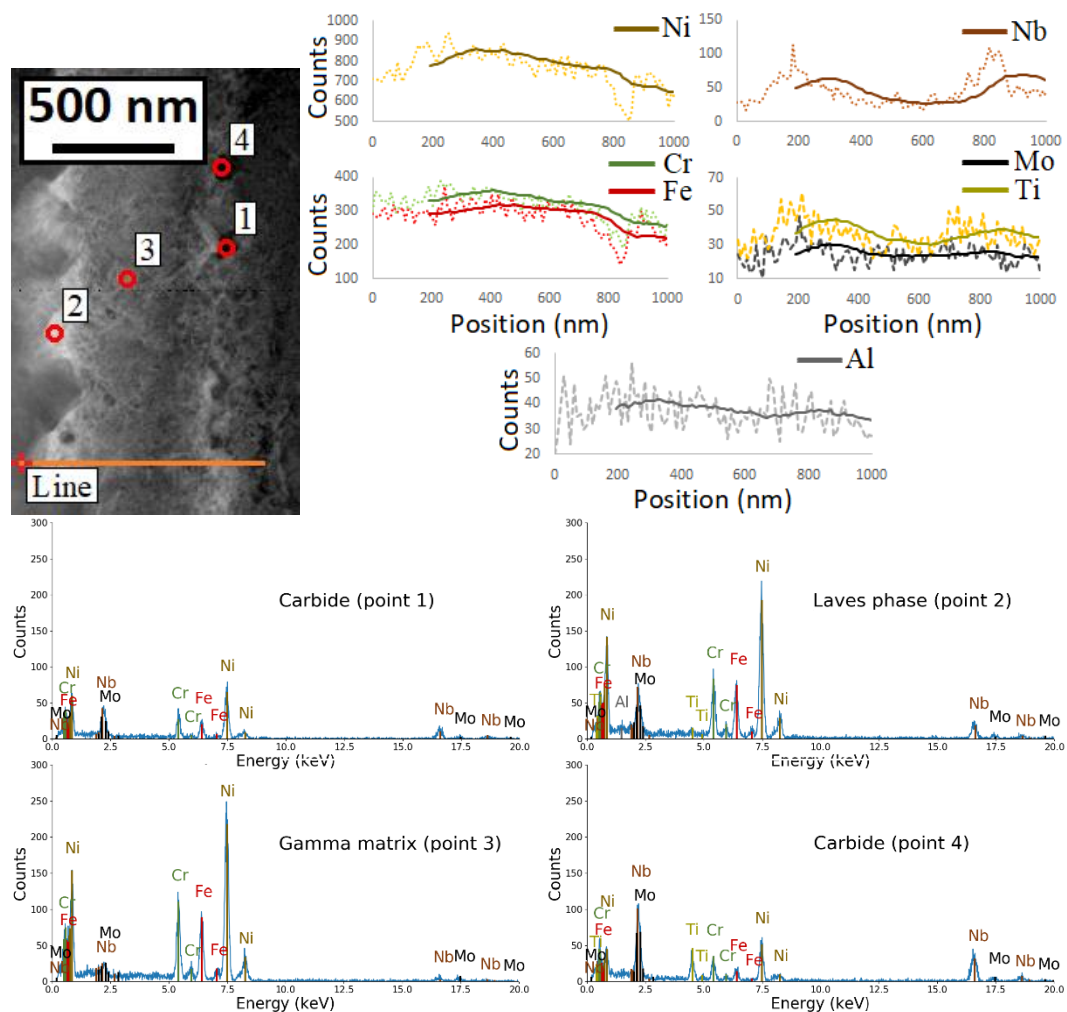


Figure 3.29. EDS analysis: line analysis across the dendrite showing the microsegregation of the alloying elements, point analysis on the matrix (point 3) and on the precipitates (carbides, points 1 and 4, and Laves, point 1). First published in [186].

The SAED patterns shown in figure 3.30 were collected respectively on the two side of the boundary between the dendrite and an interdendritic precipitate.

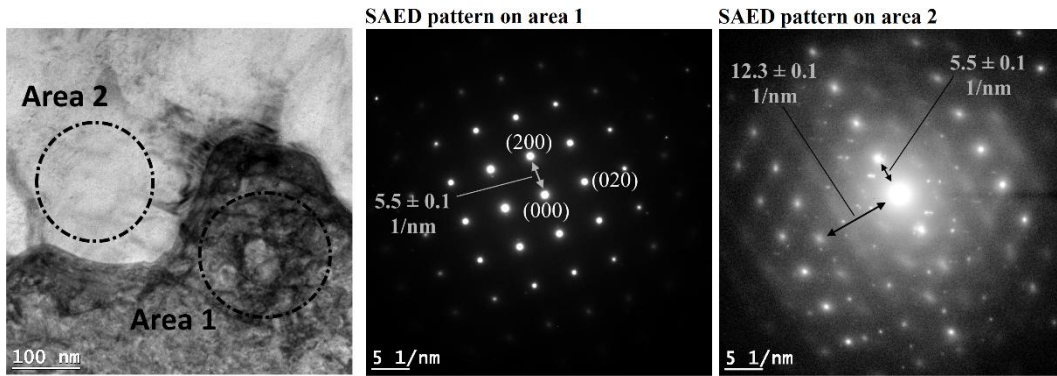


Figure 3.30. TEM image showing the matrix γ phase (dark contrast, area 1) and an interdendritic precipitate (bright contrast, area 2). Selective Area Electron Diffraction (SAED) patterns taken along the $[001]$ Zone Axis of the γ phase. First published in [186].

The SAED pattern of area 1, got from the dendrite portion, clearly indicates the face centered cubic structure of the γ matrix and the interplanar distances are very close to the theoretical values (equation 3.1):

$$\frac{1}{d_{\{200\}}} = \frac{2}{a} \cong 5.56 \text{ 1/nm} \quad \text{eq. 3.1}$$

Note that the $\{100\}$ spots are systematically absent because of kinematic extinctions (equation 2.9).

The interpretation of the SAED pattern of area 2 is more difficult. The figure is given by a superposition of different patterns, which indicates the presence of multiple phases at the interdendritic boundary. The cubic arrangement of spots circled in red in figure 3.31-A is equal to the one obtained from area 1, due to the γ phase, furthermore another phase is present which regular pattern of spots circled in green can be observed.

It is possible to assume that area 2 is made of an eutectic Laves/ γ mixture formed at the end of the solidification. Laves is the most likely phase that can generate the observed SAED pattern as shown in the following part of this paragraph. No other phases commonly found in Inconel 718 alloy (paragraph 1.3.1) can be considered as suitable candidates because their crystallographic structure and lattice parameters [18] [178] are not compatible with the experimental SAED pattern. Some examples of SAED patterns of γ' , γ'' and δ phases and MC carbides in Inconel 718 alloy are available for comparison [9] [50].

The arrangement of the spots circled in green in figure 3.31-A can be reproduced by translating the two parallelograms shown in figure 3.31-B; the resultant pattern contains some extra spots, marked with red crosses, which are not present in the experimental one. If these extra spots are added, the pattern coincides with the $[1\bar{1}2]$ Zone Axis of the Laves hexagonal structure, as shown in figure 3.31-C.

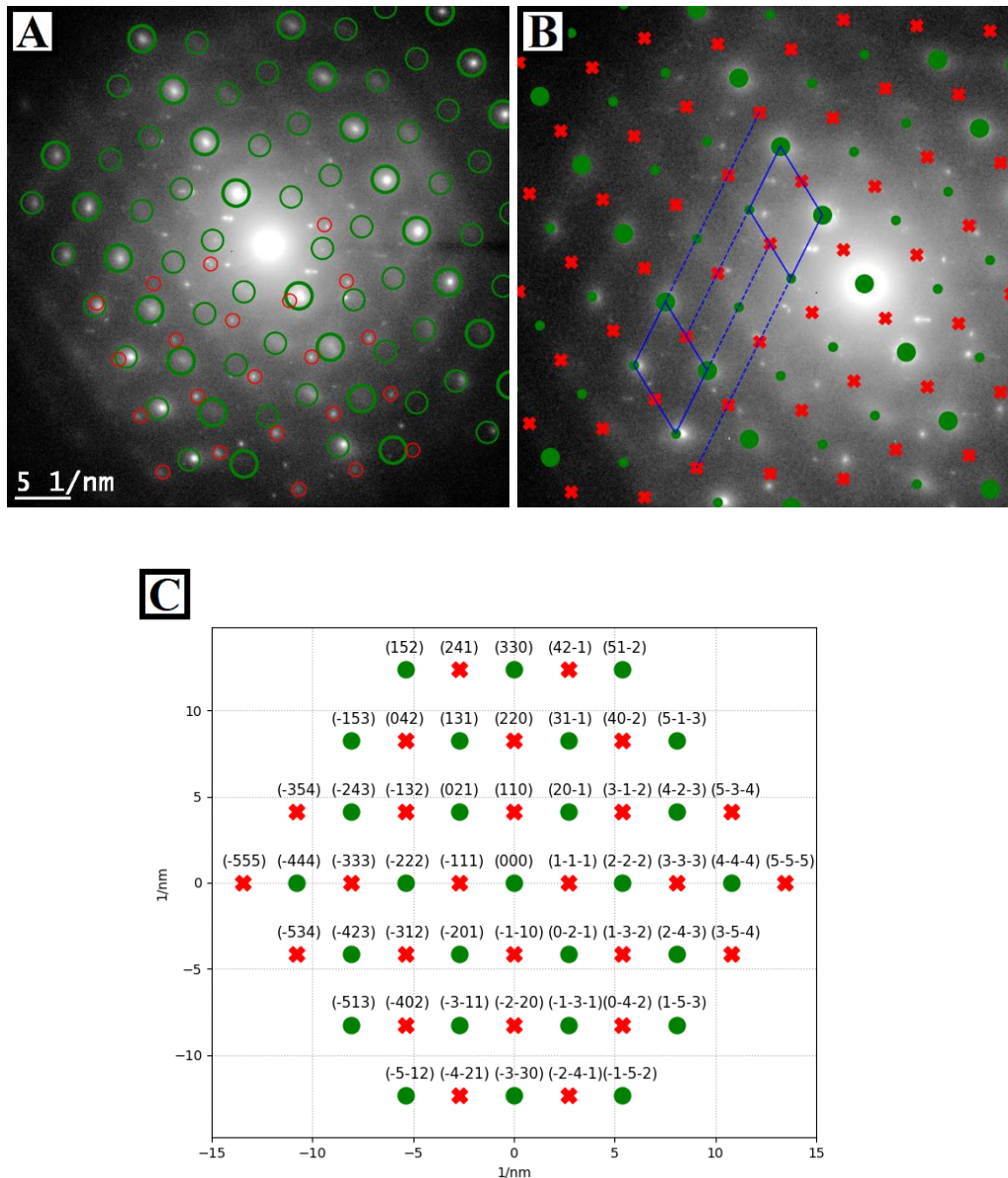


Figure 3.31. SAED pattern on area 2 of figure 3.30 showing the spots given by the γ phase, circled in red, and the ones supposed to be due to the Laves phase, circled in green (A). Construction of the second pattern by translating the repetitive unit drawn in blue and extra spots marked with red crosses (B). Indexed calculated pattern at the $[1\bar{1}2]$ Zone Axis of the Laves structure (C).

The two measured distances between spots shown at figure 3.30 are consistent with the theoretical lattice parameters (equation 3.2):

$$\frac{1}{d_{\{330\}}} = \frac{6}{a} \cong 12.37 \text{ 1/nm}$$

$$\frac{1}{d_{\{222\}}} = \sqrt{\frac{16}{3a^2} + \frac{4}{c^2}} \cong 5.39 \text{ 1/nm} \quad \text{eq. 3.2}$$

The experimental pattern is given by strong spots rows with $h + k = 3N$ and by weaker spots rows with $h + k \neq 3N$, where N is an integer and h, k, l are the

Miller's indices of the lattice planes. In the strong rows, the spots with l odd are absent, instead the spots with l even are absent in the weaker rows. The observed systematic absences cannot be explained by the cancellation of the structure factor S in equation 2.6 calculated with the set of atoms in the unit cell of the Laves structure (shown in figure 1.4), but they could be caused by the interference of the waves scattered by crystalline domains deriving from the presence of extended defects as dislocations, twins and stacking faults.

In particular, figure 3.32-B shows that a sequence of slips $s = (1/6)[223]$ on non-basal planes has the effect to introduce crystalline domains characterized by the follow displacement vectors \mathbf{D}_m : $D_0 = (0,0,0)$, $D_1 = (1/3, 1/3, 1/2)$, $D_2 = (2/3, 2/3, 0)$, $D_3 = (0,0, 1/2)$, $D_4 = (1/3, 1/3, 0)$, $D_5 = (2/3, 2/3, 1/2)$, which determine the kinematic extinction of the spots with l odd in the strong rows and of all the spots with $h + k \neq 3N$ because of the cancellation of the lattice factor L in equation 2.6. The modified lattice factor L' , which takes into account the phase difference between the waves scattered by crystalline domains, is given by equation 3.3:

$$\begin{aligned} L'(\mathbf{R}) &= \sum_p e^{-2\pi i \mathbf{U}'_p \cdot \mathbf{R}} = \sum_q \sum_{m=0}^5 e^{-2\pi i (\mathbf{U}_q + \mathbf{D}_m) \cdot \mathbf{R}} = \\ &= \sum_q e^{-2\pi i \mathbf{U}_q \cdot \mathbf{R}} \sum_{m=0}^5 f_m e^{-2\pi i \mathbf{D}_m \cdot \mathbf{R}} = L(\mathbf{R}) \cdot C(\mathbf{R}) \end{aligned} \quad \text{eq. 3.3}$$

where $\mathbf{U}'_p = \mathbf{U}_q + \mathbf{D}_m$ is the vector position of the p -th atom after the slip, as shown in figure 3.32-A; L is the lattice factor when no defects are presents and C is the corrective factor depending on the displacement vectors between the crystalline domains.

The model shown in figure 3.32-B assumes the different kinds of crystalline domains to have the same volume, i.e. the same number of unit cells, however small deviations from this hypothesis can be tolerated because they cause the formation of spots with an intensity too low to be detected and which can be considered as practically absent.

The detection of the spots with l odd in the weaker rows can be explained by assuming the occurrence of slips $s' = (1/3)[110]$ in proper positions. Figure 3.32-C shows, as an example, how a slips sequence like $s'ss'sss$ has the effect to generate a pattern qualitatively equal to that obtained experimentally due to the introduction of the new displacement vectors $D'_1 = (1/3, 1/3, 0)$ and $D'_2 = (2/3, 2/3, 1/2)$.

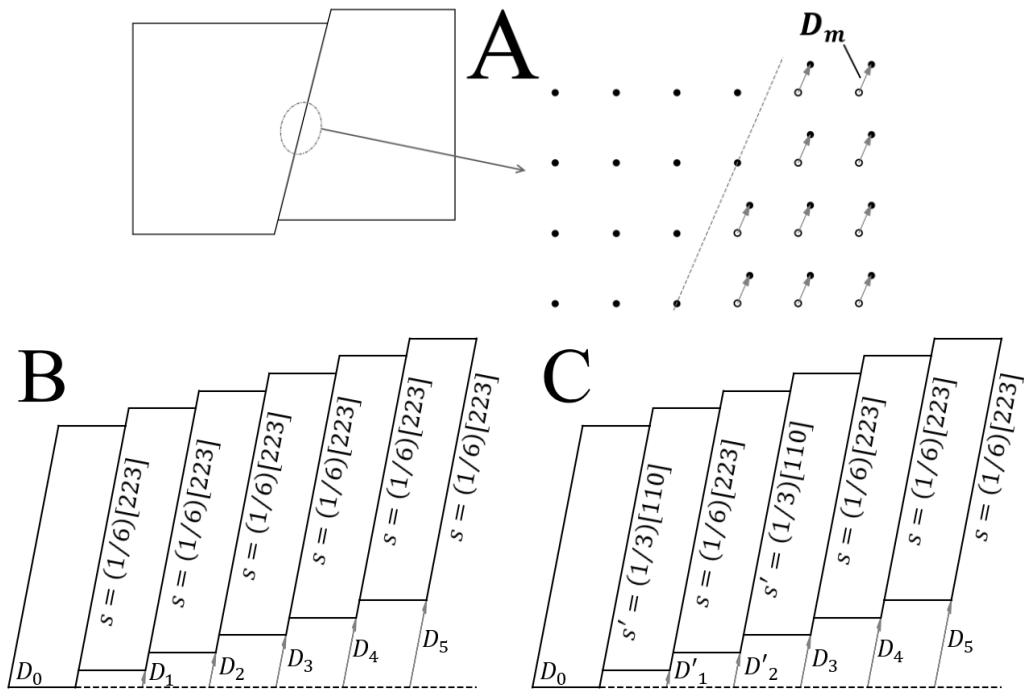


Figure 3.32. Scheme of the domain boundary along a slip and respective displacement vector D_m (A). Domains formed by a sequence of s slips (B) and by a slips sequence $s's's'ss$ (C). The configuration in B causes the kinematic extinction of the spots with l odd in the strong rows and of all the spots with $h + k \neq 3N$; the configuration in C restore the weaker spots.

The presence of the s and s' slips can be explained by the deformation caused by the stresses developed during the SLM process. Further research is required to investigate the arrangement of the crystal defects and fully clarify the reason of the observed systematic absences; however this would be beyond the scope of this thesis. The above discussion and the proposed solution have just the aim to demonstrate that the recorded SAED pattern can in principle be generated by the hexagonal Laves phase structure.

3.2.5 Origin of the as built microstructural features

The microstructural features observed at different length scale in the as built material are caused by the particular manufacturing conditions that are established during the SLM process. The high microstructural heterogeneity of the as built state is due to the several solidification steps that characterize the construction of the product. The laser passage causes the local fusion of the powder bed, but the penetration of the beam is sufficient to partially melt also the underlying material, formed during the deposition of the previous layer, and to thermally re-treat few layers below the melt ones. The molten pools, that are generated during the laser scans, are rapidly cooled down and the heat adsorbed from the laser beam is transferred to the environment and the substrate below through conduction, convection and radiation [200]. The evolution of the temperature field in the molten pool is extremely complex and characterized by high thermal gradients and cooling rates [201] [202] [203], which in turns affect the solidification of the alloy.

Therefore, the resulting microstructure can vary between different zones depending on the established local cooling conditions.

On the base of the observations reported in the previous paragraphs, it is possible to state that the solidification occurs mainly through the follow two mechanisms:

- heterogeneous nucleation of new grains at the solid/liquid interface;
- epitaxial growth of the partially re-melted grains under the molten pool.

The epitaxial growth allows the grains to maintain their crystallographic orientation during several steps of melting and re-solidification. Therefore, the grains are not constrained by the thickness of a single powder layer, but they can develop through a large number of layers as assessed both with optical microscope (figure 3.11) and EBSD analysis (figure 3.12-B).

The strong crystallographic texture detected through EBSD analysis (figures 3.13, 3.14 and 3.15) is due to the growth of crystals that belong to the cubic lattice systems is faster along the $\langle 100 \rangle$ crystallographic directions. Because of this asymmetry in the crystallographic direction, the orientation of the grains has an influence on the growth speed of them: the lower the misalignment angle between the $\langle 100 \rangle$ axis of the crystal the local thermal gradient, the faster is the growth of the crystal along the direction of the gradient. Therefore, a competitive growth occurs during the solidification of each molten pool [204], in which more favorably oriented grains prevail on the others.

If at the solid/liquid interface there are some favored oriented grains, the solidification of the liquid volume of the molten pool occurs predominantly by epitaxial growth of them. Conversely, if at the solidification front there are not favored oriented grains, then new grains with random orientation can form through the heterogeneous nucleation process, however only the grains which are nucleated with a favored orientation can further develop.

At the length scale of 10^{-5} - 10^{-6} m, it is possible to observe that the grain growth occurs by destabilization of the planar front of solidification and consequent formation and advancement of columnar dendrites without secondary branches. The dendrite formation is due to the thermal gradients in the molten pool, that lead to constitutional undercooled liquid ahead the dendrite tips, and the high solidification velocity (see paragraph 1.3.2.2). The dendrites that are originated from the same grain have virtually the same crystallographic orientation, however a small mis-orientation angle between sub-granular dendrites ($< 2^\circ$) is reported by Divya et al. [169] for SLM CM247LC Ni alloy and by Chlebus et al. [175] and Choi et al. [154] for SLM Inconel 718 alloy. The greatest resolution used for the EBSD analysis in this study, i.e. $0.71 \mu\text{m}/\text{pixel}$, is not sufficient to detect mis-orientation at the length scale of the dendrites, however the EBSD analysis has revealed the presence of sub-granular domains delimited by low-angle boundaries inside the largest grains. Unlike the material obtained with conventional cast and wrought processes, the grains obtained through SLM technique have not a well-defined and

uniform crystallographic orientation, but rather an orientation gradient can form inside them due to the slight mis-orientation between the sub-granular dendrites. It is possible to suppose that the sub-granular domains shown in figure 3.12 form because of an atoms rearrangement that allow the reduction of the mis-orientation energy related to the orientation gradient. This rearrangement process is probably activated by the repeated thermal cycles at which each layer is subjected during the deposition of the following ones.

Slightly mis-oriented intragranular zones are also visible at figure 3.19, revealing the effective presence of a sub-granular structure, made by slightly mis-oriented colonies of dendrites, that develops following a zig-zag path with abrupt variation in the growth direction of 90 degrees. A systematic zig-zag growth with 90 degrees angles is reported also in other studies [165] [166] [204] in which a powder injection technology is adopted and the scan direction is alternated at each deposition of a new layer. This occurs because the direction of the horizontal component of the thermal fluxes in the molten pool to inverted at each layer. Even Deng et al. observed a rotation of 90° of the growth direction of the dendrite across the melt pool boundaries without a change in the crystallographic orientation in an Inconel 718 alloy produced through SLM [160].

In the present work, the zig-zag growth of the dendrites is only occasionally observed due to the scan strategy used to make the samples, that includes a rotation of 67° of the scan direction at each layer and prevents periodic repetitions of the direction of the thermal gradients between successive depositions. This allows to obtain a greater isotropy on the horizontal plane, where no crystallographic texture was revealed. Conversely, a $\langle 101 \rangle$ crystallographic texture can originate on the horizontal plane if the rotation of the scan direction is not applied [154] [205].

On a macroscopic scale, the thermal fluxes are aligned on average along the building direction during the SLM process. This determines the elongated shape of the grains on the vertical plane. However, at the length scale of the molten pools, the local thermal gradients can be highly complex because they depend on the adopted process parameters and scan strategy and they are influenced by liquid fluxes due to convective phenomena and the Marangoni effect, deriving from a surface tension gradient due to the temperature gradient in the molten pool [141] [206]. As a first approximation, it is possible to consider the thermal fluxes as aligned along the direction normal to the arc shaped solidification front [151] [204] [207].

The dendrites which have a favored crystallographic orientation, that means one of the $\langle 100 \rangle$ axis oriented at a low angle respect to the local heat flux, can grow more quickly and so prevail against the ones not favorably oriented [208]. Therefore, whenever a new molten pool is formed during the SLM process, the partially melted dendrites can evolve by following one of these three possibilities, schematically illustrated in figure 3.33:

1. if the $\langle 100 \rangle$ axes, along which the growth of the dendrite has occurred during the previous layer deposition, is still aligned along the local thermal

- flux that establishes at the solidification front, then the dendrite can grow again along the same direction (e.g. like in figure 3.22);
- if the local thermal gradient is not aligned to any $\langle 100 \rangle$ axis, the growth of the dendrite is stopped and the solidification can occur through the growth of other favored oriented dendrites or in alternative, in absence of any favorably oriented dendrites, through the heterogeneous nucleation of new grains at the solid/liquid interface and the selection of the ones with a favored crystallographic orientation;
 - if the $\langle 100 \rangle$ axes, along which the growth of the dendrite has occurred during previous layer deposition, is no more favorably oriented with respect to the local thermal flux, but one of the other two $\langle 100 \rangle$ axis of the system is aligned to it, then the growth direction of the dendrite changes through a 90° degrees angle rotation (e.g. like in figure 3.23).

The arm spacing of the dendrites is related to the cooling rate. In this study, the observed mean arm spacing is very small, in the order of $0.5\text{-}1\ \mu\text{m}$, and it is comparable to what is generally reported in the literature [139] [140] [142] [156] [159] [173] [183]. In other works [158] [177] [179], where higher laser power and lower scan speed are adopted, larger arm spacings, from 2 to about $20\ \mu\text{m}$, are obtained.

The micrograph collected on the vertical plane demonstrate that the cooling rate is not constant during the solidification of the molten pool. In fact, the dendrite size tends to be lower at the base of the melt pool, where the solidification occurred with a high cooling rate, and to increase moving toward the upper portion of the melt pool because of the gradual reduction of the cooling rate. Abrupt variations in the dendrite growth direction and arm spacing in the laser overlapping regions are also reported by Mostafa et al. [178]. The change of the dendrite size across a melt pool boundary is also shown in the paper of Wan et al. [151].

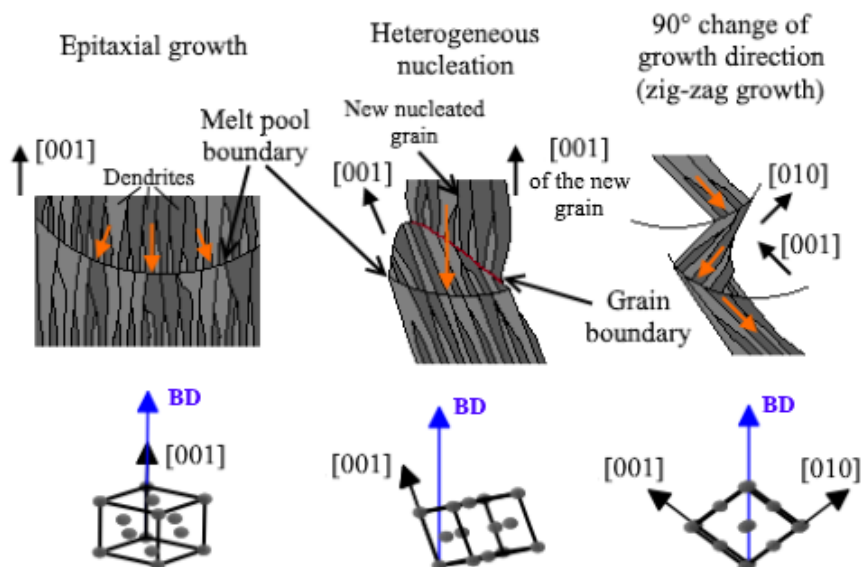


Figure 3.33. Scheme illustrating the possible ways in which the solidification of a new melt pool can occur depending on the crystallographic orientation of the dendrites with respect to the local thermal fluxes (orange arrows).

The microsegregation of the alloying elements and the presence of carbides and Laves phases at the interdendritic boundaries can be explained by considering the solidification path followed by Inconel 718 alloy in conditions of rapid cooling determined by Knorovsky and discussed at paragraph 1.3.2.3. Solidification proceeds through the advancement of the austenitic γ phase dendrites, during which the remaining liquid between the growing dendrites is progressively enriched in those elements having a partition coefficients k lower than 1 (table 1.6), i.e. Nb, Ti, Mo and Al, in accordance to what obtained with the line EDS analysis of figure 3.29. In particular, Nb is strongly segregated because of its very low k coefficient and its large atomic radius, that leads to a low diffusivity in the γ phase that prevents redistribution through solid state diffusion.

The rejection of the alloying elements with $k < 1$ in the liquid keep going until carbides start to form near the interdendritic boundaries through the binary eutectic reaction $L \rightarrow L + \gamma + \text{carbides}$. The solidification terminates with the binary eutectic reaction $L \rightarrow \gamma + \text{Laves}$, which take place at the triple points of contact between dendrites where the last remaining liquid is concentrated. The scheme reported in figure 3.34 illustrates the above described solidification steps and the resultant spatial distribution of the second phases at the dendrites length scale.

The greater cooling rate at the laser related boundaries is also confirmed by the presence of a higher volume fraction of eutectic products along them, with consequent formation of an interdendritic network (figure 3.25). According to the Brody-Flemings equation 1.5, a faster local solidification leads to a greater quantity of remaining liquid when the eutectic transformations occur, therefore a higher level of microsegregation at the interdendritic boundaries.

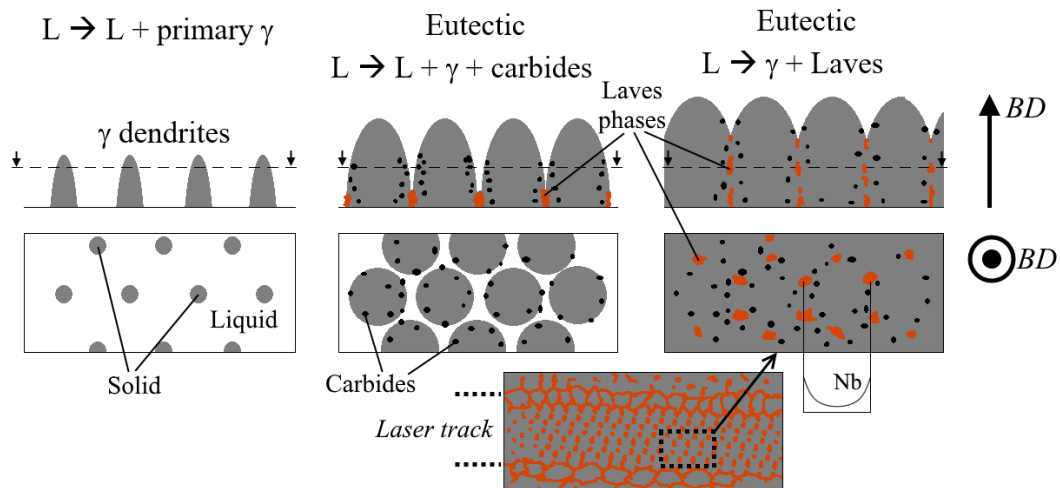


Figure 3.34. Schematic representation of the solidification process and consequent distribution of the eutectic products (carbides and Laves phases) in the dendrite structure.

The microstructural heterogeneity of Inconel 718 produced through SLM process, that is observable at this length scale, can be further increased due to the repeated thermal cycles at which the solidified material is submitted because of the heat coming from the deposition of the subsequent layers [153]. As already discussed in the literature review section (paragraph 1.4.2.1), Tian et al. [177] report

that these thermal cycles can eventually cause a partial dissolution of the interdendritic eutectic products and a redistribution of the solute, in particular of Nb, in the core of the dendrite. After that, the subsequent thermal peaks with decreasing intensity cause the precipitation of γ'' phases. A similar phenomenon can explain the occasional presence of the nanometric particles in the cells core in the as built state (e.g. blue ellipses in figure 3.27), which could be γ' or γ'' precipitates formed due to the release of Ti, Al and Nb from the interdendritic eutectic products. Conversely, no signs of formation of plate-like δ precipitates were found in the as built material. The formation of the δ precipitates is probably inhibited by the too high cooling rates and by the Nb sequestration in the eutectic phases at the interdendritic boundaries.

In addition to the heterogeneous population of precipitates, dendrites are also characterized by the presence of dislocations, which indicate the development of internal stress states due to the high thermal gradients established in the deposited material and the thermal cycles during the SLM process. The dislocation density increases when moving towards the edge of the dendrite, furthermore they tend to accumulate at the interface between the γ matrix and the inter-dendritic precipitates, probably because of the stresses generated by the thermal expansion mismatch. The microsegregation of the alloying elements, with consequent formation of carbides and Laves phases, and the dislocation network at the interdendritic boundaries are also reported by Tucho et al. [183] at the as built state. The accumulation of dislocations at the interdendritic boundaries allows to accommodate the slight mis-orientation between the cells, as reported also in other studies [169] [209].

3.3 Conclusion

The preliminary study has demonstrated that is possible to obtain near full dense Inconel 718 samples if the process parameters are set near the values recommended by the powder supplier. The process is sufficiently robust to prevent the formation of an excessive number of pores or big microstructural alterations due to the variation of the laser power, scan speed or hatching distance in the investigated ranges. However, as a rule of thumb it is better to adopt intermediate VED value, because a low VED value leads to voids due to lack of fusion. On the contrary, too high VED values can cause formation of big porosities due to gas entrapment.

The microstructure of Inconel 718 alloy produced through SLM technique appears extremely complex, anisotropic and heterogeneous as a consequence of the particular process conditions. The complicate thermal history of the deposited material, which can vary between different zones, is the main responsible for this. The main observed microstructural features are due to the strongly oriented thermal gradients and high cooling rates established during the solidification of the molten pools, to remelting and resolidification in the overlapping regions of the laser scans and to the thermal cycles generated by the deposition of successive layers. All the

detected microstructural features of the as built material are summarized in the follow and classified on the base of their characteristic length scale:

Microstructural features at the length scale of 10^{-3} - 10^{-5} m:

- prevalence of crystalline grains stretched along the building direction of the sample and quite independent from the laser related boundaries;
- presence of sub-granular domains delimited by low-angle boundaries that form to accommodate the cumulative mis-orientation between the intragranular columnar dendrites;
- preferential crystallographic orientation of the grains, which tend to have a $\langle 100 \rangle$ aligned to the building direction of the sample;
- absence of crystallographic texture along the other spatial directions.

Microstructural features at the length scale of 10^{-5} - 10^{-6} m:

- sub-granular structure made by colonies of columnar dendrites without secondary branches and with an arm spacing of about 0.5-1 μm ;
- growth direction of the dendrites determined by the reciprocal orientation between the $\langle 100 \rangle$ crystallographic axes and the local heat flux, which can cause occasional sharp turns of the dendrites at boundaries between melt pools with consequent formation of zig-zag sub-granular structure;
- slight increase of the dendrite size moving towards the upper part of the melt pool because of differences on the local cooling rate.

Microstructural features at the length scale of 10^{-6} - 10^{-8} m:

- not uniform distribution of the alloying elements inside the dendrite because of microsegregation phenomenon occurred during the solidification;
- formation of eutectic compounds, i.e. carbides and Laves phases, at the interdendritic boundaries;
- interdendritic continuous network of second phases at the laser related boundaries;
- occasional presence of a population of very small particles on the core of the dendrites;
- high density of dislocation along the edges of the dendrites and around the interdendritic precipitates.

The microstructural heterogeneity of the material at the as built state requires a mandatory post-heat treatment of solutioning and homogenization. The main purpose of this treatment is to dissolve the second phases at the inter-dendritic boundaries, in particular the brittle Laves phases, and to release Nb and the other alloying elements that are needed to obtain a uniform distribution of γ' and γ'' strengthening precipitates during the annealing steps. The microstructural evolution of the as built material after the successive heat treatment is investigated in the follow chapter.

Chapter 4

Study on the effect of the post heat treatment

After the production through Selective Laser Melting (SLM), the as built Inconel 718 possesses some microstructural features that can be advantageous for specific applications. For instance, it has very fine sub-granular dendritic structure, which confer mechanical strengthening to the alloy, and grains elongated with respect to the building direction, that can be favorable to the creep resistance when the load is applied along this direction. However, the as built state is also affected by negative aspects which preclude its direct use after the SLM process. To this purpose it is worthwhile to mention the material anisotropy and the microstructural inhomogeneity. In particular, the microsegregation of the alloying elements at the dendrites scale can lead to negative effects on the oxidation and corrosion resistance, because it can hinder the formation of a uniform protective scale. Furthermore, the extensive presence of Laves phases can lead to embrittlement and lack of mechanical properties due to the blocking of the alloying elements that are thus not available for the precipitation of the strengthening phases γ' and γ'' .

For the above mentioned reasons, it is often necessary to submit the as built material to one or more post heat treatment(s) in order to correct the unwanted microstructural features and obtain the most suitable distribution of second phases for the final application. However, due to the peculiar initial situation arising from the SLM process, the microstructural evolution of the as built material during the heat treatments can strongly differ from that of the conventional ones.

In this chapter, the response of the SLM as built material is investigated using DSC and TMA thermal analysis to identify the potential heat treatment ranges. After that, the microstructure of the material after different solution treatments is studied in greater details to identify the best condition in terms of microstructural homogenization and of the population of the remaining second phases (this work has been previously published in [194]). The study proceeds with the optimization

of the complete cycle of heat treatment, consisting on a solution annealing step and two aging steps (see figure 1.19). The response of the solutioned material to the successive heat treatments is investigated through DSC and TMA thermal analysis in order to obtain the temperature ranges at which the precipitation of the γ' , γ'' and δ second phases occurs. Furthermore, the microstructural evolution of the material submitted to aging treatment at the identified temperatures is studied through XRD and FESEM analysis and measurements of the Vickers microhardness. Part of this work has been previously published in [186].

On the base of the obtained information, the impact of the parameters (temperatures and durations) concerning the solutioning and first aging step on the mechanical properties of the alloy is determined through Brinell hardness measurements. Finally, also the effect of temperature and time of the second aging step is considered. The resulting microstructure after each step during the complete heat treatment cycle is observed through FESEM analysis and discussed.

4.1 Microstructural response to thermal exposure

The first DSC analysis was carried out to identify the melting and solidification ranges of the alloy. The presence of the non-equilibrium eutectics in the as built material can lead to the formation of liquid phase at temperatures lower than the theoretical expected one. Figure 4.1 reports the DSC analysis into the fusion range. In comparing the heating and cooling curves, it is important to consider that the signal peaks associated to thermal phenomena are slightly shifted to higher temperatures during the heating run and to lower ones during the cooling stage. This is due to kinetics reasons and these shifts depend on the heating and cooling rates, respectively [210]. As a consequence, the melting and resolidification peaks (figure 4.1) are not perfectly overlapped because of these shifts.

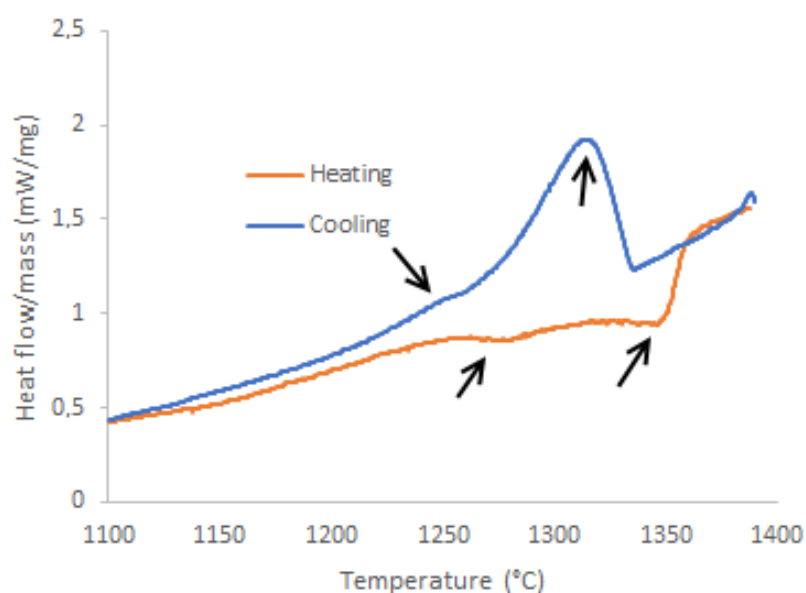


Figure 4.1. DSC analysis across the melting/solidification range. The detected peaks are indicated by the arrows.

During the heating step, two distinct endothermic peaks are detected. They are probably due to the formation of the first liquid phase at about 1230-1250°C in the interdendritic zones, where the low melting eutectics products are preferably located, and the final melting of the γ phase at about 1320-1340°C, respectively. For comparison, the melting ranges of Inconel 718 manufactured through conventional processes are 1205-1345°C for the cast and 1260-1335°C for the wrought products [66].

During the cooling stage, the exothermic peak related to solidification of the γ phase is the prevalent part of the collected signal. A very slight peak is also present at lower temperature and it is probably due to the occurring of the eutectic reactions that complete the solidification. The asymmetry between the heating and the cooling detected curves is due to the initial far from the equilibrium condition of the AM as built material, characterized by a large volume fraction of eutectic products. The solidification range during the cooling stage was assessed using a 28°C/min cooling rate, that is a very low cooling rate with respect to the one that occurs during the SLM process. Therefore, this cooling condition leads to a markedly different solidified microstructure and, in particular, to a lower level of eutectics formation than in real AM process.

Once determined the starting point of melting, thermal runs until 1200°C were carried out to detect the thermal phenomena that take place in the solid state using DSC and TMA combined techniques. DSC recorded curves for as built samples carried out at different heating rates are reported in figure 4.2. These samples were removed along the horizontal plane, i.e. on the plane perpendicular to the building direction. It is possible to note that the detected peaks become more intense and slightly shifted to higher temperature when the heating rate is increased. Therefore, a clearer signal of such peaks is obtained by adopting a higher heating rate.

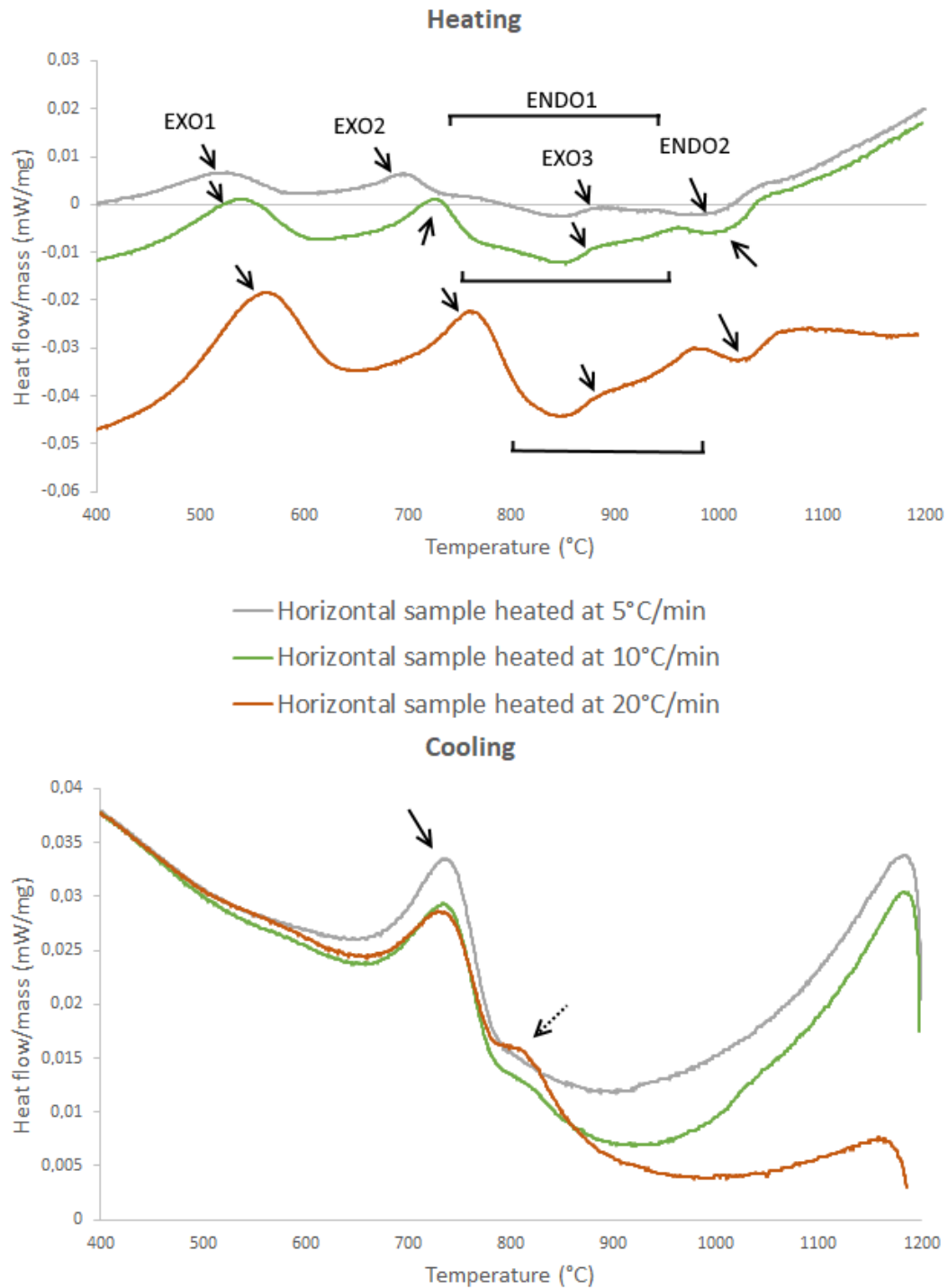


Figure 4.2. DSC curves of heating and cooling relative to the horizontal samples. The arrows indicate the detected peaks.

The DSC analysis reported in figure 4.3 indicate that the growth direction of the sample doesn't affect the DSC signal and related analysis, since no significant differences were detected between samples grown along the BD (vertical samples) or perpendicular to BD (horizontal samples).

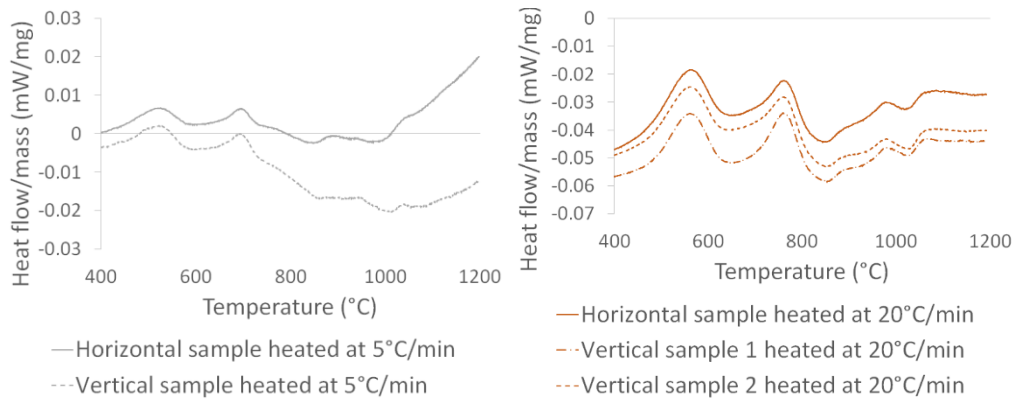


Figure 4.3. Comparison of the DSC curves of vertical and horizontal samples at the heating rate of 5°C/min and 20°C/min.

The signals collected during the TMA analysis of the as built samples are reported in figure 4.4. In this experimental set, it is possible to observe that clearer signals can be generally obtained using lower heating rate, it is to say in the experimental conditions opposite to what applied for DSC analysis. Furthermore, the comparison between the TMA curves collected on vertical and horizontal samples shows a difference starting from about 870°C, in particular an extra contraction peak (marked as “Contraction 3”) is observable in the vertical sample and the last expansion peak (Expansion 2) is greater than the one detected in the horizontal peak. Therefore, an anisotropy effect can be revealed by TMA, whereas DSC analysis were not capable to detect any difference along the different directions analyzed. An explanation of this difference will be given later.

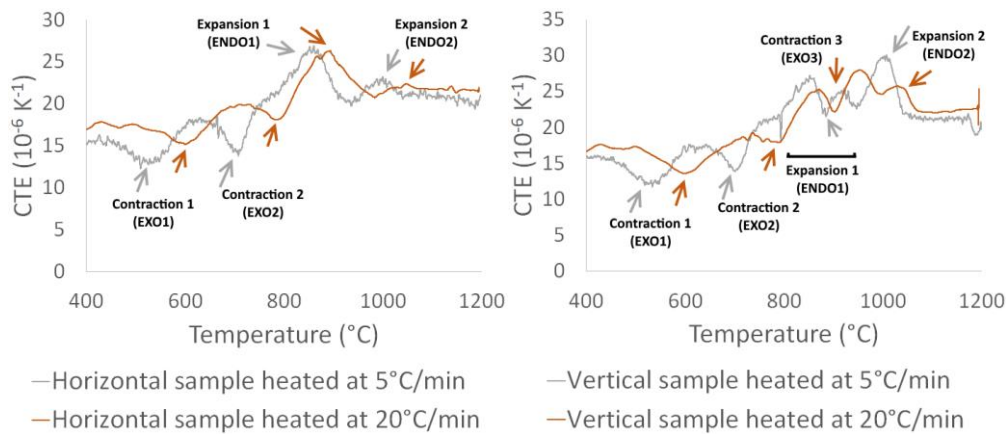
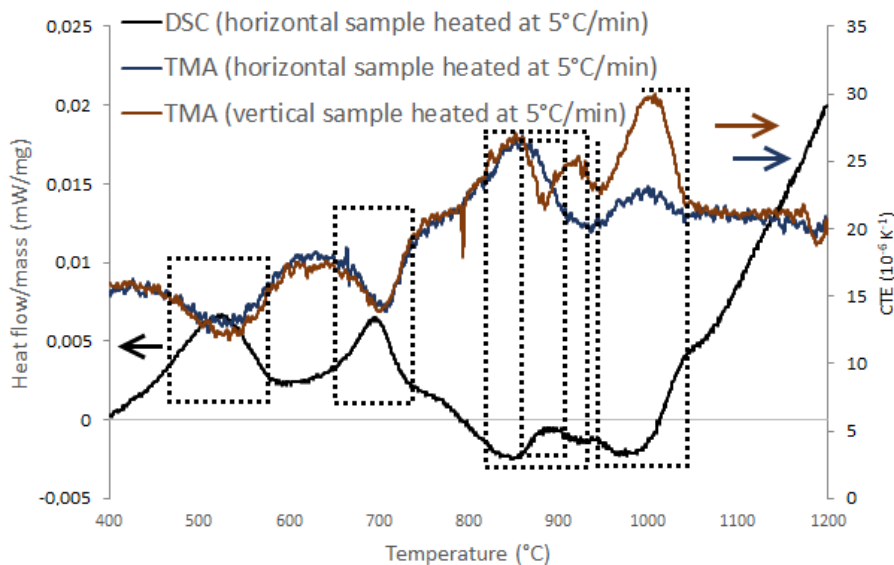


Figure 4.4. TMA heating curves of horizontal and vertical samples at the heating rate of 5°C/min and 20°C/min.

Apart from these differences in the sensitivity to anisotropy effects, the signals recorded with DSC and TMA analysis (Figure 4.5) are in good agreement and provide an efficient crosscheck. It is possible to observe that exothermic phenomena provide a reduction of the CTE, whereas endothermic ones lead to an increase of the CTE. Actually, the exothermic peaks are related to precipitation of second phases with consequent reduction of the solute dissolved in the γ phase. Therefore, the lattice distortion of the γ phase is reduced during precipitation with consequent decrease of the volume detected by the TMA equipment. Conversely,

endothermic peaks indicate dissolution of second phases in the matrix that causes increase of the solute in the γ matrix and lattice expansion.

Heating rate: 5°C/min



Heating rate: 20°C/min

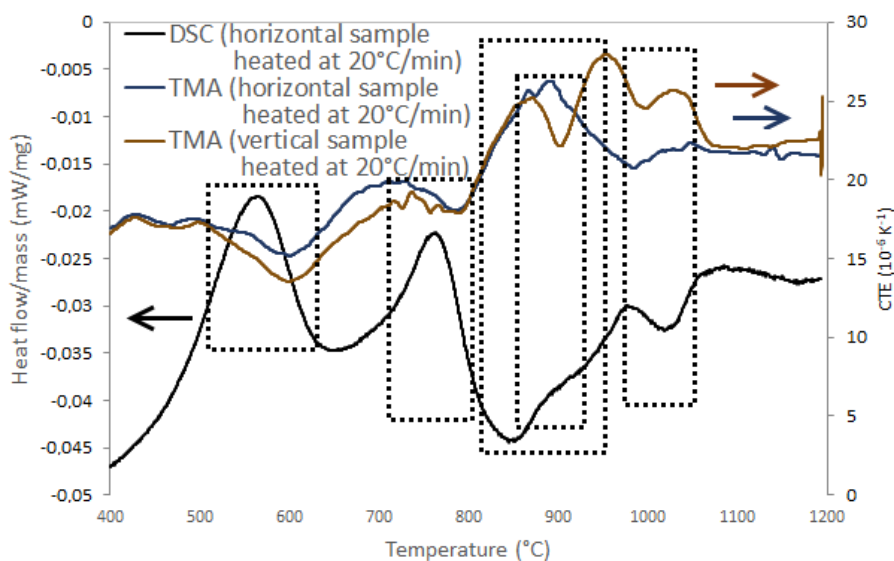


Figure 4.5. Comparison between the collected DSC and TMA curves at the heating rate of 5°C/min and 20°C/min. Dotted boxes indicate the overlapping signal peaks.

The above reported thermal analyses reveal the following thermal phenomena occurring in the as built material:

- precipitation of γ' (EXO 1) at 450-600°C;
- precipitation of γ'' (EXO 2) at 650-720°C;
- dissolution of γ' and γ'' (ENDO 1) at 780-930°C;
- precipitation of δ (EXO 3) at 860-920°C;
- dissolution of δ and preexisting second phases, in particular Laves phases, (ENDO 2) at 950-1040°C.

The above reported temperature ranges are obtained from the analyses performed with a heating rate of 5°C/min. They are quite compatible with the CCT curves of a conventional Inconel 718 alloy reported at figure 1.2. Furthermore, a similar sequence of exothermic peaks is also reported by Niang et al. [43].

During the cooling ramps, all conducted at the same cooling rate of 20°C/min, an exothermic peak is detected. Such peak is probably related to the co-precipitation of γ' and γ'' . By increasing the heating rate of the heating stage (dotted arrow in figure 4.2), during cooling an extra exothermic peak become visible. This extra peak is probably related to the growth of δ precipitates. When the heating is faster, some δ nuclei remain after passing through the high temperatures and can grow during the following cooling stage. On the other hand, a slower heating dissolves completely the δ phase, which have no time to nucleate again during the cooling ramp.

The DSC analysis doesn't reveal any difference between the response of the vertical and horizontal samples to the thermal ramps. Therefore, the difference that is observed in the TMA curves for vertical and horizontal samples (figure 4.4) cannot be due to an effective different evolution of the second phases. It is more likely to ascribe such effect to the starting heterogeneity and anisotropy of the as built material. The peak of contraction, that indicates solubilization at high temperature (ENDO 2), is lower in the horizontal sample. This occurs because, as already observed in the previous chapter, the second phases are not evenly distributed in the as built material, but they form predominantly at the interdendritic boundaries. Therefore, the solutioning of the pre-existing second phases leads to a lattice expansion that is not uniform in the material volume, but is greater at the interdendritic boundaries, where the release of solute in the matrix is more intense. Since the dendrites are predominantly aligned along the building direction, the increase of the measured CTE would be greater along this direction, where the interdendritic boundaries are disposed in parallel on average. On the other hand, along the transversal directions, where the interdendritic boundaries are disposed in series, the measured CTE will be lower. The simplified scheme in figure 4.6 explains such concept.

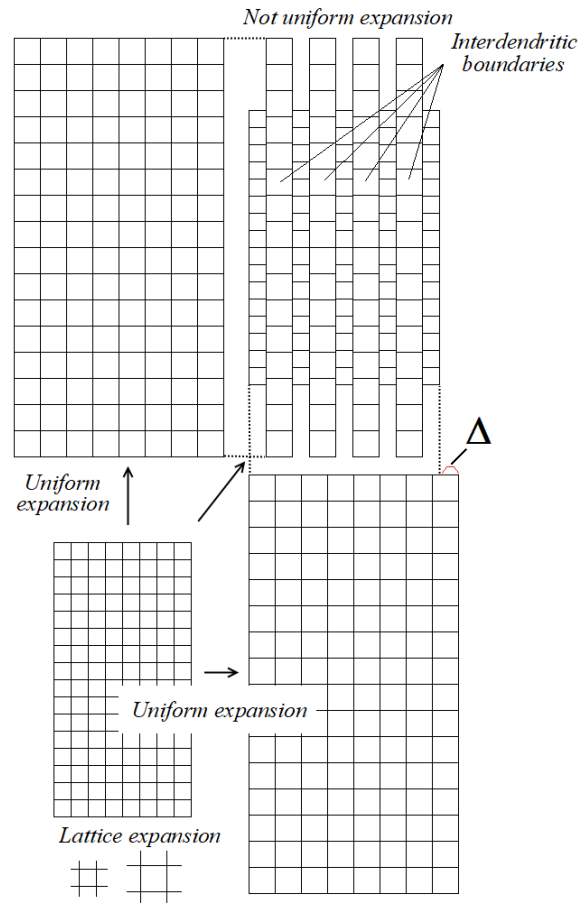


Figure 4.6. Scheme illustrating the not uniform expansion during the dissolution of the interdendritic phases in the SLM material. The expansion is lower of a Δ along the transversal direction of the interdendritic boundaries.

A similar explanation can be given also to explain the suppression of the contraction peak indicating the precipitation of δ phase (EXO 3). As it would be shown later in this chapter, δ phase tends to form precipitates with plate-like morphology and with a certain relationship with the matrix (see paragraph 1.3.1.3) that leads to the formation of a parallelepiped grid oriented along the building direction (figure 4.35). Since the plate-like δ precipitates are not randomly oriented, their formation leads to non-uniform lattice contraction that is therefore revealed in the vertical samples but not in the horizontal samples.

4.2 Response to the solution annealing

During the solution step, the main aim is to homogenize the microstructure and dissolve most of the second phases avoiding excessive loss of the mechanical properties due to grain coarsening. The two standard temperatures of solution annealing for Inconel 718 according to AMS standards, i.e. 980°C and 1065°C, fall respectively at the onset and at the offset of ENDO 2 peak detected through the thermal analysis (figure 4.2). In addition to these two standard temperatures, a third solution annealing at 1200°C is also tested in order to achieve the highest possible level of homogenization. In fact, a further increase in the solution temperature is risky because it can lead to incipient melting at the grain boundaries or at the interdendritic region where low melting eutectics are located. Further to temperature also a modulation of soaking time from 1 to 2 hours is investigated in order to optimize the solution step.

All solutioned samples are evaluated by optical and FESEM analysis. By image analysis processing the FESEM images an assessment of second phases distribution is investigated and, finally, microhardness measurements are performed.

4.2.1 Solution annealing at 980°C

After the solution treatment, the laser track boundaries are strongly blurred, but they are still recognizable after solution annealing at 980°C for 1 and 2 hours (figure 4.7). The heterogeneity of the grains size is increased because some new small grains form at the laser track boundaries due to the presence of a larger residual stress state in these regions [163] [164] and consequent greater driving force for local partial recrystallization, as also reported by Zhang et al. [180].

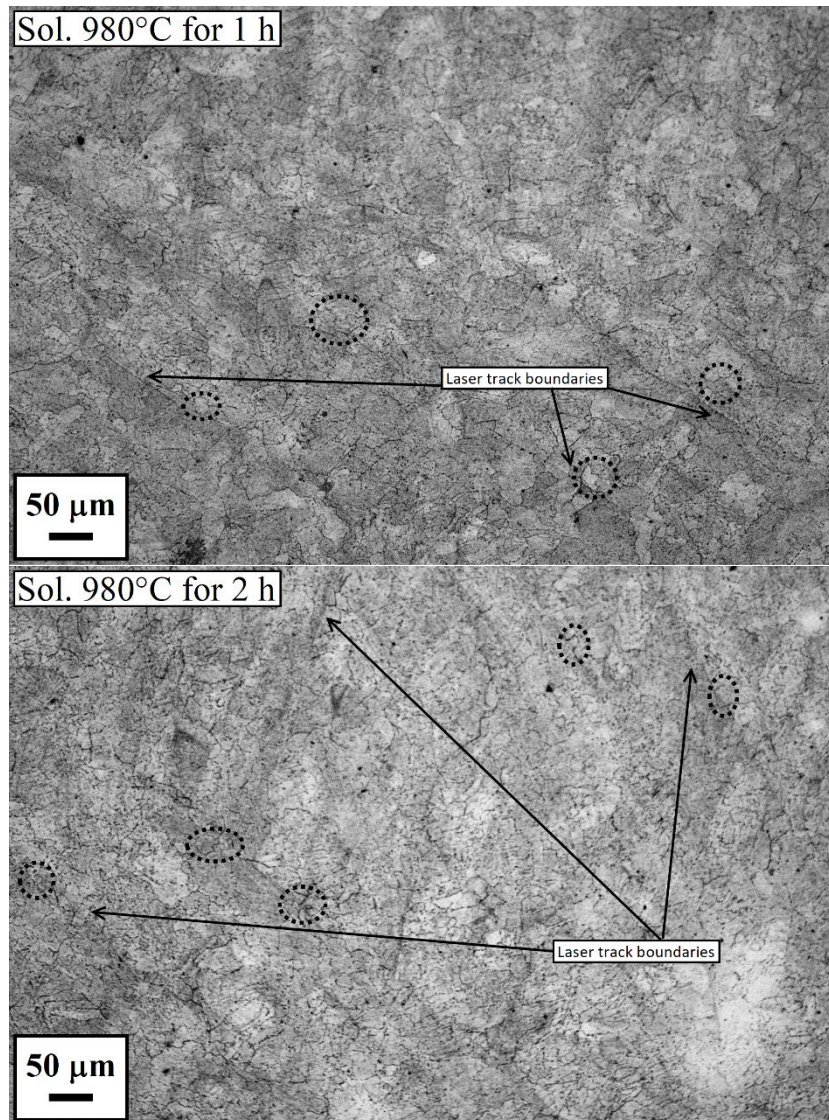


Figure 4.7. Optical micrographs of the horizontal plane after solution annealing at 980°C for 1 hour and 2 hours. Dotted ellipses indicate small recrystallized grains at the laser track boundaries.

On the vertical view the grains maintain their columnar shape oriented along the building direction of the sample. After solution annealing at 980°C, grain boundaries become completely decorated by plate-like δ precipitates (figure 4.8). The formation of δ phase is expected because the heat treatment occurs under the solvus temperature. Therefore precipitation of δ can take place as soon as part of the Nb atoms previously entrapped in the eutectic phases, is released into solid solution and at disposal for further precipitation [179].

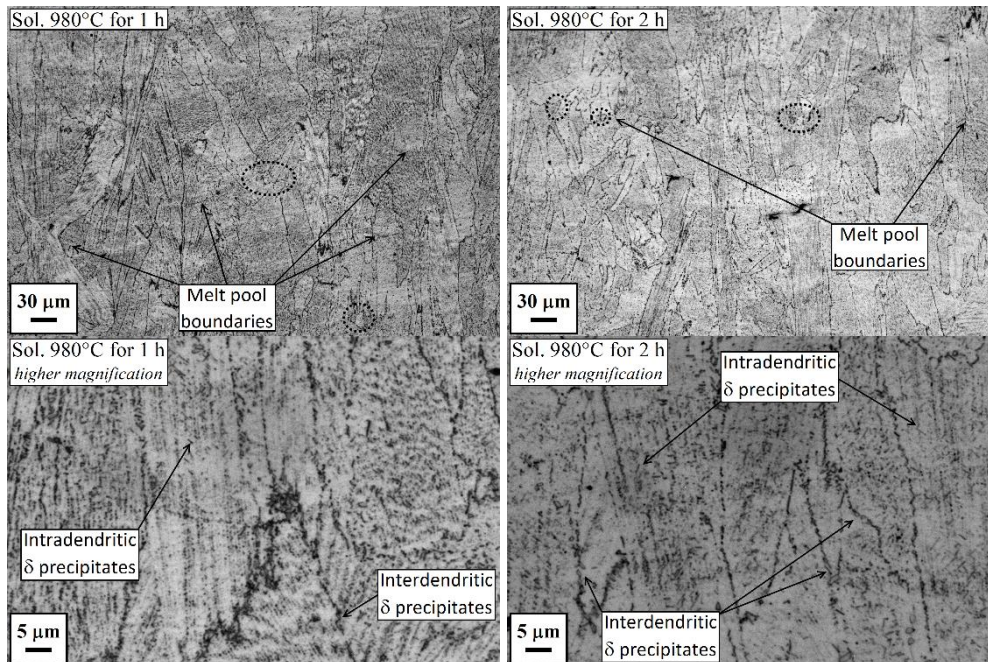


Figure 4.8. Optical micrographs of the vertical plane after solution annealing at 980°C for 1 hour and 2 hours. Dotted ellipses indicate small recrystallized grains at the laser track boundaries. The higher magnification micrographs show the interdendritic and intradendritic plate-like δ precipitates.

Smaller plate-like δ precipitates also form inside the grain but mostly at the interdendritic boundaries (figures 4.8 and 4.9). The formation of interdendritic δ makes the intragranular columnar texture still visible after solution annealing at 980°C.

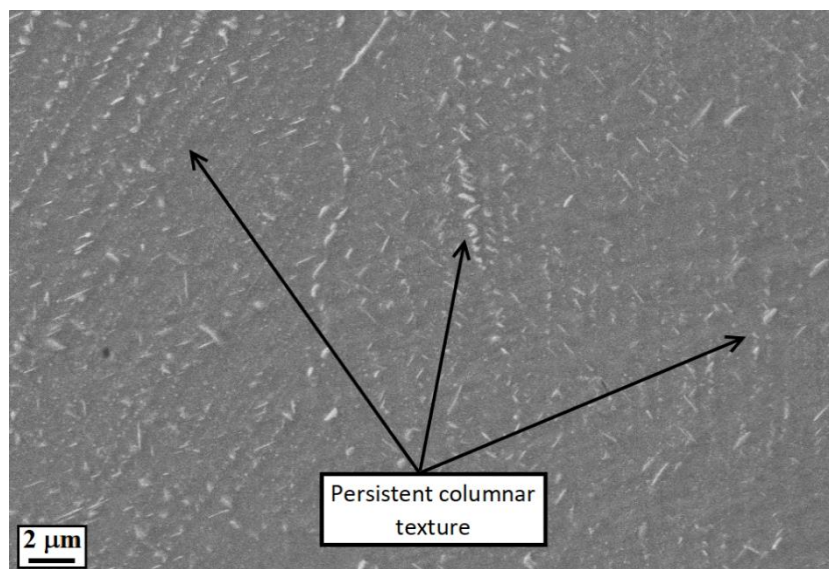


Figure 4.9. SEM micrograph of the vertical plane after solution annealing at 980°C for 1 hour showing the columnar dendrite texture still visible due to the formation of interdendritic δ precipitates.

SE FESEM micrographs (figure 4.10) show the different kinds of precipitates present within the material after solution annealing at 980°C. In addition to the

intergranular and intragranular plate-like δ phases, residuals of the interdendritic eutectic products are detectable.

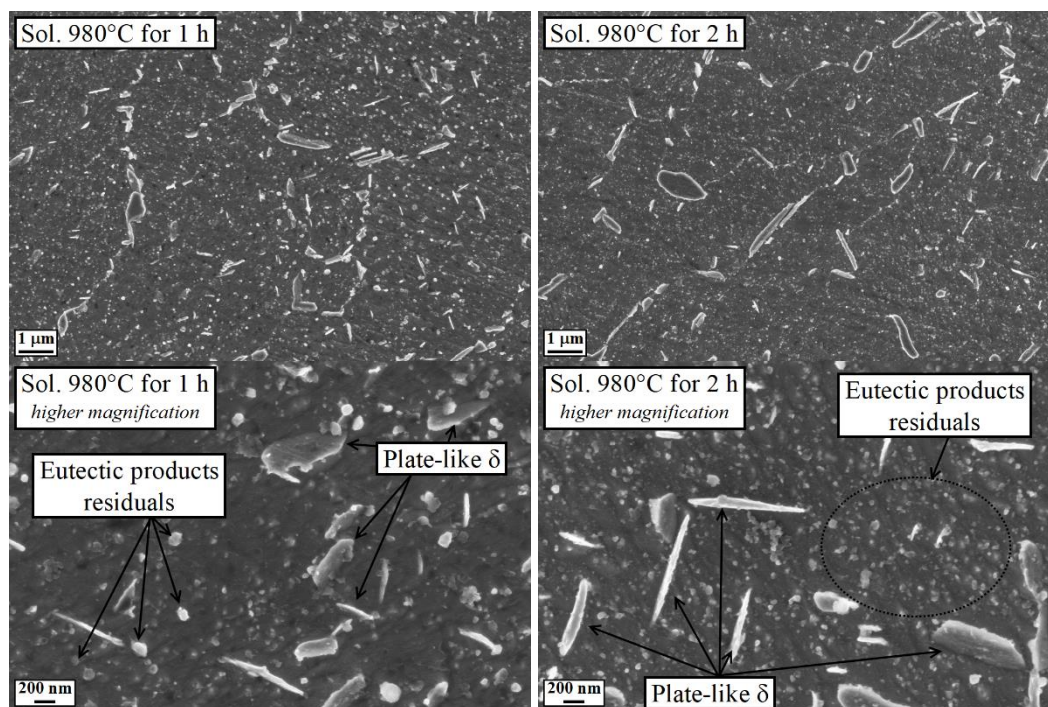


Figure 4.10. SE FESEM micrographs of the horizontal plane after solution annealing at 980°C for 1 hour and 2 hours. Newly formed plate-like δ precipitates and residuals of the eutectic products are the main present second phases.

Size distribution of precipitates were calculated through image analysis of FESEM micrographs in order to compare the population of second phases after 1 and 2 hours of heat treatment. The obtained size distributions are reported in figure 4.11. The contributions to the volume fraction given by precipitates with and without plate morphology is shown in figures 4.11-B and 4.11-C. In the image analysis, the detected objects larger than 20 pixels and with a ratio between its two main axes larger than 4 were identified as plate-like precipitates. More than half of the total volume fraction of second phases is given by precipitates smaller than 150-200 nm, i.e. residuals of the eutectic phases. In particular, globular carbides that are extremely stable and very hard to completely dissolve during solution annealing. Larger precipitates are mainly plate-like δ compounds. The sample solutioned for 2 hours contains a higher fraction of precipitates smaller than 80 nm with respect to the one solutioned for 1 hour. On the contrary, the volume fraction of precipitates with a size between 80 and 220 nm is reduced when longer solution treatment is applied. The formation of new stable carbides can explain the increase of the volume fraction related to precipitates finer than 80 nm. Actually, the progressive dissolution of the metastable Laves phases during the solution annealing, leads to an increase of available Nb atoms at the interdendritic boundaries, where nucleation of carbides can preferentially occur. The volume fraction of precipitates larger than 350 nm, which predominantly have plate-like morphology (figure 4.11), is also

increased after 2 hours of solution annealing due to the progressive growth of δ phase at this solution temperature.

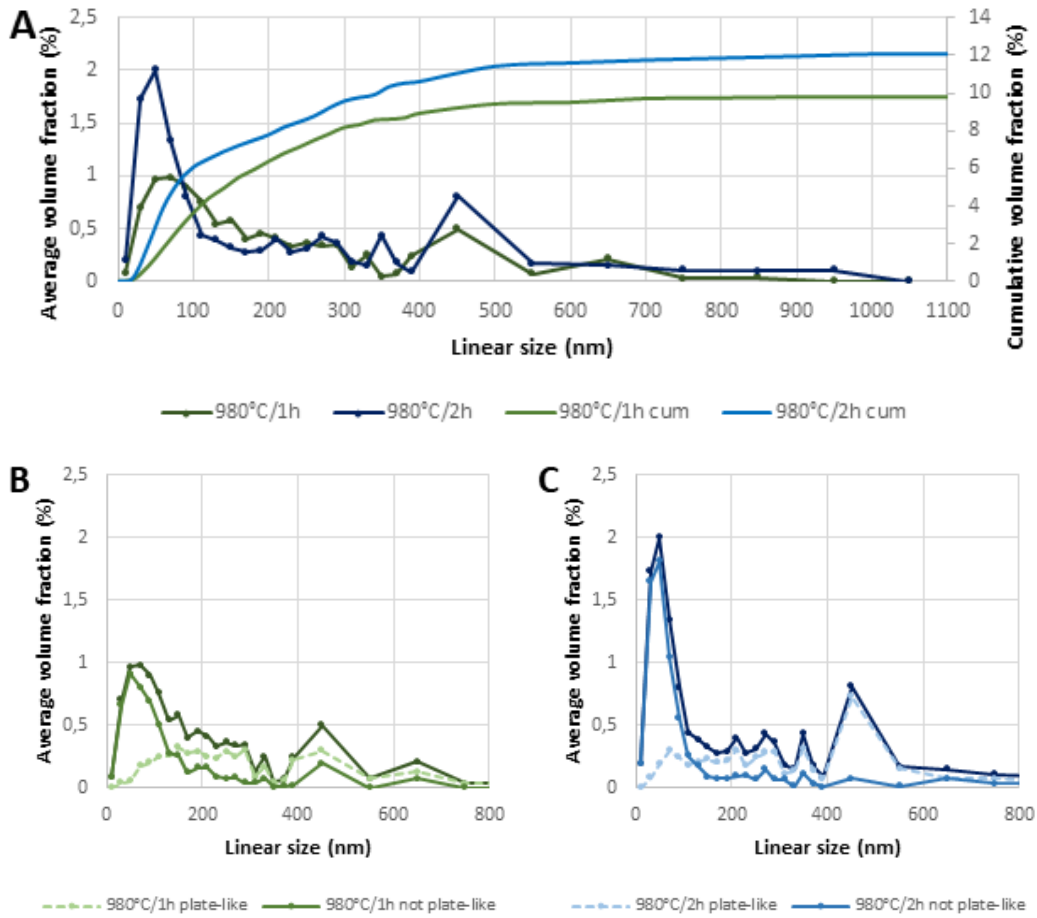


Figure 4.11. Size distributions relative to the samples solutioned at 980°C (A). Contributions of the precipitates with plate-like morphology and without plate-like morphology after 1 hour (B) and 2 hours (C) of treatment at 980°C. First published in [194].

4.2.2 Solution annealing at 1065°C

After solution annealing at 1065°C the laser track boundaries are strongly blurred, although some edges between melt pools are occasionally still visible (figures 4.12 and 4.13).

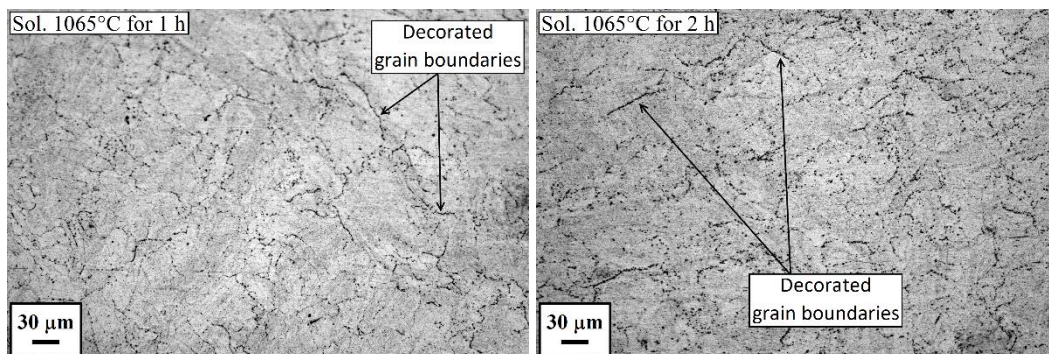


Figure 4.12. Optical micrographs of the horizontal plane after solution annealing at 1065°C for 1 hour and 2 hours.

The grains maintain their elongated shape and the boundaries between them appear decorated with a large amount of intergranular precipitates. On the contrary, δ phase doesn't form during the heat treatment because the solution temperature is above the solvus point.

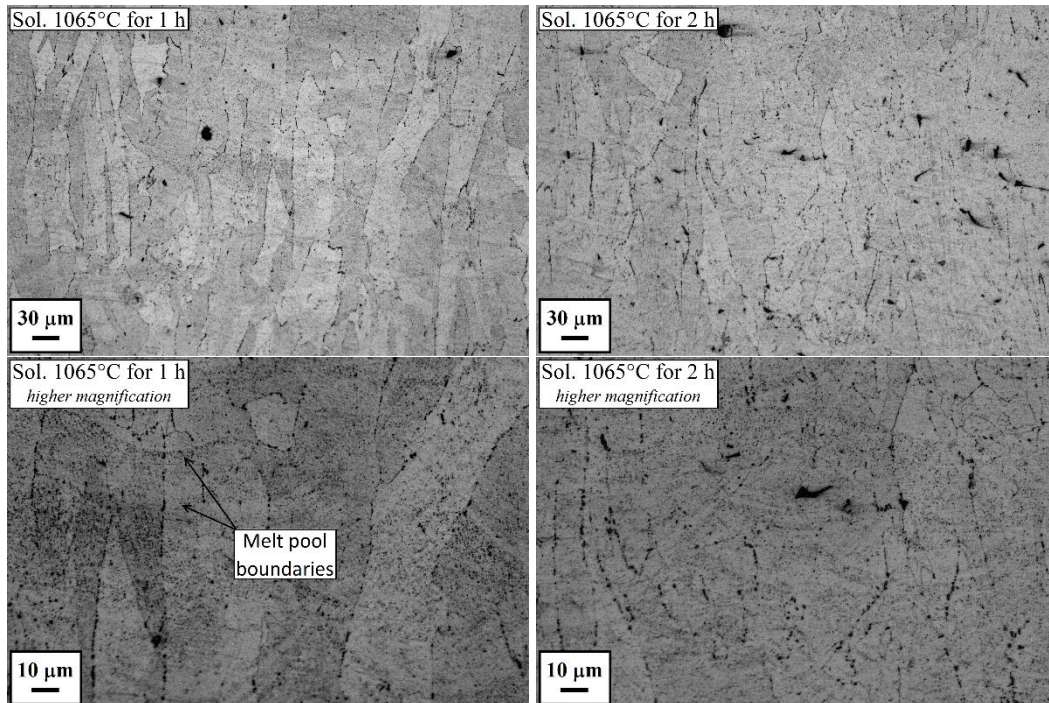


Figure 4.13. Optical micrographs of the vertical plane after solution annealing at 1065°C for 1 hour and 2 hours.

As a consequence the dissolved interdendritic phases inside each grain are no more substituted by δ phases and so the dendritic sub-granular structure is no more visible after the heat treatment at 1065°C (figure 4.14).

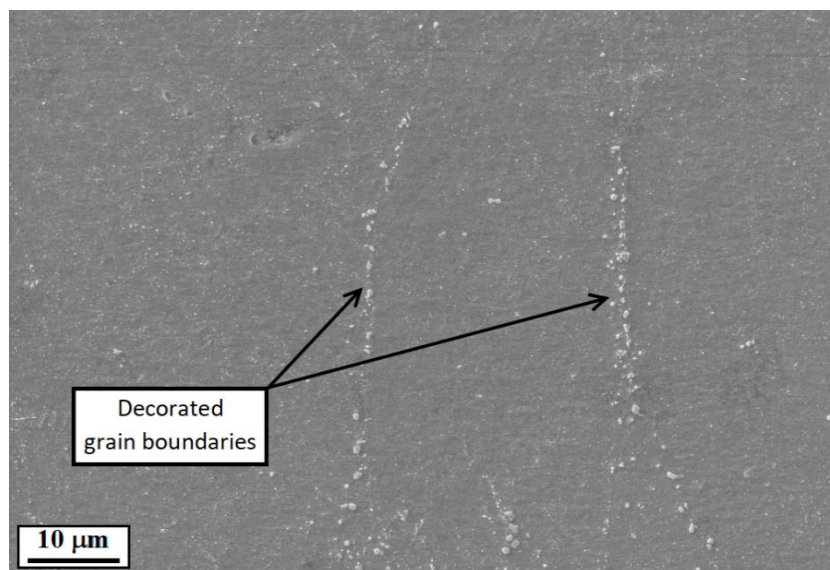


Figure 4.14. SEM micrograph of the vertical plane after solution annealing at 1065°C for 1 hour showing the grain boundaries decorated with newly formed precipitates. The columnar structure is no more visible.

SE FESEM micrographs show the presence of blocky and relative large precipitates formed during the heat treatment at the grain boundaries (figure 4.15). Based on similar observations reported in the literature [33] [175] [178] [179] [183] and on the EDS analysis reported below (figure 4.18), it is possible to state that these intergranular precipitates with blocky morphology are MC type carbides.

Furthermore, the SE FESEM micrographs also reveal the persistence of small intragranular precipitates, which are both undissolved eutectic products and new small precipitates formed due to the progressive release of Nb atoms when solutioning occurs.

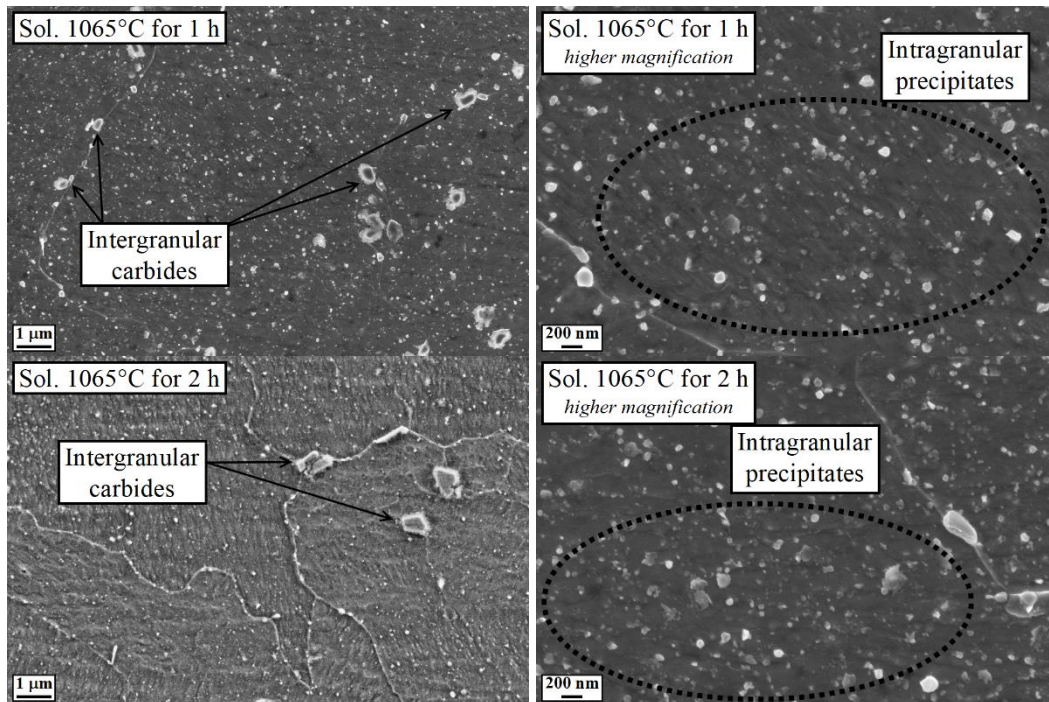


Figure 4.15. SE FESEM micrographs of the horizontal plane after solution annealing at 1065°C for 1 hour and 2 hours. Newly formed intergranular carbides and intragranular precipitates are the main present second phases.

The intragranular precipitates are slightly reduced by increasing the heat treatment time from 1 hour to 2 hours as it can be seen from the size distributions reported in figure 4.16. Actually, this analysis shows a small decrease in the volume fraction of the precipitates with a linear size between 50 and 120 nm. This is due to the progressive dissolution of metastable phases. However, an increase in volume fraction of precipitates larger than 450 nm was also detected after 2 hours of heat treatment. This size class is mostly formed by the relative coarse blocky carbides located at the grain boundaries. These intergranular precipitates can prevent the grain to coarsen due to a pinning mechanism of grain boundaries.

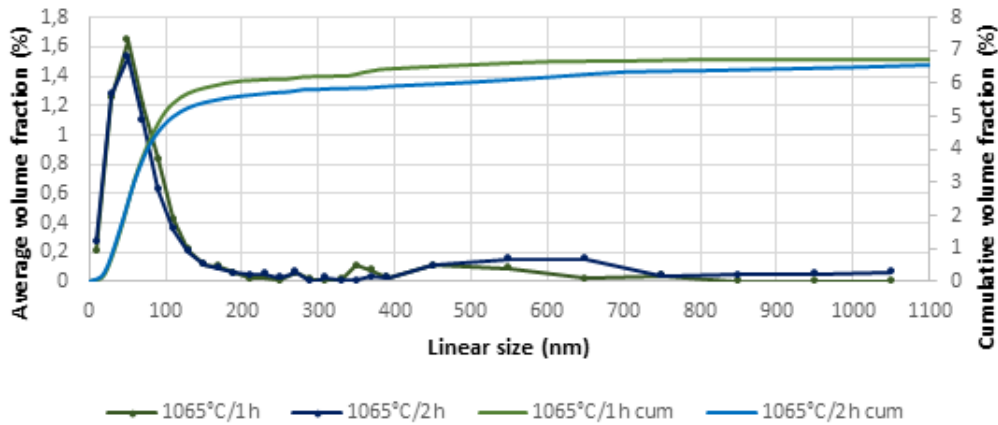


Figure 4.16. Size distributions relative to the samples solutioned at 1065°C. First published in [194].

4.2.3 Solution annealing at 1200°C

After solution annealing at 1200°C, the laser track boundaries are completely canceled (figures 4.17). Furthermore, a remarkable grain coarsening occurs during such heat treatment. It is worthwhile to note that coarsened grains still maintain an elongated shape oriented along the building direction.

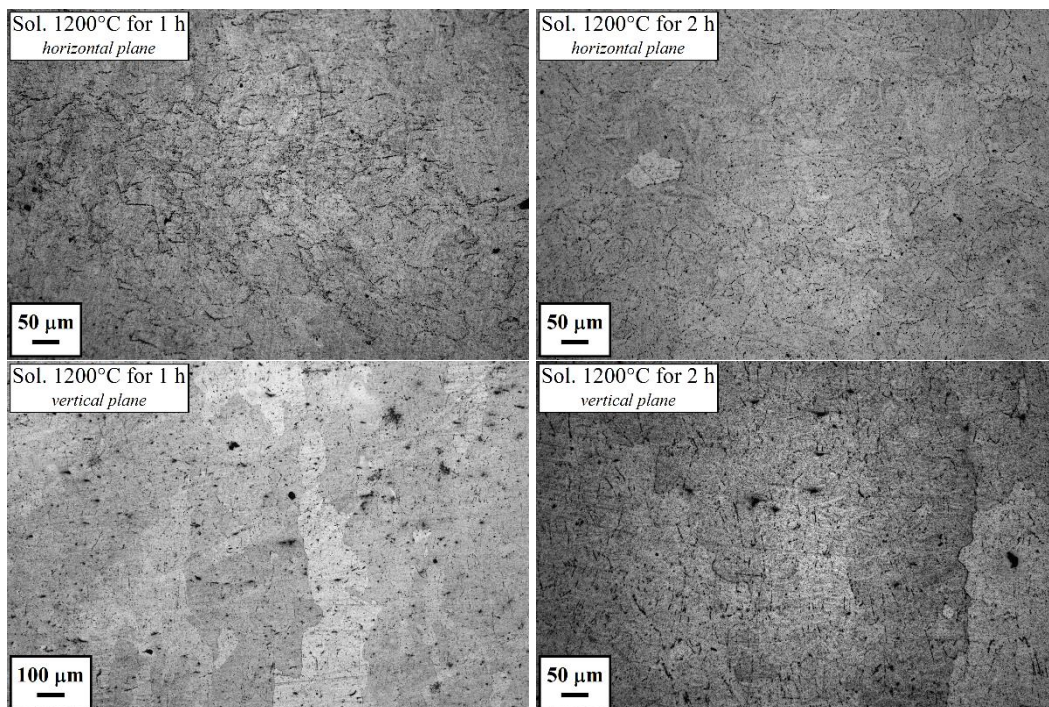


Figure 4.17. Optical micrographs of the horizontal and vertical planes after solution annealing at 1200°C for 1 hour and 2 hours. First published in [194].

The previous profiles of the grain boundaries are still visible because of the presence of cluster of Nb-rich carbides formed along them (figure 4.18). These precipitates form because of the Nb segregation at grain boundaries. Nevertheless, at a so high solution temperature such precipitates are not able to pin the boundaries, contrary to what happens during the heat treatment at 1065°C. The diffusion of Nb

is not fast enough to follow the migration of the grain boundaries, therefore during the heat treatment carbides form and growth in the zones initially occupied by the original grain boundaries rather than along their new location. Consequently, the grain boundaries observed after solution annealing at 1200°C appear almost free from precipitates (figures 4.18 and 4.19).

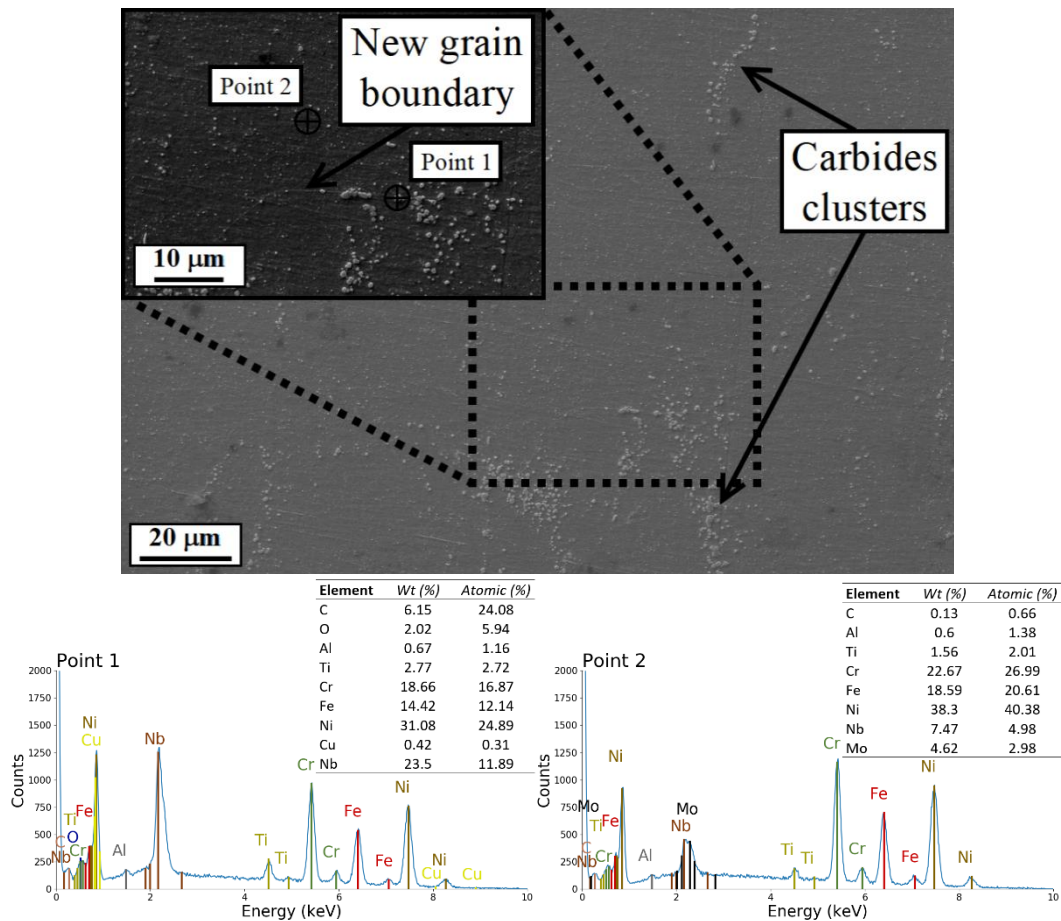


Figure 4.18. SEM micrograph of the vertical plane after solution annealing at 1200°C for 1 hour showing the carbides clusters along the previous positions of the grain boundaries and a new grain boundary unconstrained by the carbides after recrystallization (compare with figure 14). EDS point analysis on a Nb-rich carbides cluster (point 1) in comparison to the intragranular matrix zone (point 2).

The collected SE FESEM micrographs demonstrate that the removal of the interdendritic eutectic products is not complete even after achieving at 1200°C such a high dissolution degree. The complete dissolution of the second phases at the dendrite length scale cannot be obtained both because of the high thermal stability of the carbides formed by eutectic reaction during solidification in the SLM process and because of the formation of new very small precipitates resulting from the release of Nb after dissolution of the Laves phases.

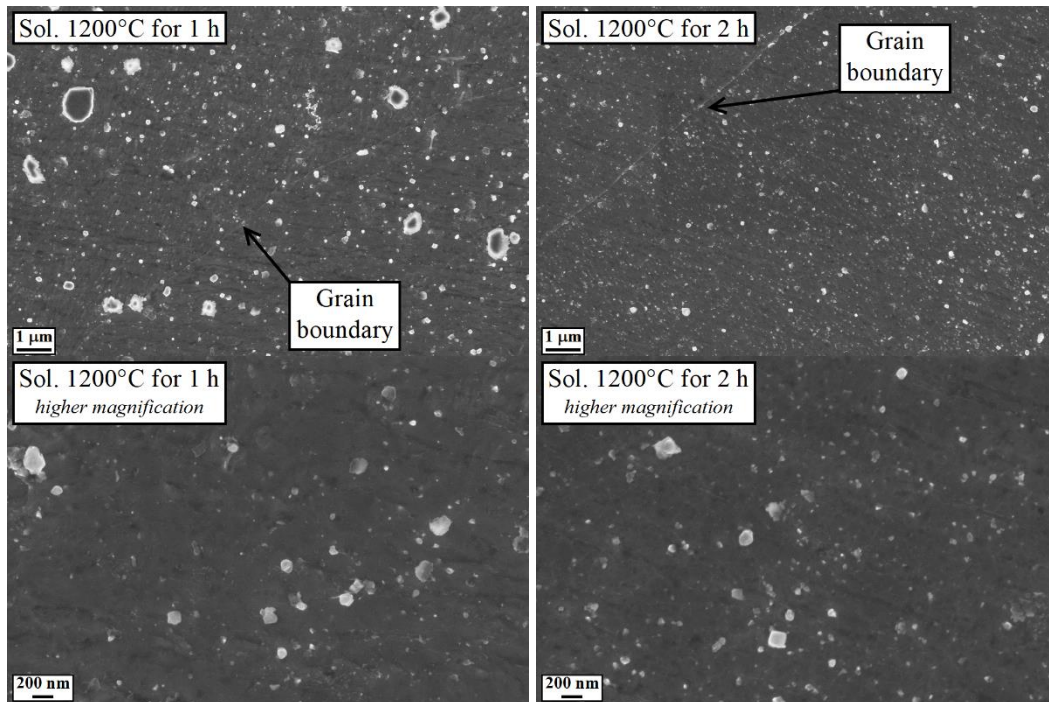


Figure 4.19. SE FESEM micrographs of the horizontal plane after solution annealing at 1200°C for 1 hour and 2 hours. Note the grain boundaries free from precipitates and the presence of residuals of the interdendritic precipitates inside the grains (higher magnification images).

The increase in volume fraction of the finest precipitates (less than 130 nm), provided by the increase in solution soaking time from 1 hour to 2 hours of heat treatment, is evident by comparing the two size distributions reported in figure 4.20. Conversely, the volume fraction of the coarser particles, in particular the ones larger than 370 nm, is reduced by increasing the heat treatment duration.

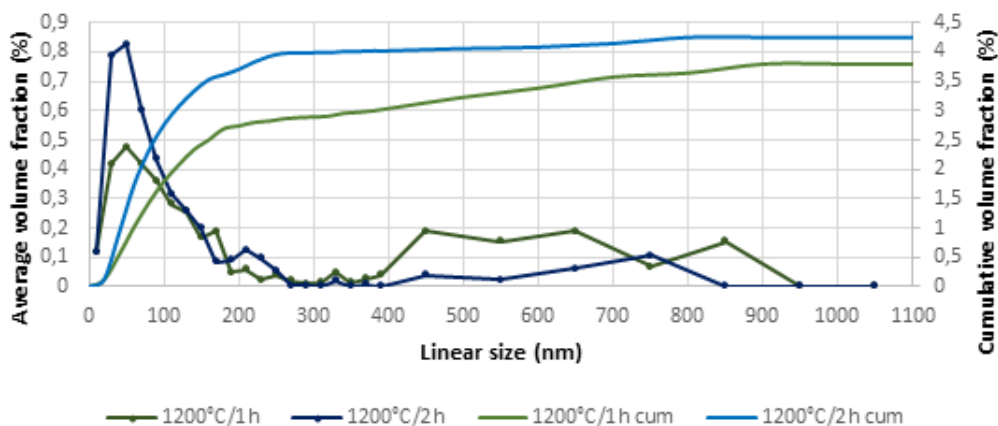


Figure 4.20. Size distributions relative to the samples solutioned at 1200°C. First published in [194].

The size distribution obtained for each solution condition are reported for sake of comparison in figure 4.21 where the effect of the solution temperature is considered at fixed time. As it was expected, the higher the solution temperature, the lower is the total volume fraction of the detected second phases. The major difference between the size distributions regards the peak related to precipitates finer than 100-120 nm, which in most cases is reduced as the solution temperature

increases. After 1 hour of treatment, the samples solution annealed at 1065°C contain a higher amount of precipitates finer than 80 nm with respect to the one solution annealed at 980°C, but the volume fraction of the larger precipitates is strongly reduced. The formation of new small precipitates during the heat treatment is faster at 1065°C because part of the Nb released at 980°C is used to form interdendritic δ phases, as earlier discussed. However, after 2 hours of heat treatment, the volume fraction of precipitates on sample treated at 1065 °C is lower for almost all dimensional ranges with respect to the one recorded on samples solutioned at 980°C. On the other hand, the measured volume fractions at 1200 °C are lower with respect to the ones recorded at 1065°C for almost all dimensional ranges both after 1 hour and 2 hours of heat treatment.

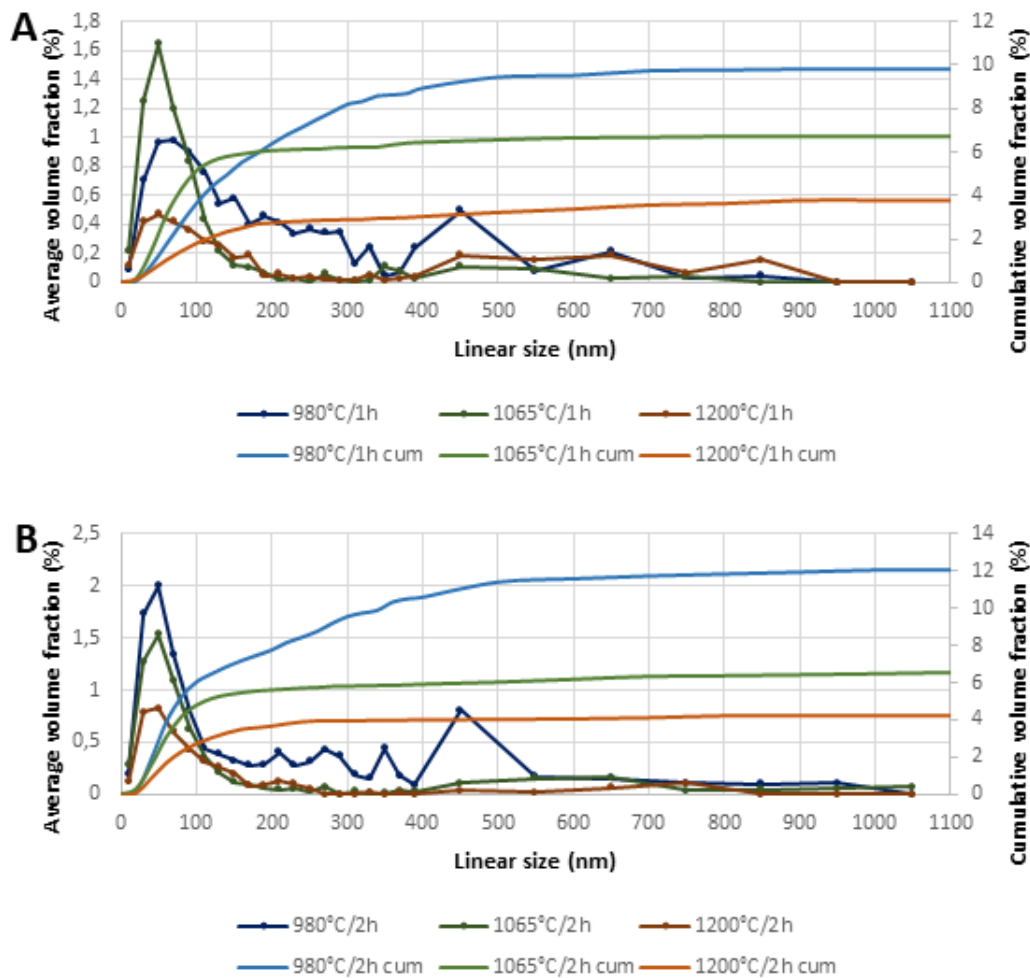


Figure 4.21. Size distributions: comparison between different solution temperature after 1 hour (A) and 2 hours (B) of heat treatment. First published in [194].

The total volume fraction of precipitated second phases is tightly connected with the hardness of the material. The relationship between the mean Vickers microhardness of the as built sample and the solution annealed samples and their relative volume fraction of detected precipitates is graphically shown in figure 4.22. A clear linear correlation stands for all the samples apart from the ones solution annealed at 1200°C, for which a Vickers microhardness lower than the value

predicted by the linear regression line was recorded. The lack of hardness in these samples, further to their lower amount of second phases, is due to the irreversible grain growth occurred during this heat treatment. Therefore, the loss of mechanical properties cannot be recovered anymore with a subsequent aging treatment. For this reason, despite the higher solution efficiency that can be obtained at 1200°C, such solution temperature is no more considered in the following study of the complete heat treatment cycle.

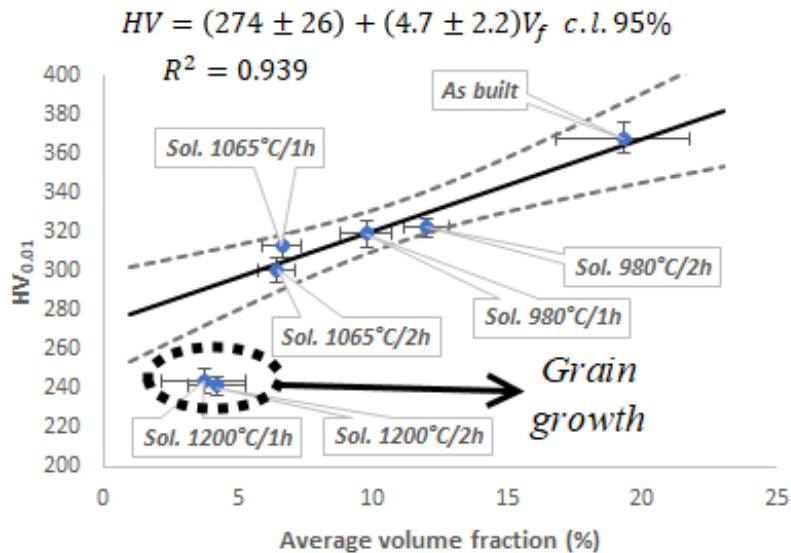


Figure 4.22. Correlation between the Vickers microhardness and the average volume fraction of precipitates in the as built sample (the volume fraction of the as built sample is obtained considering the eutectic products and neglecting eventual very small intradendritic precipitates as those in figure 3.27) and the solutioned samples. The vertical error bars refer to 95% confidence intervals on $HV_{0.01}$, the horizontal error bars refer to standard deviations of the volume fractions.

The regression line with relative 95% confidence band is obtained excluding the points of the samples solutioned at 1200 °C. First published in [194].

4.3 Optimization study of the complete heat treatment cycle

The study on the microstructural evolution of the as built material during the homogenization/solution heat treatment, reported in the previous paragraph, allows to discard the high solution temperature of 1200°C, at which severe grain coarsening occurs. On the other hand, the solubilization step at the two standard temperatures, i.e. 980°C and 1065°C, is hereby further investigated focusing on the effect of different treatment durations on the material softening, evaluated by Brinell hardness measurements, and on its response to the subsequent aging treatment.

The obtained results are the starting point for the evaluation of the best combination of solubilization + first aging. The ultimate aim of this optimization is to maximize the hardness level and to achieve a regular and uniform microstructure.

Finally, this chapter is concluded with the results of the optimization of the second aging.

4.3.1 Solution annealing step

The effects of both solution temperature and time on the Brinell hardness and the Vickers microhardness of the alloy are reported in figure 4.23. The material softens with the increase of the heat treatment duration, especially at 1065°C. The hardness is less affected by the time of the solution annealing at 980°C probably because of the occurrence of the δ phase precipitation, which is stable at this temperature and provides a certain resistance to the plastic deformation.

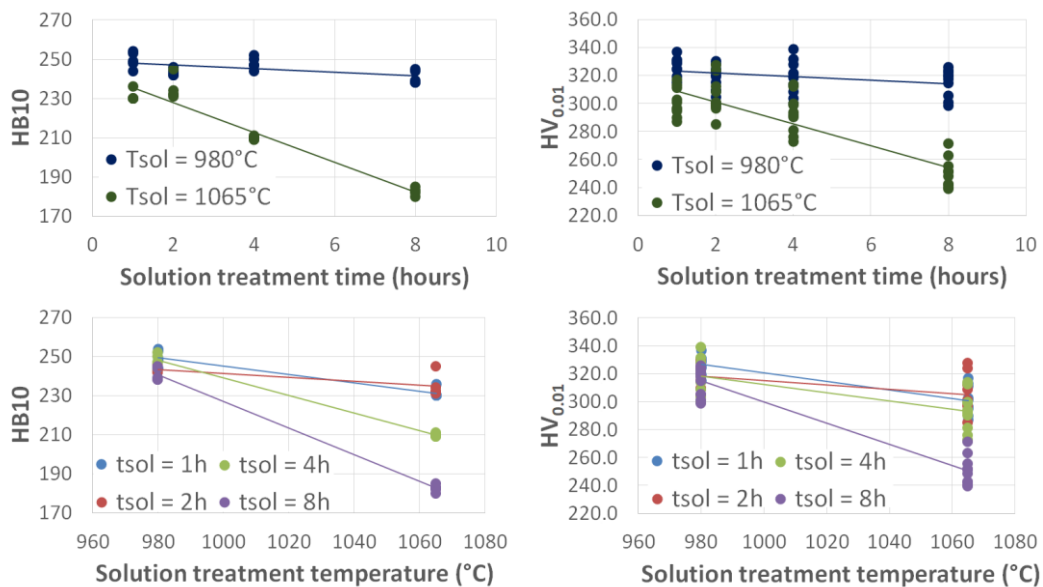


Figure 4.23. Brinell hardness (HB10) and Vickers microhardness (HV_{0.01}) in function of the temperature (T_{sol}) and time (t_{sol}) of the solution annealing.

The general microstructure of the samples solutioned for 4 and 8 hours are reported in figure 4.24. The same features already observed in the previous paragraph (figures 4.8 and 4.12) are also found after longer solutioning times, in particular the presence of a large number of intergranular and intragranular plate-like δ precipitates after heat treatment at 980°C and a lot of equiaxed particles along the grain boundaries after heat treatment at 1065°C.

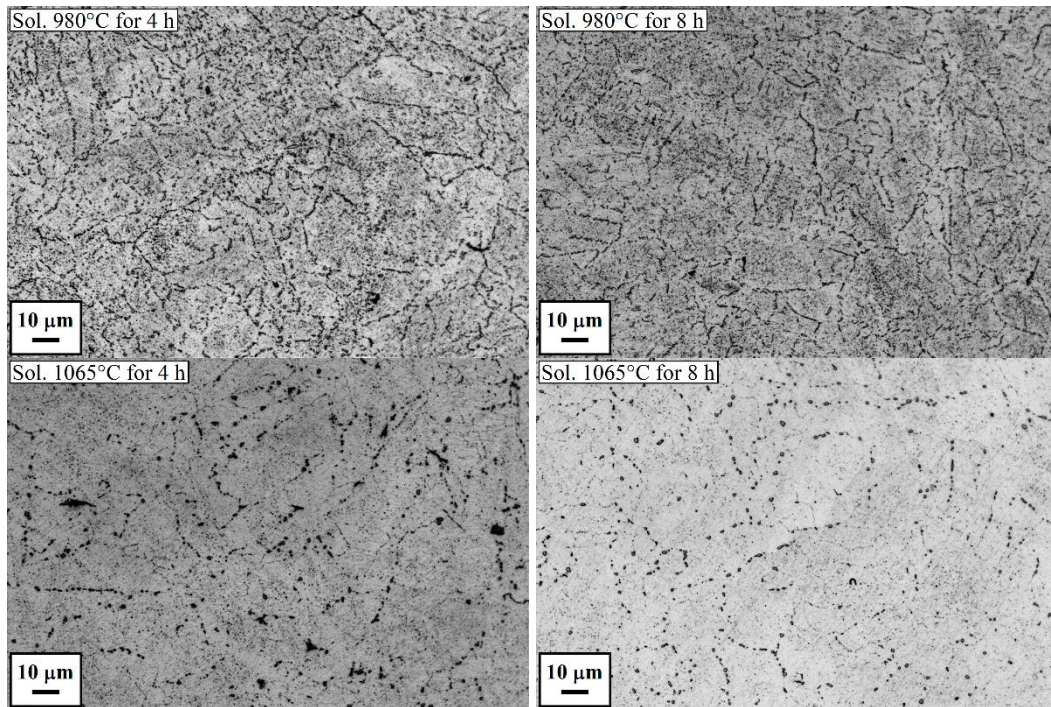


Figure 4.24. Optical micrographs of the horizontal plane of samples solutioned at 980°C and 1065°C for 4 and 8 hours.

The SEM micrographs reported in figure 4.25 show with finer details the two different kinds of intergranular precipitates formed at the two solution temperatures. The presence of intragranular precipitates in both the samples is also visible.

Grain coarsening is not detectable. This is due to the pinning effect exerted by the intergranular precipitates, that is effective also for prolonged times of solution annealing.

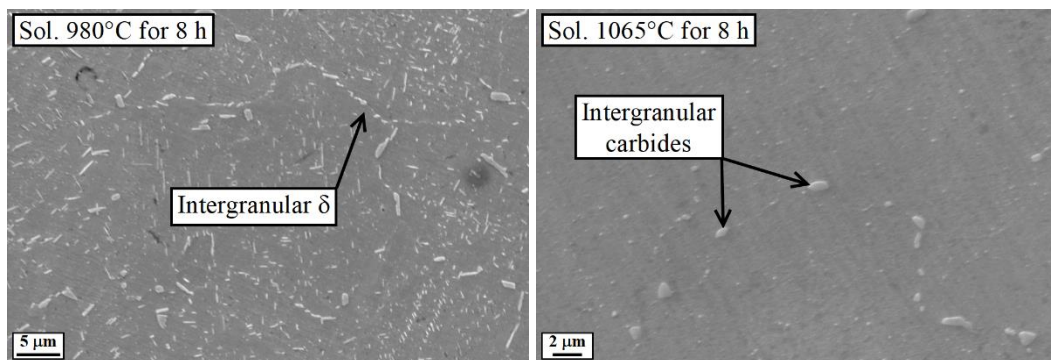


Figure 4.25. SEM micrographs of the horizontal plane of the samples solutioned for 8 hours at 980°C and 1065°C showing the different intergranular precipitates.

4.3.2 Aging response

The aging response of samples solutioned at 980°C and 1065°C for 2 and 8 hours is analyzed through DSC technique. The DSC curves obtained on solution annealed samples are compared with the as built one on figure 4.26. The EXO 1 and EXO 2 peaks, related to the precipitation of the strengthening phases γ' and γ'' , are not markedly modified by the solution annealing. A slight shift of about 20 degrees of the EXO 2 peak through lower temperature can be observed and it can be explained by the higher availability of Nb in the matrix in the solutioned state that leads to a faster precipitation of γ'' . The EXO 3 peak, related to the formation of δ phase, is not detectable in the sample solutioned at 980°C. However, this is not surprising because δ compounds already precipitate during the solution annealing as shown previously (figures 4.8 and 4.10). ENDO 2 is present in samples solutioned at 980°C and appears slightly shifted through higher temperature with respect to the as built state: in these samples the ENDO 2 peak is related to the dissolution of the δ phases formed during the solution annealing. Conversely, the ENDO 2 peak is not present in samples solutioned at 1065°C. This is again expected because most of the dissolution of the pre-existing second phases already occurs during the solution treatment and δ phase doesn't form in this case.

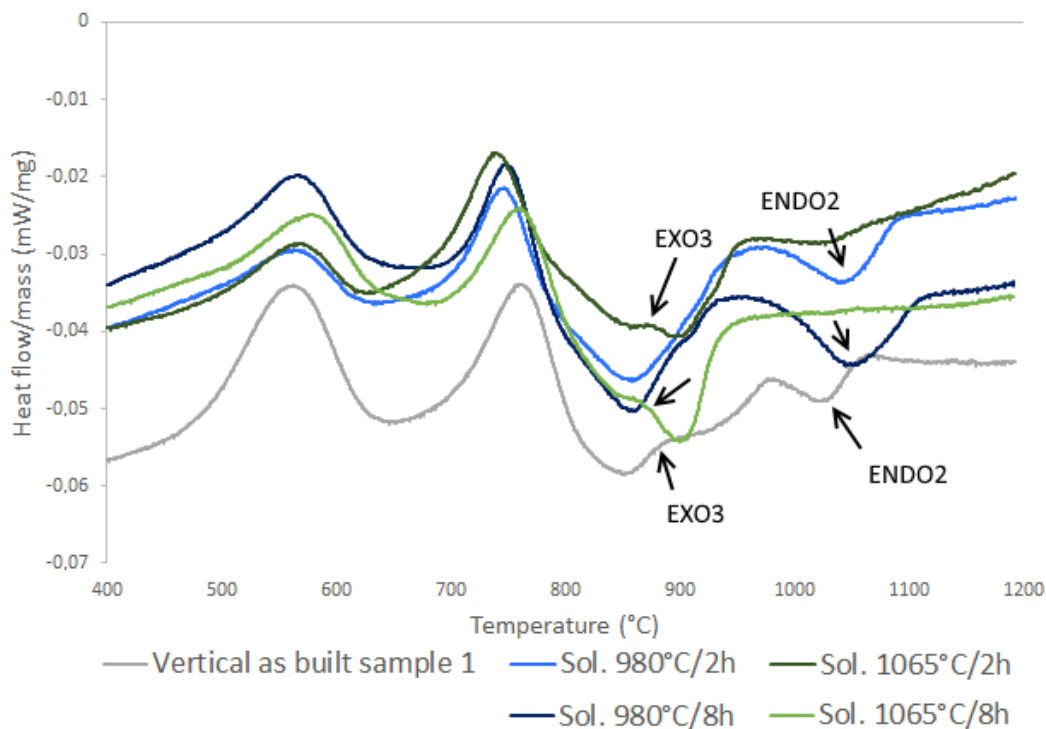


Figure 4.26. Comparison between the DSC heating curves collected on the as built material and on the previously solutioned samples. Heating rate: 20°C/min. The as built and the 1065°C/2h solution annealing curves have been previously published in [186].

TMA analysis of vertical samples solutioned for 8 hours at 980 and 1065°C were also carried out at the same heating rate of the DSC analysis in order to confirm the obtained result. As already pointed out, the quality of TMA signal is

lower at higher heating rate, however it is possible to observe a good agreement between the two types of thermal analysis (figure 4.27).

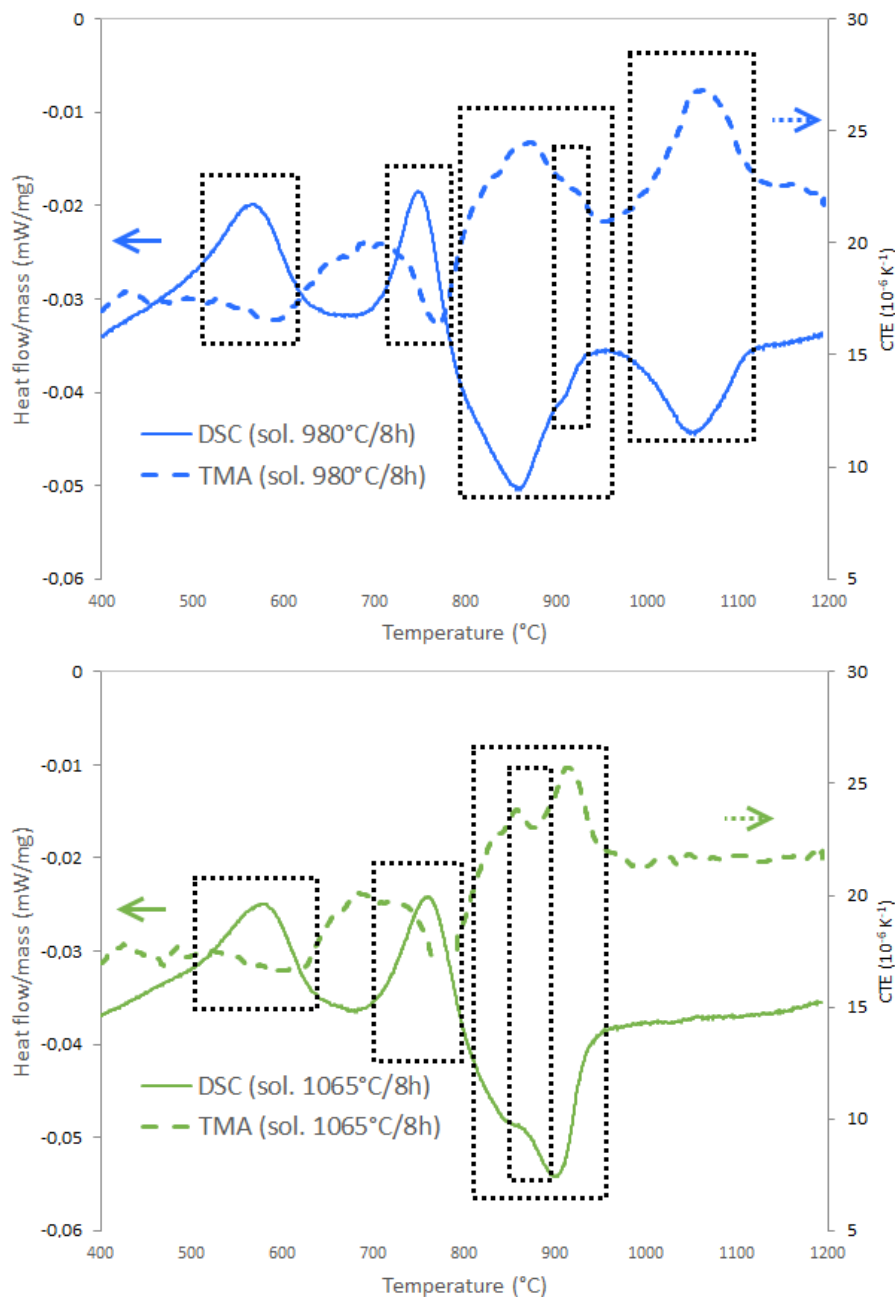


Figure 4.27. Comparison between the DSC and TMA heating curves collected on the samples previously solutioned at 980°C and 1065°C for 8 hours. Heating rate: 20°C/min. Dotted boxes indicate the overlapping signal peaks.

Based on the above reported thermal analyses, the subsequent study on the aging was focused on the follow temperatures of interest obtained from the DSC ramp performed at heating rate of 20°C/min on the sample solutioned at 1065°C for 2 hours (see table 2.5):

- peak of EXO 1: 565°C;
- peak of EXO 2: 740°C;

- offset of EXO 2: 800°C
- peak of EXO 3: 870°C

For study the effect of the first aging step on the Brinell hardness (paragraph 4.3.4), the temperatures of 650 and 720°C were considered (see table 2.6). These temperatures were chosen because they delimited the growing side of the EXO 2 peak. The choice to use the lower values was done to avoid the coarsening of the γ'' phase and the formation of δ phase during the first aging, however an aging treatment at 760°C, i.e. the highest temperature detected for the EXO 2 peak in the performed thermal analyses, was also considered (see table 2.7).

Finally, for the study of the second aging step (paragraph 4.3.5), the temperatures delimitating the peak EXO 1, i.e. 520 and 630°C (see table 2.8), were investigated.

4.3.3 Aged microstructure

The evolution of the microstructure during aging is further investigated through FESEM observations of SLM Inconel 718 samples submitted to different aging treatments at the characteristic temperatures obtained from the thermal analysis reported previously in this chapter (figures 4.5 and 4.26). The samples used for this study were previously submitted to a solution annealing treatment at 1065°C for 2 hours in order to remove the microstructural features of the as built state and obtain a small initial number of preexisting precipitates, making easier the identification of the new formed ones.

Table 2.5 summarized the thermal history of the aged samples used for this investigation. The number of the exposition steps at the characteristic temperatures and the respective durations were chosen in order to obtain some indication on the precipitation and coarsening kinetics of the second phases which are expected to form. At 565°C the formation of γ' phase is expected, the comparison between the microstructure after a relatively short exposition (4 hours) and a prolonged one (24 hours) allows to determine if a short time is sufficient to reach a saturation level of the γ' content in the aged alloy. The precipitation of γ'' is reported to be more sluggish with respect to γ' [1] [17] [211], therefore the observation after a very short period (2 hours) of exposition at 740°C is performed to verify that γ' formation precedes the γ'' phase. Conversely, the prevalence of γ'' on γ' is expected after 8 hours of exposition. The aging treatments at 800°C have the aim to verify an eventual transformation of the metastable γ'' into δ . Finally, at 870°C both γ'' and δ phases could form. The latter is expected to prevail on the former with the proceeding of the exposition. The overall aging period is 24 hours for all samples, the analysis after this period allows to verify an eventual coarsening of the phases γ' , γ'' and δ phases.

The collected Vickers microhardness are reported in figure 4.28, they provide a preliminary feedback of the evolution of the strengthening particles in the alloy during the aging treatment.

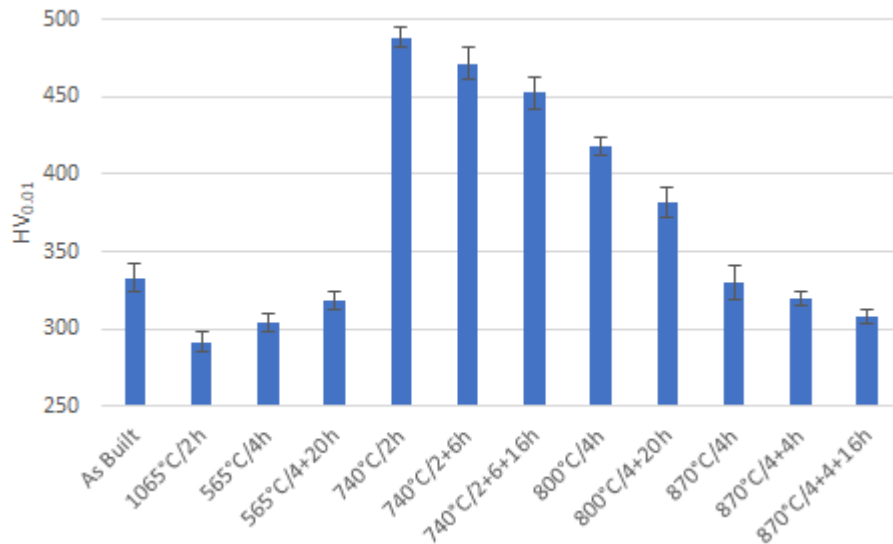


Figure 4.28. Mean Vickers microhardness obtained on the samples solutioned at 1065°C for 2 hours and then aged at the characteristic temperatures of the alloy. The bars indicate the 95% confidence ranges. Data published in [186].

The x-ray patterns obtained on the as built sample and on the 1065°C for 2 hours solutioned one are shown in figure 4.29. The peaks relative to the face centered cubic (FCC) γ matrix are clearly recognizable. No peaks related to second phases are detected. However, the present peaks are modified by the solution treatment, in fact they become narrower and shifted at a lower value of 2θ angle. In figure 4.29 is shown, as an example, the magnification of the main peak, the Full Width at Half Maximum (FWHM) of the peaks relative to the as built and the solutioned samples are 0.307° and 0.0895° , respectively. The reduction of the FWHM values is probably due to the release of the internal stresses in the as built material during solution treatment. The shift of the peaks toward lower 2θ angle, which corresponds to a greater value of the interplanar distance d according to the Bragg's law (equation 2.10), is due to the increase of the lattice distortion arising from the increase of the solute content. In particular Nb is progressively released in solid solution and this is in agreement with the results obtained with the TMA analyses (figures 4.4 and 4.27). Therefore, the shift of the peaks, also reported for Inconel 625 alloy [212] [213], is an indirect proof of the dissolution of the second phases present in the as built material during solution annealing.

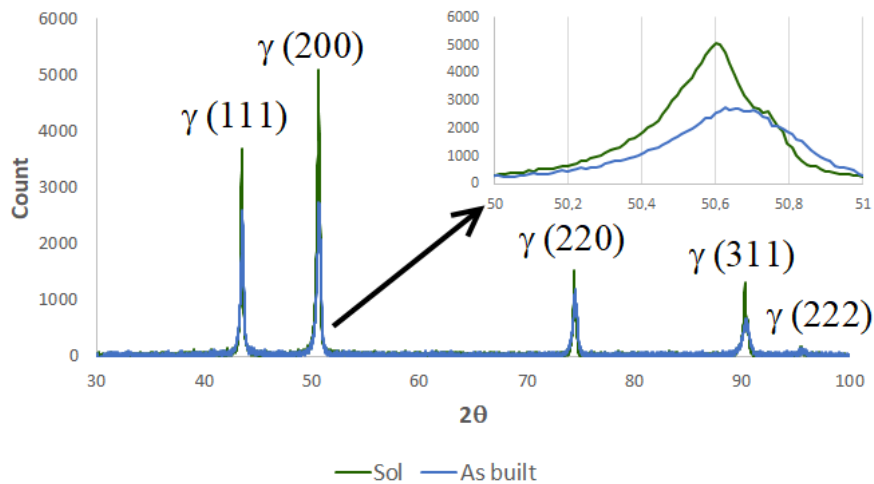


Figure 4.29. X-ray diffractograms of the as built sample and the sample solutioned at 1065°C for 2 hours. First published in [186].

The x-ray patterns obtained on the differently aged samples are shown in figure 4.30. An additional peak at $2\theta \cong 46^\circ$ is revealed only on samples treated at 870°C for 8 and 24 hours. This peak can be indexed as the (211) of the δ phase, which is the stronger peak of this compound [44]. No one of the other diffraction peaks of the δ phase was detected during the XRD analysis; similar spectra are also reported by Cao et al. on SLM Inconel 718 alloy after solution treatment at 1065°C for 1 hour and double aging at 760°C for 10 hours and 650°C for 8 hours [46]. The x-ray diffraction peaks related to the δ phase are typically observed on Inconel 178 alloy after thermal treatment between 850°C and 990°C [49] [214] [215].

The presence of the γ' and γ'' phases cannot be ascertained by XRD analysis because their peaks are superimposed to the ones of the γ matrix. Nevertheless, the precipitation of these new phases can be deduced from the shift of the peaks (a magnification of the main peak is shown in figure 4.30 as an example).

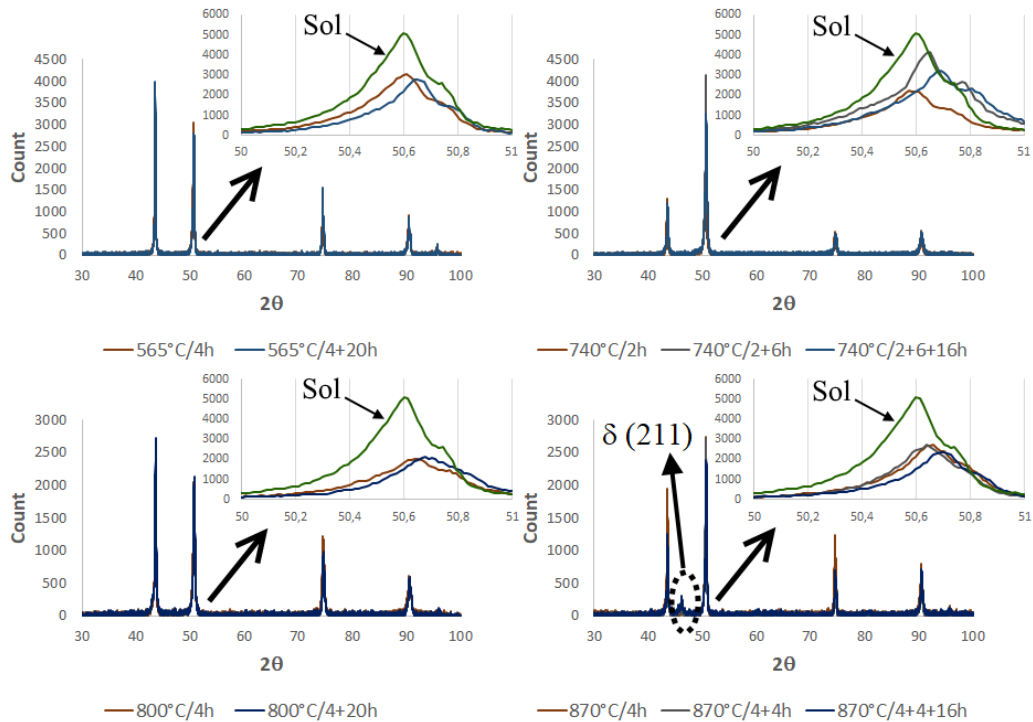


Figure 4.30. X-ray diffractograms of the samples aged at the characteristic temperatures of the alloy with magnification on the γ (200) peak in order to observe the shift respect to as solutioned state. First published in [186].

The values of lattice parameter determined on the samples evaluated by XRD analysis are shown in figure 4.31. The lattice parameter decreases with the time and the temperature of the aging treatment due to the progressive transfer of the solute from the solid solution to the precipitates. Zhang et al. also report a reduction of the lattice parameter of the FCC matrix of an Inconel 625 alloy, produced by powder bed additive manufacturing technique, during the post heat treatment caused by the precipitation of δ precipitates and the consequent reduction of the Nb content from the solid solution [216].

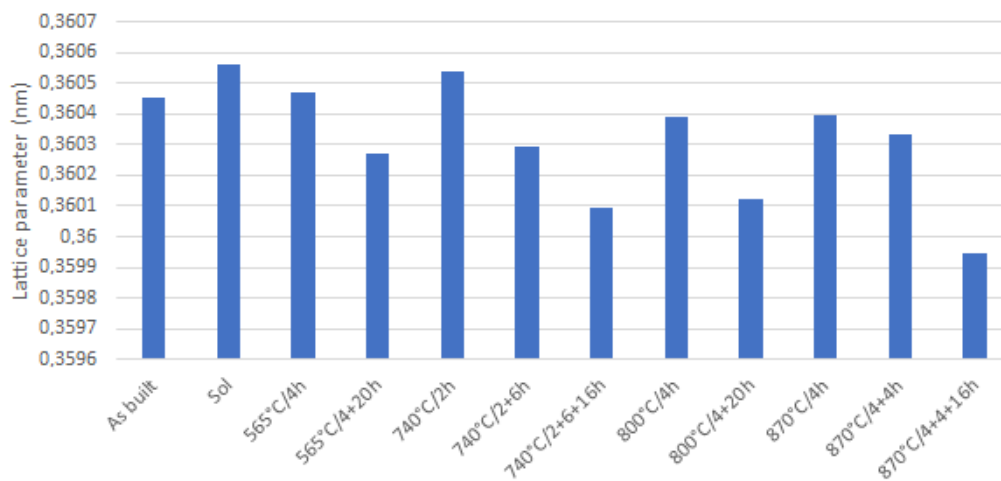


Figure 4.31. Values of the lattice parameter of γ phase with different thermal histories obtained from the XRD analyses. Data published in [186].

Most of the precipitates present after aging at 565°C are residuals of the eutectic phases, in particular small carbides that were not dissolved during the previous solution annealing, and intergranular carbides formed during the solution annealing. Also γ' is expected to form at such temperature, but it is probably too fine to be clearly defined through FESEM images, although a population of very small particles can be observed after 24 hours of aging (figure 4.32). However, the increase of the Vickers microhardness during aging at 565°C is an indirect proof of the formation of γ' strengthening phases at this temperature and it also demonstrates that the saturation level is not reached after 4 hours of exposure at this temperature, since the microhardness can still be increased by prolonging the heat treatment.

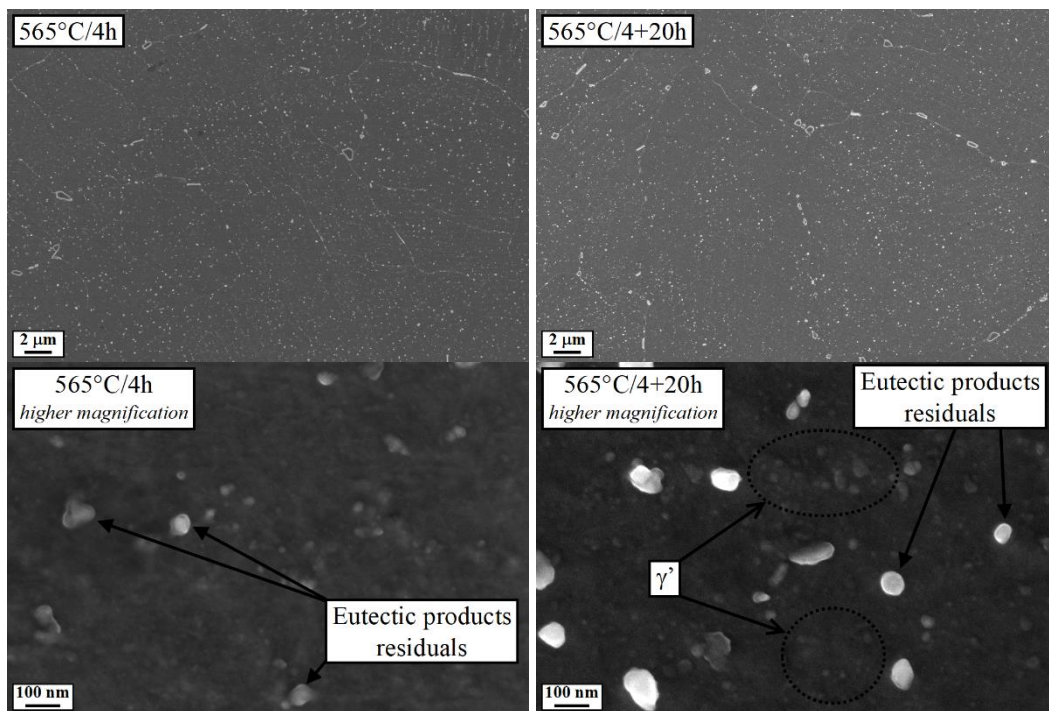


Figure 4.32. FESEM micrographs of the samples aged at 565°C. The micrographs acquired on the sample aged for 24 hours have been already published in [186].

After aging at 740°C the microstructural modification is more pronounced and an important formation of strengthening phases occurs that lead to a strong increase of the Vickers microhardness. It can be observed that new precipitates are formed already after 2 hours of treatment. The density of newly formed precipitates is not homogeneous: the interdendritic boundary are decorated with a larger number of precipitates respect to the core of each dendrite. After 2 hours the formed precipitates are extremely small, most of them are probably γ' that form with a higher kinetics with respect to γ'' . Conversely, discoidal γ'' precipitates are clearly identifiable after longer aging time. Comparing the FESEM images after 8 and 24 hours of aging, it is possible to observe that coarsening of γ'' occurs that leads to a progressive reduction of the Vickers microhardness.

The γ'' precipitates have a clear crystallographic relationship with the matrix, how it can be seen in figure 4.33. In each grain the γ'' precipitates form along one of the two orthogonal directions. The γ'' disks form parallel to the $\{100\}$ planes of

γ with the following reciprocal crystallographic orientation [46] [47]: $(001)_{\gamma''} \parallel \{100\}_{\gamma}$, $[100]_{\gamma''} \parallel \langle 001 \rangle_{\gamma}$.

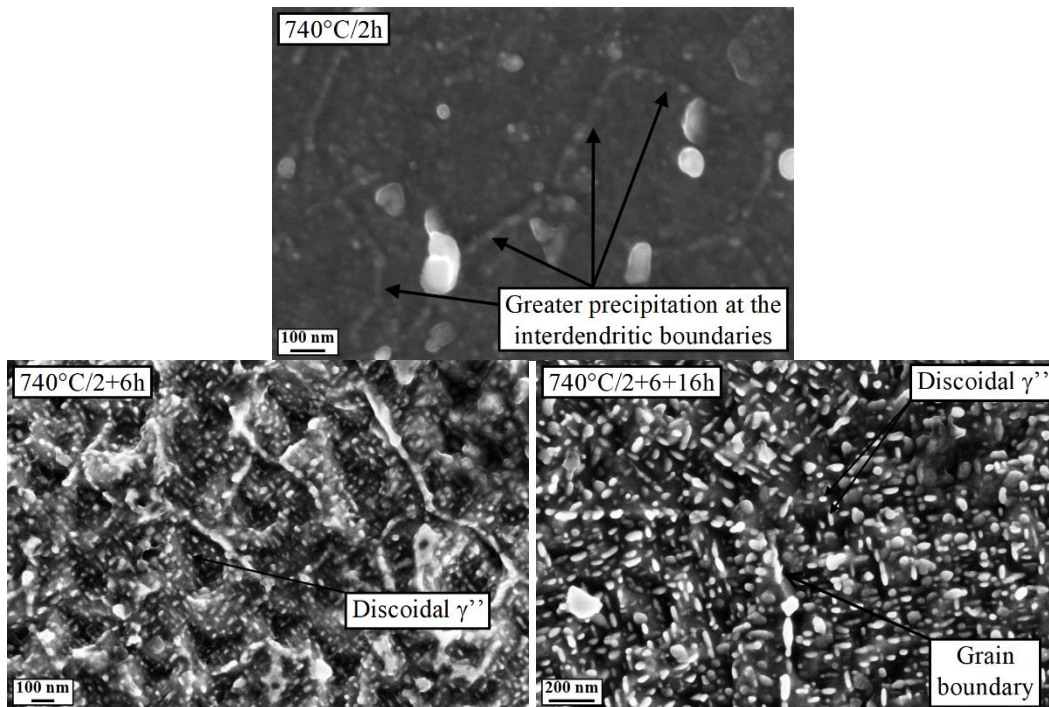


Figure 4.33. FESEM micrographs of the samples aged at 740°C. Formation of discolidal γ'' after longer aging time.

During aging at 800°C, δ precipitates start to form at the grain boundaries (figure 4.34). Inside the grain, discolidal γ'' undergo further coarsening. A precipitates depleted zone forms along grain boundaries in which γ'' precipitates are dissolved due to the formation of intergranular δ compounds that reduce the local availability of Nb. In this depleted zone, γ' particles are still present because their formation does not require Nb availability. Similar observations (absence of γ'' precipitates near the intergranular δ plates) are also reported by Wlodek and Field [18].

After 24 hours of exposition, the intergranular δ phase is coarser and precipitates with plate-like morphology are detectable also inside the grains. Intragranular δ precipitates can nucleate on the stacking fault of preexisting precipitates of γ'' [23]. Therefore at this temperature the population of γ'' is progressively substituted by δ phases leading to a decrease of the Vickers microhardness.

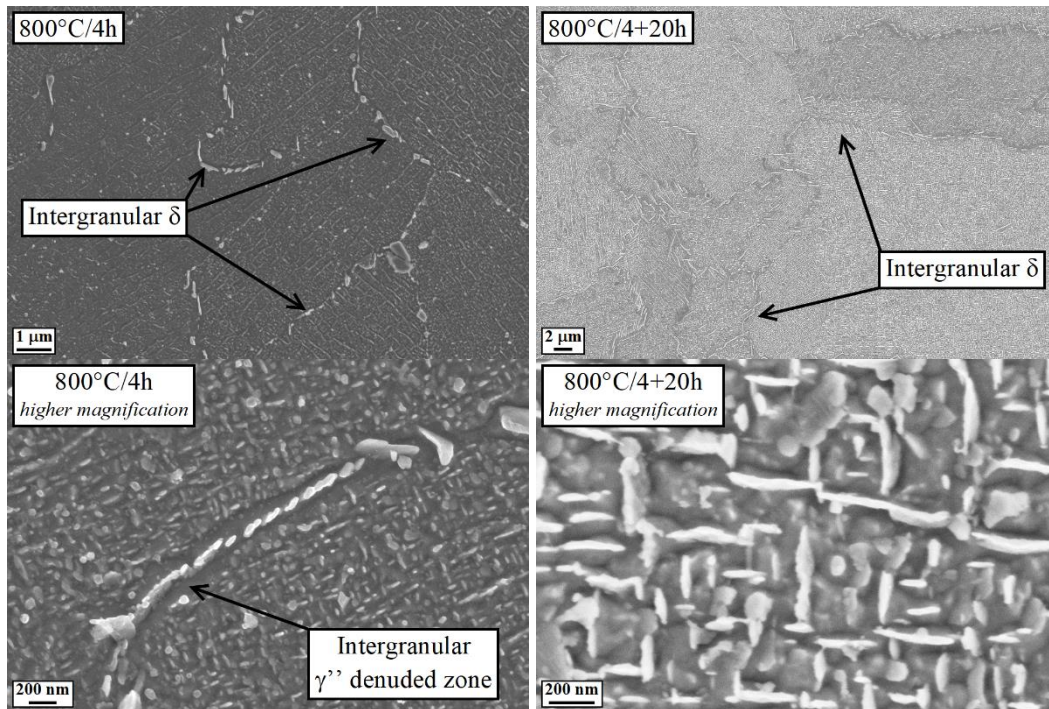


Figure 4.34. FESEM micrographs of the samples aged at 800°C. Formation of intergranular δ and further coarsening of discoidal γ'' .

After the aging temperature of 870°C the strengthening phases γ' and γ'' are completely absent and a lot of plate-like δ precipitates form (figure 4.35). At the grain boundaries the formation and growth of δ precipitates are faster, therefore coarser plates can be observed in these zones with respect to the intragranular areas. Inside each grain, the plates form a regular pattern consisting of arrays disposed in a parallelepiped grid. This regular disposition of the intragranular δ phase is due to its crystallographic relationship with the matrix (as reported at paragraph 1.3.1.3) [19] [44] [46] [47]: $(010)_{\delta} \parallel \{111\}_{\gamma}$, $[100]_{\delta} \parallel \langle 1\bar{1}0 \rangle_{\gamma}$.

The plates of each array continue to growth with time and merge leading to the formation of very long precipitates of about 6-8 μm (bottom right panel of figure 4.35).

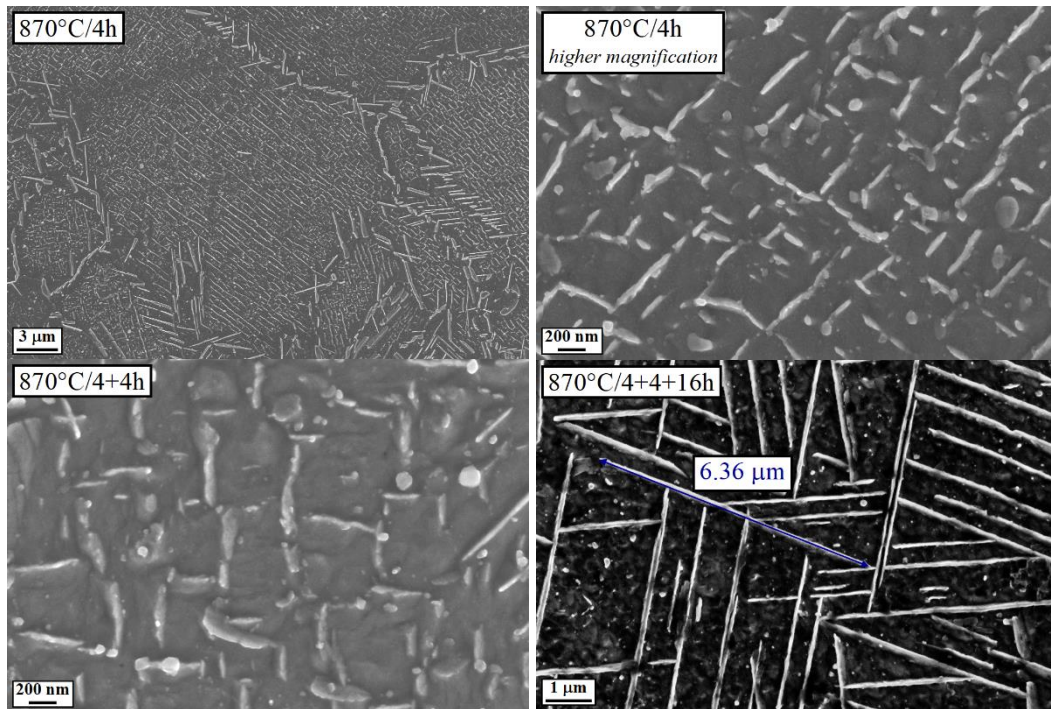


Figure 4.35. FESEM micrographs of the samples aged at 870°C. Intergranular and intragranular plate-like δ precipitates form and grow during aging.

4.3.4 First aging step

The samples submitted to different combinations of preliminary solution annealing and first aging treatment (see table 2.6) were studied using Brinell hardness. The results are plotted on figure 4.36.

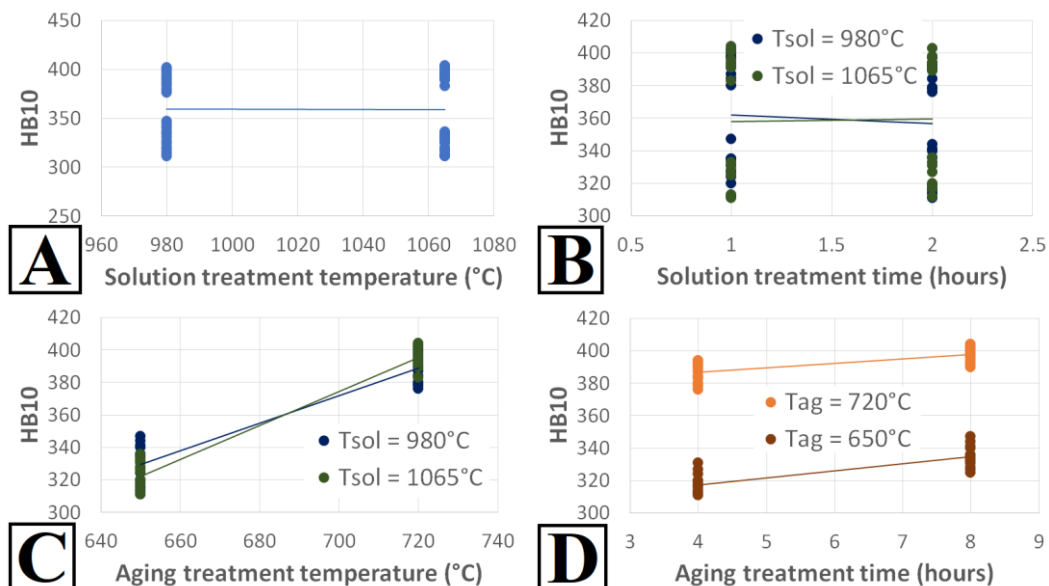


Figure 4.36. Effects on the Brinell hardness of the heat treatment factors, the solution treatment temperature (A) and time (B) and the aging treatment temperature (C) and time (D), and their most significant interactions.

The analysis of variance (ANOVA) of the 2^4 factorial plan reported in table 4.1 allows to identify the most significant factors and interactions on the final hardness of the material.

Table 4.1. Analysis of Variance (ANOVA) on the dataset made by 4 Brinell hardness measurements for each sample of the 2^4 factorial plane with the main effects of the heat treatment factors, T_{sol} , t_{sol} , T_{ag1} , t_{ag1} , and their interactions until the second order. DOF: degrees of freedom; SS: sum of squares; MS: mean squares; F: F-ratio.

	DOF	SS	MS	F	p-value
<i>Main effects</i>					
T_{sol}	1	4.00	4.00	0.27	0.6080
t_{sol}	1	60.06	60.06	4.00	0.0507
T_{ag1}	1	69960.25	69960.25	4657.06	< 0.0001
t_{ag1}	1	3277.56	3277.56	218.18	< 0.0001
<i>Second order interactions</i>					
$T_{sol} * t_{sol}$	1	196.00	196.00	13.05	0.0007
$T_{sol} * T_{ag1}$	1	742.56	742.56	49.43	< 0.0001
$T_{sol} * t_{ag1}$	1	49.00	49.00	3.26	0.0766
$t_{sol} * T_{ag1}$	1	42.25	42.25	2.81	0.0994
$t_{sol} * t_{ag1}$	1	10.56	10.56	0.70	0.4055
$T_{ag1} * t_{ag1}$	1	169.00	169.00	11.25	0.0015
<i>Residuals</i>	53	796.19	15.02		

In the considered ranges of the experimental parameters, the hardness increases with temperature and time of aging. The effects of these two factors are clearly the most significant ones. As a consequence, the aging treatment at 720°C for 8 hours is considered the best solution for each condition of solutioning. Brinell hardness and Vickers microhardness measurements were also collected after solution annealing at 1065°C for 2 hours and first aging at 760°C for 8 hours. The plots in figures 4.37 show that the final hardness after the aging step reaches a maximum at 720°C, then decreases with further increasing of the first aging temperature. According to the outcome reported in paragraph 4.3.3, one can assume that this decrease is due to excessive coarsening of the γ'' phase during the aging treatment.

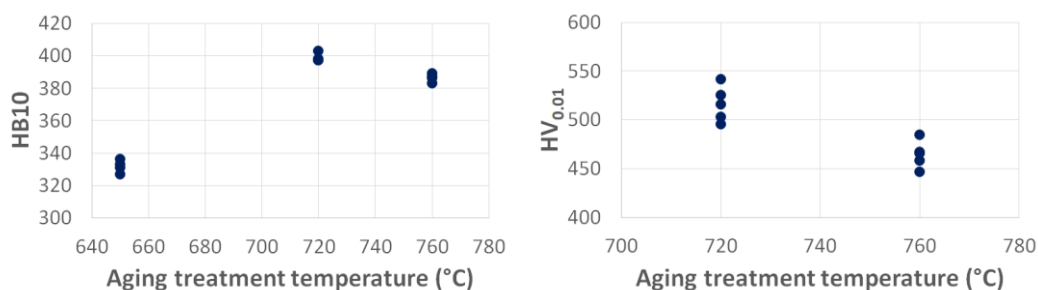


Figure 4.37. Brinell hardness (HB10) and Vickers microhardness ($HV_{0.01}$) in function of the aging temperature after solution annealing at 1065°C for 2 hours and 8 hours of aging.

The time of the preliminary solution annealing has a limited effect, in particular a little reduction of the hardness is recorded by passing from 1 to 2 hours of solution

treatment at 980°C. This can be ascribed to the formation of δ phases during the solution annealing at 980°C that reduces the availability of Nb for the formation of strengthening γ'' phase during the aging step. Actually, this reduction is negligible when the solution annealing is performed at 1065°C, during which the δ phase cannot form. The effect of factor t_{sol} was deeper investigated by assessing the effect of a prolonged solution annealing. For this reason, two extra samples were submitted to an 8 hours solution annealing at 1065°C and 980°C respectively and then aged at 720°C for 8 hours. The behavior of Brinell and Vickers hardness as a function of the time t_{sol} are reported in figure 4.38. A prolonged solution annealing leads to a loss of the final hardness after aging. The loss of hardness after 8 hours of solution annealing is more pronounced at 1065°C and is probably due to an excessive dissolution of the pre-existing intragranular carbides that leads to a softening that cannot be completely recovered by the formation of γ'' strengthening phase. On the other hand, at the solution temperature of 980°C the loss of hardness is more pronounced for short t_{sol} , due to the formation of δ as already discussed above. Nevertheless, such loss of hardness is limited after 8 hours of solutioning with respect to what observed when the solution treatment is performed at 1065°C. This is consistent with the results obtained in the study of the solutioning step (figure 4.22) and is related to the presence of δ precipitates, which hinder the development of γ'' phase on one hand but allow also to maintain the hardness for long periods of solubilization.

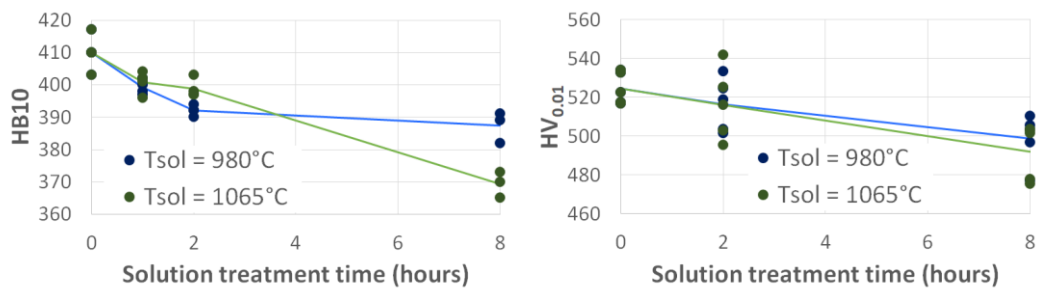


Figure 4.38. Brinell hardness (HB10) and Vickers microhardness (HV_{0.01}) as function of the solution treatment time after aging at 720°C for 8 hours.

The first order effect of the temperature T_{sol} is negligible, however the ANOVA on table 4.1 reveals that T_{sol} has a little but statistically remarkable interaction effect with T_{ag1} : the solution annealing at 1065°C enhances the impact of the aging temperature T_{ag1} on the final hardness (figure 4.36-C), therefore this solution temperature is better than 980°C when the higher value of T_{ag1} is adopted. This is in good agreement with the analysis reported at paragraph 4.2, in which the greater efficiency of the solution annealing at 1065°C in term of dissolution of preexisting second phases is ascertained with consequent higher level of Nb, Al and Ti available in the matrix for the formation of the strengthening phases. The plot in figure 4.36-C also shows that a preliminary solution annealing at 980°C is preferable if the aging treatment is performed below a certain threshold temperature of about 690°C.

This is because in such condition the increase of hardness due to the δ phase balances the missed formation of γ'' precipitates.

Finally, the effect of t_{inv1} is lower when the aging is performed at 720°C rather than at 650°C. In other words, the hardness reaches faster a saturation level when T_{inv1} is higher.

On the base of the data collected in the 2^4 factorial plan, the following fit model is proposed:

$$HB = (359 \pm 1) - (1 \pm 1)x_{t_{sol}} + (33 \pm 1)x_{T_{ag1}} + (7 \pm 1)x_{t_{ag1}} + \\ + (2 \pm 1)x_{T_{sol}}x_{t_{sol}} + (3 \pm 1)x_{T_{sol}}x_{T_{ag1}} - (2 \pm 1)x_{T_{ag1}}x_{t_{ag1}} \quad \text{eq. 4.1}$$

where x is the value of the considered factors in coded units. The higher and lower levels are denoted by $x = 1$ and $x = -1$, respectively. The hardness fitted values for each combinations of parameters are reported in table 2.

Table 4.2. Brinell hardness values evaluated with the linear regression model of equation 4.1 for each combination of T_{sol} , t_{sol} , T_{ag1} , t_{ag1} .

T_{sol} (°C)	t_{sol} (h)	T_{ag1} (°C)	t_{ag1} (h)	HB fit
980	1	650	4	323 ± 3
980	1	650	8	341 ± 3
980	1	720	4	386 ± 3
980	1	720	8	397 ± 3
980	2	650	4	318 ± 3
980	2	650	8	336 ± 3
980	2	720	4	381 ± 3
980	2	720	8	392 ± 3
1065	1	650	4	313 ± 3
1065	1	650	8	331 ± 3
1065	1	720	4	389 ± 3
1065	1	720	8	400 ± 3
1065	2	650	4	315 ± 3
1065	2	650	8	332 ± 3
1065	2	720	4	391 ± 3
1065	2	720	8	402 ± 3

The highest hardness values are thus obtained with first aging at 720°C for 8 hours and preliminary solution annealing at 1065°C/1h, 1065°C/2h and 980°C/1h. The hardness recorded on samples aged directly from the as built condition are reported in figure 4.39 in comparison with the data collected on the solutioned and aged samples.

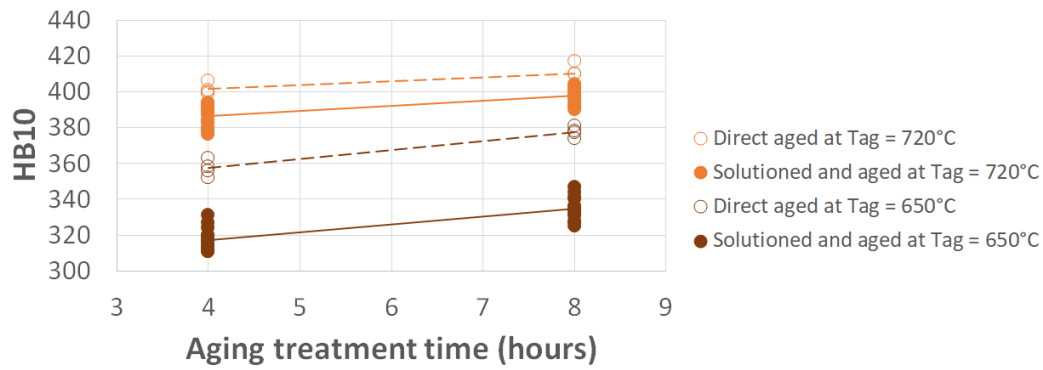


Figure 4.39. Brinell hardness at different aging condition without preliminary solution annealing (direct aging) and with solution annealing at 1065°C for 2 hours.

From this comparison, it is possible to observe that the direct aging heat treatment always provides higher hardness at the same value of aging temperature and time. This is not surprising, because after direct aging all the interdendritic precipitates present in the as built state remain unaltered and can hinder the dislocations motion and, as a consequence, the plastic deformation. However, the excessive content of undissolved prior Laves phases strongly affects the ductility and toughness of the alloy. Actually, Deng et al. report that the direct aging provides the highest hardness and tensile properties, but the lowest ductility with respect to other post treatment conditions that include a solution/homogenization step [160].

Figure 4.40 show the FESEM micrographs of the samples aged for 8 hours at 650°C and 720°C without preliminary solution annealing and after solution annealing for 2 hours at 980 and 1065°C. Many small discoidal precipitates can be observed in samples aged at 720°C, whereas some very fine rounded particles are visible on the samples aged at 650°C. On the base of thermal analysis (paragraph 4.1) and of previous investigation on the aging response (paragraph 4.3.3), one can conclude that the aging at 720°C leads to a relevant increase of the hardness because of the large precipitations of γ'' phase. Conversely, the aging at 650°C leads only to precipitation of very fine γ' particles that cause a lower strengthening of the alloy. The solution annealing step does not influence the type of strengthening precipitates formed, however it determines the homogeneity of the precipitates distribution. In the direct aged samples, the precipitation of strengthening phases occurs mostly at the interdendritic boundaries where the local level of Nb, Ti and Al is higher due to microsegregation during solidification (paragraph 3.2.4). Conversely, the γ' and γ'' precipitates distribution on the solution annealed samples is more uniform, although a film of second phases form also in these samples at the interdendritic boundaries. The plate-like δ precipitates present on the samples solution annealed at 980°C leads to further microstructural heterogeneity. Actually, it is possible to observe a precipitates depleted zone around the δ plates where γ'' precipitates don't form.

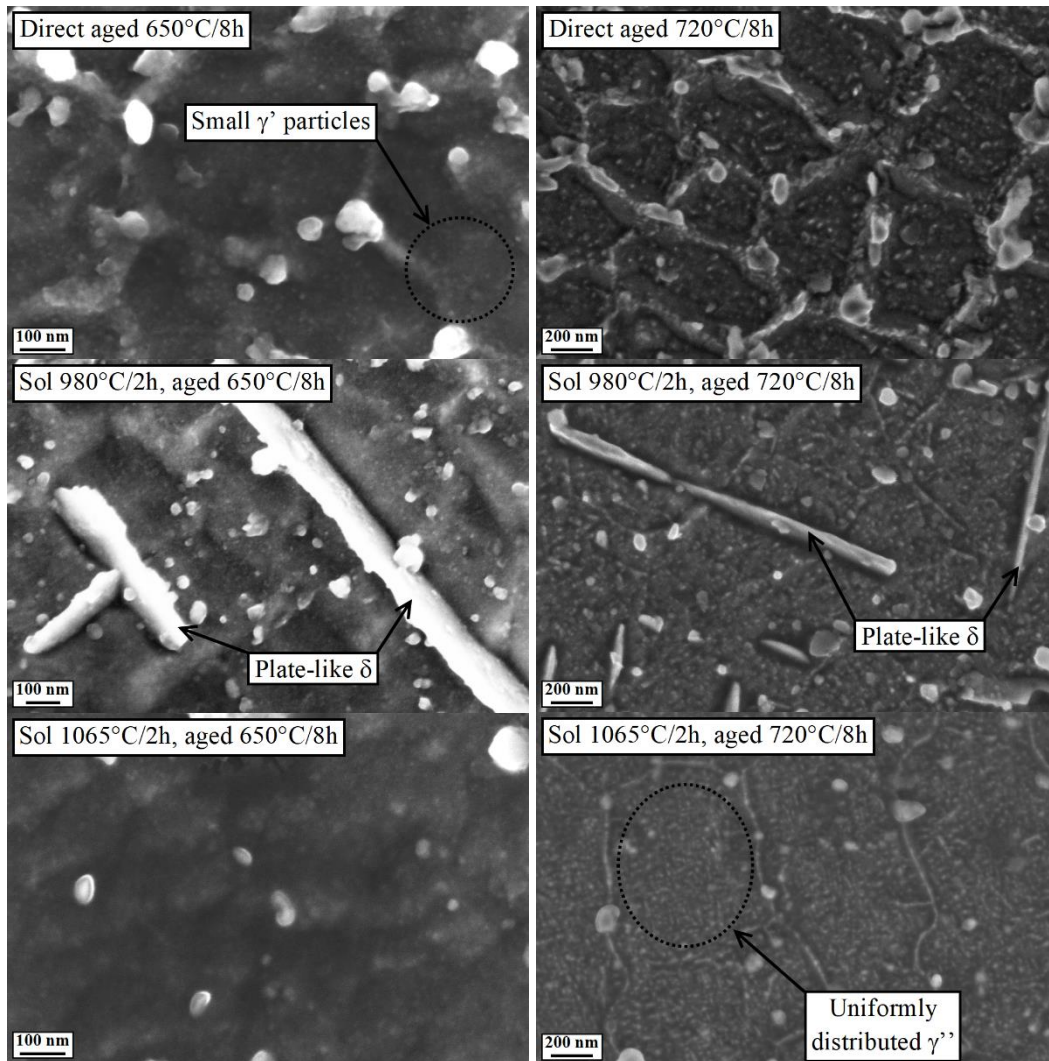


Figure 4.40. FESEM micrographs of single aged samples in different solution conditions.

The above reported observations confirm that the preliminary solution annealing at 1065°C followed by first aging at 720°C is the best heat treatment solution from the point of view of both hardness and microstructural uniformity.

4.3.5 Second aging

The Brinell hardness measurements, collected on the samples submitted to double aging treatment following the recipes of table 2.8, are graphically reported in figure 4.41. The Brinell hardness increases with the temperature T_{ag2} , but the time of aging doesn't provide a marked effect. At $T_{ag2} = 630^\circ\text{C}$ the hardness reaches a saturated value already after 4 hours of treatment and doesn't increase anymore if the aging is prolonged to 8 hours. Conversely, at $T_{ag2} = 520^\circ\text{C}$ a slight decrease of the hardness is observed with 8 hours of aging. The Vickers microhardness achieved after the double aging confirm the general trend ascertained with the Brinell measurements, however a limited difference between the data relative to two second aging temperatures is observed. Note that the Vickers microhardness measurement is less suitable to detect slight difference in the average hardness of

the samples because it is more strongly affected by the local microstructural features and, therefore, the Vickers data are characterized by a marked fluctuation.

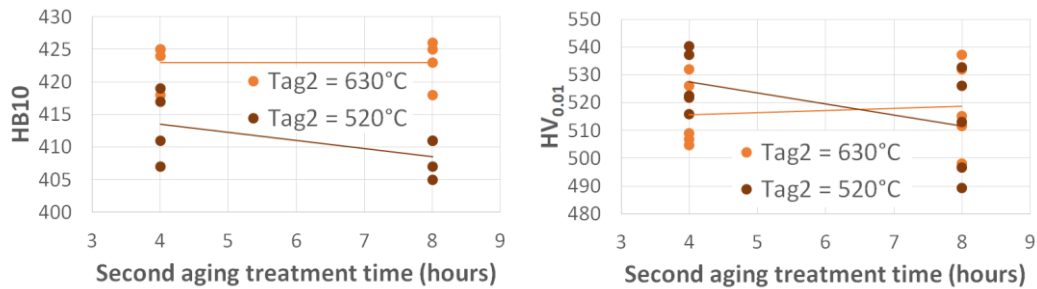


Figure 4.41. Brinell hardness (HB10) and Vickers microhardness (HV_{0.01}) in function of the second aging temperature and time after preliminary solution annealing at 1065°C for 2 hours and first aging at 720°C for 8 hours.

Figure 4.42 reports the FESEM micrographs of the samples double aged with 8 hours of second aging. During the second aging, the amount of inter-dendritic strengthening precipitates further increases. On the base of the thermal analysis outcome, γ' is expected to form at this temperature level. The γ' particles formed during the second aging plays in synergic mode with γ'' precipitates formed during the first aging resulting in the further increase of hardness detected on the double aged samples. The saturation hardness value is achieved quickly, as already earlier discussed, because of the rapid precipitation kinetic of γ' .

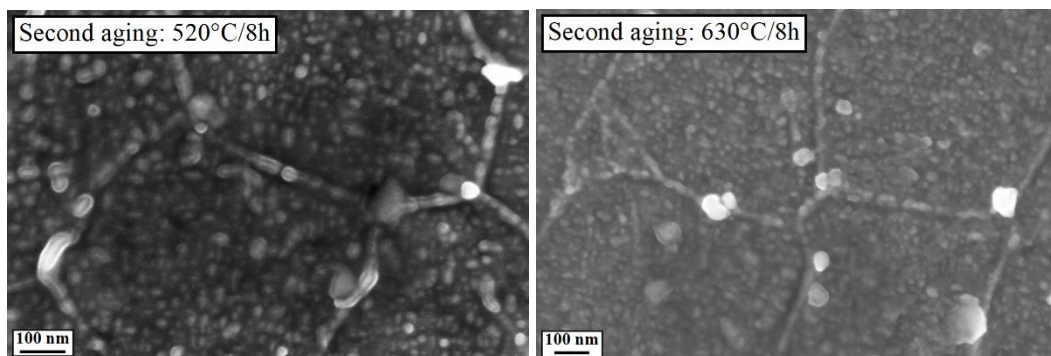


Figure 4.42. FESEM micrographs of double aged samples after preliminary solution annealing at 1065°C for 2 hours and first aging at 720°C for 8 hours.

4.4 Conclusion

The thermal analyses provided a useful basic starting point for the study of the microstructural evolution of Inconel 718 after production through SLM process. Actually, the temperature ranges at which the main thermal phenomena of dissolution and precipitation of second phases were obtained through DSC and TMA techniques.

The solution annealing at 1200°C allows to obtain the greater level of dissolution of the second phases, however the intergranular precipitates are no more able to pin the grain boundaries at this temperature, therefore severe grain coarsening occurs with consequent strong reduction of the mechanical properties, evaluated here through Vickers microhardness measurements. At the standard solution temperature, i.e. 980 and 1065°C, intergranular precipitates form that prevent grain coarsening. On the samples solutioned at 980°C, plate-like δ precipitates are present and their volume fraction increase with the time of the solution treatment. The presence of δ phase after solutioning at 980°C was also confirmed by the DSC and TMA analysis. The collected data allow to state that the δ phase have two opposite effects on the alloy hardness:

- it provides a certain strengthening that prevent an excessive softening of the alloy after prolonged time of solutioning;
- it leads to low hardness due to hindering of the γ'' formation during the aging treatment because of the Nb sequestration.

The solution treatment at 1065°C seems to be the best compromise between microstructural homogenization, dissolution of the pre-existing second phases and possibility to avoid grain coarsening. However, an excessive duration of the solution annealing at 1065°C leads to an important decrease of the hardness that cannot be completely recovered after aging. Therefore, the solution time has to be selected in order to dissolve the metastable Laves phases and reduce the microstructural heterogeneity of the as built state without causing excessively softening of the alloy. A solution time of 2 hours was found to achieve this balanced result.

The formation and evolution of the γ' , γ'' and δ phases in the material, preliminary solutioned at 1065°C for 2 hours, during exposition to four characteristic temperatures were then investigated:

- at 565°C the precipitation of γ' occurs predominantly;
- at 740°C γ' is initially formed, then an extensive precipitation of γ'' occurs; an excessive exposition leads to coarsening of γ'' and consequent reduction of the microhardness;
- at 800°C coarser γ'' precipitates form and the δ phase forms at the grain boundaries, after prolonged exposition the γ'' precipitates transform to δ ;
- at 870°C intergranular and intragranular δ precipitates form and grow with the exposure time.

These observations allow to interpret the results obtained during the optimization study of the complete heat treatment cycle, performed to identify the parameters that have the most important impact on the mechanical performances and the effect of these on the material microstructures. The final hardness of the alloy is mainly controlled by the selection of the temperatures of the two aging steps. The first aging temperature of 720°C was found to be the optimal selection for the formation of strengthening γ'' phases. Actually, a further increase of the temperature at 760°C leads to a loss of hardness due to excessive coarsening of the γ'' particles. During the second aging step, further γ' strengthening particles can be formed. The greatest increase of hardness is obtained with a second aging step at 630°C.

Although it was observed that the preliminary solution annealing leads to a reduction of the achievable hardness after first aging treatment, such heat treatment procedure was preferred to the direct aging from as built state. This is due to the possibility to achieve dissolution of the pre-existing eutectics precipitates. The microstructural observations reveal that the solution step allows to obtain a more uniform distribution of the strengthening γ'' precipitates after aging. The solution treatment is advisable also to avoid embrittlement due to the presence of undissolved Laves phases.

Figure 4.43 summarizes the hardness and microstructural evolution during each step of the optimal heat treatment cycle: solution annealing at 1065°C for 2 hours, first aging at 720°C for 8 hours and second aging at 630°C for 8 hours. The microstructural evolution of SLM Inconel 718 observed in this study after different post heat treatments is in good agreement with the results reported by Li et al. [217].

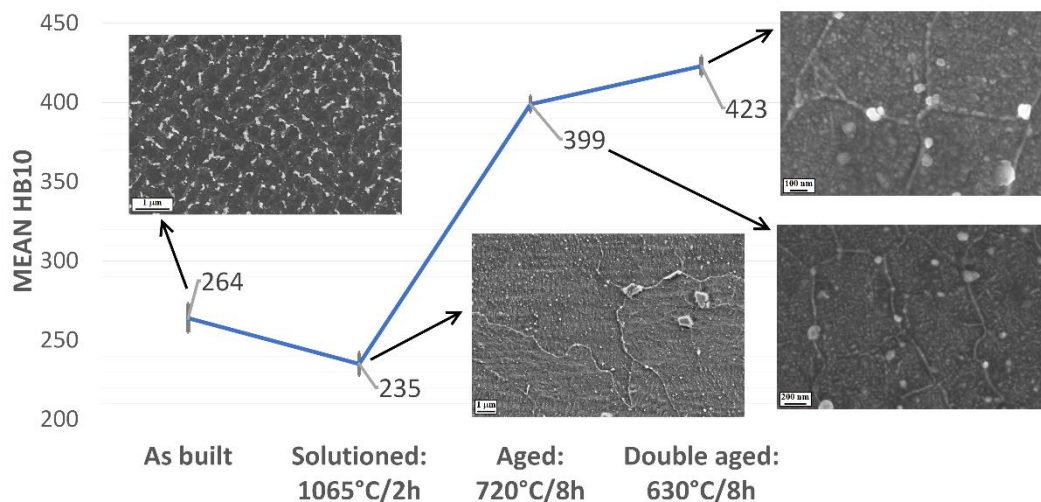


Figure 4.43. Mean Brinell hardness after each step of the optimized treatment cycle and relative microstructure. The error bars refer to 95% confidence ranges.

Chapter 5

Hot oxidation behavior

The results of the oxidation tests on Inconel 718 alloy produced through SLM technique are presented and discussed in this chapter.

The performed tests are divided in short term tests, in which the samples are oxidized until 56 hours, middle term tests, with oxidation runs up to 215 hours, and long term tests, with oxidation runs up to 908 hours. The short term tests allow to accurately observe the transition between the initial transient stage and the stationary oxidation regime. Middle term tests help to investigate the steady oxidation state. With these tests also the effects of the thermal cycling and the atmosphere of the preliminary solution annealing on the growth rate of the oxide will be also discussed (see paragraph 5.2). Finally, the long terms oxidation resistances help to identify the limit of service life of the specific SLM alloy. Besides the long period oxidation test of SLM Inconel 718 alloy also a traditionally fabricated Inconel 600 reference alloy is tested for sake of comparison. The different oxidation behavior of these alloys is evaluated also through the microstructural and composition study of the oxide scales formed on the alloys during the test. Part of the work concerning the long term oxidation tests has been previously published in [194].

The aged states were not considered during the hot oxidation tests because the aim of this study is to characterize the SLM Inconel 718 alloy in microstructural conditions in which the oxidation resistance is favored on the mechanical performances. These conditions are obtained by keeping dissolved in the γ matrix the greatest possible amounts of alloying elements, in particular Al and Ti, which can concur in the formation of the passivating scale.

Furthermore, the material was tested in view of a final application which involves long exposure periods at 850°C. As observed in the previous chapter, the strengthening phases γ' and γ'' , formed during the aging steps, are not stable at this temperature; hence they would be rapidly dissolved during the first service period,

furthermore the γ'' precipitates could accelerate the formation of intragranular δ phase by acting as nucleation sites.

5.1 Short term oxidation tests

The gravimetric curves relative to the cyclic oxidation performed at the temperatures of 850°C and 900°C in air are reported in figure 5.1. During the execution of these tests, no detachment of the oxide scale from the surface of the samples has ever been detected. The thermally grown oxide layer remain stable and well adherent on the substrate for all the test duration and, consequently, can efficiently protect the metallic surface. Furthermore, no signs of an eventual evaporation of the superficial oxide layer have been ever detected; such an event would cause the failure of the diffusion barrier and it would be registered as an abrupt reduction of the mass during this test.

Since the superficial oxide scale acts efficiently as protective barrier the oxidation resistance of the alloy can be evaluated by the oxide growth rate, that can be derived by the mass gain. A slow growth determines a reduced consumption of the oxide forming elements, typically Cr, Ti and Al, therefore the reserve of these elements in solid solution can guarantee long periods of stationary oxidation. Furthermore, a slow growth also allows to avoid an excessive fast thickening of the oxide layer that would cause the development of stresses at the metal/oxide interface and potential spallation of the protective layer.

The mass gain behavior shown in figure 5.1 doesn't reveal visible differences in the oxidation behaviors of the as built sample with respect to the ones previously submitted to solution treatments.

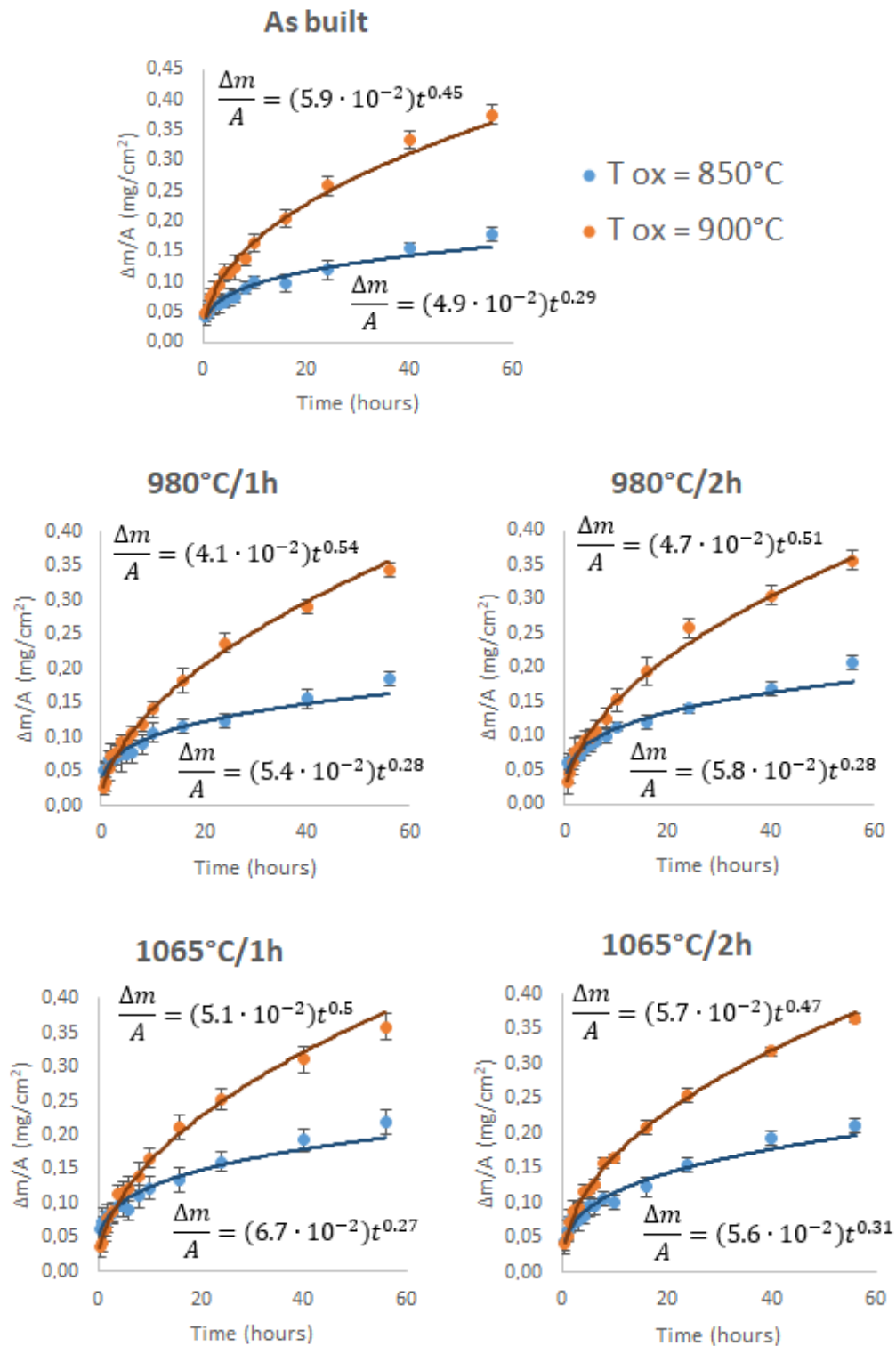


Figure 5.1. Mass gain ($\Delta m/A$) vs time (t) plots for the as built samples and the solutioned samples at the oxidation temperatures of 900°C (orange) and 850°C (blue) and relative fitting power laws.

The mass gain behaviors are fitted in figure 5.1 using a power law. It is possible to observe that exponent values close to 0.5 are obtained on the samples oxidized at 900°C , this indicates that the parabolic law is quite well respected at this test temperature. Conversely, the exponent values obtained on the samples oxidized at

850°C are always lower than the theoretical value of 0.5, therefore a sub-parabolic curve is followed in this case.

However, the sub-parabolic behavior can be described by a parabolic law in which the k_p value is not constant but decreases during the first thermal cycles until a stable value is achieved. During this initial transient step, the oxide forms rapidly on the surface through the reaction of the fresh metal with the oxygen in the atmosphere, but it cannot act as diffusion barrier yet. Once the formation of the continuous protective layer is complete, the coefficient k_p stabilizes to a constant value and the further growth of the scale becomes a totally diffusion controlled process. The formation and growth of the oxide can be approximately described by an average value $k_{p, \text{init}}$, valid during the initial transient regime, and a second value $k_{p, \text{stat}}$ constant during the next steady state regime:

$$\left(\frac{\Delta m}{A}\right)^2 = \begin{cases} k_{p, \text{init}} t & \text{when } t < t_{\text{init}} \\ k_{p, \text{init}} t_{\text{init}} + k_{p, \text{stat}} (t - t_{\text{init}}) & \text{when } t \geq t_{\text{init}} \end{cases} \quad \text{eq. 5.1}$$

The squares of the mass gains per unit of surface registered during the oxidation tests are plotted in figure 5.2 and 5.3 as function of the exposition time in order to distinguish the two oxidation regimes. At the oxidation temperature of 850°C, the initial transient regime lasts for a time t_{init} of about 8 hours (equivalent to the first 9 thermal cycles). After this run in stage then the collected experimental points lay on a straight line with lower slope, that represents the actual parabolic law followed during the stationary oxidation regime.

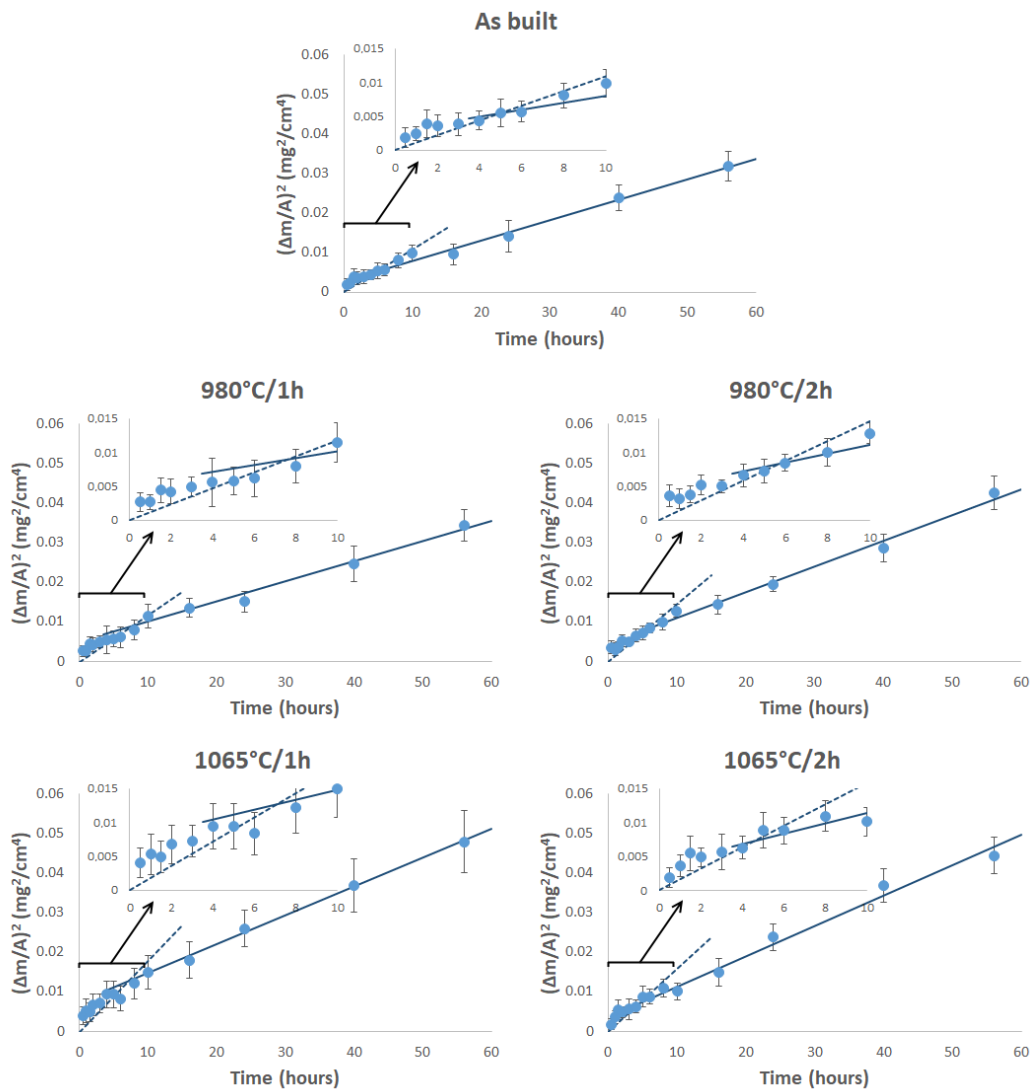


Figure 5.2. Mass gain squares vs time plots for the as built samples and the solutioned samples at the oxidation temperatures of 850°C. The first nine points are fitted with a zero-intercept regression line (initial transient oxidation), the others are fitted with a line with lower slope (stationary oxidation). The error bars indicate the measurement uncertainties.

Conversely, the collected experimental points relative to the samples oxidized at 900°C lay on a single straight line because the initial transient period is rather faster at this exposition temperature and it is already concluded after about 0.5-1 hour. Therefore, the run in stage contribution is negligible at this test temperature.

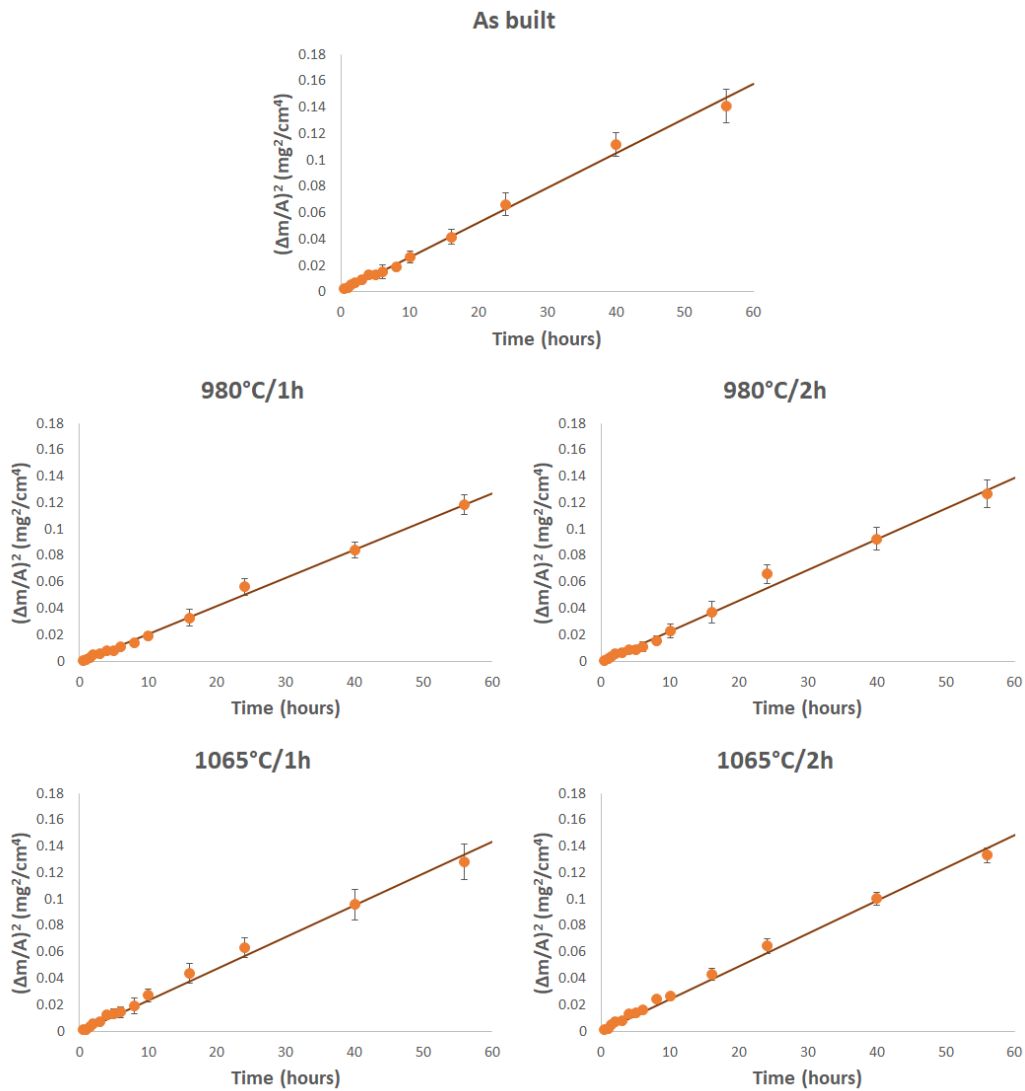


Figure 5.3. Mass gain squares vs time plots for the as built samples and the solutioned samples at the oxidation temperatures of 900°C. The error bars indicate the measurement uncertainties.

The k_p values obtained in the short term oxidation tests through fitting according to the least squares method are reported on table 5.1. These values are in good agreement with the values reported in the literature (see table 1.11). However, the k_p values obtained at 850°C are of two orders of magnitude lower than the value reported by Jia et al. for an Inconel 718 alloy produced by SLM technique applying a volumetric energy density of 130 J/mm³ ($P = 130$ W, $v = 400$ mm/s, $hd = 50$ μm, layer thickness of 50 μm) [90].

Table 5.1. Estimated k_p values of the initial and stationary oxidation regimes at the oxidation temperature 850°C and estimated k_p values at the oxidation temperature 900°C.

State	$T_{ox} = 850^\circ C$		$T_{ox} = 900^\circ C$
	$k_{p,init}$ [$10^{-4} \text{ mg}^2 \text{ cm}^{-4} \text{ h}^{-1}$]	$k_{p,stat}$ [$10^{-4} \text{ mg}^2 \text{ cm}^{-4} \text{ h}^{-1}$]	k_p [$10^{-4} \text{ mg}^2 \text{ cm}^{-4} \text{ h}^{-1}$]
As built	10.9 ± 2.2	5.1 ± 1.3	26.3 ± 0.8
980°C/1h	11.8 ± 3.1	5.1 ± 1.3	21.3 ± 0.6
980°C/2h	14.6 ± 3.1	6.5 ± 1.6	23.3 ± 0.9
1065°C/1h	17.9 ± 4.8	7.3 ± 0.8	24.0 ± 0.9
1065°C/2h	15.9 ± 3.1	7.7 ± 2.0	24.9 ± 0.9

5.2 Middle term oxidation test

The mass gains of the SLM Inconel 718 samples oxidized at 850°C for 215 hours measured at the end of the middle term oxidation test are reported in figure 5.4. The mean mass gains obtained for each combination of atmosphere of the preliminary solution treatment (air or vacuum) and oxidation modality (by isotherm exposure or thermal cycles) are also compared in figure 5.4. As already discussed at the paragraph 2.5, a very thin superficial layer forms spontaneously during the solution treatment in vacuum of Inconel 718 alloy; this layer is expected to influence the oxidation resistance of the material because it could act as a pre-existing diffusion barrier. Actually, the results reported in figure 5.4 clearly show that the samples solutioned in vacuum tend to oxidize with minor intensity with respect to the not solutioned one and the ones solutioned in air and then lapped in order to expose a fresh metal surface.

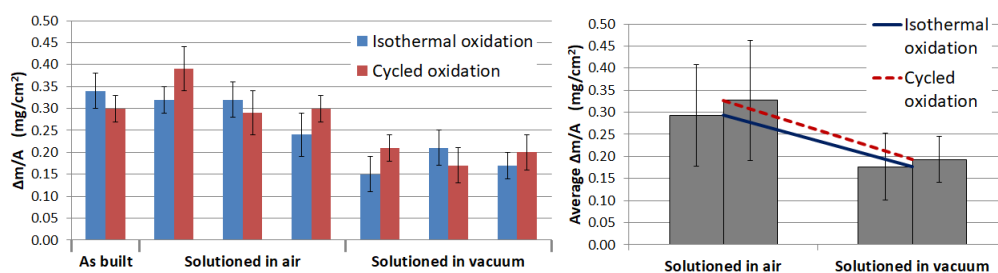


Figure 5.4. Mass gains collected after 215 hours in both cyclic (red bars) and isothermal (blue bars) oxidation at 850°C on the as built and the solutioned samples used in the middle term test (the error bars indicate the measurement uncertainties). Solution annealing was performed at 1065°C for 2 hours. The average mass gains of the samples solutioned in air and in vacuum and oxidized in isotherm or via thermal cycles are also compared (the error bars indicate 95% confidence ranges).

The Analysis of Variance (ANOVA) reported in table 5.2 confirms the statistically marked influence of the solution atmosphere on the oxide growth rate at 850°C. Furthermore, the ANOVA shows that the thermal cycling doesn't lead to an evident detrimental effect with respect to the isothermal oxidation. The thermal shocks generated by the cycles of heating and rapid cooling in air, at which the samples are submitted during the interrupted oxidation tests, cause stresses at the

metal/oxide interface which can potentially lead to cracks and voids affecting the protective capability of the passivating scale. Conversely, the observed very low influence of thermal cycling on the oxide growth rate at 850 °C is a further confirmation of the strong adhesion of the passivating oxide on the metal substrate and the resulting excellent hot oxidation resistance of Inconel 718 alloy at this temperature.

Table 5.2. Analysis of Variance (ANOVA) for the main effects of the solubilization atmosphere (air or vacuum) and the oxidation modality (isothermal or cycled oxidation) on the mass gain after 215 hours at 850°C and their combined effect. DOF: degrees of freedom; SS: sum of squares; MS: mean squares; F: F-ratio.

	DOF	SS	MS	F	p-value
<i>Main effects</i>					
solution atmosphere	1	0.0469	0.0469	28.70	0.0007
oxidation modality	1	0.0019	0.0019	1.15	0.3152
<i>Second order interactions</i>					
combined effect	1	0.0002	0.0002	0.13	0.7302
<i>Residuals</i>	8	0.0131	0.0016		

The mass gain squares vs time plot with the experimental points collected after each oxidation cycle during the middle term test is reported in figure 5.5. When the oxidation period is much higher than 8 hours, the transient oxidation regime can be neglected, therefore the parabolic law describes the oxide growth rate with sufficient accuracy. The obtained values of the k_p constants are in good agreement with the results of the short term test reported in table 5.1. The bulk microstructural modifications due to the preliminary solution treatment don't seem to affect significantly the oxidation resistance, the only effect that can be observed derives from the superficial alteration caused by the thermal treatment in vacuum, as discussed earlier.

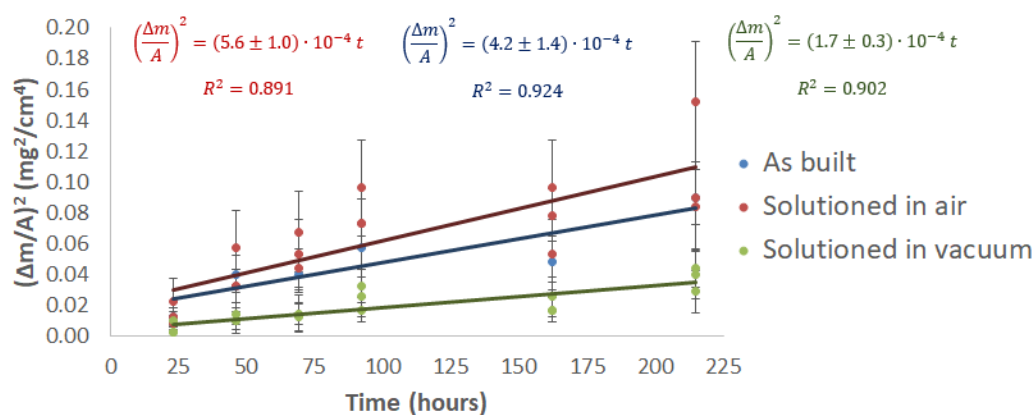


Figure 5.5. Mass gain squares vs time plots for the as built sample and the solutioned samples oxidized via thermal cycles during the middle term test. The error bars indicate the measurement uncertainties.

After 215 hours of oxidation, the mean oxide scale thickness is 1-1.5 μm . The oxide morphology can be observed in the SEM micrograph reported in figure 5.6

obtained via backscattered electrons (BSE) mode. The main features of the oxide scale will be described in fine details at paragraph 5.4. Mainly a continuous superficial layer that appears in darker contrast in BSE images constitutes the superficial layer. Although this film is continuous, it has a not uniform thickness, as some protrusions of the oxide are present at the grain boundaries. Below this first continuous layer, a discontinuous interlayer, that appears in brighter contrast in the BSE images, is present between the oxide and the metallic alloy. It is possible to observe that isolated oxides that form below the superficial layer and predominantly at the grain boundaries interrupt the interlayer. Finally, the occurrence of internal oxidation can be detected along the grain boundaries until about 10 μm in deep. No evident qualitative differences between the oxide scales grown on the samples solutioned in air and the ones solutioned in vacuum can be noted from the SEM micrographs. Apparently, they have the same morphological and microstructural features, but at a more detailed examination it is possible to observe that the interlayer tends to be thicker and more continuous on samples solubilized in vacuum, whereas this layer is sometimes even absent (figure 5.6-A) or reduced to isolated particles (figure 5.6-B) on the samples solubilized in air.

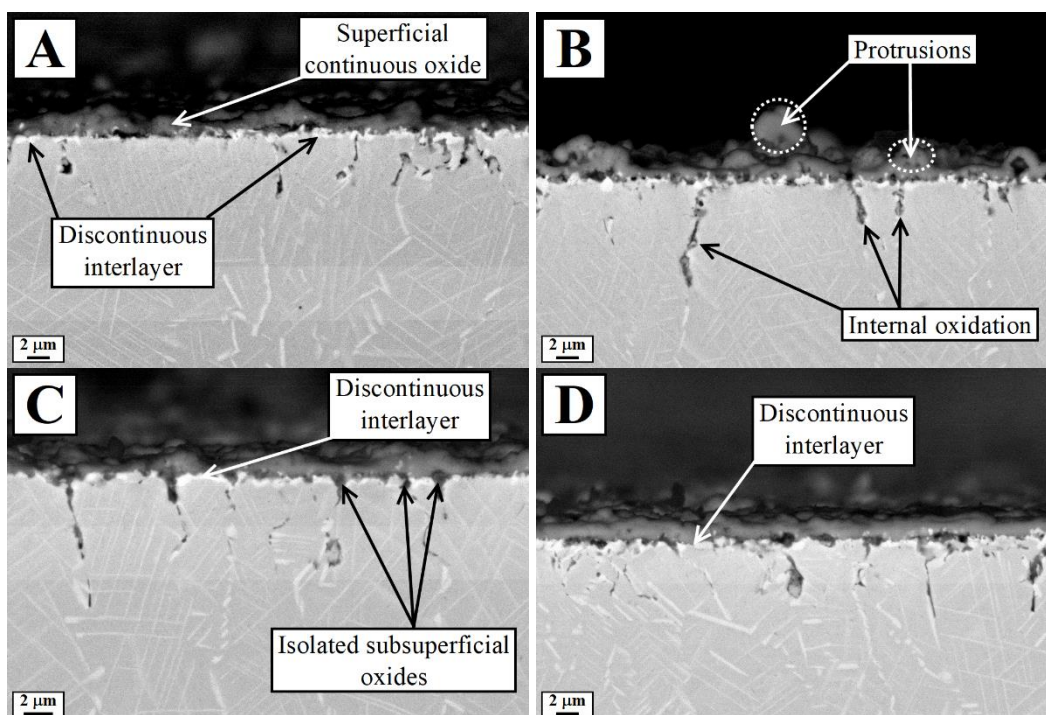


Figure 5.6. Backscattered electrons (BSE) SEM images of the cross section of samples pretreated in air (A and B) and in vacuum (C and D) and oxidized at 850°C through thermal cycles (A and C) and in isotherm (B and D) for 215 hours.

5.3 Long term oxidation test

Another oxidation test was carried out in order to investigate the oxidation resistance of SLM Inconel 718 alloy for long term period. Samples previously solutioned at 1065°C for 2 hours in vacuum atmosphere were exposed at 850°C in simple air in isothermal condition. For comparison, the same oxidation run was applied also on samples of Inconel 600.

Inconel 600 is a nickel-based alloy with high mechanical properties and good oxidation and corrosion resistance [218]. This alloy was chosen for the comparison with SLM Inconel 718 on the long term oxidation behavior because it can be considered the base of the Ni-Cr-Fe systems with simpler chemical composition (Table 5.3), microstructure [219] and oxidation behavior [220], thus providing a convenient reference for evaluating the oxidation resistance improvement achievable with SLM Inconel 718 over the traditional obtained similar nickel superalloys.

Table 5.3. Comparison between the chemical compositions of Inconel 600 and Inconel 718 superalloys.

Alloy	Ni	Cr	Fe	Nb	Mo	Ti	Al	C	Others	Source
Inconel 600	>72	14-17	6-10	-	-	-	-	<0.15	<1 Mn, <0.015 S, <0.5 Si, <0.5 Cu	[218]
Inconel 718	50-55	17-21	Bal.	4.74-5.5	2.8-3.3	0.65-1.15	0.2-0.8	<0.08	<1 Co, <0.3 Cu, <0.35 Si + Mn, <0.015 P + S, <0.006 B	[185]

The k_p constant of the parabolic law is obtained using the points collected until 351 hours of the mass gain squares vs time plot by calculating the linear regression line with the least square method (figure 5.7). The oxide growth is faster on the Inconel 600 samples and the value of the k_p constant obtained with the solutioned SLM Inconel 718 samples is comparable to the one obtained in the middle term oxidation test (figure 5.5).

In order to verify that the observed parabolic trends are maintained also for longer oxidation times, the samples removed after 351 ore were reused to collect further experimental points until a total oxidation period of 908 hours.

These extra points are reported as triangles in figure 5.7. In the case of Inconel 718 alloy, the extra points are compatible with the previously obtained parabolic model, this confirms the adherence and stability of the protective oxide scale, whose regular growth is controlled by the diffusion even after long period of oxidation. Conversely, the mass gains of the Inconel 600 samples start to be lower than the respective values predicted by the previously obtained parabolic model from 852 hours of oxidation. This mass reduction can be ascribed to an oxide mass loss due to detachment or evaporation.

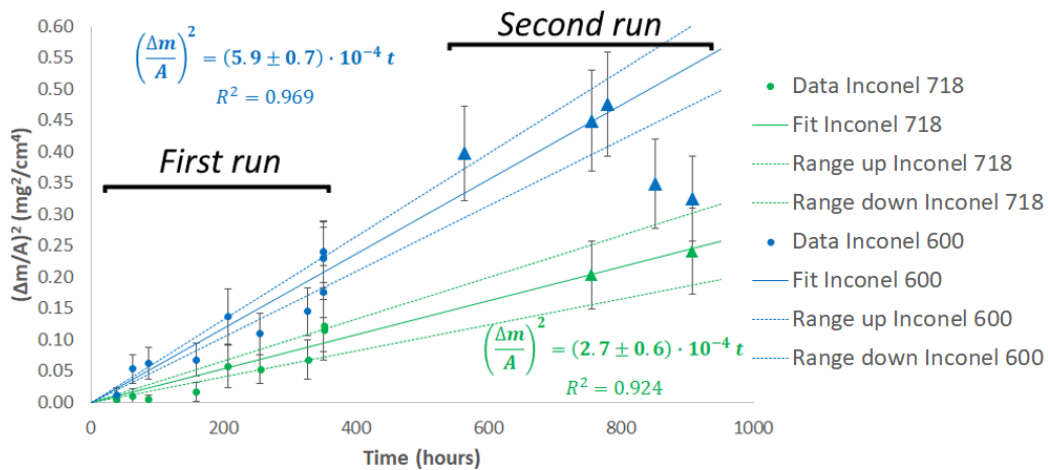


Figure 5.7. Mass gain squares vs time plot of solutioned SLM Inconel 718 and Inconel 600 oxidized at 850°C with relative zero-intercept linear regressions lines. The dotted lines indicate 95% confidence ranges, the error bars indicate the measurement uncertainties. First published in [194].

The optical images of the cross sections of the oxide scales growth on Inconel 718 and Inconel 600 after 908 hours are shown in figure 5.8. On the Inconel 718 sample, the oxide appears more regular, despite the presence of outwardly developed protrusions and internal oxidation along the grain boundaries. Nevertheless, the metal/oxide interface is flat even after such prolonged exposure to high temperature. On the Inconel 600 sample, the metal/passivating compact oxide interface has a sinusoidal profile. This is a consequence of local inward oxidation and metal consumption. Furthermore, at these locations a double layered oxide is formed: the inward layer is constituted by the compact film that assumes such wavy shape, whereas the outward layer is porous and loosely adherent with the inward layer. A certain grade of internal oxidation is also visible on Inconel 600, however these samples have not strongly oriented grain boundaries like the SLM Inconel 718 samples and therefore the internal oxidation is less evident.

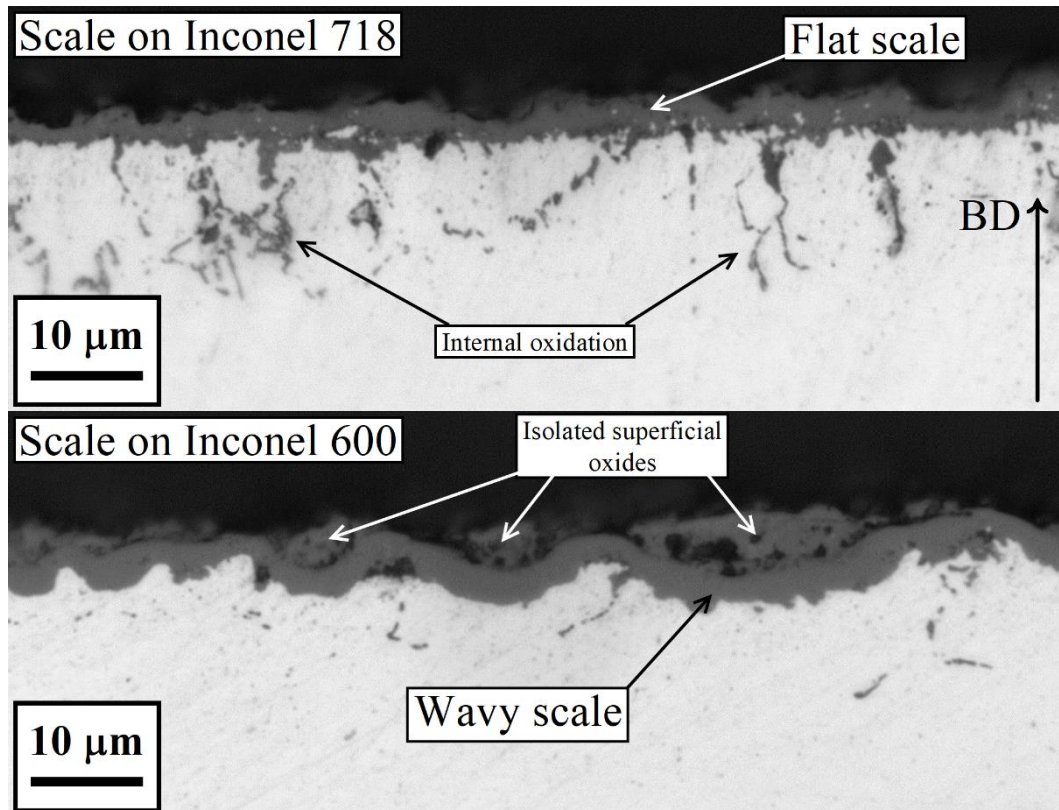


Figure 5.8. Optical micrographs of the cross section of the oxide scales grown on Inconel 718 and Inconel 600 alloys after 908 hours of isothermal oxidation. BD indicates the Building Direction of the Inconel 718 sample.

The mean thickness of the oxide scale after different oxidation time was achieved through image analysis of optical micrographs, like the representative ones shown in figure 5.8. If the assumption of a superficial scale entirely made by chromia with a theoretical density $\rho_{Cr_2O_3}$ of 5.22 g/cm^3 [221] stands, the theoretical relationship between the mass gain for unit of exposed surface $\Delta m/A$ and the thickness s of the scale is:

$$s = \frac{V_{mol,Cr_2O_3}}{3 \cdot M_{mol,O}} \frac{\Delta m}{A} = \frac{M_{mol,Cr_2O_3}}{3 \cdot M_{mol,O} \cdot \rho_{Cr_2O_3}} \frac{\Delta m}{A} \Rightarrow$$

$$\Rightarrow s [\mu m] \cong 6.07 \cdot \frac{\Delta m}{A} \left[\frac{mg}{cm^2} \right] \quad \text{eq. 5.2}$$

where $M_{mol,O}$ is the oxygen molar mass, equals to 15.9994 g/mol , $V_{mol,Cr_2O_3} = M_{mol,Cr_2O_3} / \rho_{Cr_2O_3}$ is the molar volume of chromia and M_{mol,Cr_2O_3} is the molar mass of chromia, equals to about 151.9902 g/mol . The mean thickness and the relative mass gains per unit of area, measured on the samples submitted to different time of exposure at 850°C , are plotted in figure 5.9. It is possible to observe that the theoretical value of equation 5.2 falls in the estimated range of the slope relative to the Inconel 718 samples. This gives clues to the fact that the oxide scale is mainly constituted by a uniform and dense layer of chromia and by other eventual minor microstructural constituents. For instance, the oxides of the other alloying elements such as Ni, Fe, Ti and Al, and the interlayer observed in the SEM micrograph of

figure 5.6, can be neglected in first approximation. This justifies the use of the parabolic model to describe the oxide growth.

As for the Inconel 600 alloy, the estimated slope value is very lower than the theoretical value (figure 5.9). This indicates that in this case the scale is not constituted only by a dense chromium oxide. Actually, some large isolated oxides are visible in the cross sections (figure 5.8) above the continuous layer. In these conditions, the parabolic model, based on the hypothesis of formation of a uniform and dense protective layer, is less suitable to describe the hot oxidation behaviors of the alloy, especially for long period of exposure as observed in figure 5.7.

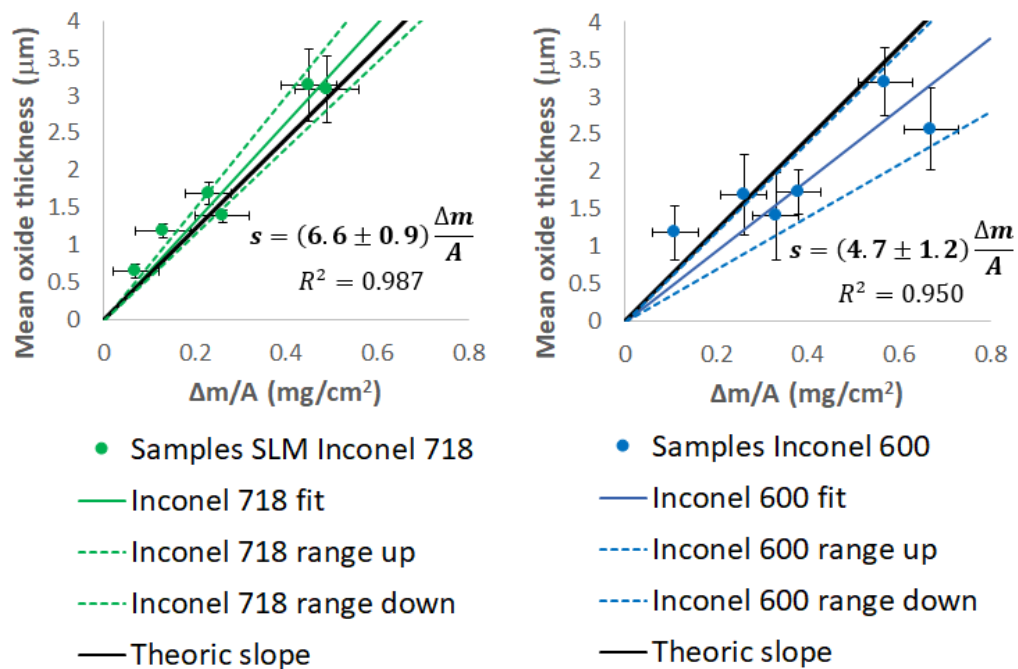


Figure 5.9. Oxide thickness vs mass gain plots for Inconel 718 and Inconel 600 alloys in comparison with the theoretical value of equation 5.2. The dotted lines indicate 95% confidence ranges.

5.4 Morphological and microstructural features of the oxide scale

The structure of the oxide scale formed during the long term oxidation test on Inconel 718 was studied and compared with the reference Inconel 600 alloy using FESEM micrographs and EDS analysis. As already pointed out at paragraph 2.7.3, the EDS analysis cannot provide an exact quantitative information, but they can still be used to determine the nature of the observed constituents of the oxide scales.

The FESEM micrograph in figure 5.10 shows the oxide scale formed after 908 hours of oxidation on Inconel 718. The interface between the scale and the metal substrate is shown in greater detail in figure 5.11. The point EDS analyses of all the observed constituents are reported in figure 5.12. It is possible to observe that the superficial scale is mainly composed by a dense layer of chromia with minor contents of Al, Ti and Fe impurities (point 1 in figure 5.12). Inside the chromia

layer, some small areas rich in Fe and Ni (point 2 in figure 5.12), that appear in brighter contrast near the interface, are also present. These regions are probably not oxidized fragments of the alloy remaining embedded in the chromia scale during the inward growth of the oxide layer.

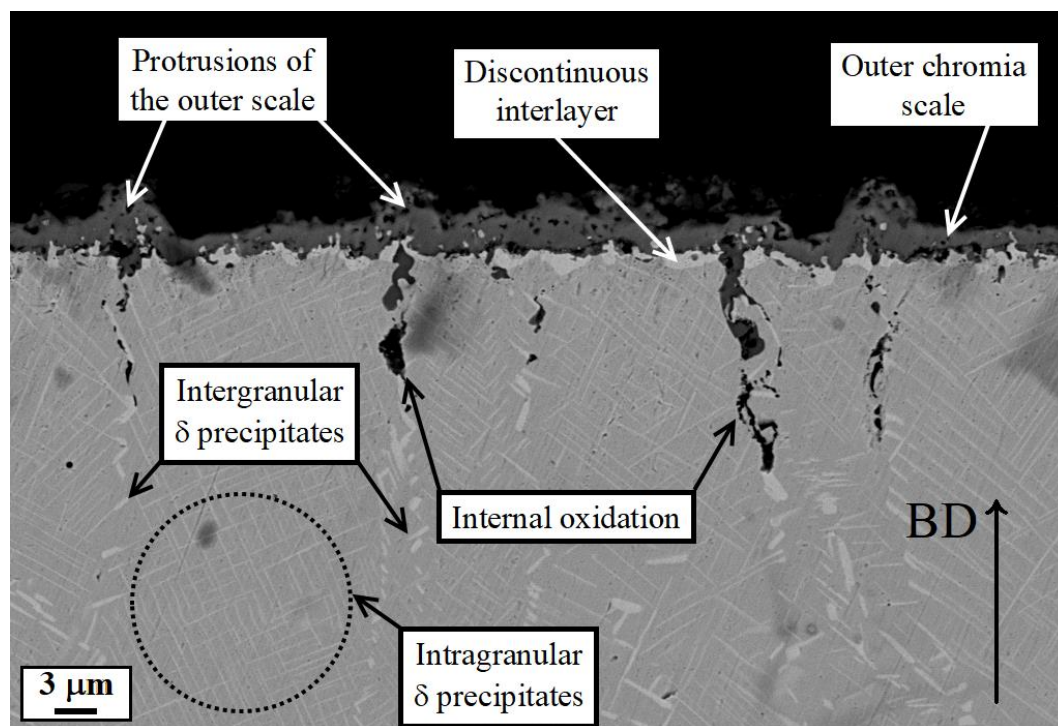


Figure 5.10. Backscattered electrons (BSE) FESEM image of the cross section of the oxide scale grown on SLM Inconel 718 after 908 hours of isothermal exposure at 850°C. The sample was previously solutioned at 1065°C for 2 hours in vacuum. BD indicates the Building Direction of the sample. First published in [194].

The discontinuous interlayer, already mentioned on the samples submitted to the middle term oxidation test (figure 5.6), is here clearly visible (figures 5.10 and 5.11). The presence of a discontinuous interlayer between the oxide and the metal alloy was also observed by Delaunay et al. [86] and Al-Hatab et al. [87], who identify it as an intermetallic layer with Ni_3Nb stoichiometry. This film can act as a second diffusion barrier to both the O^{2-} anions and the cations. Therefore, it can increase the oxidation resistance of the alloy. According to these studies, the EDS analyses (point 3 in figure 5.12) indicate that the interlayer is actually richer in Nb.

Internal oxides that develop along grain boundaries interrupt this interlayer.

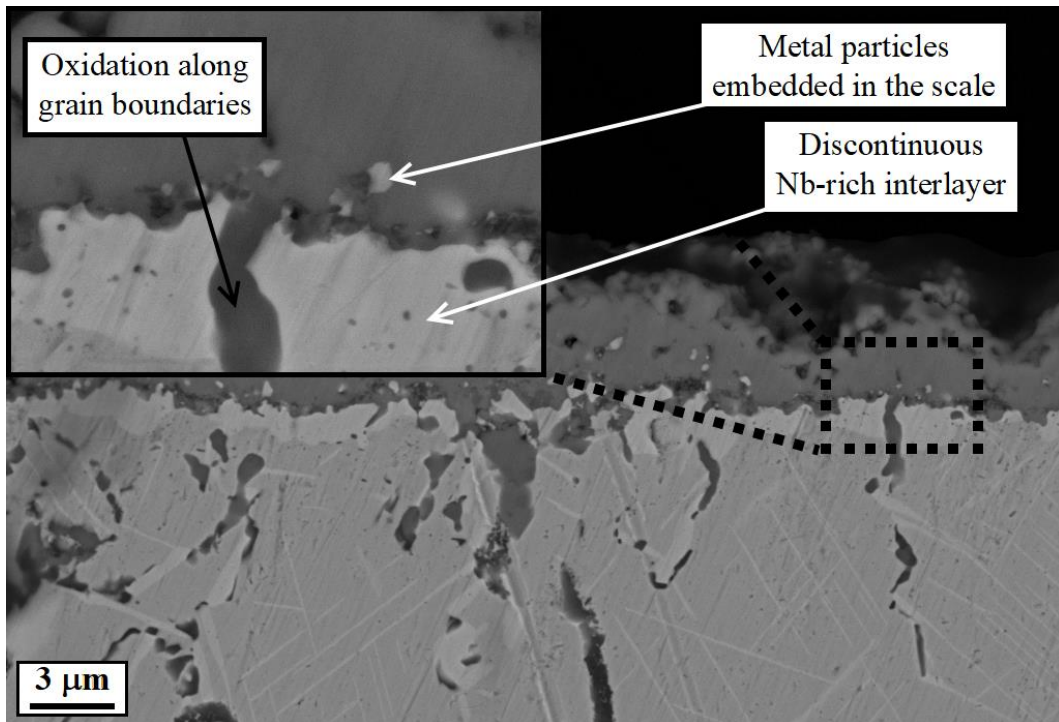


Figure 5.11. Backscattered electrons (BSE) FESEM images showing in greater details the morphology and structure of the oxide scale on SLM Inconel 718 after 908 hours of isothermal exposure at 850°C. First published in [194].

Compared to the superficial layer, the internal oxides close to the oxide/metal interface are richer in Ti (point 4 in figure 5.12), instead the deeper ones are mainly constituted by Al (point 5 in figure 5.12).

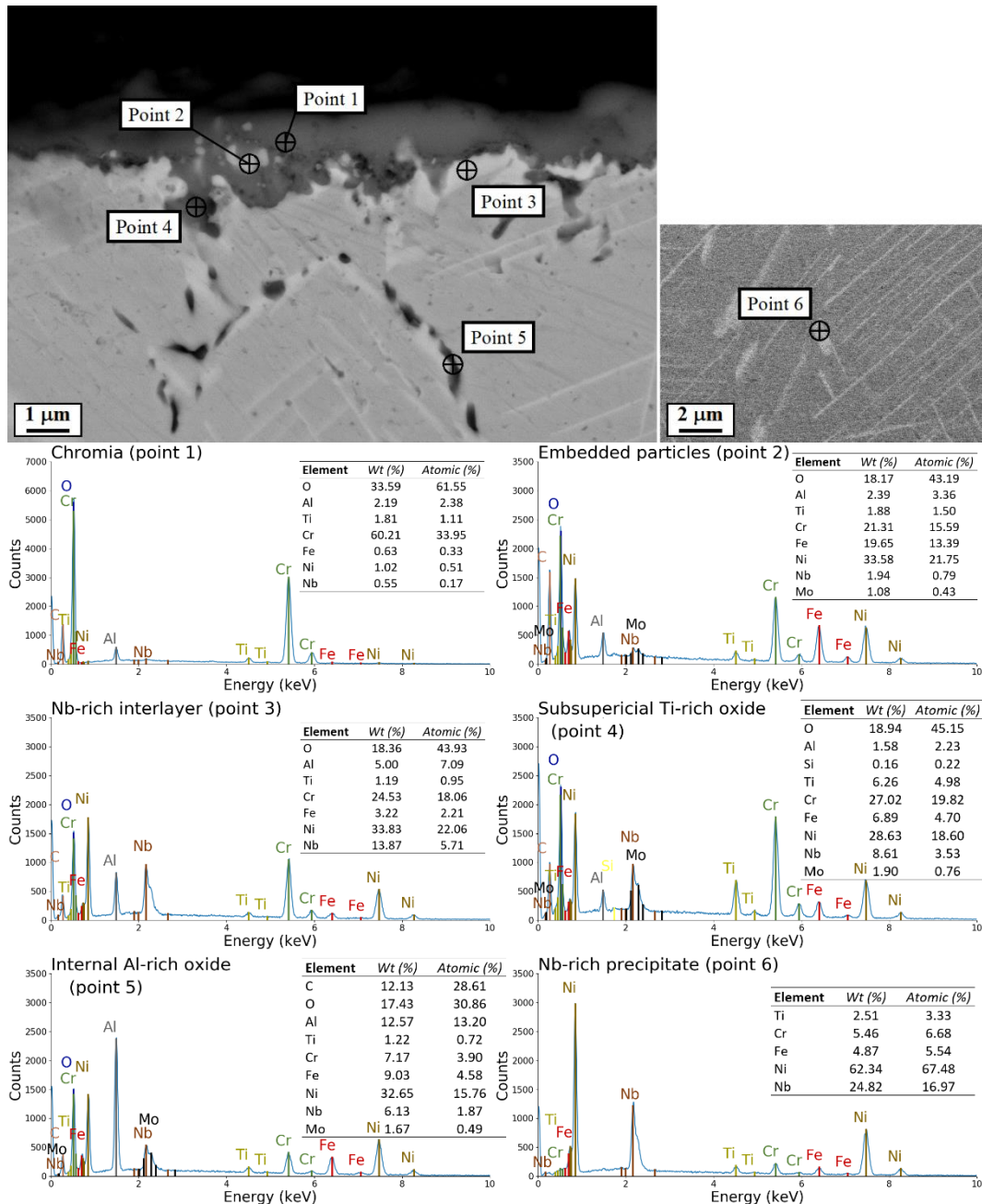


Figure 5.12. Sample of Inconel 718 oxidized for 160 hours at 850°C. Spot EDS analysis on: superficial oxide layer (spectrum 1); particles embedded in it (spectrum 2); thin interlayer at metal/oxide interface (spectrum 3); internal oxides rich in Ti (spectrum 4); deeper internal oxides rich in Al (spectrum 5); intergranular precipitate (spectrum 6). First published in [194].

The above reported observations on the morphology of the oxide scale allow to state that Inconel 718 belongs to the group II according to the classification of Giggins and Pettit (see paragraph 1.3.6), on which a chromia scale forms on the surface and an aluminum oxide subscale forms beneath. After a first step of transient oxidation, the steady-state oxidation kinetics of the oxide is controlled by the outward diffusion of cations, mainly Cr^{3+} , and by the inward diffusion of O^{2-} anions through the scale. The outward diffusion of Cr^{3+} and other cations (Al^{3+} and Ti^{2+}) allows the growth of the superficial doped chromia layer, that constitutes almost all of the total volume of the scale. At the same time the inward diffusion of

O^{2-} anions leads to the formation of the internal Ti and Al oxides. The oxides sequence found here on Inconel 718 starting from the surface and moving inwards is also reported by Chen et al. [222] on Astroloy, Waspaloy and Udimet 720 alloys oxidized between 900°C and 1000°C. This sequence reflects the oxygen affinity of the oxide-forming elements present in the alloy. An oxygen concentration gradient is formed during the thermal exposure between the surface and the metal substrate that drives the diffusion of the O^{2-} anions. Therefore, moving in depth from the surface, the oxygen concentration decreases until the equilibrium value $p_{O_2,eq,Cr_2O_3}(T = 850^\circ C)$, relative to the reaction of chromium oxidation $2Cr + 3/2 O_2 \rightleftharpoons Cr_2O_3$, cannot be attained. At this point chromia ceases to form, but Ti and Al can still oxidize because they have a higher oxygen affinity (see the plot of figure 1.30), i.e. a lower value of $p_{O_2,eq}(T = 850^\circ C)$, leading to the formation of the observed internal oxides. The aluminum oxides are formed at a greater depth than Ti oxides because $p_{O_2,eq,TiO_2}(T = 850^\circ C) > p_{O_2,eq,Al_2O_3}(T = 850^\circ C)$.

The development of the oxide scale is further complicated by the role of the thin Nb-rich interlayer observed at the oxide/metal interface, which appears to act as a diffusion barrier to the inward diffusion of O^{2-} anions, greatly reducing the formation of internal oxides in intragranular areas. However, the growth of the oxide is faster along grain boundaries, which represent preferential paths along which the mobility of the diffusion species is higher.

This results in a greater thickening of the superficial chromia layer, due to more intense outward diffusion of Cr^{3+} and consequent formation of the observed oxide protrusions, and in the interruptions of the interlayer along with the formation of internal Ti and Al oxides along grain boundaries due to inward diffusion of the O^{2-} anions.

The Nb-rich interlayer is detectable also on the samples solutioned in air after the middle term oxidation test (see figure 5.6), therefore this thin interlayer forms during the thermal exposure. However, the pre-existent superficial layer that forms during solution annealing in vacuum due to Nb segregation (see paragraph 2.5) probably facilitate the stabilization of the Nb-rich interlayer in the intragranular zone. This explains the better oxidation resistance observed in the samples solutioned in vacuum with respect to the as built or treated in air ones (figure 5.4).

The structure of the oxide scale formed on the Inconel 600 alloy after 908 hours is shown in the FESEM micrograph of figure 5.13. The relative EDS analyses are also reported in figure 5.13. The oxide scale developed in Inconel 600 alloy appears quite different from that observed on Inconel 718. Actually, the chromia layer (point 2 in figure 5.13), visible in darker contrast, is more corrugated and its formation is disturbed in some points by the presence of isolated and less dense oxides, visible brighter in contrast, that form a discontinuous superficial layer. EDS analysis reveals that the superficial discontinuous layer is mainly constituted by nickel oxide (point 1 in figure 5.13), therefore this alloy belongs to the group I in the classification of Giggins and Pettit.

This explains the discrepancy between the theoretical slope of equation 5.2, calculated by assuming an oxide scale mainly composed of chromia, and the one experimentally obtained on the oxidized samples of Inconel 600 (figure 5.9). The superficial isolated nickel oxides are poorly protective, therefore the chromia scale below continues to grow during the thermal exposure.

Also on the Inconel 600 samples some internal oxidation occurs. The EDS analysis (point 3 in figure 5.13) indicates that the deep oxides are again mainly rich in aluminum. In Inconel 600, the interlayer between the superficial oxide scale and the metallic substrate is completely absent. The thickening of the chromia layer seems to occur mainly due to inward growth because the diffusion of O^{2-} anions is not hindered by the presence of a second diffusive barrier. Such inward growth explains the formation of a wavy oxide/metal interface.

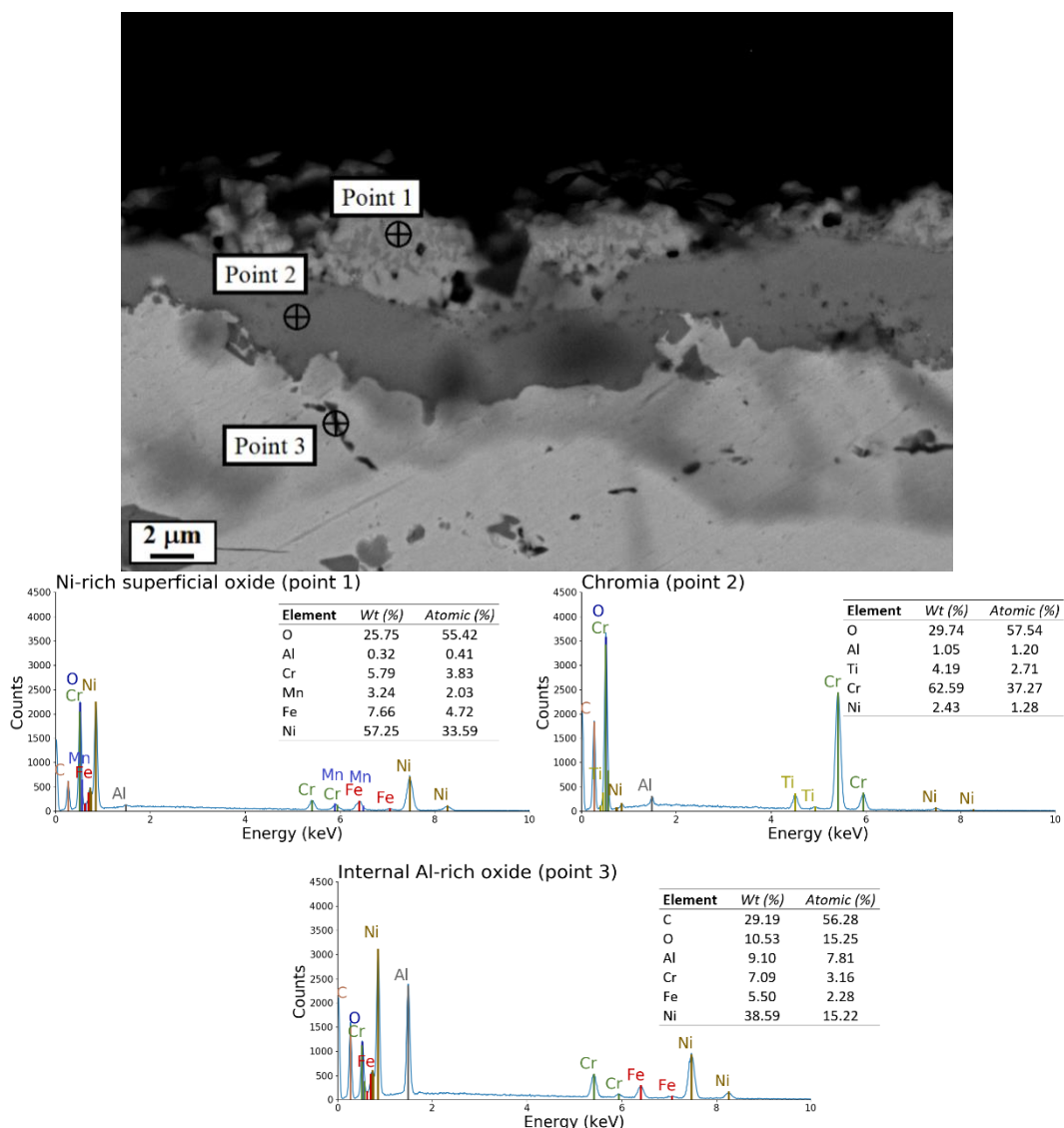


Figure 5.13. Backscattered electrons (BSE) FESEM image of the cross section of the oxide scale grown on Inconel 600 alloy after 908 hours of isothermal exposure at 850°C. Spot EDS analysis on an isolated superficial oxide (point 1), the continuous oxide layer (point 2) and an internal oxide (point 3).

5.5 Conclusion

The performed tests clearly demonstrate the high oxidation resistance of Inconel 718 alloy produced by SLM process. Actually, cracking, detachment or evaporation of the protective oxide scale have never been observed during the execution of these tests. Therefore, the alloy can certainly be used in applications involving long term exposures at temperatures up to 850°C

The short term tests show that the alloy passes through an initial transient period of oxidation in which the growth rate is faster because the superficial protective layer is not fully formed yet. After this run in step, the growth of the oxide stabilizes on a parabolic behavior, which indicates a process of further oxidation controlled by diffusion through the protective layer. The initial transient regime lasts about 8 hours at the oxidation temperature of 850°C, instead it is very rapid and ends within the first test hours for oxidation runs at 900°C.

The preliminary solution treatment does not visibly affect the oxidation resistance of SLM Inconel 718. The only clear effect found concerns the solubilization atmosphere. In particular performing the solution annealing in vacuum provokes the spontaneous formation of a thin superficial layer which reduces the kinetic constant k_p of the parabolic law. It is believed that this thin layer formed during the thermal exposition in vacuum can help the stabilization of the Nb-rich layer between the oxide and the metal substrate, which acts as a second barrier to diffusion.

The thermal cycling doesn't affect the stability of the oxide scale, that is able to withstand thermal shocks without losing its protective function.

A denser and more uniform oxide scale forms on the SLM Inconel 718 alloy with respect to the reference Inconel 600 alloy. As a consequence, the parabolic law is respected even for long term exposure at 850°C. The oxide scale is mainly constituted by slightly doped chromia, but some Ti and Al oxides are also present especially along grain boundaries.

Chapter 6

Study on the pack aluminization process on SLM Inconel 718 alloy

In the last part of the research, aluminization trials were performed modulating both the process temperature and the composition of powder pack compositions. The results of such trials are hereby reported and discussed.

Three heat treatment recipes were studied during the aluminization trials:

- heating at 7-8 °C/min, holding at 900°C for 5 hours and slow furnace cooling (intermediate temperature test);
- heating at 7-8 °C/min, holding at 1065°C for 2 hours and slow furnace cooling (high temperature test);
- heating at 7-8 °C/min, holding at 800°C for 5 hours and slow furnace cooling (low temperature test).

The mechanism of formation of the coating for each set of process parameters is deduced from the analysis of the morphology and the structure of the obtained coatings.

At the intermediate temperature, further aluminization tests were performed in order to evaluate the possibility to operate in over pack mode, i.e. with a sample not completely embedded in the aluminization pack. The interest in the over pack mode derives from the possibility to avoid the problems related to removal of the powders from hard accessible surfaces after the aluminization process. Furthermore, the feasibility of the pack aluminization technique to obtain a suitable coating on the internal surfaces of narrow channels. These last trials were particularly challenging for pack aluminization, but practically impossible for all deposition techniques which require a free line of sight between the deposited material source and the substrate to be coated.

6.1 Intermediate temperature aluminizing trials

6.1.1 The coating structure

All the samples of the intermediate temperature test have gain mass after the process, the mass gains for unit of surface area are reported in table 6.1.

Table 6.1. Mass gains for unit of surface area collected after the aluminizing test performed at 900 °C for 5 hours.

Samples	Pack composition (wt. %)	$\Delta m/A$ (mg/cm^2)
A1	10% Al, 5% NH ₄ Cl, 85% Al ₂ O ₃	7.1 ± 0.2
A2	15% Al, 5% NH ₄ Cl, 80% Al ₂ O ₃	9.9 ± 0.2
A3	10% Al, 10% NH ₄ Cl, 80% Al ₂ O ₃	7.5 ± 0.2
A4	15% Al, 10% NH ₄ Cl, 75% Al ₂ O ₃	10.1 ± 0.3

The mass gain is due to the addition of Al during the treatment and it increases with the Al content in the pack, whereas the quantity of activators in the pack has a lower influence.

In figure 6.1 the optical micrograph of the cross section of the coating obtained on the samples aluminized in the intermediate temperature test are reported. With the only exception of sample A3, the coatings developed on these samples have all the same qualitatively morphology. In particular, the coatings formed on samples A1, A2 and A4 appear regular and uniform in thickness. However, a superficial porous layer with different extension characterizes all of them.

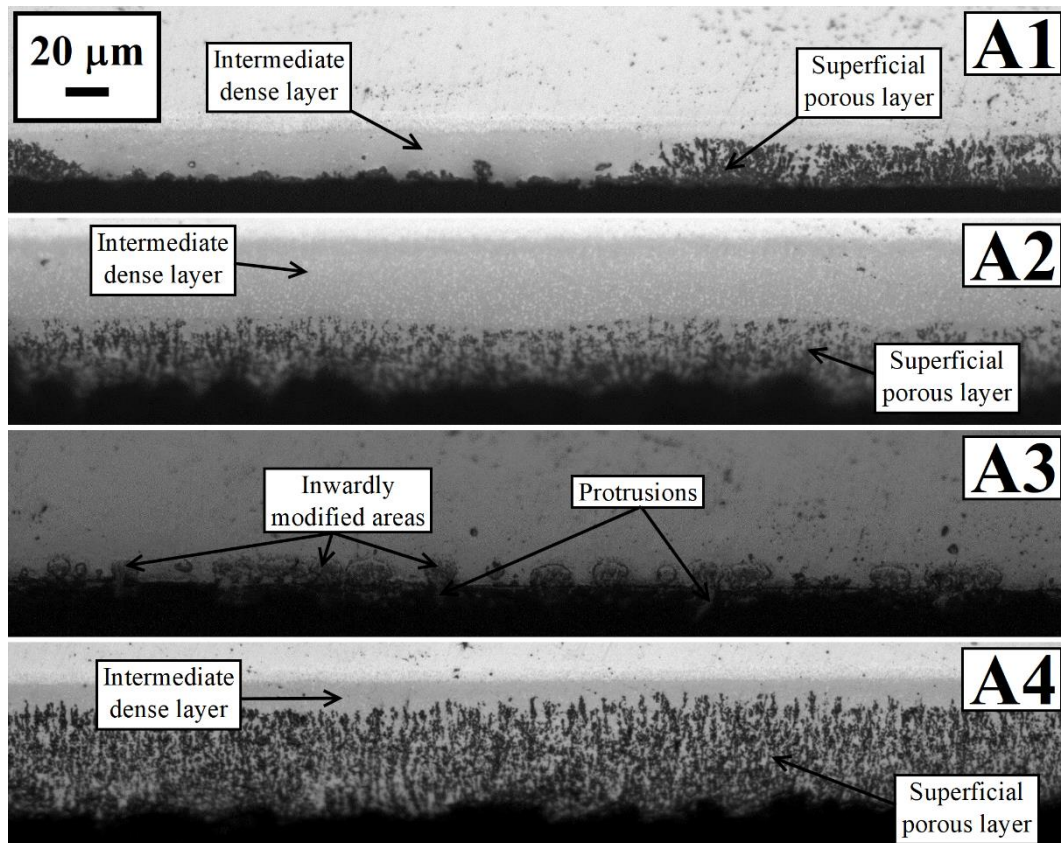


Figure 6.1. Optical micrographs of the cross sections of the coatings developed on the samples during the intermediate temperature test (900°C for 5 hours).

The microstructure of the coatings can be observed in finer details through the SEM micrographs of figure 6.2. The coating on samples A1, A2 and A4 show the general layered structure described below:

- an outer layer with a high degree of porosity and cracks is present;
- beneath the superficial layer, there is an intermediate dense layer;
- finally, a thin inner interdiffusion layer with thickness between 4 and 8 μm is present.

The overall thickness of the coating on sample A1 is about 23 μm . In this coating, the extension of the outer superficial porous layer is irregular. Actually, it is very thin in some regions, whereas in others it extends through all the coating section. On the contrary, on the sample A2 and A4, that were treated with the same amount of aluminum in the pack, the overall thickness of the coating is similar and lays between 50 and 60 μm . However, the extension of the superficial porous layer is different in these two samples. Actually, the porous layer covers from one third to half of the overall coating thickness on the sample A2, whereas it covers almost entirely the coating on sample A4.

Finally, the aluminization process didn't provide a uniform coating on sample A3. A discontinuous layer didn't develop on the surface of such sample and, on the contrary, it is possible to observe isolated superficial regions in which protrusion growth outwardly for about 9 μm and areas elliptical in shape formed inwardly for about 9-12 μm in depth.

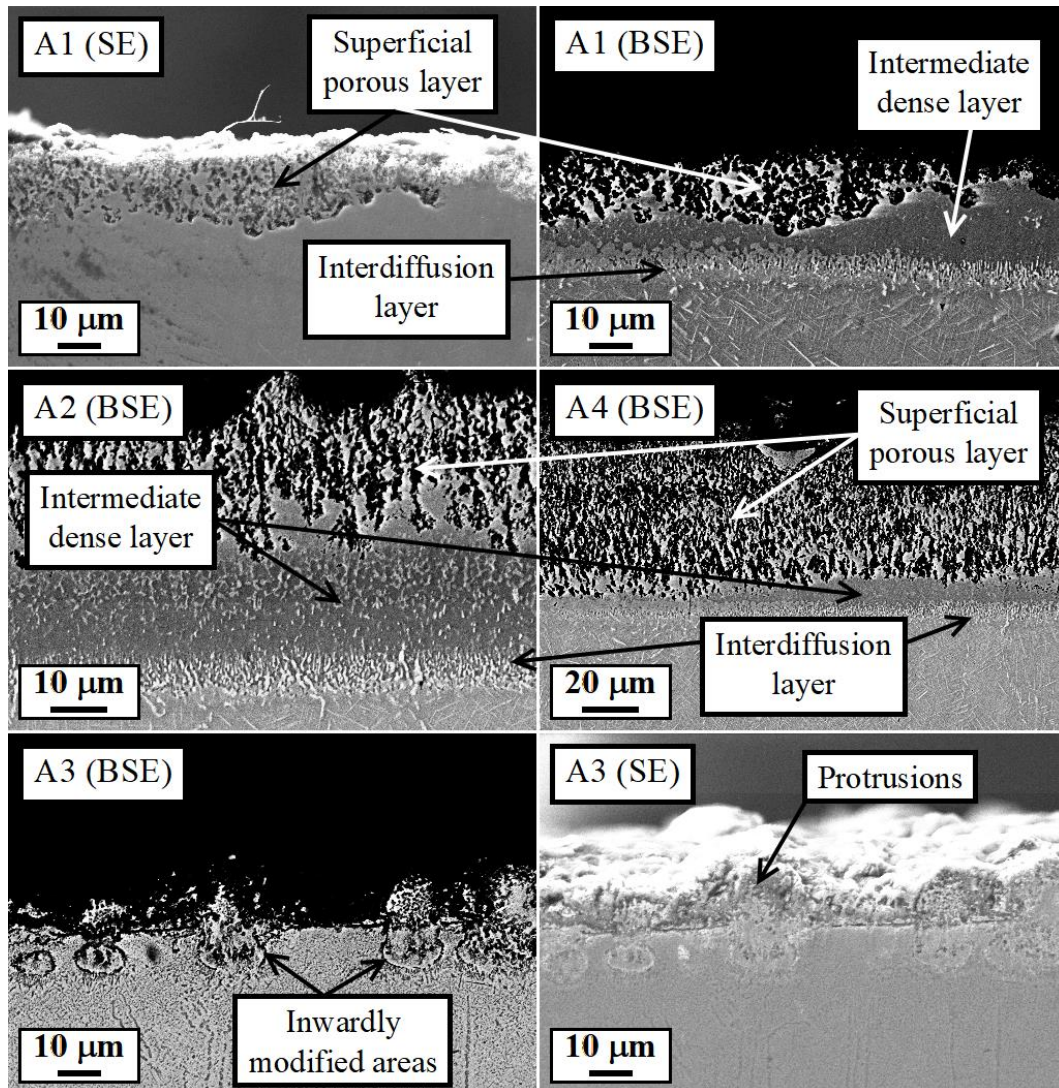


Figure 6.2. SEM micrographs of the cross sections of the coatings developed on the samples during the intermediate temperature test (900°C for 5 hours). BE: Backscattered Electrons mode; SE: Secondary Electrons mode.

The microstructure of the coating on sample A2 was further investigated through FESEM observations and EDS analysis. The FESEM images reported in figure 6.3 show with finer details the characteristic features of the different layers that compose the coating.

A large number of precipitates with elongated shape characterizes the inner interdiffusion layer. These precipitates tend to be disposed along the normal direction with respect to the coating/substrate interface.

In the dense intermediate layer there are a lot of small dispersed precipitates. This layer can be further subdivided in two sublayers (figure 6.3-A): a minor amount of fine precipitates ($< 1 \mu\text{m}$) is present in the more internal sublayer, whereas there are more dispersed precipitates and, generally, with greater size (about $2\text{-}3 \mu\text{m}$) in the outer sub-layer.

Between the intermediate layer and the external porous layer there is a progressive transition. In the backscattered SEM images, the superficial layer appears in brighter contrast with respect to the intermediate layer, indicating a

compositional difference and, in particular, a higher average atomic number. The superficial layer is almost completely covered by porosities and microcracks (Figure 6.3-C) that nucleate during high temperature aluminizing. The superficial layer is also characterized by a certain degree of oxidation.

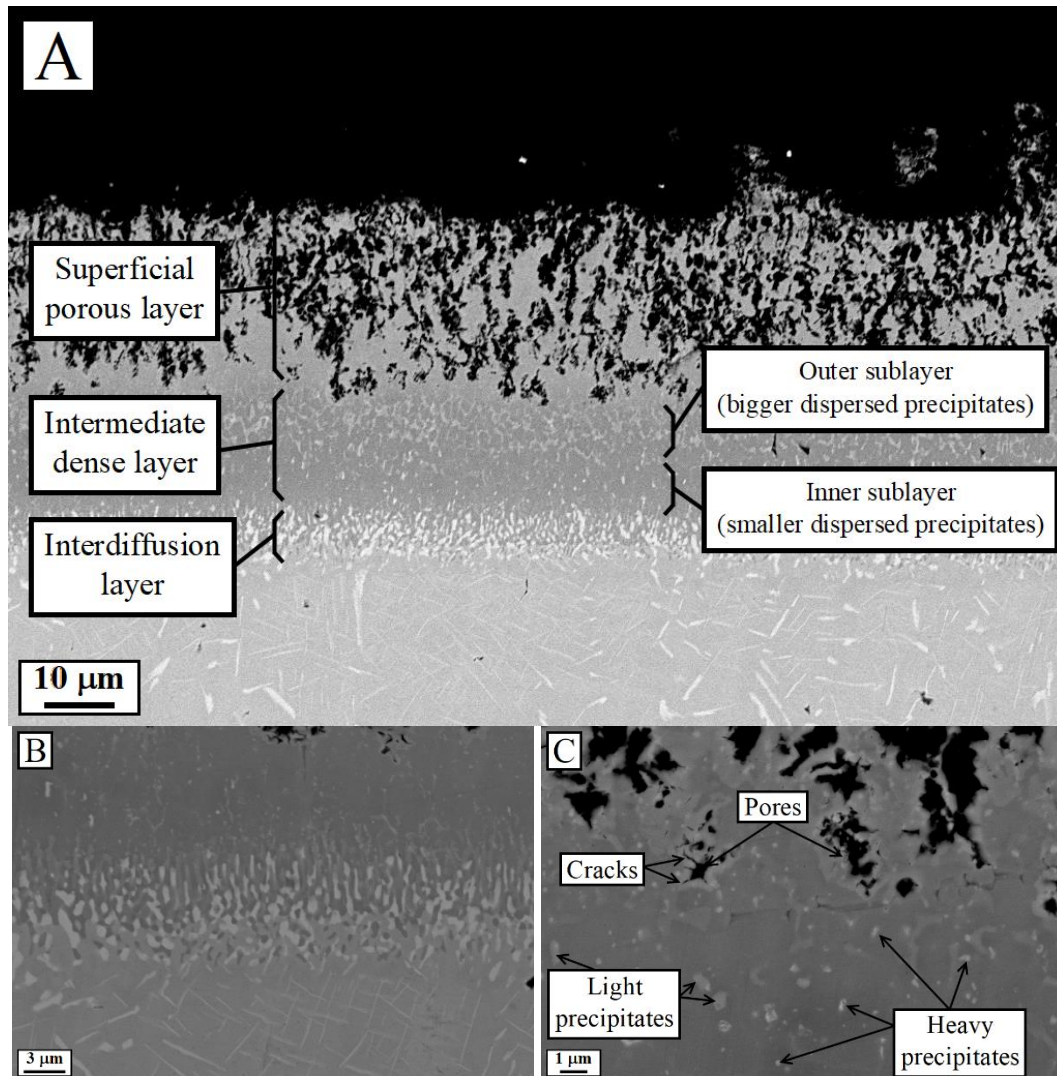


Figure 6.3. BSE FESEM image of the coating on sample A2 showing the layered structure (A). Higher magnification of the interdiffusion layer (B) and the passage between the dense layer and the porous one (C).

The EDS analysis (figure 6.4) shows that the intermediate layer has relative amounts of Al and Ni that are compatible with the β -AlNi phase. Actually, the ratio between the atomic content of Ni and the one of Al is about 0.9. Therefore, the observed layer is reasonably constituted by intermetallic AlNi. The other elements are probably entrapped in the precipitates that can be distinguished in heavier elements (Nb, Mo) rich precipitates (brighter in figure 6.3-C) and in lighter elements (Cr, Fe) rich precipitates (darker in figure 6.3-C). The presence of these two types of precipitates is confirmed also by the EDS line analysis carried out along the intermediate layer and reported in figure 6.5. In fact, it is possible to observe that peaks of the signals relative to Cr, Fe, Ti, Nb and Mo and valleys of Ni and Al are present (black arrows in figure 6.5) whenever a precipitate is crossed

by the analyzed line. Conversely, the precipitates placed on the interlayer are predominantly rich in heavier elements Nb and Mo.

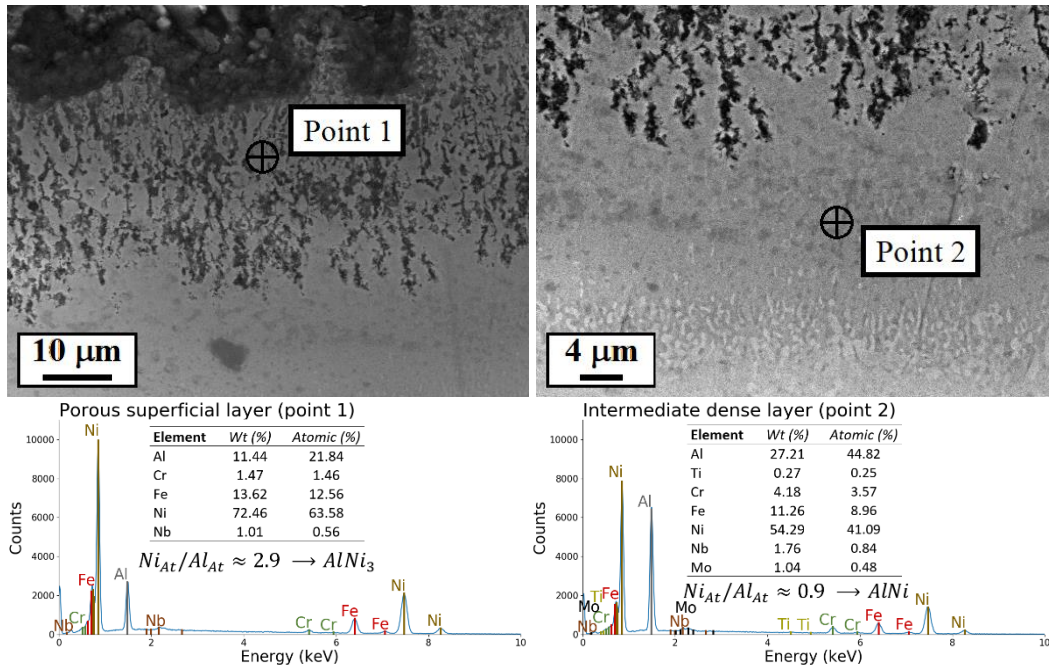


Figure 6.4. Spot EDS analyses on the porous superficial layer (point 1) and on the intermediate dense layer (point 2) of sample A2.

The porous superficial layer has a considerably smaller quantity of Al, in fact the ratio between the atomic content of Ni to the one of Al increases to about 2.9. Therefore, it is reasonable to assume that the superficial layer is constituted by $AlNi_3$ phase. The presence of a lower amount of Al in the superficial layer denotes that a depletion of aluminum along a certain thickness of the forming coating can already occur during the pack aluminization process. The reasons and the consequence of the observed de-aluminization of the superficial layer is addressed below. No or very few heavier elements (Nb and Mo) are present in the superficial layer, whereas some lighter elements (Cr and Fe) are still detectable.

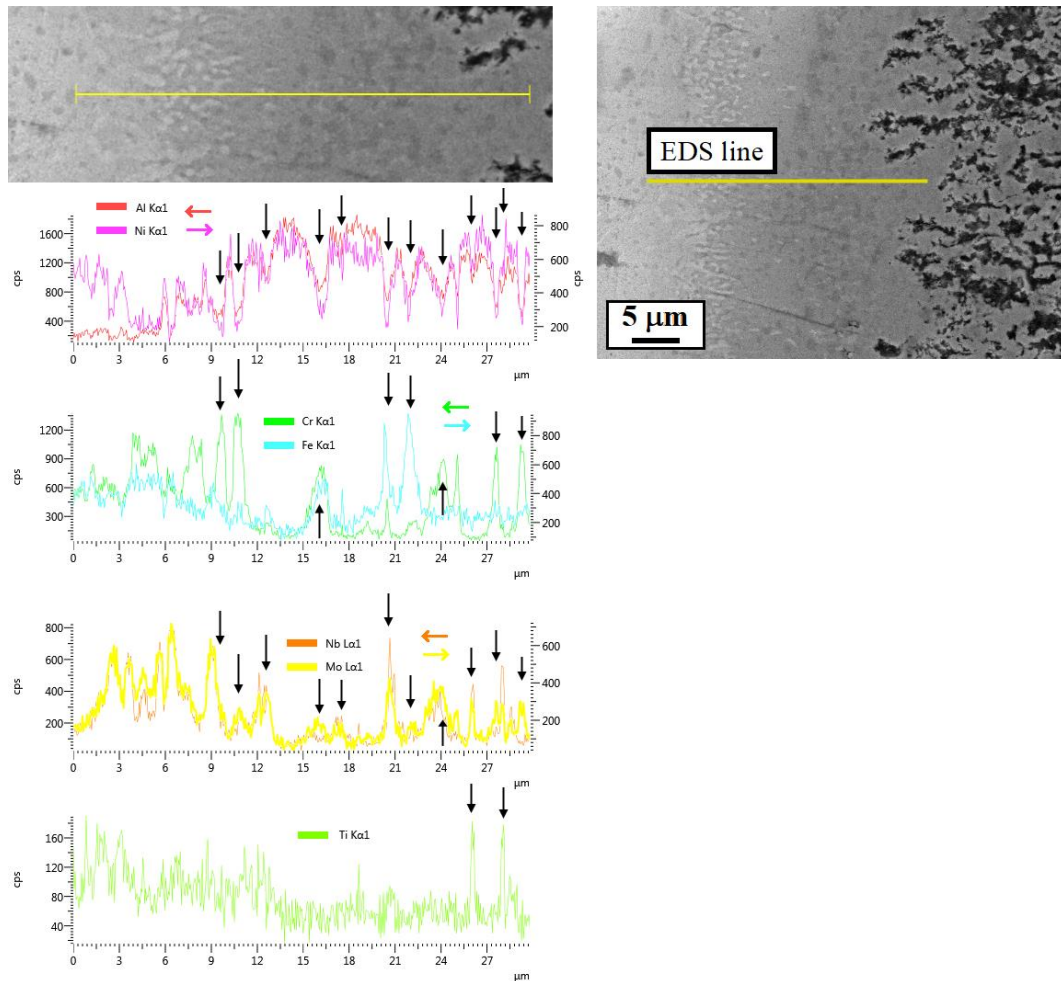


Figure 6.5. EDS line analysis showing the profile of the chemical elements present along the intermediate layer of the coating (sample A2). Black arrows indicate the peaks of the Cr, Fe, Nb, Mo and Ti signals and the valleys of the Al and Ni signals in presence of a precipitate on the intermediate layer.

6.1.2 Aluminate coating formation mechanism

The aluminization test performed at intermediate temperature can be classified as high aluminum activity process because of the large amount of Al in the pack and the relative low treatment temperature. Therefore, a LTHA mechanism of formation of the coating could be expected, i.e. a predominantly inward growth of the aluminized layer. Nevertheless, the observed coating structure shows evidences of both inward and outward grown. The inward growth is due to diffusion of Al from the surface in contact with the aluminizing vapors that leads to the conversion of the alloy into intermetallic β -AlNi. The alloying elements, i.e. Cr, Fe, Ti, Nb and Mo, tend to segregate after the conversion of the metallic matrix into the intermetallic phase due to the low solubility of these elements in the β -AlNi phase. This causes the formation of the already observed precipitates in the intermediate layer.

However, the β -AlNi layer is partially formed also by the outward diffusion of Ni from the metallic alloy as occurred in the low aluminum activity process.

Actually, the formation at the inner layer of precipitates perpendicularly oriented with respect to the substrate/coating interface is a well-known sign of the Ni depletion that occurs below the initial interface due to its outward diffusion. The outer sub-layer with coarser precipitates is formed through the inward growth of the intermetallic and it must be constituted by hyper-stoichiometric AlNi to allow the inward diffusion of Al towards the substrate. Conversely, the inner sub-layer is formed through outward growth and the few small precipitates present in it can be explained by a limited diffusion of the alloying elements. Therefore, the inner sub-layer must be constituted by hypo-stoichiometric AlNi to allow the outward diffusion of Ni.

To explain this structure, one can argue that conditions of high aluminum activity occur during the first part of the aluminization. During this step the formation of the coating occur predominantly through inward growth of hyperstoichiometric β -AlNi, in which the diffusion of Al prevails on the diffusion of Ni. When the coating reaches a certain thickness, the content of Al near the interface with the substrate falls below the 1:1 stoichiometric ratio. In this region the outward diffusion of Ni become predominant leading to the growth of hypostoichiometric β -AlNi. This coating formation model is schematically shown in figure 6.6. Similar aluminide coating structures, which are produced by contemporary presence of features of both high and low activity process, are also reported by Das et al. [110] (see also figure 1.34).

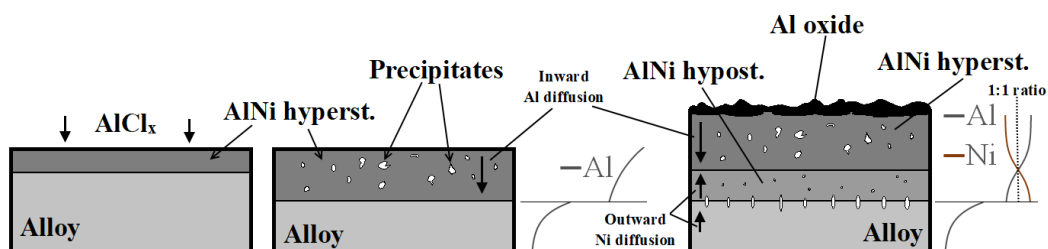


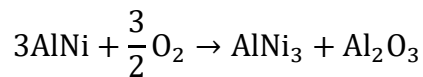
Figure 6.6. Schematic representation of the coating formation mechanism.

6.1.3 Aluminate coating degradation mechanism

The micrographs reported in figure 6.3 show that degradation of the coating occur during the aluminization treatment leading to the formation of the superficial porous and cracked layer. Based on the EDS analysis reported in figure 6.4, one can assume that the coating degradation is activated by a de-aluminization of the superficial layer. According to Smialek and Lowell [223], the superficial depletion of Al on AlNi coatings in oxidizing environment is due to the combined effect of the interdiffusion with the substrate and the spalling of aluminum oxides formed at the surface. Because of the rapid consumption of the Al source pack during the first stage of the aluminization [110], the superficial de-aluminization can already occur during the pack aluminization treatment as soon as the introduction of new Al from the aluminizing vapors become insufficient to compensate for the reduction of the superficial Al content due to inter-diffusion. Actually, the aluminide coating can

still grow in thickness, even after that the Al source in the pack is exhausted, during the remaining part of the heat treatment due to the concurrent inward diffusion of Al and outward diffusion of Ni from the substrate. However, the growth of the coating occurs by consuming the Al content in the superficial layer. Furthermore, isolated aluminum oxides can form on the surface of the coating even with a very low oxygen pressure, this leads to further de-aluminization. In these conditions, the Al content in the β -AlNi phase is progressively reduced until AlNi₃ is formed. The presence of AlNi₃ at the interface between AlNi and the forming oxide was observed also by Zhang et al. [224], which demonstrated that the formation and stability of this layer depend on the balance between the aluminum consumed by the oxidation and the aluminum supplied by the AlNi layer through outward diffusion. If the oxidation rate is high enough, the Al content in the upper part of the AlNi layer is reduced until the stability field of the AlNi₃ phase is reached (see Ni-Al phase diagram in figure 1.32).

Therefore, the process of progressive degradation of the coating is driven by the oxidation reaction of AlNi:



A similar degradation mechanism of an aluminide coating, driven by the superficial depletion of Al, on a Hastelloy X alloy is also proposed by Lee and Kuo [106].

The superficial layer of AlNi₃ cannot act as an effective diffusion barrier due to the formation of a large number of voids on it, as it can be observed in the micrographs in figure 6.3. The formation of voids at the interface with the oxide scale can occur even during the oxidation of AlNi bulk [225]. The presence of voids in the aluminide coating on Ni based substrate is also reported in several studies [97] [224] [226] [227] [228] [229] and their formation is usually ascribed to the Kirkendall effect. The pore production through Kirkendall effect usually takes place at the interface between two different metals due to reciprocal interdiffusion [230]. This occurs when two opposite and unbalanced diffusive fluxes are established with consequent formation of a net flux of vacancies. Pores are formed by condensation of the vacancies that are accumulated on the side of the faster diffusion metal.

Because of the high difference in the diffusion coefficients of Al and Ni in the not stoichiometric AlNi phase (see figure 1.36), the Kirkendall effect can have a role in the formation of pores in the superficial layer. Furthermore, Angenete et al. explained the formation of voids through a stress-driven vacancy coalescence mechanism [231]: the transformation of AlNi phase in the AlNi₃ intermetallic occurs with a certain volume variation and consequent formation of internal stresses, after that pores can form by coalescence of the vacancies that accumulate in the region where a tensile stress state is present. Beside the phases transformation, also the formation of the oxides can generate internal stresses that, in turn, can originate microcracks in the brittle AlNi₃, as shown in figure 6.3-C, with consequent further degradation of the coating.

In order to investigate the degradation of the aluminized coating under thermal exposure, the sample A2 of table 6.1 was submitted, after the aluminization process, to 72 hours of oxidation at 850°C in simple air. The FESEM micrographs reported in figure 6.7 show the alterations that have occurred in the coating during such oxidation test.

First of all, it is possible to observe that the overall thickness of the coating is increased of few tens of micrometers. Some care should be taken in comparing the thickness of the single layers because of a certain inhomogeneity of the coating that leads to not negligible differences of the thicknesses between different zones also on the surface of the same sample. However, by comparing with the micrograph of figure 6.3, it is possible to note that both the intermediate layer and the superficial porous layer tend to increase during the thermal exposure. Inside the intermediate dense layer, the thickness of the sublayer 2, rich in coarser precipitates, doesn't appear greatly modified, instead the thickness of the beneath sublayer 1 increased slightly. Furthermore, a newly formed sub-layer 3 is visible above sub-layer 2 (figure 6.7). These observations confirm that the further growth of the intermediate layer can occur, even without an aluminizing atmosphere, due to inter-diffusion mechanisms of Ni and Al. It is possible to argue that an initial thickening of the sub-layer 1 occur, at the beginning of the thermal exposition, due to outward diffusion of Ni through the hypo-stoichiometric AlNi layer. This growth of sub-layer 1 occurs at the expenses of the Al content in the sub-layer 2. When the sub-layer 2 is sufficiently depleted in Al, it becomes hypostoichiometric and then the outward diffusion of Ni through this sub-layer becomes possible leading to the formation of sub-layer 3.

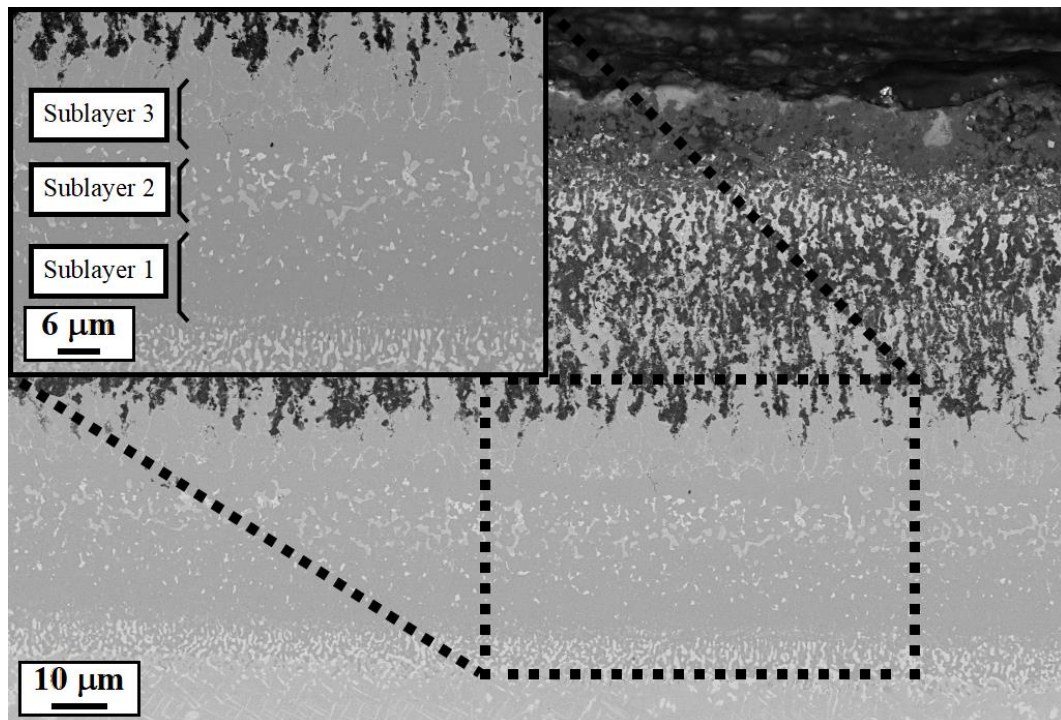


Figure 6.7. Aluminide coating on sample A2 after oxidation for 72 hours at 850°C.

During the thermal exposure, the interdiffusion and the formation of aluminum oxides cause further degradation of the superficial layer, which advances consuming the intermediate layer (figure 6.8).

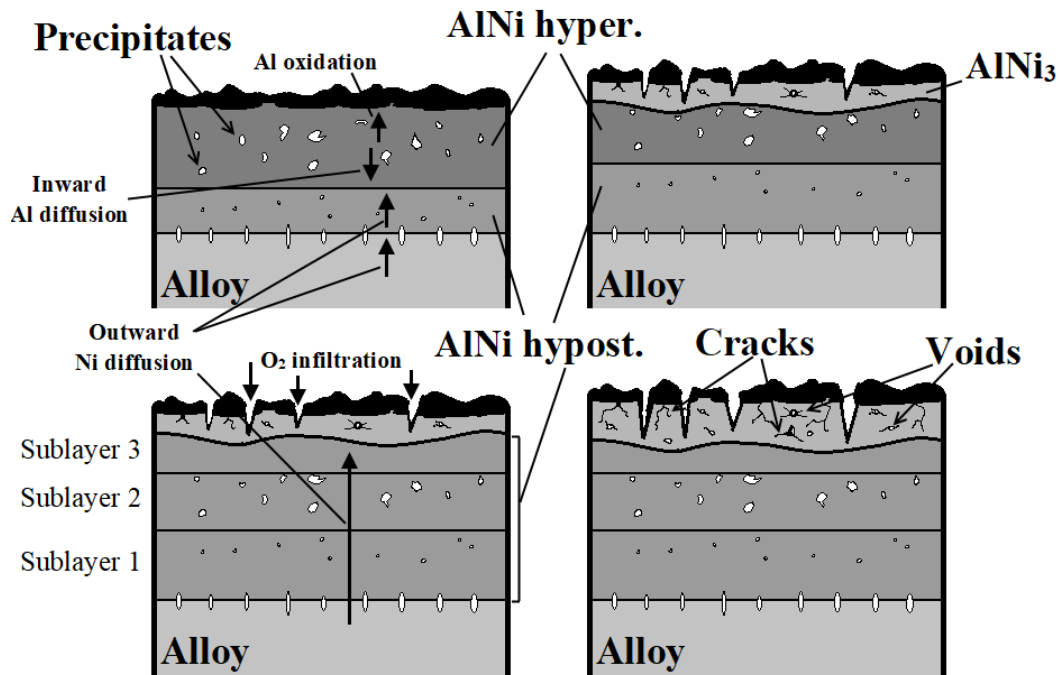


Figure 6.8. Schematic representation of the coating degradation mechanism.

The degraded layer has a mixed structure made by aluminum oxides and intermetallic phases as shown in figure 6.9. The oxides are probably formed by infiltration of the oxygen throughout the voids formed in the intermetallic layer as above discussed.

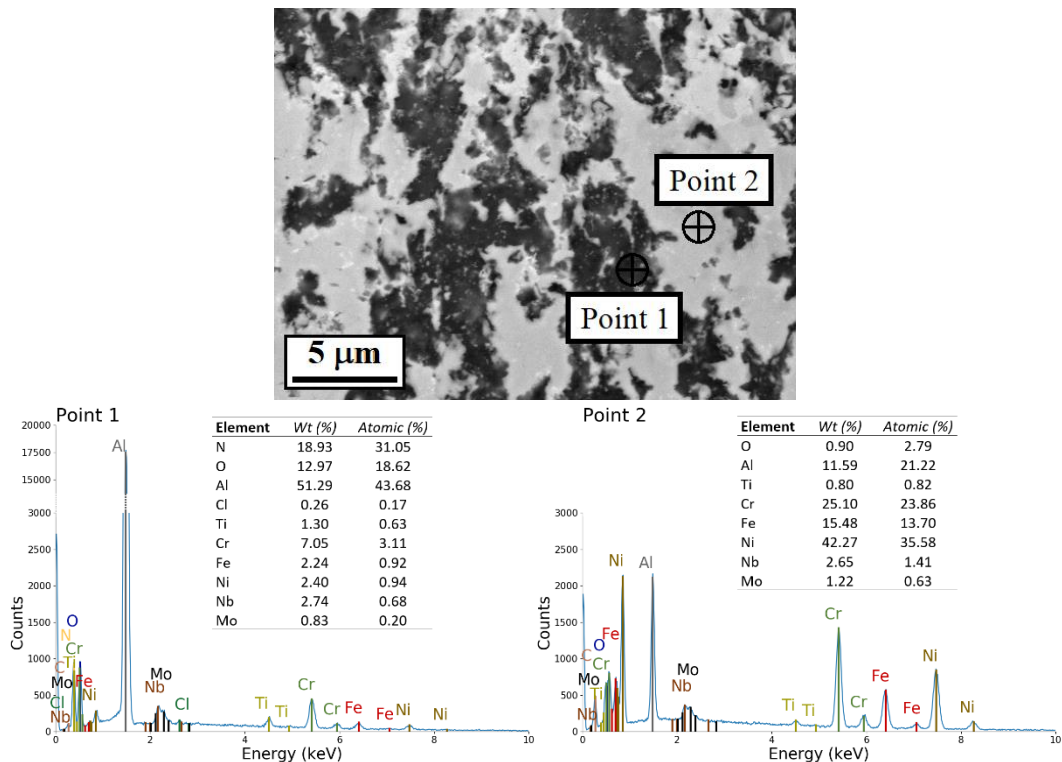


Figure 6.9. Spot EDS analyses on the oxidized zone (point 1) and on the intermetallic part (point 2) of the superficial layer of the coating on sample A2 after thermal exposure for 72 hours at 850°C in air.

The internal stresses, developed due to progressive oxidation of the superficial layer, can cause spalling of the coating due to local detachments at the oxide/intermediate layer interface. In figure 6.10 it is possible to observe that where spalling occurred the intermediate layer is exposed to the air and suffers for further oxidation and degradation during the thermal exposure.

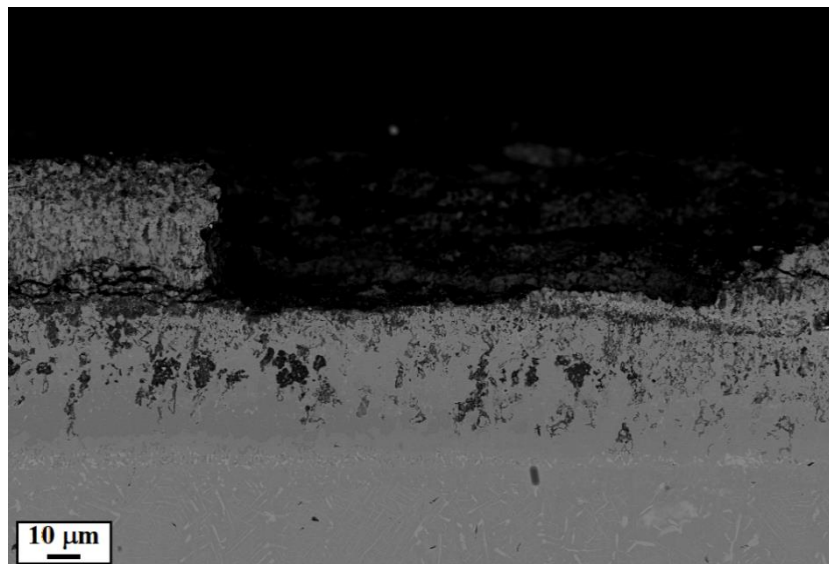


Figure 6.10. BSE FESEM micrograph showing the spalling of the coating on sample A2 observed after exposition at 850°C for 72 hours.

6.1.4 The over pack mode

The analysis of the coating formed on the bars semi-embedded in the aluminizing pack allows to compare the quality of the coating formed on a completely embedded surface with respect to one coated in over pack mode when all the other conditions, i.e. pack composition, temperature and time of the heat treatment, are the same. The two packs used to coat the bars differ only for the content of the activator (3% for bar B1, 7% for bar B2) and have 15% of Al as in the samples A2 and A4.

On the totally embedded zones the coating develops with the same features (figure 6.11) already observed in the samples A2 and A4 consisting of an inter-diffusion layer, a dense layer with dispersed precipitates and actually constituted by two sub-layers and a superficial porous and oxidized zone. The coating on bar B1 has an average thickness of about 46 μm and an inter-diffusion layer beneath of about 7 μm . Bar B2 has a thicker aluminide coating of about 62 μm on average and an inter-diffusion layer of about 11 μm . In both the samples, the extension of the degraded part of the coating varies greatly between different zones on the surface.

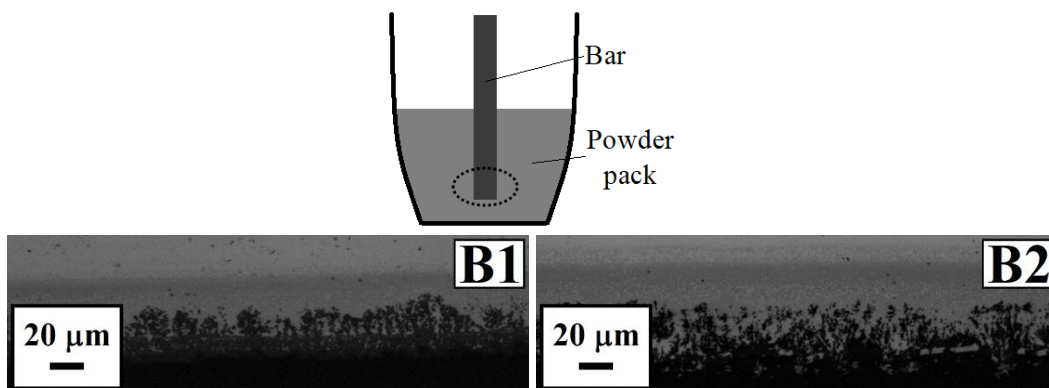


Figure 6.11. Optical micrographs of the cross sections of the coatings developed on the totally embedded part of the bars (dotted ellipse in the schematic drawing).

On the not embedded end of the bars, the coating has a poor adherence with the substrate and, therefore, tends to exfoliate and to expose the metal substrate below. The detachment between the coating and the substrate tends to occur below the inter-diffusion layer as shown in the optical micrographs of figure 6.12.

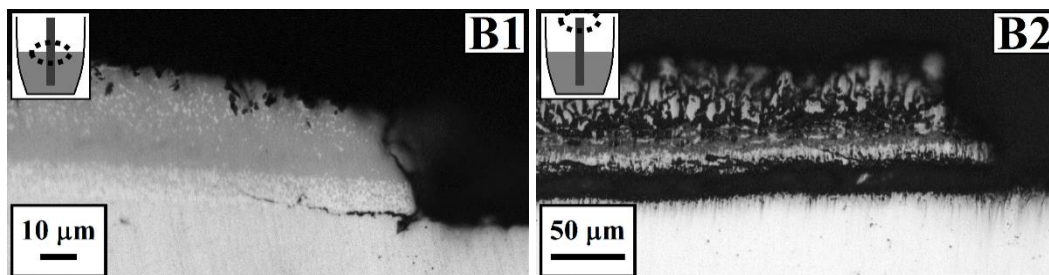


Figure 6.12. Optical micrographs showing the spalling of the aluminide coating formed in the middle of bar B1 and at the not embedded end of bar B2.

The degradation of the coating became more and more severe moving towards the not embedded end. In the totally embedded end of the bars, the coating achieves the same morphology and structure observed in figure 6.1, but the extension of the porous and oxidized layer tends to increase moving towards the opposite end (figure 6.13-A). On the section placed near the surface of the powder pack, the thickness of the coating is lower. Additionally, the dense intermediate layer is still detectable in some zones, for example the one shown in figure 6.13-B, but it is completely consumed in the others, as shown in figure 6.13-C. Finally, at the not embedded ends the coating strongly damages and exfoliates along the most of the surface (figure 6.13-D).

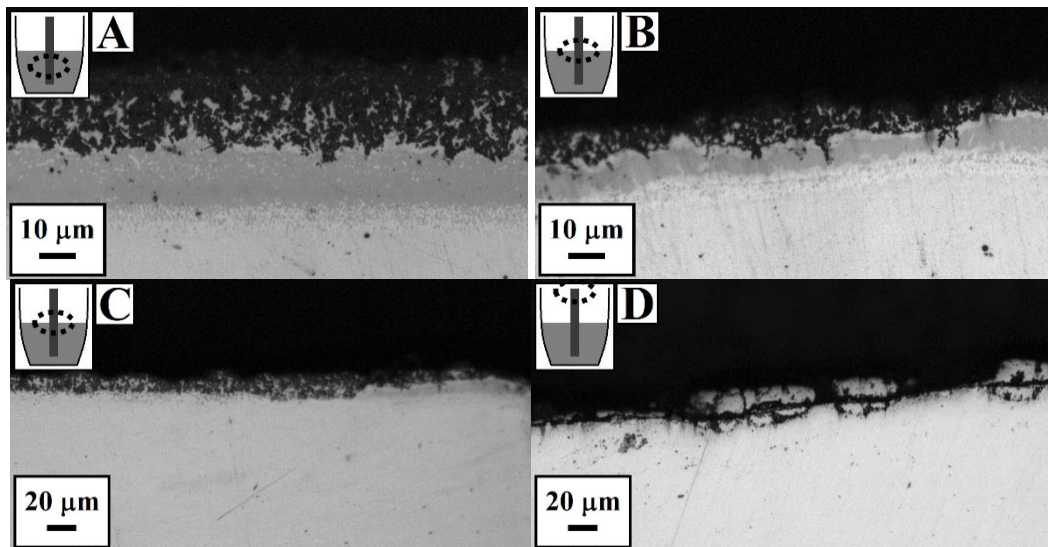


Figure 6.13. Optical micrographs showing the coating formed on bar B1 in different positions respect to the powder pack.

The obtained results clearly demonstrate that the over pack mode cannot be used in the treatment conditions adopted in this study. Coating with good quality can be obtained only if the surface to be coated is embedded sufficiently deep in the powder pack, where the partial pressure of the aluminizing vapors, achieved during the treatment, is sufficiently high to guarantee the formation of a thick and uniform aluminate layer and to prevent an excessive degradation due to superficial oxidation.

6.1.5 Effect of the Al and activator contents in the pack

Based on the above reported observations on the coatings obtained by performing the aluminization treatment at 900°C for 5 hours it is possible to give some considerations on the effect of the Al and activator contents in the pack. The plot in figure 6.14 shows the mean coating thickness in function of the activator content in the pack when the aluminum level is fixed at 10% (blue curve) and 15% (red curve). The reported values are the averages of the thickness measured on optical micrographs collected on each aluminized sample like those shown in figures 6.1 and 6.11. The reported thickness of sample A3, in which a continuous layer didn't form, is the sum of the height of the outwardly grown protrusions and the depth of the inwardly developed areas with elliptic shape.

It is clearly possible to note that the thickness of the coating increase with the Al content in the pack. The obtained thickness is related to the duration of the initial aluminization stage, in which the aluminum is transferred from the Al powders in the pack to the substrate. This initial stage ends when the Al source in the pack runs out. Conversely, it is also possible to observe that the coating thickness is not so strongly affected by the activator quantity, in agreement with the study of Tong et al. [120]. A slight increase of the thickness can be observed passing from 3% to 5% of activator in the pack, then a saturation value of the thickness is reached and a further increase of the activator content doesn't lead to a significant change in it. However, the activator quantity determines the partial pressure of the $AlCl_x$ vapour species at the initial stage of the aluminization and so the actual Al activity in the pack [93] [118] [119], therefore it has a strong influence on the coating formation mechanism and, as a consequence, on its final quality.

The ratio between the thickness of the porous layer and the total one can be used as a measurement of the obtained quality of the aluminide coating. In figure 6.14 the variation of this ratio is shown as a function of the activator content in the pack with a fixed aluminum percentage (15%). The optimal quantity of activator is 5%. When a too larger quantity of activator is used (as in the sample A4) the degradation of the dense aluminized layer is almost complete. As pointed out in the paragraph 6.1.3, the consumption of the dense intermediate layer and the relative formation of the porous layer is due to the depletion of Al on the surface. A higher content of activator determines the formation of a larger quantity of $AlCl_x$ aluminized vapors and, as a consequence, the initial Al source in the pack is consumed more rapidly and so the degradation stage, in which the depletion of Al on the surface is no more compensated by the introduction of new Al from the pack, starts earlier. The result is a larger degradation of the aluminate coating. Furthermore, also a reduced amount of activator may result in a too low partial pressure of the $AlCl_x$ aluminized vapors, in these conditions the rate of aluminization is not high enough to compensate the superficial Al depletion. The correct ratio between Al and activator contents in the pack allows the optimal flux of Al from the Al source in the pack to the alloy for the formation of a thick and stable coating avoiding excessive degradation.

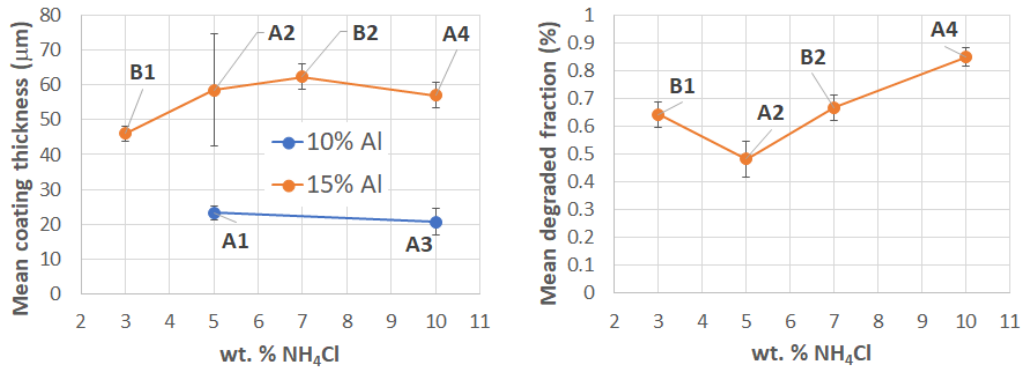


Figure 6.14. Coating thickness in function of the pack composition (contents of Al and activator) after aluminization at 900°C for 5 hours. The degraded fraction, i.e. porous layer thickness/(porous layer + dense layer thicknesses) ratio, are also shown in function of the activator content for the samples treated with 15% of Al in the pack.

When the Al content in the pack is 10%, an abrupt change of the mechanism of coating formation occurs when the activator content is increased from 5% (sample A1) to 10% (sample A3). In fact, the coating formed on sample A3 seems to be formed by a low activity process, i.e. mainly by the outward growth through prevalent diffusion of Ni from the substrate to the surface, furthermore the outward growth of the coating doesn't take place uniformly leading to the formation of isolated protrusions. A certain grade of inward diffusion of Al also occurs in this sample below the superficial protrusions (figures 6.1 and 6.2), but this is not sufficient to form a continuous intermetallic layer as that observed in the sample A1.

The net change in the formation mechanism of the coating didn't occur on the sample A4 for which a pack with the same mass of activator as A3 was used but with a higher mass of aluminum. This confirms that the mechanism of coating formation and degradation is strongly influenced by the ratio between the Al and the NH₄Cl contents in the pack, rather than by their absolute quantities. On the base of the results obtained from the aluminization test at 900°C, the identified optimal Al/NH₄Cl mass ratio falls around 3:1.

6.2 High temperature aluminizing test

The gain masses of samples aluminized during the high temperature test are reported in table 6.2.

Table 6.2. Mass gains for unit of surface area collected after the aluminizing test performed at 1065 °C for 2 hours.

Samples	Pack composition (wt. %)	$\Delta m/A$ (mg/cm ²)
H1	9% Al, 3.0% NH ₄ Cl, 88.0% Al ₂ O ₃	11.3 ± 0.2
H2	9% Al, 4.5% NH ₄ Cl, 86.5% Al ₂ O ₃	10.2 ± 0.2
H3	15% Al, 5.0% NH ₄ Cl, 80.0% Al ₂ O ₃	17.7 ± 0.3
H4	15% Al, 7.5% NH ₄ Cl, 77.5% Al ₂ O ₃	17.3 ± 0.3

The detected mass gains are larger than the ones obtained after the intermediate temperature tests, even if the Al contents in the pack are comparable. This indicates that at high temperature, the acquisition of Al during the aluminization process is more intense.

Figure 6.15 reports some optical micrographs collected on samples aluminized in the high temperature test. The morphology of the obtained coatings is very different with respect to the one observed in the intermediate temperature tests.

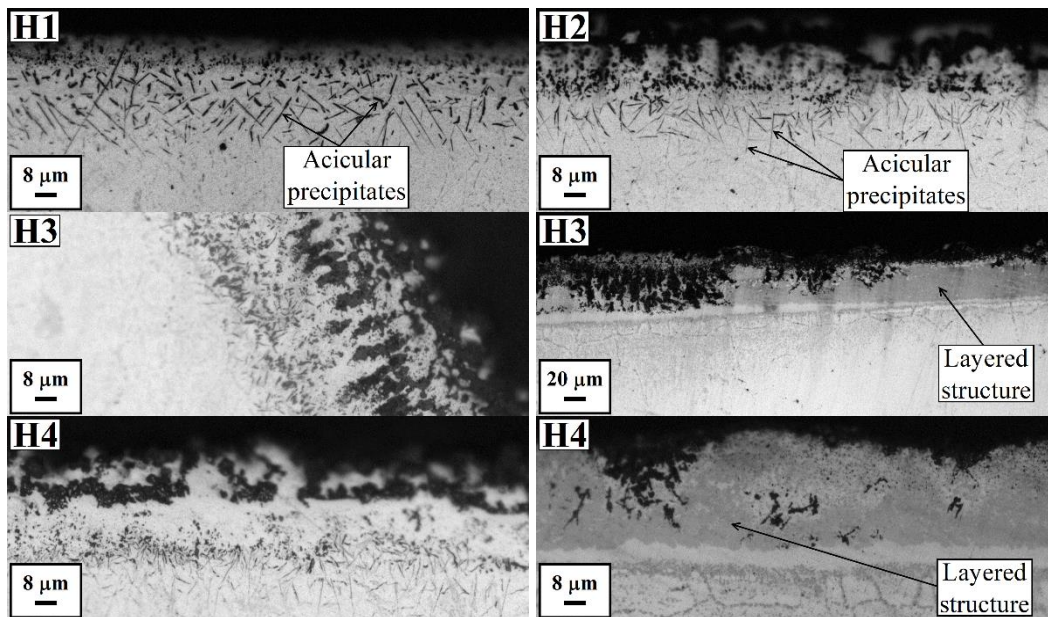


Figure 6.15. Optical micrographs of the cross sections of the coatings developed on the samples during the high temperature test (1065°C for 2 hours).

The coatings have not the general layered structure observed before. Only an irregular layer of oxides on the surface without a clear visible interface between the coating and the substrate is detectable. In the samples H1 and H2 a lot of acicular precipitates can also be revealed below the superficial oxides. The acicular precipitates are also reported by Angenete et al. after long oxidation exposure at 1050°C [231], which explain them as a consequence of the outward diffusion of Ni from the substrate. In the samples H3 and H4 the acicular precipitates are less present and in piecewise it is still possible to recognize a layered structure somehow similar to that observed at the intermediate temperature test. The samples aluminized at high temperature are also characterized by a deep zone of intergranular corrosion beneath the coating (figure 6.16). The internal corrosion is probably due to the formation of aggressive species, as NH_3 and HCl vapors, during the pack aluminization process and it can have deleterious effect on the oxidation resistance of the alloy making it more prone to severe intergranular oxidation.

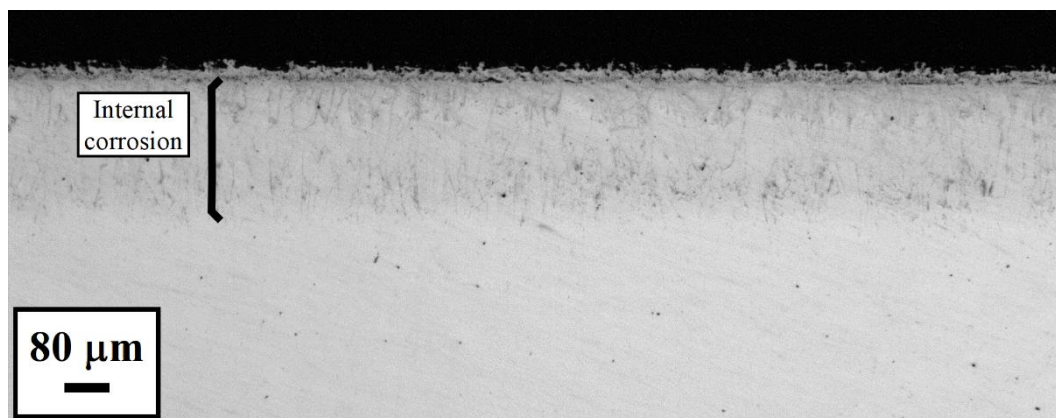


Figure 6.16. Intergranular corrosion about 250 μm in deep beneath the coating on sample H4.

The above reported results indicate that the aluminate coating cannot form adequately at the process temperature of 1065°C. In fact, the coating is formed discontinuously and the effects of a corrosive attack, due to the aluminizing vapors, and extensive oxidation are observed in the remaining parts of the surface.

6.3 Low temperature aluminizing test

In the samples aluminized during the low temperature test a very low mass gain was measured despite the higher quantity of Al in the packs with respect the previous tests. The measured mass gains after the low temperature test are reported in table 6.3.

Table 6.3. Mass gains for unit of surface area collected after the aluminizing test performed at 800 °C for 5 hours.

Samples	Pack composition (wt. %)	$\Delta m/A$ (mg/cm^2)
L1	15% Al, 3.75% NH_4Cl , 81.25% Al_2O_3	0.9 ± 0.1
L2	15% Al, 5.00% NH_4Cl , 80.00% Al_2O_3	0.5 ± 0.1
L3	20% Al, 5.00% NH_4Cl , 75.00% Al_2O_3	0.5 ± 0.1
L4	20% Al, 6.67% NH_4Cl , 73.33% Al_2O_3	0.6 ± 0.1

All the coatings obtained at the aluminizing temperature of 800°C are similar in thickness and morphology regardless the pack composition. However, the coatings appear not uniform because on certain zones it is possible to observe a thin and continuous aluminized layer of about 4-7 μm (images of the samples L1, L2 and L3 on the left in figure 6.17), but some isolated protrusion of about 10-20 μm in height are also present. Where these protrusions form, the coating forms discontinuously (images of the sample L4 and of the samples L1, L2 and L3 on the right in figure 6.17).

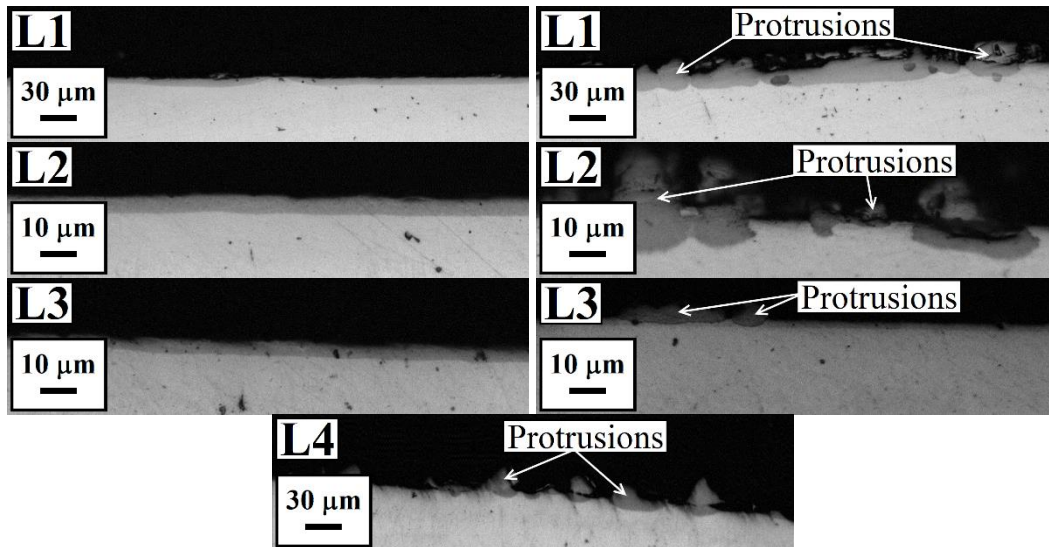


Figure 6.17. Optical micrographs of the cross sections of the coatings developed on the samples during the low temperature test (800°C for 5 hours).

The isolated protrusions were examined in greater details through SEM observations (figure 6.18).

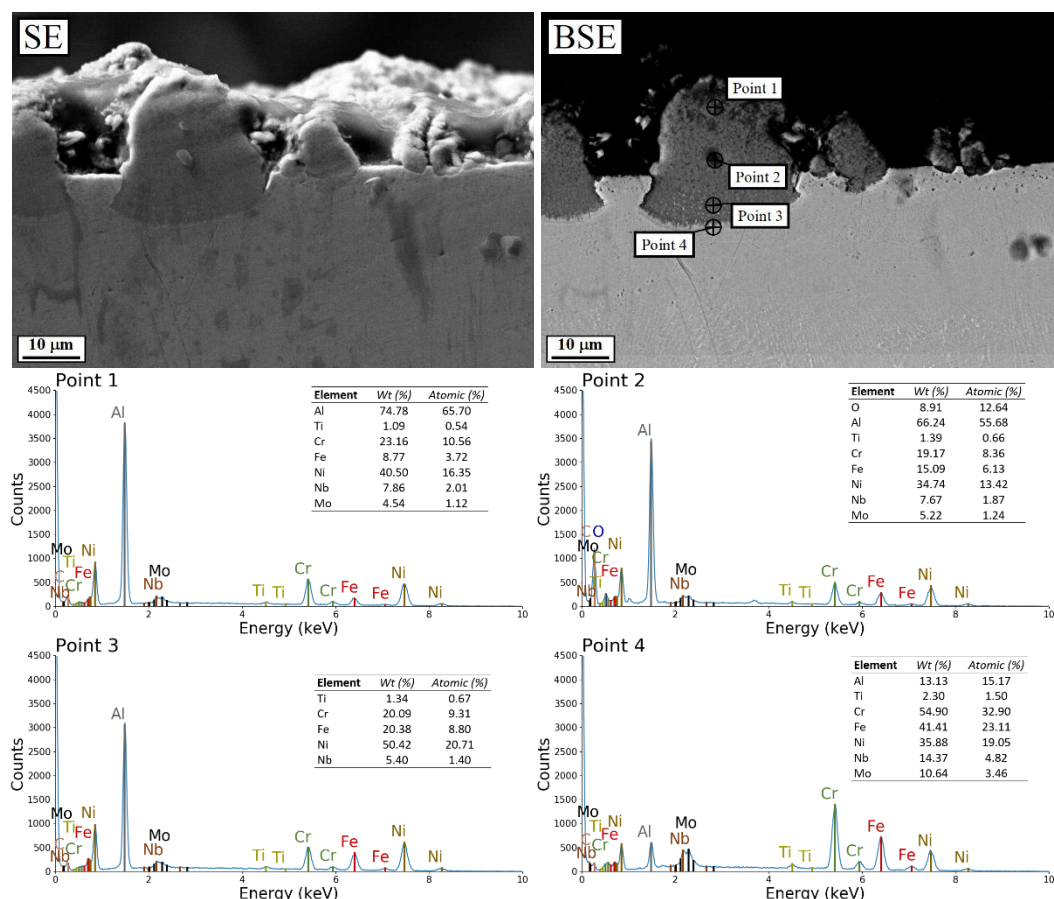


Figure 6.18. SEM micrographs of the cross sections of the coating developed on the sample L1 showing the superficial isolated protrusions. BSE: Backscattered Electrons mode; SE: Secondary Electrons mode. Spot EDS analysis on a protrusion.

In this process the aluminization occurs predominantly through outward growth of the intermetallic compounds. Although the base of each protrusion is rooted in

the substrate due to the occurring of a certain grade of inward growth of the intermetallic, as it can be ascertained by the presence of precipitates in the zone of the protrusion below the initial surface of the substrate. The EDS analysis reported at figure 6.18 shows that the protrusions are very rich in aluminum. The detected quantities are compatible with the Al_3Ni intermetallic stoichiometry. The presence of Ni even above the original surface level in these isolated protrusions confirm that an outward diffusion of Ni from the substrate occurs.

The formation of the thin and continuous layer occurs probably by inward growth as in a typical LTHA process, but the formation of the protrusion disturbs the formation of this layer making it discontinuous. A possible explanation for the formation of the isolated protrusions is that the superficial diffusion of the Al adsorbed on the surface prevails on the assimilation of Al in the substrate, leading to the accumulation of Al around an already existing defect on the surface or a grain boundary. Once the accumulation is formed, the deposition of Al from the atmosphere occurs predominantly on it, therefore the surrounding area cannot be adequately coated.

6.4 Pack aluminization on hard-accessible internal surface

6.4.1 Aluminizing tests on modules

On the base of the above reported aluminization tests, the process parameters that allow to obtain the best result in term of uniformity of the coating and low level of degradation are:

- temperature: 900°C
- time: 5 hours
- pack composition: 15% Al, 5% NH_4Cl , 80% Al_2O_3

These process parameters were adopted for the aluminization trials of the modules. The aim of this study is to test the capability of the pack aluminization process to efficiently coat hard accessible internal surfaces. During the coating treatment, both the external and internal surfaces of each module are aluminized under different conditions. In particular, each module is completely inserted in the pack, but one end results located at the bottom of the crucible, deeply embedded in the powder mixture, whereas the opposite end is near the surface of the pack. As already pointed out during the aluminization test of the bars half embedded in the powder (paragraph 6.1.4), the local partial pressure of the generated AlCl_x aluminizing species and the oxygen vary moving toward the surface of the pack, leading to a different level of degradation of the obtained coating. Furthermore, the internal surfaces of the channels have a higher roughness and they are in contact with a lower amount of powders with respect to the external ones. These conditions are expected to affect the coating formation.

The optical micrographs collected on the external surface of the module n.1 are reported in figure 6.19, the aspect of the coating is shown starting from the deeper embedded end and moving toward the surface of the pack. In agreement to what already observed after the aluminization of the half embedded bars (figure 6.13), the coating formed at the bottom of the pack has the thicker intermediate layer, but this dense layer progressively reduces in section moving towards the surface of the pack until the coating is entirely constituted by a porous and oxidized layer.

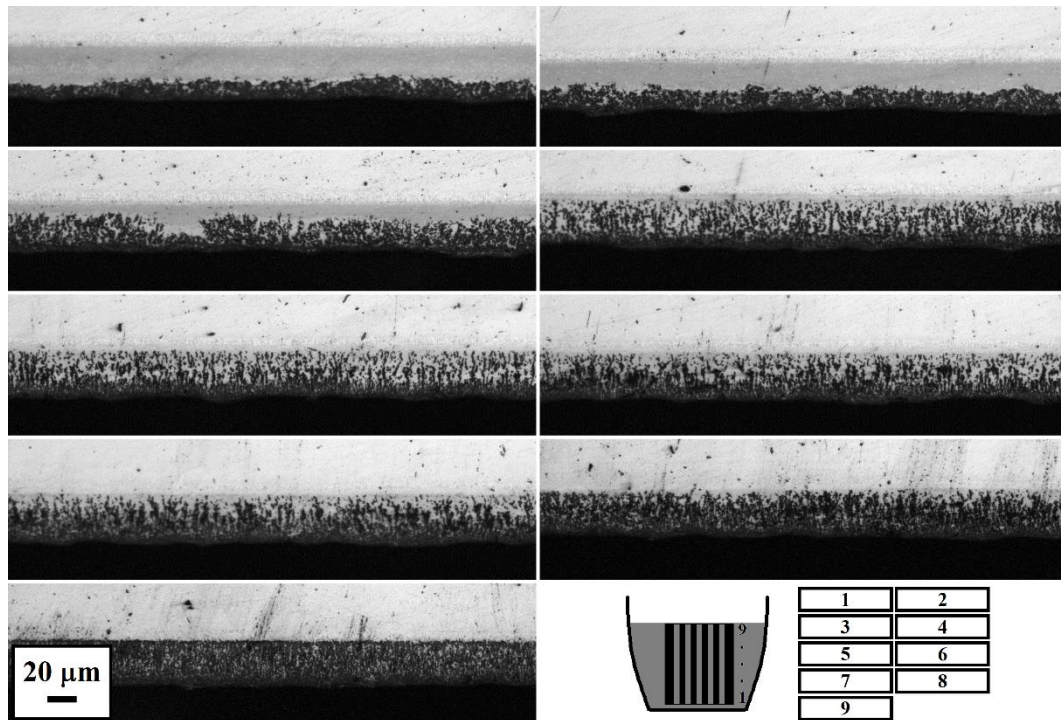


Figure 6.19. Optical micrographs showing the coating on the external surface of module n.1 from the deeper embedded end to the surface of the pack.

Obtaining a homogeneous coating on the internal surfaces is even more complicate because of the above reported reasons of differential partial pressure of the aluminum chloride. The coating formed on the internal surfaces appear inhomogeneous both in thickness and in structure: in some areas the coating develops the usual layered structure, as it can be seen in figure 6.20-A, and the dense and precipitates-rich layer constitutes the greatest part of the overall thickness. However, an intermetallic phase with a clear coating/substrate interface doesn't form in some areas and rather a thin layer probably constituted of oxides and other corrosion products is visible (figure 6.20-B).

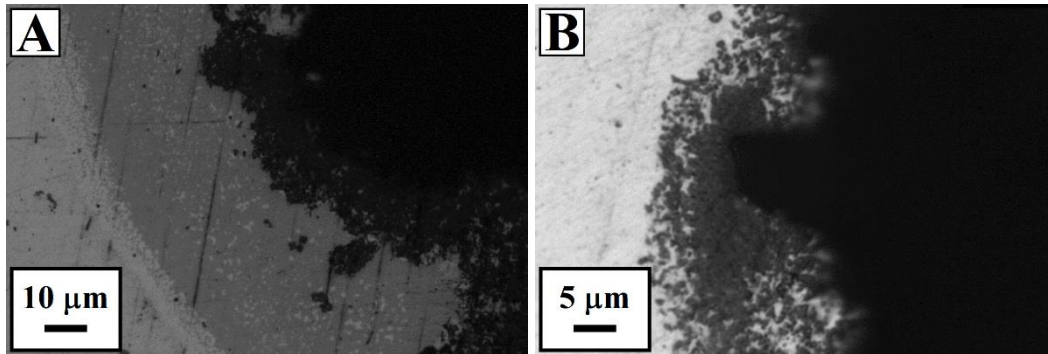


Figure 6.20. Optical micrographs showing the coating formed in the internal surfaces. A zone in which the typical structure forms (A) and a zone in which only a degraded layer forms (B).

6.4.2 Cyclic oxidation test on aluminized modules

The quality of the obtained coating is expected to have a great influence on its oxidation resistance. In this paragraph, the observed microstructural alterations of the coating formed on the most deeply embedded external surface of module n.2 after repeated thermal cycles at 850°C in air are reported. As expected, the aluminide coating can act more efficiently as a protective diffusion barrier where the initial coating structure is characterized by a thick and dense AlNi layer with a low level of superficial degradation.

The possibility to achieve good stability and oxidation resistance of the aluminide coating is demonstrated by the optical micrographs collected on zones where the initial structure is the correct one (figure 6.21). The oxidized superficial layer did not visibly expand and the intermediate AlNi layer was not markedly consumed during the thermal cycles. In these conditions, the coating doesn't undergo important structural changes, therefore it can act as an effective protective barrier.

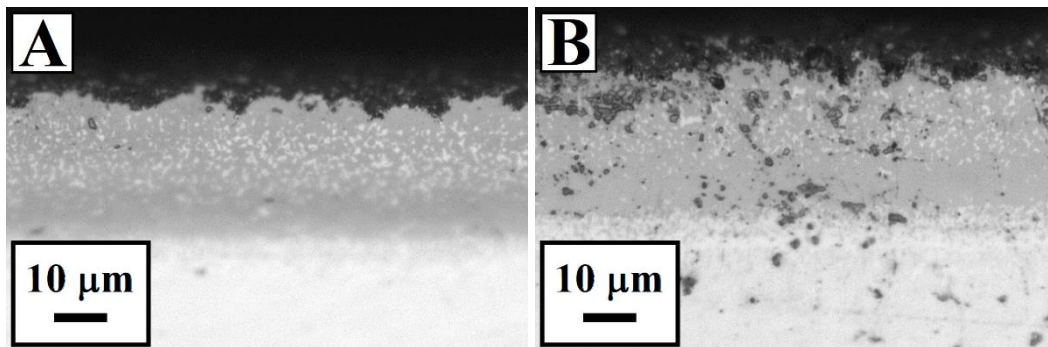


Figure 6.21. Properly formed aluminide coating on an external surface of module n.2 before the thermal cycles (A) and after five thermal cycles at 850°C (B).

However, it is also possible to observe zones of the surface in which the coating is not stable during the thermal cycles. In these zones the intermediate layer is rapidly consumed (figure 6.22), therefore only an oxidized layer, that is not able to effectively protect the substrate from further oxidation, remains on the surface at the end of the thermal cycles.

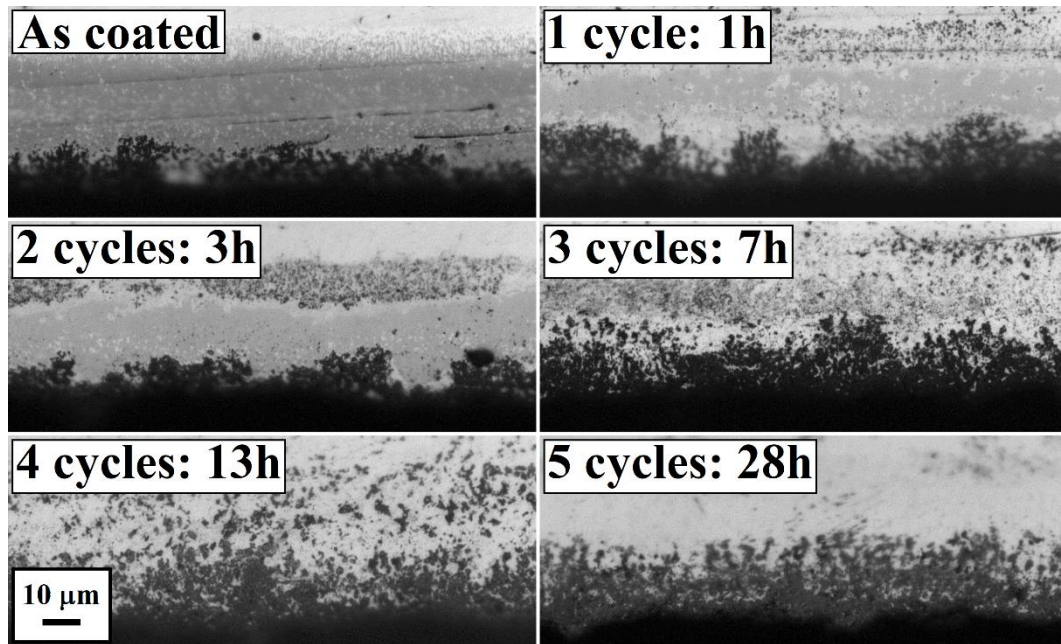


Figure 6.22. Oxidation/degradation of the aluminide coating on an external surface of module n.2 in a zone in which the coating is unstable during the thermal cycles at 850°C.

The performed cyclic oxidation test reveals the degradation mechanism of the aluminide coating, that is mainly based on further depletion of Al in the intermetallic matrix on the surface due to the formation of oxides. If a continuous and passivating layer of aluminum oxide is formed on the surface, the growth of this oxide scale proceeds slowly and the AlNi layer can supply aluminum for long time. This favorable condition occurs in the part of coating shown in figure 6.21. On the contrary, if the superficial layer is too structurally damaged because of the presence of a lot of microcracks and voids, the oxygen can penetrate and reach the underlying layers. In these conditions, the depletion of Al in the AlNi layer is fast and the transformation into AlNi₃ occurs with consequent formation of further voids though the mechanism described at paragraph 6.1.3. Then, the oxidizing atmosphere can infiltrate the formed voids to reach the underlying layers, leading to further oxidation. The degradation process goes on in the above described way through a rapid consumption of the AlNi layer and the advancement of a not protective oxide scale, as shown in figure 6.22.

On the internal surfaces of the channel, the formed coating is already partially degraded before to start the thermal cycles and its initial thickness is low and not uniform. In these conditions, a protective oxide layer can form only piecewise on the surface during the thermal cycles. The remaining part of the coating suffer further degradation and it is rapidly substituted by a layer of discontinuous oxides (figure 6.23).

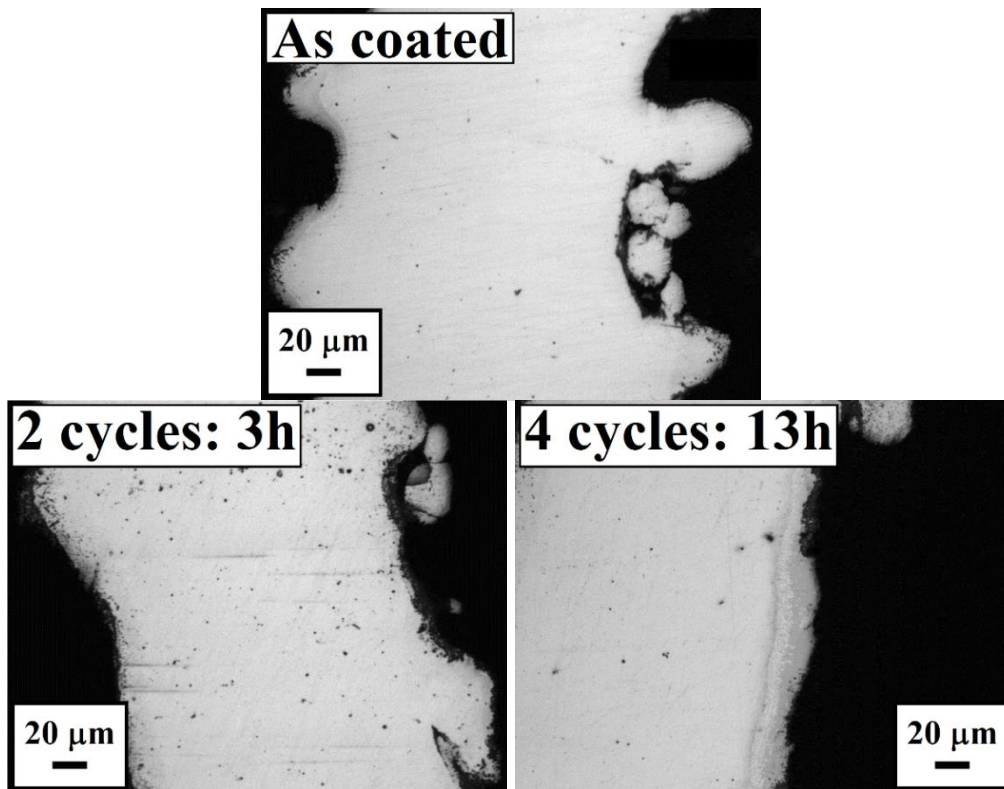


Figure 6.23. Optical micrographs showing the cross section of the coating on the internal surface of the channels in module n.2 before the thermal cycles and after 2 and 4 cycles at 850°C.

6.5 Conclusion

In the design of a suitable aluminization process, the more challenging aim is to obtain a uniform coating on the entire surface of the piece. Actually, the performed tests have demonstrated that mechanisms of formation, growth and evolution of the coating are extremely sensitive to the process parameters, in particular to the temperature and the ratio between the Al and the activator mass in the pack, and the local conditions of aluminization, which can vary significantly between different locations of the substrate in the pack (fully embedded, near the pack surface, over-pack mode).

The better coating quality and the more stable conditions were obtained with a powder pack containing 15% wt. of Al, an Al/NH₄Cl mass ratio of about 3 and a treatment temperature of 900 °C. This recipe was applied successfully on flat and polished SLM Inconel 718 samples. In these conditions, a layered structure develops with a superficial porous layer consisting mainly of AlNi₃ and aluminum oxides, an intermediate dense AlNi layer with a lot of embedded precipitates and an inter-diffusion layer characterized by precipitates of heavy elements at the substrate/coating interface.

The strong dependence of the diffusivity of Ni and Al in the AlNi phase on the composition of the phase itself leads to a not trivial diffusion behavior and a resulting complex structure. For this reason, it is not possible to uniquely classify the coating process in one of the two main categories, i.e. low activity process, in which the outward diffusion of Ni prevails, or high activity process, in which the

growth of the coating is dominated by the inward diffusion of Al. Conversely, a coating with the characteristic features of both types is observed in most of the cases, giving clues to the fact that the formation of the coating occurs through a mixed mechanism.

Further heterogeneity is due to the instability of the dense AlNi layer in oxidizing environment. AlNi suffers of aluminum depletion due to the capture of Al into oxides and to diffusion towards the underlying layers, that leads to a structural damage connected with the transformation into the more brittle AlNi₃ phase. The coating degradation already starts during the aluminization process, as soon as the Al source in the pack runs out, even with a very low oxygen partial pressure. The degradation of the coating can continue during further exposition to high temperature (850 °C in the current study) in air unless a protective and slowly growing oxide scale forms on the surface. The problem of the superficial Al depletion is even more severe when the task is the aluminization of complex or hardly accessible surfaces, such as those of the narrow channels in the modules tested in the current work.

Therefore, future studies should focus on enhance the repeatability of the aluminization process and the uniformity and stability of the obtained coating in order to ensure an effective diffusion barrier with a long duration in strongly oxidizing working conditions.

Overall conclusions

The superalloy systems are highly complex due to the large number of alloying elements involved, the interactions of which can affect markedly the solidification mode and consequently can influence the evolution of the microstructure and the formation of the second phases. The Selective Laser Melting (SLM) technique leads to the formation of great thermal gradients and rapid cooling rates from the liquid, which in turns causes a solidification process that occurs far from the equilibrium conditions. The consolidation of the material during SLM can be compared to a welding process with a very high cooling rate, in the order of 10^6 K^{-1} . Furthermore, the deposited material is submitted to a series of rapid thermal cycles due to the heat coming from the deposition of the following layers; these thermal cycles can markedly alter the initial microstructure. For these reasons, the microstructure in the as built state is so complex, heterogeneous and hard to be predicted a priori.

Within the three years of the thesis project a preliminary study was performed so as to identify the optimal processing parameters to fabricate Inconel 718 alloy via additive manufacturing. Further to the identification of the optimized parameters the definition of a relatively large processability window for this material allowed to demonstrate that the proposed fabrication process is robust and can be considered for technology transfer to industrial environment. Actually, porosity levels lower than 0.5% and material completely free from cracks in a wide window of the main process parameters (laser power, scan speed and layer thickness), can be obtained. As built microstructures of SLM Inconel 718 alloy achieved by modulating the fabrication parameters were investigated within the framework of this thesis focusing on the most important features at each specific length scales. The laser related features and the grain boundaries are the main microstructural features at the length scale of 0.1-1 mm. These features appear independent one from each other, i.e. the grains can develop during several depositions in the additive process without be confined by the laser tracks and by the single layers because of the epitaxial type growth. The fastest growth directions correspond to the $\langle 100 \rangle$ crystallographic lines. Therefore, the most favorably oriented grains with respect to the temperature field in the molten pool, i.e. with a $\langle 100 \rangle$ direction set to a lower angle with respect to the local thermal gradient, can grow more rapidly and supplant the others. The competitive growth of the grains causes the formation of the strong observed [001] texture. In this work, the characterized samples have always been built adopting the 67° rotation scanning strategy, therefore it is not surprising that the performed EBSD analysis does not reveal any preferential orientation of the grains around the building direction. The effect of the scanning strategy and its periodicity grade between the deposited layers has probably an important influence on the competition between the grains and their

confinement in the laser related features, i.e. the laser tracks and the melt pools. The study of this effect can be further deepened in future researches.

At the length scale from 1 to 10 μm , it is possible to observe a sub-granular structure made of fine parallel dendrites without secondary branches and separated by eutectic products rich in Nb, Mo and Ti. The eutectic products form a dense interconnected network in specific zones of the as built microstructure. A similar structure, due to rapid cooling, is typically observed in the welds, but the one observed in the SLM products is characterized by the extremely small dendrite size, about 1 micrometer, caused by a very drastic cooling rate experienced during the SLM process. Some heterogeneities of the dendrites have been observed inside the melt pools. The dendrite size tends to slightly grow from the bottom of the melt pool towards the upper part. Furthermore, some occasional changes of 90° in the dendrites growth direction have been detected along the edges between laser tracks. The 90° deviations occur every time one $\langle 100 \rangle$ crystallographic direction that is perpendicular to the previous growth direction becomes favorably oriented with respect to the local thermal flux in the new layer. These local heterogeneities are direct consequence of the complex dynamic that takes place during the solidification of the molten pools, involving not constant cooling rates and thermal gradients. At the length scale of the single dendrite, the TEM analysis reveals the micro-segregation of the alloying elements and a high density of dislocations at the inter-dendritic boundaries, which indicate a certain level of residual tension in the as built state. The solutes with a partition coefficient k greater than 1, mainly Fe and Cr, tend to accumulate along the dendrite central axis, instead the elements with k lower than 1, in particular Nb, segregate at the inter-dendritic boundaries.

The micro-segregation at the dendrites level plays an important role on the following solution treatment. Actually, it has been observed that the solution annealing at 980°C leads to the formation not only of intergranular plate-like δ phase as expected, but also of a large quantity of intra-granular δ precipitates along the inter-dendritic boundaries deriving from the partial dissolution of the eutectic products and the consequent greater local availability of niobium. Since the intra-granular δ phase is usually unwanted, it is necessary to increase the temperature of the solution annealing above the solvus point of this phase. The volume fraction of the detected precipitates reduces by increasing the solution temperature. After a thermal treatment at 1065°C , it is possible to observe grain boundaries decorated with blocky or globular precipitates. This impedes the grain growth through a pinning mechanism. Furthermore, a large number of very small precipitates can be observed inside the grains. During the solution annealing at 980°C and at 1065°C , the recrystallization occurs only partially and it is limited to the zones in which the level of residual tension is greater, i.e. along the laser tracks boundaries. On the other hand, the complete recrystallization and grain coarsening can be ascertained after the solution treatment at 1200°C leading to a strong reduction of the measured Vickers microhardness. The presence of grain boundaries free from precipitates

after the thermal treatment at 1200°C indicates that the migration of the new grain boundaries cannot be hindered by the precipitates at this temperature.

According to this study, the best solution temperature found is 1065°C. Actually, at this temperature a good level of homogenization and dissolution of the precipitates is obtained, but, at the same time, the formation of new unwanted phases and an excessive increase in the grain size is avoided.

The next step of the research was to define the aging sequence that stabilizes the microstructure. Here the key of the development is to obtain the precipitation of the strengthening γ' and γ'' precipitates. The response of the material to the aging treatment was investigated through DSC and TMA thermal analyzes with the aim to establish the temperature ranges in which the precipitation of the γ' , γ'' and δ phases occurs. Some samples solutioned at 1065°C for 2 hours and then treated at these temperatures were studied through XRD analysis, electron microscopy and Vickers microhardness measurement in order to understand how the population of precipitates evolves during the aging treatment. Very fine γ' precipitates, which cause a moderate increase in the mean microhardness of the alloy, form during the treatment at 565°C. However, a much greater increase in the microhardness level is obtained by performing the aging at 740°C due to an extensive precipitation of γ' and then of discoidal γ'' . An excessively prolonged treatment or a too high aging temperature can cause the alloy softening due to the coarsening of the strengthening precipitates and to the transformation of the metastable γ'' phase in the thermodynamically stable δ phase. The effect of the temperature and time of each treatment step, i.e. solutioning, first aging and second aging, on the Brinell and Vickers hardness and on the microstructure was determined through dedicated factorial plans. The highest hardness value, 423 HB10, was obtained with the following treatment cycle: solution annealing at 1065°C for 2 hours, first aging at 720°C for 8 hours, second aging at 630°C for 8 hours. A single direct aging treatment, i.e. not preceded by any solution step, was also studied. Although the Brinell hardness after direct aging results to be higher than the one measured on fully heat treated samples, the interdendritic eutectic products in the matrix, which can strongly affect the ductility and leading to unevenly distribution of the strengthening precipitates, remain completely undissolved.

The oxidation tests presented and discussed in this thesis demonstrate that the excellent densification level of the Inconel 718 alloy obtained via SLM and the absence of structural defects imply a hot oxidation resistance comparable with that of the material produced by traditional technology. The rapid formation of a continuous superficial layer, consisting predominantly of doped chromia, provides an effective and stable protection against further oxidation, as the passivating scale does not tend to crack, detach or evaporate from the metallic substrate. When exposed to a temperature of 850°C in simple air, the alloy goes through an initial transitory period of about 8 hours during which the oxide scale is formed over the whole surface. At the end of such period, the system enters into the steady state regime during which the further thickening of the oxide is controlled only by

diffusion through the protective barrier. The begin of the stationary regime is indicated by the settling of the measured mass gain trend on a parabolic curve. The middle term test also showed that the parabolic constant measured at the oxidation temperature of 850°C is not markedly influenced by an oxidation mode performed through thermal cycling respect to an isothermal exposure. This provides further evidence of the high resistance and stability of the protective scale. The parabolic trend is also maintained for oxidation times above 900 hours at 850°C. The superficial chromia layer remains regular and uniform over the entire oxidation period, although some metal particles embedded in the scale and a certain grade of internal discontinuous oxidation along the grain boundaries have been observed. The internal oxides are mainly constituted by titanium oxides and, at greater depth, aluminum oxides. Furthermore, a Nb rich quasi-continuous interlayer, which can act as a second barrier against the inward diffusion of the oxygen, was observed to form between the chromia scale and the metal substrate. All the reported oxidation tests have been performed after a preliminary lapping of the samples with the aim of reducing the high surface roughness that is found after the SLM production. In real applications it might be possible that the topological complexity of the surfaces of the parts obtained with additive technology or their hard accessibility can make a post finishing treatment not practical. Therefore, as a prosecution of the work reported in this thesis, it would be interesting to investigate the possible influence of the surface roughness of the parts produced by SLM on the effective resistance to hot oxidation and on the stability of the protective scale.

For all that applications in which the intrinsic oxidation resistance of the Inconel 718 alloy is not sufficient due to the high operating temperatures or the very aggressive environment, the coating of the parts by pack aluminization technique can represent an effective and economical solution. Several aluminization tests using samples produced via SLM were performed by varying the treatment temperature and the powder pack composition. The best result was obtained with a pack with 15% of Al, 5% of NH_4Cl activator and alumina for the remaining part. The aluminized coating consists of a thick layer of intermetallic AlNi with a large amount of dispersed precipitates and an interdiffusion layer with precipitates disposed transversely to the interface between the intermetallic and the metallic substrate. The AlNi layer tends to degrade at the surface through a de-aluminization mechanism caused by inter-diffusion and the oxidation of the aluminum. De-aluminization involves a phase transformation with the formation of AlNi_3 compound and consequent formation of pores and cracks which causes the loss of the protective capability of the coating. It was not possible to avoid a certain degree of degradation to occur already during the coating process. The instability of the AlNi layer is the main cause of the failure of the coating and further work is required to improve this aspect. The coating of hard to access surfaces, as the internal ones of narrow channels, can potentially be obtained in over pack mode by exploiting the diffusion of the Al carrying vapors, formed during the heat treatment, from the powder pack to the surfaces to be coated. However, the performed tests have demonstrated that a very degraded coating, which easily detaches from the

substrate, is obtained in over-pack mode on areas far from the powder pack. Therefore, it is necessary to maintain a close contact between the powder pack and the surface to be coated, therefore the coating of internal channels should be performed by filling them with the aluminizing pack even if this can lead to some difficulties in removing the powder from them after the treatment. The reported results demonstrate the feasibility of using the pack aluminization technique to obtain an aluminized coating on hardly accessible and rough internal surfaces, however it is not easy to obtain a uniform thickness and a regular microstructure because the quality of the coating get worse moving towards the surfaces less deeply buried in the powder pack. Therefore, future work should focus on making the aluminization process more controllable and improving the uniformity of the obtained coating.

References

- [1] R. C. Reed, *The Superalloys - Fundamentals and Applications*, 1st edition, Cambridge University Press, New York, USA, 2006. ISBN-13 978-0-511-24546-6.
- [2] M. J. Donachie, S. J. Donachie, *Superalloys A Technical Guide*, 2nd edition, ASTM International, Materials Park, Ohio, USA, 2002. ISBN 0-87170-749-7.
- [3] E. Akca, A. Gürsel, A Review on Superalloys and IN718 Nickel-Based INCONEL Superalloy, *Periodicals of Engineering and Natural Sciences (PEN)* 3 (2015) 15–27. <https://doi.org/10.21533/pen.v3i1.43>.
- [4] H. Fecht, D. Furrer, Processing of nickel-base superalloys for turbine engine disc applications, *Advanced Engineering Materials* 2 (2000) 777–787. [https://doi.org/10.1002/1527-2648\(200012\)2:12<777::AID-ADEM777>3.0.CO;2-R](https://doi.org/10.1002/1527-2648(200012)2:12<777::AID-ADEM777>3.0.CO;2-R).
- [5] E. O. Ezugwu, Z. M. Wang, A. R. Machado, The machinability of nickel-based alloys: a review, *Journal of Materials Processing Technology* 86 (1999) 1–16. [https://doi.org/10.1016/S0924-0136\(98\)00314-8](https://doi.org/10.1016/S0924-0136(98)00314-8).
- [6] G. Maurer, W. Castledine, F. Schweizer, S. Mancuso, Development of HIP consolidated P/M superalloys for conventional forging to gas turbine engine components, in: *Superalloys 1996: 8th International Symposium on Superalloys* (Ed.: R. D. Kissinger, D. J. Deye, D. L. Anton, A. D. Cetel, M. V. Nathal, T. M. Pollock, D. A. Woodford), The Minerals, Metals & Materials Society (1996) 645–652. https://doi.org/10.7449/1996/Superalloys_1996_645_652.
- [7] U. Habel, Microstructure and Mechanical Properties of HIP PM 718, in: *Superalloys 718, 625, 706 and Various Derivatives* (Ed.: E. A. Loria), The Minerals, Metals & Materials Society (2001) 593–604. https://doi.org/10.7449/2001/Superalloys_2001_593_604.
- [8] G. A. Rao, M. Srinivas, D. S. Sarma, Influence of modified processing on structure and properties of hot isostatically pressed superalloy Inconel 718, *Materials Science and Engineering A* 418 (2006) 282–291. <https://doi.org/10.1016/j.msea.2005.11.031>.
- [9] S.-H. Chang, In situ TEM observation of γ' , γ'' and δ precipitations on Inconel 718 superalloy through HIP treatment, *Journal of Alloys and Compounds* 486 (2009) 716–721. <https://doi.org/10.1016/j.jallcom.2009.07.046>.
- [10] D. Tomus, Y. Tian, P. A. Rometsch, M. Heilmaier, X. Wu, Influence of post heat treatments on anisotropy of mechanical behaviour and microstructure of Hastelloy-X parts produced by selective laser melting, *Materials Science and Engineering A* 667 (2016) 42–53. <https://doi.org/10.1016/j.msea.2016.04.086>.
- [11] W. Tillmann, C. Schaak, J. Nellesen, M. Schaper, M. E. Aydinöz, K. P. Hoyer, Hot isostatic pressing of IN718 components manufactured by selective laser melting, *Additive Manufacturing* 13 (2017) 93–102. <https://doi.org/10.1016/j.addma.2016.11.006>.

- [12] H.-S. Wang, Y.-L. Kuo, C.-M. Kuo, C.-N. Wei, Microstructural evolution and mechanical properties of hot isostatic pressure bonded CM 247LC superalloy cast, *Materials and Design* 91 (2016) 104–110. <https://doi.org/10.1016/j.matdes.2015.11.102>.
- [13] J. F. Shackelford, W. Alexander, *Materials Science and Engineering Handbook*, 3rd edition, CRC Press, Boca Raton, Florida, USA, 2001. ISBN 0-8493-2696-6.
- [14] J. N. DuPont, J. C. Lippold, S. D. Kiser, *Welding Metallurgy and Weldability of Nickel-Base Alloys*, 1st edition, John Wiley & Sons, Inc., Hoboken, New Jersey, USA, 2009. ISBN 978-0-470-08714-5.
- [15] S. A. David, J. A. Siefert, J. N. DuPont, J. P. Shingledecker, Weldability and weld performance of candidate nickel based superalloys for advanced ultrasupercritical fossil power plants Part I: fundamentals, *Science and Technology of Welding and Joining* 20 (2015) 532–552. <https://doi.org/10.1080/13621718.2016.1143708>.
- [16] C. Slama, C. Servant, G. Cizeron, Aging of the Inconel 718 alloys between 500 and 750°C, *Journal of Materials Research* 12 (1997) 2298–2316. <https://doi.org/10.1557/JMR.1997.0306>.
- [17] A. Lingenfelter, Welding of Inconel Alloy 718: A Historical Overview, in: *Superalloys 718 - Metallurgy and Applications* (Ed.: E. A. Loria), The Minerals, Metals & Materials Society (1989) 673–683. https://doi.org/10.7449/1989/Superalloys_1989_673_683.
- [18] S. T. Wlodek, R. D. Field, The Effects of Long Time Exposure on Alloy 718, in: *Superalloys 718, 625, 706 and Various Derivatives* (Ed.: E. A. Loria), The Minerals, Metals & Materials Society (1994) 659–670. https://doi.org/10.7449/1994/Superalloys_1994_659_670.
- [19] M. Sundararaman, P. Mukhopadhyay, S. Banerjee, Precipitation and Room Temperature Deformation Behaviour of Inconel 718, in: *Superalloys 718, 625, 706 and Various Derivatives* (Ed.: E. A. Loria), The Minerals, Metals & Materials Society (1994) 419–440. https://doi.org/10.7449/1994/Superalloys_1994_419_440.
- [20] J. F. Radavich, The Physical Metallurgy of Cast and Wrought Alloy 718, in: *Superalloys 718 - Metallurgy and Applications* (Ed.: E. A. Loria), The Minerals, Metals & Materials Society (1989) 229–240. https://doi.org/10.7449/1989/Superalloys_1989_229_240.
- [21] A. S. Wilson, Formation and effect of topologically close-packed phases in nickel-base superalloys, *Materials Science and Technology* 33 (2017) 1108–1118. <https://doi.org/10.1080/02670836.2016.1187335>.
- [22] G. Sjöberg, N.-G. Ingesten, R. G. Carlson, Grain Boundary delta-phase Morphologies, Carbides and Notch Rupture Sensitivity of Cast Alloy 718, in: *Superalloys 718, 625 and Various Derivatives* (Ed.: E. A. Loria), The Minerals, Metals & Materials Society (1991) 603–620. https://doi.org/10.7449/1991/Superalloys_1991_603_620.
- [23] S. Azadian, L. Y. Wei, R. Warren, Delta phase precipitation in Inconel 718, *Materials Characterization* 53 (2004) 7–16. <https://doi.org/10.1016/j.matchar.2004.07.004>.
- [24] R. Cozar, A. Pineau, Morphology of Y' and Y'' precipitates and thermal stability of Inconel 718 type alloys, *Metallurgical Transactions* 4 (1973) 47–59. <https://doi.org/10.1007/BF02649604>.

- [25] C. I. Garcia, A. K. Lis, E. A. Loria, A. J. DeArdo, Thermomechanical Processing and Continuous Cooling Transformation Behavior of IN-718, in: *Superalloys 1992: 7th International Symposium on Superalloys* (Ed.: S. D. Antolovich, R. W. Stusrud, R. A. MacKay, D. L. Anton, T. Khan, R. D. Kissinger, D. L. Klarstrom), The Minerals, Metals & Materials Society (1992) 527–536. https://doi.org/10.7449/1992/Superalloys_1992_527_536.
- [26] K. B. Yoo, H. S. Lee, Y. K. Yoon, J. H. Kim, Correlation of the microstructural degradation and mechanical strength of Ni-based superalloy after thermal exposure, *Procedia Engineering* 10 (2011) 2490–2495. <https://doi.org/10.1016/j.proeng.2011.04.410>.
- [27] X. Chen, Z. Yao, J. Dong, H. Shen, Y. Wang, The effect of stress on primary MC carbides degeneration of Waspaloy during long term thermal exposure, *Journal of Alloys and Compounds* 735 (2018) 928–937. <https://doi.org/10.1016/j.jallcom.2017.11.166>.
- [28] S. Gao, J. S. Hou, K. X. Dong, L. Z. Zhou, Influences of cooling rate after solution treatment on microstructural evolution and mechanical properties of superalloy Rene 80, *Acta Metallurgica Sinica (English Letters)* 30 (2017) 261–271. <https://doi.org/10.1007/s40195-016-0500-4>.
- [29] H. A. Shahsavari, A. H. Kokabi, S. Nategh, Effect of preweld microstructure on HAZ liquation cracking of Rene 80 superalloy, *Materials Science and Technology* 23 (2007) 547–555. <https://doi.org/10.1179/174328407X179539>.
- [30] C. Yang, Y. Xu, H. Nie, X. Xiao, G. Jia, Z. Shen, Effects of heat treatments on the microstructure and mechanical properties of Rene 80, *Materials and Design* 43 (2013) 66–73. <https://doi.org/10.1016/j.matdes.2012.06.039>.
- [31] H.-E. Huang, C.-H. Koo, Characteristics and Mechanical Properties of Polycrystalline CM 247 LC Superalloy Casting, *Materials Transactions* 45 (2004) 562–568. <https://doi.org/10.2320/matertrans.45.562>.
- [32] X. Ye, X. Hua, Y. Wu, S. Lou, Precipitates in coarse-grained heat-affected zone of Ni-based 718 superalloy produced by tungsten inert gas welding, *Journal of Materials Processing Technology* 217 (2015) 13–20. <https://doi.org/10.1016/j.jmatprotec.2014.10.021>.
- [33] C.-M. Kuo, Y.-T. Yang, H.-Y. Bor, C.-N. Wei, C.-C. Tai, Aging effects on the microstructure and creep behavior of Inconel 718 superalloy, *Materials Science and Engineering: A* 510–511 (2009) 289–294. <https://doi.org/10.1016/j.msea.2008.04.097>.
- [34] J. X. Yang, Q. Zheng, X. F. Sun, H. R. Guan, Z. Q. Hu, Topologically close-packed phase precipitation in a nickel-base superalloy during thermal exposure, *Materials Science and Engineering A* 465 (2007) 100–108. <https://doi.org/10.1016/j.msea.2007.01.152>.
- [35] R. Krakow, D. N. Johnstone, A. S. Eggeman, D. Hünert, M. C. Hardy, C. M. F. Rae, P. A. Midgley, On the crystallography and composition of topologically close-packed phases in ATI 718Plus[®], *Acta Materialia* 130 (2017) 271–280. <https://doi.org/10.1016/j.actamat.2017.03.038>.
- [36] S.G.K. Manikandan, D. Sivakumar, K. Prasad Rao, M. Kamaraj, Laves phase in alloy 718 fusion zone — microscopic and calorimetric studies, *Materials Characterization* 100 (2015) 192–206. <https://doi.org/10.1016/j.matchar.2014.11.035>.

- [37] Ch. Radhakrishna, K. Prasad Rao, The formation and control of Laves phase in superalloy 718 welds, *Journal of Mater. Sci.* 32 (1997) 1977–1984. <https://doi.org/10.1023/A:1018541915113>.
- [38] X. Cao, B. Rivaux, M. Jahazi, J. Cuddy, A. Birur, Effect of pre- and post-weld heat treatment on metallurgical and tensile properties of Inconel 718 alloy butt joints welded using 4 kW Nd:YAG laser, *Journal of Materials Science* 44 (2009) 4557–4571. <https://doi.org/10.1007/s10853-009-3691-5>.
- [39] G. D. J. Ram, A. V. Reddy, K. P. Rao, G. M. Reddy, Microstructure and mechanical properties of Inconel 718 electron beam welds, *Materials Science and Technology* 21 (2005) 1132–1138. <https://doi.org/10.1179/174328405X62260>.
- [40] J. J. Schirra, R. H. Caless, R. W. Hatala, The effect of laves phases on the mechanical properties of wrought and cast + HIP Inconel 718, in: *Superalloys 718, 625 and Various Derivatives* (Ed.: E. A. Loria), The Minerals, Metals & Materials Society (1991) 375–388. https://doi.org/10.7449/1991/Superalloys_1991_375_388.
- [41] Y. Chen, F. Lu, K. Zhang, P. Nie, S. R. E. Hosseini, K. Feng, Z. Li, P. K. Chu, Investigation of dendritic growth and liquation cracking in laser melting deposited Inconel 718 at different laser input angles, *Materials and Design* 105 (2016) 133–141. <https://doi.org/10.1016/j.matdes.2016.05.034>.
- [42] H. Y. Zhang, S. H. Zhang, M. Cheng, Z. X. Li, Deformation characteristics of δ phase in the delta-processed Inconel 718 alloy, *Materials Characterization* 61 (2010) 49–53. <https://doi.org/10.1016/j.matchar.2009.10.003>.
- [43] A. Niang, B. Viguier, J. Lacaze, Some features of anisothermal solid-state transformations in alloy 718, *Materials Characterization* 61 (2010) 525–534. <https://doi.org/10.1016/j.matchar.2010.02.011>.
- [44] R. M. Nunes, D. Pereira, T. Clarke, T. K. Hirsch, Delta Phase Characterization in Inconel 718 Alloys Through X-ray Diffraction, *ISIJ International* 55 (2015) 2450–2454. <https://doi.org/10.2355/isijinternational.ISIJINT-2015-111>.
- [45] M. Anderson, A.-L. Thielin, F. Bridier, P. Bocher, J. Savoie, δ Phase precipitation in Inconel 718 and associated mechanical properties, *Materials Science & Engineering A* 679 (2017) 48–55. <https://doi.org/10.1016/j.msea.2016.09.114>.
- [46] G. H. Cao, T. Y. Sun, C. H. Wang, X. Li, M. Liu, Z. X. Zhang, P. F. Hu, A. M. Russell, R. Schneider, D. Gerthsen, Z. J. Zhou, C. P. Li, G. F. Chen, Investigations of γ' , γ'' and δ precipitates in heat-treated Inconel 718 alloy fabricated by selective laser melting, *Materials Characterization* 136 (2018) 398–406. <https://doi.org/10.1016/j.matchar.2018.01.006>.
- [47] Y. Rong, S. Chen, H. U. Gengxiang, M. Gao, R. P. Wei, Prediction and characterization of variant electron diffraction patterns for γ'' and δ precipitates in an INCONEL 718 alloy, *Metallurgical and Materials Transactions A* 30 (1999) 2297–2303. <https://doi.org/10.1007/s11661-999-0239-x>.
- [48] N. Vanderesse, M. Anderson, F. Bridier, P. Bocher, Inter- and intragranular delta phase quantitative characterization in Inconel 718 by means of image analysis, *Journal of Microscopy* 261 (2016) 79–87. <https://doi.org/10.1111/jmi.12317>.

- [49] C. Slama, M. Abdellaoui, Structural characterization of the aged Inconel 718, *Journal of Alloys and Compounds* 306 (2000) 277–284. [https://doi.org/10.1016/S0925-8388\(00\)00789-1](https://doi.org/10.1016/S0925-8388(00)00789-1).
- [50] G. A. Rao, M. Kumar, M. Srinivas, D. S. Sarma, Effect of standard heat treatment on the microstructure and mechanical properties of hot isostatically pressed superalloy inconel 718, *Materials Science and Engineering A* 355 (2003) 114–125. [https://doi.org/10.1016/S0921-5093\(03\)00079-0](https://doi.org/10.1016/S0921-5093(03)00079-0).
- [51] I. S. Kim, B. G. Choi, H. U. Hong, Y. S. Yoo, C. Y. Jo, Anomalous deformation behavior and twin formation of Ni-base superalloys at the intermediate temperatures, *Materials Science and Engineering A* 528 (2011) 7149–7155. <https://doi.org/10.1016/j.msea.2011.05.083>.
- [52] J. Safari, S. Nategh, On the heat treatment of Rene-80 nickel-base superalloy, *Journal of Materials Processing Technology* 176 (2006) 240–250. <https://doi.org/10.1016/j.jmatprotec.2006.03.165>.
- [53] D. A. Porter, K. E. Easterling, *Phase Transformations in Metals and Alloys*, 2nd edition, Chapman & Hall, London, UK, 1992. ISBN 978-1-4899-3051-4.
- [54] M. J. Cieslak, G. A. Knorovsky, T. J. Headley, A. D. Romig Jr., The Solidification Metallurgy of Alloy 718 and Other Nb-Containing Superalloys, in: *Superalloys 718 - Metallurgy and Applications* (Ed.: E. A. Loria), The Minerals, Metals & Materials Society (1989), 59–68. https://doi.org/10.7449/1989/Superalloys_1989_59_68.
- [55] G. A. Knorovsky, M. J. Cieslak, T. J. Headley, A. D. Romig, W. F. Hammetter, INCONEL 718: A Solidification Diagram, *Metallurgical Transactions A* 20 (1989) 2149–2158. <https://doi.org/10.1007/BF02650300>.
- [56] S.-H. Kang, Y. Deguchi, K. Yamamoto, K. Ogi, M. Shirai, Solidification Process and Behavior of Alloying Elements in Ni-Based Superalloy Inconel718, *Materials Transactions* 45 (2004) 2728–2733. <https://doi.org/10.2320/matertrans.45.2728>.
- [57] J. S. Lee, J. H. Gu, H. M. Jung, E. H. Kim, Y. G. Jung, J. H. Lee, Directional solidification microstructure control in CM247LC superalloy, *Materials Today: Proceedings* 1 (2014) 3–10. <https://doi.org/10.1016/j.matpr.2014.09.002>.
- [58] D. M. Stefanescu, R. Ruxanda, Fundamentals of Solidification, in: *ASM Handbook*, vol. 9 - Metallography and Microstructures (Ed.: G. F. Vander Voort), ASM International, Materials Park, Ohio, USA, 2004, pp. 71–92. ISBN 978-0-87170-706-2.
- [59] S. Kou, *Welding Metallurgy*, 2nd edition, Chapman & Hall, London, UK, 2003. ISBN 0-471-43491-4.
- [60] W. Kurz, D. J. Fisher, Dendrite growth at the limit of stability: tip radius and spacing, *Acta Metallurgica* 29 (1981) 11–20. [https://doi.org/10.1016/0001-6160\(81\)90082-1](https://doi.org/10.1016/0001-6160(81)90082-1).
- [61] J. N. DuPont, C. V. Robino, J. R. Michael, M. R. Notis, A. R. Marder, Solidification of Nb-Bearing Superalloys: Part I. Reaction Sequences, *Metallurgical and Materials Transactions A* 29 (1998) 2785–2796. <https://doi.org/10.1007/s11661-998-0319-3>.
- [62] J. N. DuPont, C. V. Robino, A. R. Marder, M. R. Notis, Solidification of Nb-bearing superalloys: Part II. Pseudoternary solidification surfaces,

- Metallurgical and Materials Transactions A 29 (1998) 2797–2806.
<https://doi.org/10.1007/s11661-998-0320-x>.
- [63] J. N. Dupont, C. V. Robino, A. R. Marder, Modeling solute redistribution and microstructural development in fusion welds of Nb-bearing superalloys, *Acta Materialia* 46 (1998) 4781–4790.
[https://doi.org/10.1016/S1359-6454\(98\)00123-2](https://doi.org/10.1016/S1359-6454(98)00123-2).
- [64] M. J. Sohrabi, H. Mirzadeh, M. Rafiei, Solidification behavior and Laves phase dissolution during homogenization heat treatment of Inconel 718 superalloy, *Vacuum* 154 (2018) 235–243.
<https://doi.org/10.1016/j.vacuum.2018.05.019>.
- [65] N. Anbarasan, G. Bikash Kumar, S. Prakash, P. Muthukumar, R. Oyyaravelu, R. John Felix Kumar, S. Jerome, Effect of Heat Treatment on the Microstructure and Mechanical Properties of Inconel 718, *Materials Today: Proceedings* 5 (2018) 7716–7724. <https://doi.org/10.1007/s40195-018-0790-9>.
- [66] High temperature high strength nickel base alloys, Nickel Development Institute publication number 393, 1995. Available online: https://www.nickelinstitute.org/media/1700/high_temperaturehigh_strength_nickel_basealloys_393_.pdf (last access: 6th June 2019).
- [67] L. Zheng, G. Schmitz, Y. Meng, R. Chellali, R. Schlesiger, Mechanism of intermediate temperature embrittlement of ni and ni-based superalloys, *Critical Reviews in Solid State and Materials Sciences* 37 (2012) 181–214.
<https://doi.org/10.1080/10408436.2011.613492>.
- [68] L. Y. Sheng, F. Yang, J. T. Guo, T. F. Xi, Anomalous yield and intermediate temperature brittleness behaviors of directionally solidified nickel-based superalloy, *Transactions of Nonferrous Metals Society of China* 24 (2014) 673–681. [https://doi.org/10.1016/S1003-6326\(14\)63110-1](https://doi.org/10.1016/S1003-6326(14)63110-1).
- [69] X. Liang, Y. Yang, B. Shen, B. Cai, F. Huang, Y. Han, L. Qi, M. Gu, X. Xie, The Structure and Mechanical Properties of Alloy 718 DA Disk on Hammer, in: *Superalloys 718, 625, 706 and Various Derivatives* (Ed.: E. A. Loria), The Minerals, Metals & Materials Society (1994) 957–966.
https://doi.org/10.7449/1994/Superalloys_1994_957_966.
- [70] D. Jinhui, L. Xudong, D. Qun, L. Ying, Effect of Solution Treatment on the Microstructure and Mechanical Properties of IN718 Alloy, *Rare Metal Materials and Engineering* 46 (2017) 2359–2365.
[https://doi.org/10.1016/S1875-5372\(17\)30197-2](https://doi.org/10.1016/S1875-5372(17)30197-2).
- [71] G. E. Korth, C. L. Trybus, Tensile Properties and Microstructure of Alloy 718 Thermally Aged to 50,000 Hours, in: *Superalloys 718, 625 and Various Derivatives* (Ed.: E. A. Loria), The Minerals, Metals & Materials Society (1991) 437–446.
https://doi.org/10.7449/1991/Superalloys_1991_437_446.
- [72] B. Pieraggi, J. F. Uginet, Fatigue and Creep Properties in Relation with Alloy 718 Microstructure, in: *Superalloys 718, 625, 706 and Various Derivatives* (Ed.: E. A. Loria), The Minerals, Metals & Materials Society (1994) 535–544. https://doi.org/10.7449/1994/Superalloys_1994_535_544.
- [73] L.-C. Yang, Y.-T. Pan, I.-G. Chen, D.-Y. Lin, Constitutive Relationship Modeling and Characterization of Flow Behavior under Hot Working for Fe–Cr–Ni–W–Cu–Co Super-Austenitic Stainless Steel, *Metals* 5 (2015) 1717–1731. <https://doi.org/10.3390/met5031717>.

- [74] A. Thomas, M. El-Wahabi, J. M. Cabrera, J. M. Prado, High temperature deformation of Inconel 718, *Journal of Materials Processing Technology* 177 (2006) 469–472. <https://doi.org/10.1016/j.jmatprotec.2006.04.072>.
- [75] W. Chen, M. C. Chaturvedi, The Influence of Grain Boundary Precipitates on Creep Fracture of Inconel 718, in: *Superalloys 718, 625, 706 and Various Derivatives* (Ed.: E. A. Loria), The Minerals, Metals & Materials Society (1994) 567–577. https://doi.org/10.7449/1994/Superalloys_1994_567_577.
- [76] D. Fournier, A. Pineau, Low cycle fatigue behavior of inconel 718 at 298 K and 823 K, *Metallurgical Transactions A* 8 (1977) 1095–1105. <https://doi.org/10.1007/BF02667395>.
- [77] D. Gustafsson, J. Moverare, K. Simonsson, S. Johansson, M. Hörnqvist, T. Månsson, S. Sjöström, Fatigue crack growth behaviour of Inconel 718 - The concept of a damaged zone caused by high temperature hold times, *Procedia Engineering* 10 (2011) 2821–2826. <https://doi.org/10.1016/j.proeng.2011.04.469>.
- [78] M. Jambor, O. Bokůvka, F. Nový, L. Trško, J. Belan, Phase Transformations in Nickel base Superalloy Inconel 718 during Cyclic Loading at High Temperature, *Production Engineering Archives* 15 (2017) 15–18. <https://doi.org/10.30657/pea.2017.15.04>.
- [79] C. S. Giggins, F. S. Pettit, Oxidation of Ni-Cr-Al Alloys Between 1000° and 1200°C, *Journal of The Electrochemical Society* 118 (1971) 1782–1790. <https://doi.org/10.1149/1.2407837>.
- [80] Dissemination of IT for the Promotion of Materials Science (DoITPoMS) - TLP Library Ellingham Diagrams - The interactive Ellingham diagram, University of Cambridge. Available online: https://www.doitpoms.ac.uk/tlplib/ellingham_diagrams/interactive.php (last access: 6th June 2019).
- [81] H. A. Miley, Theory of Oxidation and Tarnishing of Metals. I. The Linear, Parabolic and Logarithmic Laws, *Journal of The Electrochemical Society* 81 (1942) 391–411. <https://doi.org/10.1149/1.3071387>.
- [82] C. Wagner, The formation of thin oxide films on metals, *Corrosion Science* 13 (1973) 23–52. [https://doi.org/10.1016/0010-938X\(73\)90047-4](https://doi.org/10.1016/0010-938X(73)90047-4).
- [83] G. A. Greene, C. C. Finfrock, Oxidation of Inconel 718 in Air at High Temperatures, *Oxidation of Metals* 55 (2001) 505–521. <https://doi.org/10.1023/A:1010359815550>.
- [84] D. Caplan, M. Cohen, The Volatilization of Chromium Oxide, *Journal of The Electrochemical Society* 108 (1961) 438–442. <https://doi.org/10.1149/1.2428106>.
- [85] C. S. Tedmon Jr., The Effect of Oxide Volatilization on the Oxidation Kinetics of Cr and Fe-Cr Alloys, *Journal of The Electrochemical Society* 113 (1966) 766–768. <https://doi.org/10.1149/1.2424115>.
- [86] F. Delaunay, C. Berthier, M. Lenglet, J.-M. Lameille, SEM-EDS and XPS Studies of the High Temperature Oxidation Behaviour of Inconel 718, *Microchimica Acta* 132 (2000) 337–343. <https://doi.org/10.1007/s006040050027>.
- [87] K. A. Al-Hatab, M. A. Al-Bukhaiti, U. Krupp, M. Kantehm, Cyclic oxidation behavior of in 718 superalloy in air at high temperatures, *Oxidation of Metals* 75 (2011) 209–228. <https://doi.org/10.1007/s11085-010-9230-6>.

- [88] V. B. Trindade, U. Krupp, P. E. G. Wagenhuber, H. J. Christ, Oxidation mechanisms of Cr-containing steels and Ni-base alloys at high-temperatures - Part I: The different role of alloy grain boundaries, *Materials and Corrosion* 56 (2005) 785–790. <https://doi.org/10.1002/maco.200503879>.
- [89] D. M. England, A. V. Virkar, Oxidation Kinetics of Some Nickel-Based Superalloy Foils and Electronic Resistance of the Oxide Scale Formed in Air Part I, *Journal of The Electrochemical Society* 146 (1999) 3196–3202. <https://doi.org/10.1149/1.1392454>.
- [90] Q. Jia, D. Gu, Selective laser melting additive manufactured Inconel 718 superalloy parts: High-temperature oxidation property and its mechanisms, *Optics and Laser Technology* 62 (2014) 161–171. <https://doi.org/10.1016/j.optlastec.2014.03.008>.
- [91] S. P. Jiang, X. Chen, Chromium deposition and poisoning of cathodes of solid oxide fuel cells - A review, *International Journal of Hydrogen Energy* 39 (2013) 505–531. <https://doi.org/10.1016/j.ijhydene.2013.10.042>.
- [92] Z. D. Xiang, P. K. Datta, Relationship between pack chemistry and aluminide coating formation for low-temperature aluminisation of alloy steels, *Acta Materialia* 54 (2006) 4453–4463. <https://doi.org/10.1016/j.actamat.2006.05.032>.
- [93] A. Naji, M. C. Galetz, M. Schütze, Design model for diffusion coatings formed via pack cementation, *Materials and Corrosion* 65 (2014) 312–318. <https://doi.org/10.1002/maco.201307393>.
- [94] Y.Q. Wang, Y. Zhang, D.A. Wilson, Formation of Aluminide Coatings on Ferritic–Martensitic Steels by a Low-Temperature Pack Cementation Process, *Surface & Coatings Technology* 204 (2010) 2737–2744. <https://doi.org/https://doi.org/10.1016/j.surfcoat.2010.02.025>.
- [95] H.R. K. Zarchi, M. Soltanieh, M.R. Aboutalebi, X. Guo, Kinetic study on NaF-activated pack-aluminizing of pure titanium at 950–1100 °C, *Transactions of Nonferrous Metals Society of China* 24 (2014) 1959–1968. [https://doi.org/10.1016/S1003-6326\(14\)63277-5](https://doi.org/10.1016/S1003-6326(14)63277-5).
- [96] R. Bianco, R. A. Rapp, Pack Cementation Aluminide Coatings on Superalloys: Codeposition of Cr and Reactive Elements, *Journal of The Electrochemical Society* 140 (1993) 1181. <https://doi.org/10.1149/1.2056219>.
- [97] F. Bozza, G. Bolelli, C. Giolli, A. Giorgetti, L. Lusvardi, P. Sassatelli, A. Scrivani, A. Candeli, M. Thoma, Diffusion mechanisms and microstructure development in pack aluminizing of Ni-based alloys, *Surface & Coatings Technology* 239 (2014) 147–159. <https://doi.org/10.1016/j.surfcoat.2013.11.034>.
- [98] G. F. Slattery, Microstructural aspects of aluminized coatings on nickel-base alloys, *Metals Technology* 10 (1983) 41–51. <https://doi.org/10.1179/030716983803291325>.
- [99] Z. Zhan, Z. Liu, J. Liu, L. Li, Z. Li, P. Liao, Microstructure and high-temperature corrosion behaviors of aluminide coatings by low-temperature pack aluminizing process, *Applied Surface Science* 256 (2010) 3874–3879. <https://doi.org/10.1016/j.apsusc.2010.01.043>.
- [100] R. Mévrel, C. Duret, R. Pichoir, Pack cementation processes, *Materials Science and Technology* 2 (1986) 201–206. <https://doi.org/10.1179/026708386790123297>.

- [101] A. M. Hodge, D. C. Dunand, Synthesis of nickel-aluminide foams by pack-aluminization of nickel foams, *Intermetallics* 9 (2001) 581–589. [https://doi.org/10.1016/S0966-9795\(01\)00047-4](https://doi.org/10.1016/S0966-9795(01)00047-4).
- [102] Q. Pang, G. H. Wu, D. L. Sun, Z. Y. Xiu, L. T. Jiang, A dual-layer Ce-Cr/Al oxidation resistant coating for 3D open-cell nickel based foams by a two-step pack cementation, *Materials Science and Engineering A* 568 (2013) 228–238. <https://doi.org/10.1016/j.msea.2013.01.032>.
- [103] H. Omar, D. P. Papadopoulos, S. A. Tsipas, H. Lefakis, Aluminizing nickel foam by a slurry coating process, *Materials Letters* 63 (2009) 1387–1389. <https://doi.org/10.1016/j.matlet.2009.02.069>.
- [104] H. Okamoto, Al-Ni (Aluminum-Nickel), *Journal of Phase Equilibria and Diffusion* 25 (2004) 394. <https://doi.org/10.1007/s11669-004-0163-0>.
- [105] C. Houngrinou, S. Chevalier, J. P. Larpin, Synthesis and characterisation of pack cemented aluminide coatings on metals, *Applied Surface Science* 236 (2004) 256–269. <https://doi.org/10.1016/j.apsusc.2004.04.026>.
- [106] J. W. Lee, Y. C. Kuo, A study on the microstructure and cyclic oxidation behavior of the pack aluminized Hastelloy X at 1100 °C, *Surface & Coatings Technology* 201 (2006) 3867–3871. <https://doi.org/10.1016/j.surcoat.2006.07.257>.
- [107] G. W. Goward, D. H. Boone, Mechanisms of formation of diffusion aluminide coatings on nickel-base superalloys, *Oxidation of Metals* 3 (1971) 475–495. <https://doi.org/10.1007/BF00604047>.
- [108] ASTM B875–96, Standard Specification for Aluminum Diffusion Coating Applied by Pack Cementation Process, 2003.
- [109] J. R. Nicholls, K. A. Long, N. J. Simms, Diffusion coatings, in: *Shreir's Corrosion*, vol. 4, Elsevier, Oxford, UK, 2010, pp. 2532–2555. <https://doi.org/10.1016/B978-044452787-5.00176-1>.
- [110] O. K. Das, V. Singh, S. V. Joshi, Evolution of aluminide coating microstructure on nickel-base cast superalloy CM-247 in a single-step high-activity aluminizing process, *Metallurgical and Materials Transactions A* 29 (1998) 2173–2188. <https://doi.org/10.1007/s11661-998-0042-0>.
- [111] S. Kim, Y. A. Chang, An Interdiffusion Study of a NiAl Alloy Using Single-Phase Diffusion Couples, *Metallurgical and Materials Transactions A* 31 (2000) 1519–1524. <https://doi.org/10.1007/s11661-000-0162-7>.
- [112] H. Wei, X. Sun, Q. Zheng, G. Hou, H. Guan, Z. Hu, An inverse method for determination of the interdiffusivity in aluminide coatings formed on superalloy, *Surface & Coatings Technology* 182 (2004) 112–116. [https://doi.org/10.1016/S0257-8972\(03\)00879-X](https://doi.org/10.1016/S0257-8972(03)00879-X).
- [113] S. Shankar, L. L. Seigle, Interdiffusion and Intrinsic Diffusion in the NiAl (δ) Phase of the Al-Ni System, *Metallurgical Transactions A* 9 (1978) 1467–1476. <https://doi.org/10.1007/BF02661819>.
- [114] H. Wei, H. Y. Zhang, G. C. Hou, X. F. Sun, M. S. Dargusch, X. Yao, Z. Q. Hu, On interdiffusion in the multicomponent β -NiAl phase, *Journal of Alloys and Compounds* 481 (2009) 326–335. <https://doi.org/10.1016/j.jallcom.2009.02.130>.
- [115] C. Herzig, S. Divinski, Essentials in diffusion behavior of nickel- and titanium-aluminides, *Intermetallics* 12 (2004) 993–1003. <https://doi.org/10.1016/j.intermet.2004.03.005>.
- [116] R. Nakamura, K. Fujita, Y. Iijima, M. Okada, Diffusion mechanisms in B2 NiAl phase studied by experiments on Kirkendall effect and interdiffusion

- under high pressures, *Acta Materialia* 51 (2003) 3861–3870.
[https://doi.org/10.1016/S1359-6454\(03\)00210-6](https://doi.org/10.1016/S1359-6454(03)00210-6).
- [117] A. Paul, A. A. Kodentsov, F. J. J. van Loo, On diffusion in the β -NiAl phase, *Journal of Alloys and Compounds* 403 (2005) 147–153.
<https://doi.org/10.1016/j.jallcom.2005.04.194>.
- [118] Z. D. Xiang, J. S. Burnell-Gray, P. K. Datta, Aluminide coating formation on nickel-base superalloys by pack cementation process, *Journal of Materials Science* 36 (2001) 5673–5682.
<https://doi.org/10.1023/A:1012534220165>.
- [119] Z. D. Xiang, P. K. Datta, Codeposition of Al and Si on nickel base superalloys by pack cementation process, *Materials Science and Engineering A* 356 (2003) 136–144. [https://doi.org/10.1016/S0921-5093\(03\)00107-2](https://doi.org/10.1016/S0921-5093(03)00107-2).
- [120] L. Tong, Y. Dengzun, Z. Chungen, Low-temperature Formation of Aluminide Coatings on Ni-base Superalloys by Pack Cementation Process, *Chinese Journal of Aeronautics* 23 (2010) 381–385.
[https://doi.org/10.1016/S1000-9361\(09\)60231-4](https://doi.org/10.1016/S1000-9361(09)60231-4).
- [121] X. Yan, P. Gu, A review of rapid prototyping technologies and systems, *Computer-Aided Design* 28 (1996) 307–318. [https://doi.org/10.1016/0010-4485\(95\)00035-6](https://doi.org/10.1016/0010-4485(95)00035-6).
- [122] F. P. W. Melchels, J. Feijen, D. W. Grijpma, A review on stereolithography and its applications in biomedical engineering, *Biomaterials* 31 (2010) 6121–6130. <https://doi.org/10.1016/j.biomaterials.2010.04.050>.
- [123] K. P. Karunakaran, A. Bernard, S. Suryakumar, L. Dembinski, G. Taillandier, Rapid manufacturing of metallic objects, *Rapid Prototyping Journal* 18 (2012) 264–280. <https://doi.org/10.1108/13552541211231644>.
- [124] A. Zocca, P. Colombo, C. M. Gomes, J. Günster, Additive Manufacturing of Ceramics: Issues, Potentialities, and Opportunities, *Journal of the American Ceramic Society* 98 (2015) 1983–2001.
<https://doi.org/10.1111/jace.13700>.
- [125] S. Kumar, J. P. Kruth, Composites by rapid prototyping technology, *Materials and Design* 31 (2010) 850–856.
<https://doi.org/10.1016/j.matdes.2009.07.045>.
- [126] W. J. Sames, F. A. List, S. Pannala, R. R. Dehoff, S. S. Babu, The metallurgy and processing science of metal additive manufacturing, *International Materials Reviews* 61 (2016) 315–360.
<https://doi.org/10.1080/09506608.2015.1116649>.
- [127] S. Seetharaman, M. Krishnan, F. G. C. Wen, N. A. Khan, G. N. K. Lai, Research Updates on the Additive Manufacturing of Nickel Based Superalloys, in: *Solid Freeform Fabrication Symposium*, The University of Texas at Austin, USA (2016) 469–486. Available online: <http://sffsymposium.engr.utexas.edu/sites/default/files/2016/034-Seetharaman.pdf> (last access: 6th June 2019).
- [128] A. Heralić, A. K. Christiansson, B. Lennartson, Height control of laser metal-wire deposition based on iterative learning control and 3D scanning, *Optics and Lasers in Engineering* 50 (2012) 1230–1241.
<https://doi.org/10.1016/j.optlaseng.2012.03.016>.
- [129] J. Park, M. J. Tari, H. T. Hahn, Characterization of the laminated object manufacturing (LOM) process, *Rapid Prototyping Journal* 6 (2000) 36–49.
<https://doi.org/10.1108/13552540010309868>.

- [130] C. Y. Kong, R. C. Soar, P. M. Dickens, Characterisation of aluminium alloy 6061 for the ultrasonic consolidation process, *Materials Science and Engineering A* 363 (2003) 99–106. [https://doi.org/10.1016/S0921-5093\(03\)00590-2](https://doi.org/10.1016/S0921-5093(03)00590-2).
- [131] M. Agarwala, D. Bourell, J. Beaman, H. Marcus, J. Barlow, Direct selective laser sintering of metals, *Rapid Prototyping Journal* 1 (1995) 26–36. <https://doi.org/10.1108/13552549510078113>.
- [132] J.P. Kruth, X. Wang, T. Laoui, L. Froyen, Lasers and materials in selective laser sintering, *Assembly Automation* 23 (2003) 357–371. <https://doi.org/10.1108/01445150310698652>.
- [133] J. P. Kruth, L. Froyen, J. Van Vaerenbergh, P. Mercelis, M. Rombouts, B. Lauwers, Selective laser melting of iron-based powder, *Journal of Materials Processing Technology* 149 (2004) 616–622. <https://doi.org/10.1016/j.jmatprotec.2003.11.051>.
- [134] L. E. Murr, S. M. Gaytan, A. Ceylan, E. Martinez, J. L. Martinez, D. H. Hernandez, B. I. Machado, D. A. Ramirez, F. Medina, S. Collins, R. B. Wicker, Characterization of titanium aluminide alloy components fabricated by additive manufacturing using electron beam melting, *Acta Materialia* 58 (2010) 1887–1894. <https://doi.org/10.1016/j.actamat.2009.11.032>.
- [135] C. Atwood, M. Griffith, L. Harwell, E. Schlienger, M. Ensz, J. Smugeresky, T. Romero, D. Greene, D. Reckaway, Laser engineered net shaping (LENSTM): A tool for direct fabrication of metal parts, in: *International Congress on Applications of Lasers & Electro-Optics*, Laser Institute of America, Orlando, Florida, USA (1998) 1–7. <https://doi.org/10.2351/1.5059147>.
- [136] M. L. Griffith, D. M. Keicher, C. L. Atwood, J. A. Romero, J. E. Smugeresky, L. D. Harwell, D. L. Greene, Free form fabrication of metallic components using laser engineered net shaping (LENSTM), in: *Solid Freeform Fabrication Symposium*, The University of Texas at Austin, USA (1996) 125–131. <http://hdl.handle.net/2152/69929>.
- [137] C. Y. Yap, C. K. Chua, Z. L. Dong, Z. H. Liu, D. Q. Zhang, L. E. Loh, S. L. Sing, Review of selective laser melting: Materials and applications, *Applied Physics Reviews* 2 (2015) 1–21. <https://doi.org/10.1063/1.4935926>.
- [138] A. Simchi, Direct laser sintering of metal powders: Mechanism, kinetics and microstructural features, *Materials Science and Engineering A* 428 (2006) 148–158. <https://doi.org/10.1016/j.msea.2006.04.117>.
- [139] W. Shifeng, L. Shuai, W. Qingsong, C. Yan, Z. Sheng, S. Yusheng, Effect of molten pool boundaries on the mechanical properties of selective laser melting parts, *Journal of Materials Processing Technology* 214 (2014) 2660–2667. <https://doi.org/10.1016/j.jmatprotec.2014.06.002>.
- [140] Z. Wang, K. Guan, M. Gao, X. Li, X. Chen, X. Zeng, The microstructure and mechanical properties of deposited-IN718 by selective laser melting, *Journal of Alloys and Compounds* 513 (2012) 518–523. <https://doi.org/10.1016/j.jallcom.2011.10.107>.
- [141] M. Xia, D. Gu, G. Yu, D. Dai, H. Chen, Q. Shi, Selective laser melting 3D printing of Ni-based superalloy: understanding thermodynamic mechanisms, *Science Bulletin* 61 (2016) 1013–1022. <https://doi.org/10.1007/s11434-016-1098-7>.

- [142] Q. Jia, D. Gu, Selective laser melting additive manufacturing of Inconel 718 superalloy parts: Densification, microstructure and properties, *Journal of Alloys and Compounds* 585 (2014) 713–721. <https://doi.org/10.1016/j.jallcom.2013.09.171>.
- [143] H. Gong, H. Gu, K. Zeng, J. J. S. Dilip, D. Pal, B. Stucker, D. Christiansen, J. Beuth, J. J. Lewandowski, Melt pool characterization for selective laser melting of Ti-6Al-4V pre-alloyed powder, in: *Solid Freeform Fabrication Symposium, The University of Texas at Austin, USA* (2014) 256–267. Available online: <http://sffsymposium.engr.utexas.edu/sites/default/files/2014-022-Gong.pdf> (last access: 6th June 2019).
- [144] K. Moussaoui, W. Rubio, M. Mousseigne, T. Sultan, F. Rezai, Effects of Selective Laser Melting additive manufacturing parameters of Inconel 718 on porosity, microstructure and mechanical properties, *Materials Science and Engineering A* 735 (2018) 182–190. <https://doi.org/10.1016/j.msea.2018.08.037>.
- [145] L. N. Carter, M. M. Attallah, R. C. Reed, Laser Powder Bed Fabrication of Nickel-Base Superalloys: Influence of Parameters; Characterisation, Quantification and Mitigation of Cracking, in: *Superalloys 2012: 12th International Symposium on Superalloys* (Ed.: E. S. Huron, R. C. Reed, M. C. Hardy, M. J. Mills, R. E. Montero, P. D. Portella, J. Telesman), The Minerals, Metals & Materials Society (2012) 577–586. <https://doi.org/10.1002/9781118516430.ch64>.
- [146] B. Zhang, Y. Li, Q. Bai, Defect Formation Mechanisms in Selective Laser Melting: A Review, *Chinese Journal of Mechanical Engineering (English Edition)* 30 (2017) 515–527. <https://doi.org/10.1007/s10033-017-0121-5>.
- [147] P. Mercelis, J. P. Kruth, Residual stresses in selective laser sintering and selective laser melting, *Rapid Prototyping Journal* 12 (2006) 254–265. <https://doi.org/10.1108/13552540610707013>.
- [148] I. A. Roberts, C. J. Wang, R. Esterlein, M. Stanford, D. J. Mynors, A three-dimensional finite element analysis of the temperature field during laser melting of metal powders in additive layer manufacturing, *International Journal of Machine Tools and Manufacture* 49 (2009) 916–923. <https://doi.org/10.1016/j.ijmachtools.2009.07.004>.
- [149] M. Shiomi, K. Osakada, K. Nakamura, T. Yamashita, F. Abe, Residual stress within metallic model made by selective laser melting process, *CIRP Annals* 53 (2004) 195–198. [https://doi.org/10.1016/S0007-8506\(07\)60677-5](https://doi.org/10.1016/S0007-8506(07)60677-5).
- [150] H. Ali, H. Ghadbeigi, K. Mumtaz, Effect of scanning strategies on residual stress and mechanical properties of Selective Laser Melted Ti6Al4V, *Materials Science & Engineering A* 712 (2018) 175–187. <https://doi.org/10.1016/j.msea.2017.11.103>.
- [151] H. Y. Wan, Z. J. Zhou, C. P. Li, G. F. Chen, G. P. Zhang, Effect of scanning strategy on grain structure and crystallographic texture of Inconel 718 processed by selective laser melting, *Journal of Materials Science & Technology* 34 (2018) 1799–1804. <https://doi.org/10.1016/j.jmst.2018.02.002>.
- [152] L. N. Carter, C. Martin, P. J. Withers, M. M. Attallah, The influence of the laser scan strategy on grain structure and cracking behaviour in SLM

- powder-bed fabricated nickel superalloy, *Journal of Alloys and Compounds* 615 (2014) 338–347. <https://doi.org/10.1016/j.jallcom.2014.06.172>.
- [153] M. M. Kirka, P. Nandwana, Y. Lee, R. R. Dehoff, Solidification and solid-state transformation sciences in metals additive manufacturing, *Scripta Materialia* 135 (2017) 130–134. <https://doi.org/10.1016/j.scriptamat.2017.01.005>.
- [154] J. P. Choi, G. H. Shin, S. Yang, D. Y. Yang, J. S. Lee, M. Brochu, J. H. Yu, Densification and microstructural investigation of Inconel 718 parts fabricated by selective laser melting, *Powder Technology* 310 (2017) 60–66. <https://doi.org/10.1016/j.powtec.2017.01.030>.
- [155] X. Gong, K. Chou, Microstructures of Inconel 718 by Selective Laser Melting, in: *TMS 2015 144th Annual Meeting & Exhibition: Supplemental Proceedings*, The Minerals, Metals & Materials Society (2015) 461–468. https://doi.org/10.1007/978-3-319-48127-2_58.
- [156] Y. L. Kuo, S. Horikawa, K. Kakehi, The effect of interdendritic δ phase on the mechanical properties of Alloy 718 built up by additive manufacturing, *Materials and Design* 116 (2017) 411–418. <https://doi.org/10.1016/j.matdes.2016.12.026>.
- [157] X. Wang, K. Chou, Effects of thermal cycles on the microstructure evolution of Inconel 718 during selective laser melting process, *Additive Manufacturing* 18 (2017) 1–14. <https://doi.org/10.1016/j.addma.2017.08.016>.
- [158] V. A. Popovich, E. V. Borisov, A. A. Popovich, V. Sh. Sufiiarov, D. V. Masaylo, L. Alzina, Functionally graded Inconel 718 processed by additive manufacturing: Crystallographic texture, anisotropy of microstructure and mechanical properties, *Materials and Design* 114 (2017) 441–449. <https://doi.org/10.1016/j.matdes.2016.10.075>.
- [159] K. N. Amato, S. M. Gaytan, L. E. Murr, E. Martinez, P. W. Shindo, J. Hernandez, S. Collins, F. Medina, Microstructures and mechanical behavior of Inconel 718 fabricated by selective laser melting, *Acta Materialia* 60 (2012) 2229–2239. <https://doi.org/10.1016/j.actamat.2011.12.032>.
- [160] D. Deng, R. L. Peng, H. Brodin, J. Moverare, Microstructure and mechanical properties of Inconel 718 produced by selective laser melting: Sample orientation dependence and effects of post heat treatments, *Materials Science & Engineering A* 713 (2018) 294–306. <https://doi.org/10.1016/j.msea.2017.12.043>.
- [161] D. H. Smith, J. Bicknell, L. Jorgensen, B. M. Patterson, N. L. Cordes, I. Tsukrov, M. Knezevic, Microstructure and mechanical behavior of direct metal laser sintered Inconel alloy 718, *Materials Characterization* 113 (2016) 1–9. <https://doi.org/10.1016/j.matchar.2016.01.003>.
- [162] F. Liu, X. Lin, C. Huang, M. Song, G. Yang, J. Chen, W. Huang, The effect of laser scanning path on microstructures and mechanical properties of laser solid formed nickel-base superalloy Inconel 718, *Journal of Alloys and Compounds* 509 (2011) 4505–4509. <https://doi.org/10.1016/j.jallcom.2010.11.176>.
- [163] F. Liu, X. Lin, G. Yang, M. Song, J. Chen, W. Huang, Microstructure and residual stress of laser rapid formed Inconel 718 nickel-base superalloy, *Optics and Laser Technology* 43 (2011) 208–213. <https://doi.org/10.1016/j.optlastec.2010.06.015>.

- [164] J. Cao, F. Liu, X. Lin, C. Huang, J. Chen, W. Huang, Effect of overlap rate on recrystallization behaviors of Laser Solid Formed Inconel 718 superalloy, *Optics and Laser Technology* 45 (2013) 228–235. <https://doi.org/10.1016/j.optlastec.2012.06.043>.
- [165] G. P. Dinda, A. K. Dasgupta, J. Mazumder, Texture control during laser deposition of nickel-based superalloy, *Scripta Materialia* 67 (2012) 503–506. <https://doi.org/10.1016/j.scriptamat.2012.06.014>.
- [166] L. L. Parimi, G. Ravi, D. Clark, M. M. Attallah, Microstructural and texture development in direct laser fabricated IN718, *Materials Characterization* 89 (2014) 102–111. <https://doi.org/10.1016/j.matchar.2013.12.012>.
- [167] R. J. Moat, A. J. Pinkerton, L. Li, P. J. Withers, M. Preuss, Crystallographic texture and microstructure of pulsed diode laser-deposited Waspaloy, *Acta Materialia* 57 (2009) 1220–1229. <https://doi.org/10.1016/j.actamat.2008.11.004>.
- [168] R. Muñoz-Moreno, V. D. Divya, S. L. Driver, O. M. D. M. Messé, T. Illston, S. Baker, M. A. Carpenter, H. J. Stone, Effect of heat treatment on the microstructure, texture and elastic anisotropy of the nickel-based superalloy CM247LC processed by selective laser melting, *Materials Science and Engineering A* 674 (2016) 529–539. <https://doi.org/10.1016/j.msea.2016.06.075>.
- [169] V. D. Divya, R. Muñoz-Moreno, O. M. D. M. Messé, J. S. Barnard, S. Baker, T. Illston, H. J. Stone, Microstructure of selective laser melted CM247LC nickel-based superalloy and its evolution through heat treatment, *Materials Characterization* 114 (2016) 62–74. <https://doi.org/10.1016/j.matchar.2016.02.004>.
- [170] L. E. Murr, E. Martinez, X. M. Pan, S. M. Gaytan, J. A. Castro, C. A. Terrazas, F. Medina, R. B. Wicker, D. H. Abbott, Microstructures of Rene 142 nickel-based superalloy fabricated by electron beam melting, *Acta Materialia* 61 (2013) 4289–4296. <https://doi.org/10.1016/j.actamat.2013.04.002>.
- [171] P. Kanagarajah, F. Brenne, T. Niendorf, H. J. Maier, Inconel 939 processed by selective laser melting: Effect of microstructure and temperature on the mechanical properties under static and cyclic loading, *Materials Science and Engineering A* 588 (2013) 188–195. <https://doi.org/10.1016/j.msea.2013.09.025>.
- [172] X. Wang, L. N. Carter, B. Pang, M. M. Attallah, M. H. Loretto, Microstructure and yield strength of SLM-fabricated CM247LC Ni-Superalloy, *Acta Materialia* 128 (2017) 87–95. <https://doi.org/10.1016/j.actamat.2017.02.007>.
- [173] L. Shuai, W. Qingsong, D. Q. Zhang, C. C. Kai, Microstructures and Texture of Inconel 718 Alloy Fabricated by Selective Laser Melting, in: 1st International Conference on Progress in Additive Manufacturing (Ed.: C. C. Kai, Y. W. Yee, T. M. Jen, L. Erjia), Singapore (2014) 139–144. <https://doi.org/10.3850/978-981-09-0446-3>.
- [174] D. Ma, A. D. Stoica, Z. Wang, A. M. Beese, Crystallographic texture in an additively manufactured nickel-base superalloy, *Materials Science & Engineering A* 684 (2017) 47–53. <https://doi.org/10.1016/j.msea.2016.12.028>.
- [175] E. Chlebus, K. Gruber, B. Kuźnicka, J. Kurzac, T. Kurzynowski, Effect of heat treatment on microstructure and mechanical properties of Inconel 718

- processed by selective laser melting, *Materials Science and Engineering: A* 639 (2015) 647–655. <https://doi.org/10.1016/j.msea.2015.05.035>.
- [176] J. Strößner, M. Terock, U. Glatzel, Mechanical and Microstructural Investigation of Nickel-Based Superalloy IN718 Manufactured by Selective Laser Melting (SLM), *Advanced Engineering Materials* 17 (2015) 1099–1105. <https://doi.org/10.1002/adem.201500158>.
- [177] Y. Tian, D. McAllister, H. Colijn, M. Mills, D. Farson, M. Nordin, S. Babu, Rationalization of microstructure heterogeneity in INCONEL 718 builds made by the direct laser additive manufacturing process, *Metallurgical and Materials Transactions A* 45 (2014) 4470–4483. <https://doi.org/10.1007/s11661-014-2370-6>.
- [178] A. Mostafa, I. P. Rubio, V. Brailovski, M. Jahazi, M. Medraj, Structure, Texture and Phases in 3D Printed IN718 Alloy Subjected to Homogenization and HIP Treatments, *Metals* 7 (2017) 1–23. <https://doi.org/10.3390/met7060196>.
- [179] V. A. Popovich, E. V. Borisov, A. A. Popovich, V. Sh. Sufiarov, D. V. Masaylo, L. Alzina, Impact of heat treatment on mechanical behaviour of Inconel 718 processed with tailored microstructure by selective laser melting, *Materials & Design* 131 (2017) 12–22. <https://doi.org/10.1016/j.matdes.2017.05.065>.
- [180] D. Zhang, W. Niu, X. Cao, Z. Liu, Effect of standard heat treatment on the microstructure and mechanical properties of selective laser melting manufactured Inconel 718 superalloy, *Materials Science and Engineering: A* 644 (2015) 32–40. <https://doi.org/https://doi.org/10.1016/j.msea.2015.06.021>.
- [181] S. Sui, J. Chen, E. Fan, H. Yang, X. Lin, W. Huang, The influence of Laves phases on the high-cycle fatigue behavior of laser additive manufactured Inconel 718, *Materials Science & Engineering A* 695 (2017) 6–13. <https://doi.org/10.1016/j.msea.2017.03.098>.
- [182] B. Farber, K. A. Small, C. Allen, R. J. Causton, A. Nichols, J. Simbolick, M. L. Taheri, Correlation of mechanical properties to microstructure in Inconel 718 fabricated by Direct Metal Laser Sintering, *Materials Science & Engineering A* 712 (2018) 539–547. <https://doi.org/10.1016/j.msea.2017.11.125>.
- [183] W. M. Tucho, P. Cuvillier, A. Sjolyst-Kverneland, V. Hansen, Microstructure and hardness studies of Inconel 718 manufactured by selective laser melting before and after solution heat treatment, *Materials Science and Engineering A* 689 (2017) 220–232. <https://doi.org/10.1016/j.msea.2017.02.062>.
- [184] T. Trosch, J. Strößner, R. Völkl, U. Glatzel, Microstructure and mechanical properties of selective laser melted Inconel 718 compared to forging and casting, *Materials Letters* 164 (2016) 428–431. <https://doi.org/10.1016/j.matlet.2015.10.136>.
- [185] EOS NickelAlloy IN718, in: EOS GmbH - Electro Optical Systems (www.eos.info), Material data sheet, 2014. Available online: http://ip-saas-eos-cms.s3.amazonaws.com/public/4528b4a1bf688496/ff974161c2057e6df56db5b67f0f5595/EOS_NickelAlloy_IN718_en.pdf (last access: 6th June 2019).

- [186] M. Calandri, S. Yin, B. Aldwell, F. Calignano, R. Lupoi, D. Ugues, Texture and Microstructural Features at Different Length Scales in Inconel 718 Produced by Selective Laser Melting, *Materials* 12 (2019) 1–32. <https://doi.org/10.3390/ma12081293>.
- [187] D. Manfredi, F. Calignano, M. Krishnan, R. Canali, E. P. Ambrosio, E. Atzeni, From powders to dense metal parts: Characterization of a commercial alsiing alloy processed through direct metal laser sintering, *Materials* 6 (2013) 856–869. <https://doi.org/10.3390/ma6030856>.
- [188] D. C. Montgomery, *Progettazione e analisi degli esperimenti*, 1st edition, McGraw Hill, Milano, Italia, 2005. ISBN-13 978-8838661792.
- [189] ASTM B962-17, Standard Test Methods for Density of Compacted or Sintered Powder Metallurgy (PM) Products Using Archimedes' Principle, 2017
- [190] X. J. Pang, D. J. Dwyer, M. Gao, P. Valerio, R. P. Wei, Surface enrichment and grain boundary segregation of niobium in Inconel 718 single- and polycrystals, *Scripta Metallurgica et Materialia* 31 (1994) 345–350. [https://doi.org/10.1016/0956-716X\(94\)90294-1](https://doi.org/10.1016/0956-716X(94)90294-1).
- [191] M. Gao, D. J. Dwyer, R. P. Wei, Niobium enrichment and environmental enhancement of creep crack growth in nickel-base superalloys, *Scripta Metallurgica et Materialia* 32 (1995) 1169–1174. [https://doi.org/10.1016/0956-716X\(95\)00120-K](https://doi.org/10.1016/0956-716X(95)00120-K).
- [192] 11067 Aluminum powder, -325 mesh, 99.5% (metals basis), in: Alfa Aesar, Product specification. Available online: <https://www.alfa.com/it/prodspec/011067> (last access: 6th June 2019).
- [193] W. Vanderlinde, Scanning Electron Microscopy, in: *Microelectronics Failure Analysis*, 5th edition, Chapter 12: General Imaging Techniques, ASTM International, Materials Park, Ohio, USA, 2004, pp. 559–573. ISBN 0-87170-804-3.
- [194] M. Calandri, D. Manfredi, F. Calignano, E. P. Ambrosio, S. Biamino, R. Lupoi, D. Ugues, Solution Treatment Study of Inconel 718 Produced by SLM Additive Technique in View of the Oxidation Resistance, *Advanced Engineering Materials* 20 (2018) 1–16. <https://doi.org/10.1002/adem.201800351>.
- [195] JEOL Ltd., SEM Q&A. In JEOL USA Electron Optics Documents & Downloads. Available online: <https://www.jeolusa.com/RESOURCES/Electron-Optics/Documents-Downloads> (last access: 6th June 2019).
- [196] M. M. Nowell, R. A. Witt, B. W. True, EBSD Sample Preparation: Techniques, Tips, and Tricks, *Microscopy Today* 13 (2005) 44–49. <https://doi.org/10.1017/S1551929500053669>.
- [197] Vander Voort Metallography, Failure Analysis & Archeometallography Consulting - EBSD. Available online: <http://www.georgevandervoort.com/metallography/general/ebsd.html> (last access: 6th June 2019).
- [198] ARGUS™ FSE/BSE imaging system for the e⁻Flash detector, in: Bruker Nano GmbH (www.bruker.com/quantax-ebsd), Product specification. Available online: https://www.bruker.com/fileadmin/user_upload/8-PDF-Docs/X-rayDiffraction_ElementalAnalysis/Microanalysis_EBSD/Flyers/Fly_fse_bse_en_rev3_lores.pdf (last access: 6th June 2019).

- [199] T. Rymer, *Electron Diffraction (Science Paperbacks)*, Chapman & Hall, London, UK, 1975. ISBN 0412212404.
- [200] Z. Yan, W. Liu, Z. Tang, X. Liu, N. Zhang, M. Li, H. Zhang, Review on thermal analysis in laser-based additive manufacturing, *Optics and Laser Technology* 106 (2018) 427–441. <https://doi.org/10.1016/j.optlastec.2018.04.034>.
- [201] P. A. Hooper, Melt pool temperature and cooling rates in laser powder bed fusion, *Additive Manufacturing* 22 (2018) 548–559. <https://doi.org/10.1016/j.addma.2018.05.032>.
- [202] S. Li, H. Xiao, K. Liu, W. Xiao, Y. Li, X. Han, J. Mazumder, L. Song, Melt-pool motion, temperature variation and dendritic morphology of Inconel 718 during pulsed- and continuous-wave laser additive manufacturing: A comparative study, *Materials and Design* 119 (2017) 351–360. <https://doi.org/10.1016/j.matdes.2017.01.065>.
- [203] J. Song, Y. Chew, G. Bi, X. Yao, B. Zhang, J. Bai, S. K. Moon, Numerical and experimental study of laser aided additive manufacturing for melt-pool profile and grain orientation analysis, *Materials and Design* 137 (2018) 286–297. <https://doi.org/10.1016/j.matdes.2017.10.033>.
- [204] H. L. Wei, J. Mazumder, T. DebRoy, Evolution of solidification texture during additive manufacturing, *Scientific Reports* 5 (2015) 1–7. <https://doi.org/10.1038/srep16446>.
- [205] X. Wang, K. Chou, Electron Backscatter Diffraction Analysis of Inconel 718 Parts Fabricated by Selective Laser Melting Additive Manufacturing, *JOM* 69 (2017) 402–408. <https://doi.org/10.1007/s11837-016-2198-1>.
- [206] R. Acharya, J. A. Sharon, A. Staroselsky, Prediction of microstructure in laser powder bed fusion process, *Acta Materialia* 124 (2017) 360–371. <https://doi.org/10.1016/j.actamat.2016.11.018>.
- [207] H. L. Wei, J. W. Elmer, T. DebRoy, Origin of grain orientation during solidification of an aluminum alloy, *Acta Materialia* 115 (2016) 123–131. <https://doi.org/10.1016/j.actamat.2016.05.057>.
- [208] X. Wang, P. W. Liu, Y. Ji, Y. Liu, M. H. Horstemeyer, L. Chen, Investigation on Microsegregation of IN718 Alloy During Additive Manufacturing via Integrated Phase-Field and Finite-Element Modeling, *Journal of Materials Engineering and Performance* 28 (2019) 657–665. <https://doi.org/10.1007/s11665-018-3620-3>.
- [209] M. Pröbstle, S. Neumeier, J. Hopfenmüller, L. P. Freund, T. Niendorf, D. Schwarze, Superior creep strength of a nickel-based superalloy produced by selective laser melting, *Materials Science & Engineering A* 674 (2016) 299–307. <https://doi.org/10.1016/j.msea.2016.07.061>.
- [210] L. A. Chapman, Application of high temperature DSC technique to nickel based superalloys, *Journal of Materials Science* 39 (2004) 7229–7236. <https://doi.org/10.1023/B:JMSE.0000048736.86794.12>.
- [211] K.-M. Chang, A. H. Nahm, Rene 220: 100°F Improvement Over Alloy 718, in: *Superalloys 718 - Metallurgy and Applications* (Ed.: E. A. Loria), The Minerals, Metals & Materials Society (1989) 631–646. https://doi.org/10.7449/1989/Superalloys_1989_631_646.
- [212] S. Li, Q. Wei, Y. Shi, C. K. Chua, Z. Zhu, D. Zhang, Microstructure Characteristics of Inconel 625 Superalloy Manufactured by Selective Laser Melting, *Journal of Materials Science & Technology* 31 (2015) 946–952. <https://doi.org/10.1016/j.jmst.2014.09.020>.

- [213] C. Li, R. White, X. Y. Fang, M. Weaver, Y. B. Guo, Microstructure evolution characteristics of Inconel 625 alloy from selective laser melting to heat treatment, *Materials Science and Engineering A* 705 (2017) 20–31. <https://doi.org/10.1016/j.msea.2017.08.058>.
- [214] L. Wenchang, X. Furen, Y. Mei, C. Zonglin, W. Shaogang, L. Weihong, Quantitative Phase Analysis of Inconel 718 by X-ray Diffraction, *Journal Of Materials Science Letters* 16 (1997) 769–771. <https://doi.org/10.1023/A:1018553703030>.
- [215] W. C. Liu, M. Yao, Z. L. Chen, S. G. Wang, Niobium segregation in Inconel 718, *Journal of Materials Science* 34 (1999) 2583–2586. <https://doi.org/10.1023/A:1004648615561>.
- [216] F. Zhang, L. E. Levine, A. J. Allen, M. R. Stoudt, G. Lindwall, E. A. Lass, M. E. Williams, Y. Idell, C. E. Campbell, Effect of heat treatment on the microstructural evolution of a nickel- based superalloy additive-manufactured by laser powder bed fusion, *Acta Materialia* 152 (2018) 200–214. <https://doi.org/10.1016/j.actamat.2018.03.017>.
- [217] X. Li, J. J. Shi, C. H. Wang, G. H. Cao, A. M. Russell, Z. J. Zhou, C. P. Li, G. F. Chen, Effect of heat treatment on microstructure evolution of Inconel 718 alloy fabricated by selective laser melting, *Journal of Alloys and Compounds* 764 (2018) 639–649. <https://doi.org/10.1016/j.jallcom.2018.06.112>.
- [218] INCONEL Alloy 600. In Special Metals Company, Publication Number SMC-027. 2008. Available online: http://www.specialmetals.com/assets/smc/documents/inconel_alloy_600.pdf (last access: 6th June 2019).
- [219] G. P. Airey, Microstructural Aspects of the Thermal Treatment of Inconel Alloy 600, *Metallography* 13 (1980) 21–41. [https://doi.org/10.1016/0026-0800\(80\)90020-8](https://doi.org/10.1016/0026-0800(80)90020-8).
- [220] N. S. McIntyre, D. G. Zetaruk, D. Owen, XPS study of the initial growth of oxide films on Inconel 600 alloy, *Applications of Surface Science* 2 (1978) 55–73. [https://doi.org/10.1016/0378-5963\(78\)90006-5](https://doi.org/10.1016/0378-5963(78)90006-5).
- [221] ICSC database - International Chemical Safety Cards 1531 – Chromia. Available online: https://www.ilo.org/dyn/icsc/showcard.display?p_lang=en&p_card_id=1531&p_version=2 (last access: 6th June 2019).
- [222] J. H. Chen, P. M. Rogers, J. A. Little, Oxidation behavior of several chromia-forming commercial nickel-base superalloys, *Oxidation of Metals* 47 (1997) 381–410. <https://doi.org/10.1007/BF02134783>.
- [223] J. Smialek, C. Lowell, Effects of Diffusion on Aluminum Depletion and Degradation of NiAl Coatings, *Journal of the Electrochemical Society* 121 (1974) 800–805. <https://doi.org/10.1149/1.2401922>.
- [224] Z. Zhang, B. Gleeson, K. Jung, L. Li, J. C. Yang, A diffusion analysis of transient subsurface γ' -Ni₃Al formation during β -NiAl oxidation, *Acta Materialia* 60 (2012) 5273–5283. <https://doi.org/10.1016/j.actamat.2012.06.021>.
- [225] H. Svensson, M. Christensen, P. Knutsson, G. Wahnström, K. Stiller, Influence of Pt on the metal-oxide interface during high temperature oxidation of NiAl bulk materials, *Corrosion Science* 51 (2009) 539–546. <https://doi.org/10.1016/j.corsci.2008.12.016>.

- [226] S. Shiomi, M. Miyake, T. Hirato, A. Sato, Aluminide Coatings Fabricated on Nickel by Aluminium Electrodeposition from DMSO₂-Based Electrolyte and Subsequent Annealing, *Materials Transactions* 52 (2011) 1216–1221. <https://doi.org/10.2320/matertrans.M2010421>.
- [227] X. Montero, M.C. Galetz, M. Schütze, Low-activity aluminide coatings for superalloys using a slurry process free of halide activators and chromates, *Surface & Coatings Technology* 222 (2013) 9–14. <https://doi.org/10.1016/j.surfcoat.2013.01.033>.
- [228] D. F. Susan, A. R. Marder, Ni-Al composite coatings: Diffusion analysis and coating lifetime estimation, *Acta Materialia* 49 (2001) 1153–1163. [https://doi.org/10.1016/S1359-6454\(01\)00022-2](https://doi.org/10.1016/S1359-6454(01)00022-2).
- [229] C. Choux, A. J. Kulińska, S. Chevalier, High temperature reactivity of nickel aluminide diffusion coatings, *Intermetallics* 16 (2008) 1–9. <https://doi.org/10.1016/j.intermet.2007.07.014>.
- [230] D. Kim, J. H. Chang, J. Park, J. J. Pak, Formation and behavior of Kirkendall voids within intermetallic layers of solder joints, *Journal of Materials Science: Materials in Electronics* 22 (2011) 703–716. <https://doi.org/10.1007/s10854-011-0357-2>.
- [231] J. Angenete, K. Stiller, E. Bakchinova, Microstructural and microchemical development of simple and Pt-modified aluminide diffusion coatings during long term oxidation at 1050 °C, *Surface & Coatings Technology* 176 (2004) 272–283. [https://doi.org/10.1016/S0257-8972\(03\)00767-9](https://doi.org/10.1016/S0257-8972(03)00767-9).

List of symbols and acronyms

A1, A2, A3, A4	Samples aluminized in the intermediate temperature test (table 2.12)
AM	Additive Manufacturing
ANOVA	Analysis of Variance
APB	Antiphase Boundaries
ASB	Anti-structure Bridge
B1, B2	Bars aluminized in half embedded mode (table 2.13)
BCT	Body Centered Tetragonal
BD	Building Direction
BSE	Backscattered Electrons
C_0	Nominal composition
C_L	Solute concentration in the liquid
C_S	Solute concentration in the solid
$C_{S,mean}$	Mean solute concentration in the solid
CAD	Computer Aided Design
CCT	Continuous Cooling Transformation curves
CTE	Thermal expansion Coefficient
CVD	Chemical Vapor Deposition
$d_{\{hkl\}}$	Interplanar distance of the lattice planes with h, k, l Miller indices
D_L	Solute diffusivity in the liquid
D_m	Displacement Vector (figure 3.32)
D_S	Solute diffusivity in the solid
DOF	Degree of Freedom
DSC	Differential Scanning Calorimetry
EBM	Electron Beam Melting
EBSD	Electron Backscattered Diffraction
EDM	Electrical Discharge Machining

EDS	Energy Dispersive Spectroscopy
EI	Elongation to failure
ENDO	Endothermal peak in DSC analysis
EXO	Exothermal peak in DSC analysis
F	F (Fisher) ratio
f_n	Atomic form factor
f_L	Volume fractions of the liquid
f_S	Volume fractions of the solid
FCC	Face Centered Cubic
FESEM	Field Emission Scanning Electron Microscopy
FIB	Focused Ion Beam
FWHM	Full Width at Half Maximum
G	Temperature gradient
H. p.	Horizontal plane, i.e. normal to BD of the SLM sample
h, k, l	Miller indices
H1, H2, H3, H4	Samples aluminized in the high temperature test (table 2.14)
HAZ	Heat Affected Zone
HB	Brinell Hardness
hd	hatching distance
HIP	Hot Isostatic Pressing
HT	Heat Treatment
HTLA	High Temperature Low Activity
HV	Vickers Microhardness
IDL	Interdiffusion Layer
IPF	Inverse Pole Figure
k	Partition coefficient C_S/C_L
k_d	Wavevectors of the diffracted electron beam in SAED analysis
k_i	Wavevectors of the incident electron beam in SAED analysis
k_p	Parabolic constant
$k_{p,init}$	Parabolic constant during the transient oxidation regime

$k_{p,stat}$	Parabolic constant during the stationary oxidation regime
L	Length scale of the microsegregation
\mathcal{L}	Linear size of a precipitate
$L(\mathbf{R})$	Lattice factor
L1, L2, L3, L4	Samples aluminized in the low temperature test (table 2.15)
LENS	Laser Engineered Net Shaping
LMWD	Laser Metal Wire Deposition
LOM	Laminated Object Manufacturing
LTHA	Low Temperature High Activity
M_{mol}	Molar mass
MPB	Molten Pool Boundaries
MS	Mean Squares
n	creep exponent
OR	Overlap Ratio
P	Laser Power
\mathcal{P}	Pixel size of a precipitate in a FESEM image
PF	Pole Figure
p_{O_2}	Oxygen partial pressure
$p_{O_2,eq}$	Oxygen partial pressure at the metal/oxide equilibrium
PLT	Powder Layer Thickness
PPB	Prior Particle Boundaries
PWHT	Post-Weld Heat Treatment
Q	activation energy for the creep
R	growth rate
RT	Product between the gas constant ($8.314 \text{ J mol}^{-1} \text{ K}^{-1}$) and the absolute temperature in Arrhenius equations
\mathbf{R}	Reciprocal lattice vector
R1, R2, R3	Sample coordinates system axes (R1 denotes the axis parallel to the building direction of the sample)
\mathbf{s}	Unit vector along the diffracted beam in SAED analysis
\mathbf{s}_0	Unit vector along the incident beam in SAED analysis
S	FESEM image length scale in nm/pixel

s	Oxide thickness
$S(\mathbf{R})$	Structure factor
s, s'	Slip vectors (figure 3.32)
SAED	Selective Area Electron Diffraction
SE	Secondary Electrons
SEM	Scanning Electron Microscopy
SLM	Selective Laser Melting
SLS	Selective Laser Sintering
SS	Sum of Squares
SSGB	Solidification Sub-Grain Boundary
STEM	Scanning/Transmission Electron Microscopy
T	Temperature
t	Time or duration
T_1	Start solidification temperature
T_{ag1}	First aging temperature
t_{ag1}	First aging duration
T_{ag2}	Second aging temperature
t_{ag2}	Second aging duration
t_f	Local solidification time
t_{init}	Duration of the transient oxidation regime
T_L	Liquidus curve
T_m	Melting point
T_{sol}	Solution annealing temperature
t_{sol}	Solution annealing duration
TCP	Topologically Close Packed phases
TEM	Transmission Electron Microscopy
TMA	Thermomechanical Analysis
\mathbf{U}	Direct lattice vector
UC	Ultrasonic Consolidation
UTS	Ultimate Tensile Stress

UVW	Local coordinate system in figure 2.12
v	Scan speed
V_{mol}	Molar volume
V_L	Liquid molar volume
V_S	Solid molar volume
V. p.	Vertical plane, i.e. parallel to BD of the SLM sample
VED	Volumetric Energy Density
w	Sample weight
w_{H_2O}	Sample weight when immersed in water
XRD	X-Ray Diffraction
XYZ	Sample coordinate system in figure 2.12
YS	Yield Stress
Z	Atomic number
ΔG°	Standard Gibbs free energy of formation
Δk	Scattering vector in SAED analysis
$\Delta m/A$	Mass gain per unit of exposed area during hot oxidation
ΔT	Solidification range
ε	Strain
$\dot{\varepsilon}$	Strain rate
θ	Diffraction angle in XRD analysis
θ_{mis}	Highest mis-orientation (figure 2.13)
θ_{th}	Threshold mis-orientation value for grain boundary (figure 2.13)
λ	Wavelength
ρ	Density
ρ_{ap}	Apparent density
ρ_{H_2O}	Water density
σ	Stress
φ, θ, ψ	Euler Angles